

Development, Implementation and Validation of Excited-State Gradients for Local Hybrid Functionals

vorgelegt von

M. Sc.

Robin Grotjahn

ORCID: 0000-0002-7160-2581

an der Fakultät II - Mathematik und Naturwissenschaften
der Technischen Universität Berlin
zur Erlangung des akademischen Grades

Doktor der Naturwissenschaften

– Dr. rer. nat. –

genehmigte Dissertation

Promotionsausschuss:

Vorsitzender: Prof. Dr. Reinhard Schomäcker

Gutachter: Prof. Dr. Martin Kaupp

Gutachter: Prof. Dr. Christoph Jacob

Tag der wissenschaftlichen Aussprache: 25. Februar 2021

Berlin 2021

Für meine Eltern

Acknowledgements

First of all, I would like to thank Prof. Martin Kaupp for supervising my doctoral thesis. The regular and intensive exchange about my projects and the great freedom in working on them were great conditions for my scientific development. I am very grateful for the numerous opportunities to participate in summer and winter schools, workshops, and conferences. Moreover, the possibility for a research stay at UC Irvine, California has enriched my doctoral studies enormously.

In this regard I also thank Prof. Filipp Furche for the opportunity to be part of his research group at UC Irvine during my research stay. His great hospitality and the intensive scientific exchange made my stay very pleasant and rewarding. I would like to thank Toni Maier for the numerous discussions on theoretical issues and implementation details, Sascha Klawohn for the discussions on implementation issues and his patient assistance with technical problems, and Marc Reimann for the discussions on symmetry. I also thank Caspar Schattenberg and Susanne Fürst for the pleasant working atmosphere in the office and for always being the first point of contact for problems and questions. Furthermore, I thank all current and former members of the working group Kaupp for the good cooperation and the scientific exchange.

I acknowledge scholarships from Fonds der chemischen Industrie (German Chemical Industry Fund) and Studienstiftung des deutschen Volkes (German Academic Scholarship Foundation). Additional funding was provided by Deutsche Forschungsgemeinschaft (German Research Foundation) through Project No. KA1187/14-1 and under Germany's Excellence Strategy – EXC 2008/1-390540038 – UniSysCat.

Abstract

In the present work, excited-state nuclear gradients within linear-response time-dependent density functional theory are developed for local hybrid functionals (local hybrids). The derived equations are implemented in the quantum chemical program TURBOMOLE using an efficient seminumerical integration scheme. The implementation is used to validate local hybrids for a range of excited-state properties that have not been accessible with this class of functionals before. While the performance of local hybrids for excited-state structural parameters, adiabatic singlet excitation energies, fluorescence energies, and harmonic excited-state vibrational frequencies is comparable to that of established global and range-separated hybrid functionals, results for adiabatic triplet excitation energies and phosphorescence energies are outstanding. Combined with a robust performance for the prediction of the shapes of vibronic spectra, this makes local hybrids a promising tool for the calculation of phosphorescence spectra.

In a second part, local hybrids are assessed for the prediction of more fundamental properties namely electric dipole moments and polarizabilities. Competitive and robust performance was found for both properties, in particular with more recent local hybrids. Compared to some highly parameterized global hybrid functionals, no signs of overparameterization leading to unrealistic electron densities and related properties were observed. It is argued that this also supports the optimization procedure used in the development of recent local hybrids.

Zusammenfassung

In der vorliegenden Arbeit werden Gradienten elektronisch angeregter Zustände bezüglich Kernausslenkungen innerhalb der zeitabhängigen Dichtefunktionaltheorie für lokale Hybridfunktionale (lokale Hybride) entwickelt. Die abgeleiteten Gleichungen werden im quantenchemischen Programm TURBOMOLE unter Verwendung eines effizienten seminumerischen Integrationsschemas implementiert. Die Implementierung wird verwendet, um lokale Hybride für eine Reihe von Eigenschaften angeregter Zustände zu validieren, die mit dieser Funktionalklasse bisher nicht zugänglich waren. Während die Leistungsfähigkeit lokaler Hybride für Strukturparameter angeregter Zustände, adiabatische Singulett-Anregungsenergien, Fluoreszenzenenergien und harmonische Schwingungsfrequenzen angeregter Zustände mit der von etablierten globalen und reichweiten-separierten Hybridfunktionalen vergleichbar ist, sind die Ergebnisse für adiabatische Triplett-Anregungsenergien und Phosphoreszenzenenergien herausragend. Kombiniert mit einer robusten Leistung für die Vorhersage der Form von vibronischen Spektren macht dies lokale Hybride zu einem vielversprechenden Werkzeug für die Berechnung von Phosphoreszenzspektren.

In einem zweiten Teil werden lokale Hybride für die Vorhersage grundlegenderer Eigenschaften, nämlich elektrischer Dipolmomente und Polarisierbarkeiten, untersucht. Dabei wurde eine solide und konkurrenzfähige Leistungsfähigkeit für beide Eigenschaften gefunden, insbesondere mit neueren lokalen Hybriden. Im Vergleich zu einigen hochgradig parametrisierten globalen Hybridfunktionalen wurden keine Anzeichen einer Überparametrisierung beobachtet, die zu unrealistischen Elektronendichten und damit verbundenen Eigenschaften führten. Es wird dargelegt, dass diese Befunde auch die Eignung des Optimierungsverfahrens, das bei der Entwicklung neuerer lokaler Hybride angewandt wird, bestätigen.

List of Publications

- I. R. Grotjahn, T. M. Maier, J. Michl, and M. Kaupp. Development of a TDDFT-Based Protocol with Local Hybrid Functionals for the Screening of Potential Singlet Fission Chromophores. *J. Chem. Theory Comput.* **2017**, *13*, 4984–4996.
- II. R. Grotjahn, F. Furche and M. Kaupp. Development and Implementation of Excited-State Gradients for Local Hybrid Functionals. *J. Chem. Theory Comput.* **2019**, *15*, 5508–5522.
- III. R. Grotjahn and M. Kaupp. Validation of Local Hybrid Functionals for Excited States: Structures, Fluorescence, Phosphorescence, and Vibronic Spectra. *J. Chem. Theory Comput.* **2020**, *16*, 5821–5834.
- IV. R. Grotjahn, G. J. Lauter, M. Haasler and M. Kaupp. Evaluation of Local Hybrid Functionals for Electric Properties: Dipole Moments and Static and Dynamic Polarizabilities. *J. Phys. Chem. A* **2020**, *124*, 8346–8358.
- V. H. Dolati, L. C. Haufe, L. Denker, A. Lorbach, R. Grotjahn, G. Hörner, and R. Frank. Two π -Electrons Make the Difference: From BODIPY to BODIIM Switchable Fluorescent Dyes. *Chem. Eur. J.* **2020**, *26*, 1422–1428.
- VI. J. Wen, M. Turowski, P. I. Dron, J. Chalupský, R. Grotjahn, T. M. Maier, S. M. Fatur, Z. Havlas, J. C. Johnson, M. Kaupp, and J. Michl. Electronic States of 2,3-Diamino-1,4-naphthoquinone and Its N-Alkylated Derivatives. *J. Phys. Chem. C* **2020**, *124*, 60–69.
- VII. S. G. Balasubramani, G. P. Chen, S. Coriani, M. Diedenhofen, M. S. Frank, Y. J. Franzke, F. Furche, R. Grotjahn, M. E. Harding, C. Hättig *et al.* TURBOMOLE: Modular program suite for ab initio quantum-chemical and condensed-matter simulations. *J. Chem. Phys.* **2020**, *152*, 184107.
- VIII. M. Haasler, T. M. Maier, R. Grotjahn, S. Gückel, A. V. Arbuznikov, and M. Kaupp. A Local Hybrid Functional with Wide Applicability and Good Balance between (De)Localization and Left–Right Correlation. *J. Chem. Theory Comput.* **2020**, *16*, 5645–5657.

Copyright

- Chapter 3, Section 4.3.2 starting from the second paragraph including Figure 4.3, Sections 4.3.3, 5.2.1, 5.3.1, 5.4.1, 5.5.1, and Appendices A.1, A.3, A.4, A.8, Table A.4, and parts of Sections 5.1 and 5.6 are reproduced/ adapted and reprinted with permission from R. Grotjahn, F. Furche and M. Kaupp. Development and Implementation of Excited-State Gradients for Local Hybrid Functionals. *J. Chem. Theory Comput.* **2019**, *15*, 5508–5522, DOI: 10.1021/acs.jctc.9b00659. Copyright 2019 American Chemical Society.
- Sections 5.2.2, 5.2.3, 5.2.4, 5.3.2, 5.4.2, 5.4.3, 5.5.2, Appendices A.7, A.9, A.10, and A.11, as well as parts of Sections 5.1 and 5.6 are reproduced/ adapted and reprinted with permission from R. Grotjahn and M. Kaupp. Validation of Local Hybrid Functionals for Excited States: Structures, Fluorescence, Phosphorescence, and Vibronic Spectra. *J. Chem. Theory Comput.* **2020**, *16*, 5821–5834, DOI: 10.1021/acs.jctc.0c00520. Copyright 2020 American Chemical Society.
- Table 2.1, Chapter 6, and Appendix A.12 are reproduced/ adapted and reprinted with permission from R. Grotjahn, G. J. Lauter, M. Haasler and M. Kaupp. Evaluation of Local Hybrid Functionals for Electric Properties: Dipole Moments and Static and Dynamic Polarizabilities. *J. Phys. Chem. A* **2020**, *124*, 8346–8358, DOI: 10.1021/acs.jpca.0c06939. Copyright 2020 American Chemical Society.

List of Abbreviations

AA	adiabatic approximation
AC	adiabatic connection
AEE	adiabatic excitation energy
AO	atomic orbital
au	atomic units
BO	Born–Oppenheimer
BODIPY	boron dipyrromethene (dipyrrometheneboron difluoride)
CASPT2	complete active space with second-order perturbation theory
CASSCF	complete active space self-consistent field
CBS	complete basis set
CC	coupled cluster / carbon-carbon
CF	calibration function
CI	configuration interaction
CN	carbon-nitrogen
CO	carbon-oxygen / carbonyl
CS/Se	carbon-sulfur/selenium / thionyl, selenonyl
CIS	configuration interaction with singles
COSX	chain-of-spheres exchange
CPU	central processing unit
DFT	density functional theory
DH	double hybrid
EOM-CCSD	equation-of-motion coupled-cluster singles and doubles
EH	element hydrogen
ES	excited state
EXX	exact exchange
FC	Franck–Condon
FD	finite difference
GGA	generalized gradient approximation
GH	global hybrid functional
GS	ground state
HF	Hartree–Fock
hGGA	hyper generalized gradient approximation
HOMO	highest occupied molecular orbital
KS	Kohn–Sham

LCAO	linear combination of atomic orbitals
LDA	local density approximation
LH	local hybrid functional
LMF	local mixing function
LR	linear response
LSDA	local spin-density approximation
LUMO	lowest unoccupied molecular orbital
MAE	mean absolute error
MaxE	maximum error
MCSCF	multi-configurational self-consistent field
mGGA	meta generalized gradient approximation
MO	molecular orbital
MP	Møller–Plesset
MSE	mean signed error
NSP	non-spin-polarized
PES	potential energy surface
pig	partial integration gauge
RHS	right-hand side
RI	resolution-of-identity
RMSE	root-mean-square error
RPA	random phase approximation
RS	range-separation
RSH	range-separated hybrid functional
SAC-CI	symmetry adapted cluster configuration interaction
SCF	self consistent field
SOPPA	second-order polarization propagator approximation
SP	spin-polarized
SR	short range
TDA	Tamm–Dancoff approximation
TDDFT	time-dependent density functional theory
TDKS	time-dependent Kohn–Sham
UEG	uniform electron gas
UV-Vis-NIR	ultraviolet-visible-near infrared
VEE	vertical excitation energy
XC	exchange-correlation
ZPVE	zero-point vibrational energy

Contents

1	Introduction	1
2	Theoretical Background	5
2.1	Fundamentals of Quantum Chemistry	5
2.1.1	The Wave Function	5
2.1.2	The Schrödinger Equation	7
2.1.3	The Hartree–Fock Method	8
2.1.4	Basis Sets and Integral Evaluation	10
2.1.5	Post Hartree–Fock Methods	11
2.2	Density Functional Theory	13
2.2.1	The Electron Density as the Central Quantity	13
2.2.2	Kohn–Sham Density Functional Theory	15
2.2.3	The Quest for the Exact Exchange–Correlation Functional	16
2.2.4	Exchange–Correlation Functional Approximations	19
2.3	Local Hybrid Functionals	27
2.3.1	General Formulation	28
2.3.2	Local Mixing Functions	29
2.3.3	Calibration Functions	31
2.3.4	Established Local Hybrids Used in this Work	33
2.4	Excited State Theory	36
2.4.1	Response Theory	37
2.4.2	Time-Dependent Density Functional Theory	42
2.4.3	Vibrational Corrections	50
3	Development of Excited-State Gradients for Local Hybrid Functionals	57
3.1	Derivation of TDDFT Excited State Gradients	57
3.2	Derivation of the LH Hyper-Kernel and Potential/ Kernel Gradients	63
3.2.1	Formalism and Notation	64
3.2.2	The LH Hyper-Kernel	72
3.2.3	The LH Potential and Kernel Gradients	75

4	Implementation	79
4.1	Existing Program Structure	79
4.1.1	The Software Package TURBOMOLE	79
4.1.2	The egrad Program	80
4.1.3	Local Hybrid Specific Software Infrastructure	83
4.2	Implementation of ES Gradients for Local Hybrids	84
4.2.1	Implementation of the Contracted LH Hyper-Kernel	84
4.2.2	Implementation of the LH Potential and Kernel Gradients	86
4.3	Technical Evaluation	87
4.3.1	Numerical Validation	87
4.3.2	Grid Dependence	89
4.3.3	Neglect of the Current Density Response	93
4.3.4	Timings	94
5	Validation of Local Hybrids for Excited-State Properties	101
5.1	Introduction	101
5.2	Computational Details	104
5.2.1	Furche and Ahlrichs Test Set	104
5.2.2	Jaquemin Test Set	105
5.2.3	Adamo and Ehara Test Set	106
5.2.4	Dierksen and Grimme Test Set	107
5.3	Results for Excited-State Structures	108
5.3.1	Furche and Ahlrichs Test Set	108
5.3.2	Jacquemin Test Set	109
5.4	Results for Excitation Energies	112
5.4.1	Adiabatic Excitation Energies and 0–0 Energies	112
5.4.2	Fluorescence Energies	114
5.4.3	Phosphorescence Energies	115
5.5	Results for Vibrational Frequencies and Vibronic Spectra	118
5.5.1	Harmonic Excited-State Vibrational Frequencies	118
5.5.2	Vibronic Spectra	119
5.6	Conclusions	127
6	Validation of Local Hybrid Functionals for Electric Properties	129
6.1	Introduction	129
6.2	Computational Details	131

6.3	Results	134
6.3.1	Dipole Moments	134
6.3.2	Static Polarizabilities	139
6.3.3	Influence of the LMF Prefactor and GH Mixing Factor	142
6.3.4	Dynamic Polarizabilities	144
6.4	Conclusions	146
7	Conclusions and Outlook	149
A	Appendix	155
A.1	Solutions for the Energy-Weighted Difference Density Matrix \mathbf{W}	155
A.2	Derivation of the Local Hybrid Hyper-Kernel	155
A.3	Derivatives w.r.t. MO Coefficients	157
A.4	Expanded Form of Operators	158
A.4.1	Semilocal Potential Operators	158
A.4.2	Semilocal Gradient Operators	159
A.5	Timings	160
A.6	Grid Dependence	162
A.7	Effect of the Calibration Function on ESs	165
A.8	Additional Statistics for the Furche and Ahlrichs Test Set	166
A.9	Analysis of Excitation Character in Carbonyl Compounds	170
A.10	New Reference Values for the Adamo and Ehara Test Set	171
A.11	Vibronic Absorption Spectra	172
A.12	Additional Data for Studies on Dipole Moments and Polarizabilities	177
	Bibliography	179

1 Introduction

Chemistry tries to understand the properties and behavior of matter using the concept of molecules, atoms, and electrons. The submicroscopic size of these particles puts them in the realm of quantum mechanics. Citing Paul Dirac, the physical laws to treat molecular systems are “completely known, and the difficulty is only that the exact application of these laws leads to equations much too complicated to be soluble.”^[1] Therefore, it has been and still is the mission of quantum chemistry to develop methods that produce approximate yet useful results within reasonable computation times. One of the most successful theories in this regard is density functional theory (DFT)^[2] within the Kohn–Sham formalism,^[3] which has allowed calculations for systems with hundreds of atoms within a few hours of computation time already on personal computers from the 1990s.^[4] With today’s hardware, parallel computing architectures, and advances in algorithms, calculations on systems with several thousand atoms are feasible.^[5] Of course, even the fastest calculation is useless if the results are not sufficiently accurate or cannot be trusted. The accuracy of DFT calculations crucially depends on the chosen exchange-correlation (XC) functional. Hundreds of XC functionals were developed over time,^[6,7] and selecting an appropriate functional can be a difficult task. Although there are attempts to automatize this step,^[8] the traditional approach relies on the user’s experience and knowledge from benchmark studies.^[6,7] Many of the most popular and accurate XC functionals are so-called hybrid functionals that incorporate a portion of exact exchange (EXX) to mitigate unphysical self-interaction.^[9,10] The two most widespread hybrid schemes are global hybrid functionals (global hybrids), where a globally constant EXX admixture is used, and range-separated hybrid functionals for which the amount of EXX is flexible along the interelectronic coordinate.

Another class of hybrid functionals and the focus of this work are local hybrid functionals (local hybrids).^[11,12] They use a local mixing function (LMF) that controls the position-dependent admixture of EXX within real space. Thereby, the self-interaction error is reduced adaptively in different electronic regions of the system. One of the earliest local hybrids by Bahmann *et al.* from 2007 has shown competitive performance for thermochemistry despite using just local spin-density exchange and correlation functionals for

the DFT part and a simple one-parameter LMF model based on the well-known iso-orbital indicator τ_W/τ .^[13] Since then, the field has made massive progress.^[12] Several conceptual problems were addressed including the ambiguity encountered when mixing different exchange energy densities known as the “gauge problem”,^[14–16] new LMF models were proposed, and several functionals were constructed.^[12] One recently reported local hybrid is LH20t,^[17] which exhibits wide chemical applicability and excellent performance for the GMTKN55 test suite for main-group energetics outperforming all global hybrids.^[17] Apart from this general applicability, local hybrids are particularly well suited for problems that involve a fine balance of mitigating delocalization errors and emulating left-right correlation as encountered, e.g., in mixed-valence systems.^[17–20] Another area where local hybrids were shown to provide substantial benefits is electronic excitations. The method of choice^[21] to treat excitations within DFT is linear-response time-dependent density functional theory (LR-TDDFT)^[22] that just like conventional DFT offers an excellent cost-performance ratio. Development of LR-TDDFT excitation energies for a given XC functional involves the implementation of the XC kernel, which was reported by Maier *et al.* for local hybrids.^[23] While the performance for singlet valence excitations was found to be comparable to that of standard global hybrids,^[17,24,25] remarkable performance was seen for triplet excitations, Rydberg excitations, and first-row core excitations from the Thiel^[26,27] and Tozer^[28,29] test sets.^[17,24] The good performance for triplet excitations has been deployed for the development of a local hybrid based protocol for the screening of singlet fission chromophores,^[25] where accurate predictions of singlet-triplet gaps are crucial. Even for the quite demanding singlet fission test set of captodatively stabilized biradicaloids from that work, it could be shown that some local hybrids reach an accuracy close to 0.2 eV for the prediction of triplet absorption energies, which is the targeted accuracy for reliable predictions in this field.^[25] The new protocol has recently been applied in a spectroscopic study of potential singlet fission chromophores.^[30]

The above-mentioned findings refer to excitation energies obtained at ground-state structures, i.e. vertical excitation energies. Although they are in common use for the emulation of absorption spectra, they generally do not coincide with the experimentally measured absorption maxima.^[31,32] To obtain the proper shape and position of these maxima, vibronic effects have to be considered, which require knowledge of the ground- and excited-state minimum structures and vibrational frequencies. Furthermore, excited-state structures are required for the prediction of vertical emission energies such as fluorescence and phosphorescence energies. Insights into the structural changes during excitations can also provide a basis for a deeper understanding of the respective photophysical or photochemical processes. Since energy-based numerical optimizations of excited-state

structures become prohibitively expensive for larger molecules, excited-state analytical gradients are required for convenient access to excited-state structures and any related property. The first implementation of excited-state gradients within LR-TDDFT was realized in the CADPAC package by Van Caillie *et al.*^[33,34] Furche and Ahlrichs presented an alternative approach^[35] that was implemented in the TURBOMOLE program^[36,37] and which is the basis for the present work. Several implementations in other quantum chemistry codes with various modifications and extensions were reported since then.^[38–46]

To extend the applicability of local hybrids within LR-TDDFT beyond vertical excitation energies, the development and implementation of their excited-state gradients are reported here and constitute the core subject of this thesis. In general, a LR-TDDFT implementation of excited-state gradients requires the XC hyper-kernel, i.e. the third functional derivative of the XC energy w.r.t. to the density as well as the nuclear derivatives of the XC kernel and potential. Due to the position-dependent mixing of EXX in local hybrids, the derivation and implementation of higher-order functional derivatives for this class of functionals lead to several additional terms compared to global hybrids that also involve non-standard integrals. As already successfully done for LR-TDDFT energies^[23] and ground-state gradients,^[47] those are tackled here using seminumerical integration techniques.^[48]

The outline of this thesis is as follows. After a review of the underlying theory (Chapter 2), the necessary equations for an implementation are derived in Chapter 3. The implementation (Chapter 4) was realized in the TURBOMOLE program suite as an extension of the global hybrid excited-state gradients implementation in the **egrad** program by Furche and Ahlrichs.^[35] In Chapter 5, the new implementation is used to validate local hybrids for a wide range of excited-state properties including structural parameters, adiabatic excitation energies, 0–0 energies, emission energies, and harmonic vibrational frequencies. Moreover, the implementation is used for the emulation of absorption and emission spectra within the Franck–Condon approximation. In addition to the extensive studies for excited states, a more fundamental assessment of local hybrids is presented in Chapter 6. In this chapter, a comprehensive benchmark study for electric properties including dipole moments and static and dynamic polarizabilities is reported. This aims at analyzing if local hybrids “have strayed from the path toward the exact functional”, which was lately claimed to have happened with several other XC functionals developed past the year 2000 as they tend to fail more often at reproducing correct electron densities than earlier XC functionals.^[49–56]

2 Theoretical Background

In this chapter, the basics of quantum chemistry relevant to the derivations in subsequent chapters are reviewed. Starting with the Schrödinger equation and Hartree–Fock approximation, two different routes in quantum chemistry are discussed. On one side there are wave function based methods that aim at systematically improving on Hartree–Fock results by refining the ansatz for the wave function. The focus here is, however, on the other side, i.e. density functional theory which takes the electron density as the central quantity. The details of the theory are described and various approximations are discussed with an emphasis on local hybrid functionals which are most relevant for the work at hand. Finally, time-dependent density functional theory is presented as a method to treat excited states within density functional theory, and the formalism that is used to derive the excited-state gradients for local hybrid functionals is outlined.

2.1 Fundamentals of Quantum Chemistry

2.1.1 The Wave Function

According to the basic principles of quantum mechanics, the physical state of a particle is fully described by a ket $|\Psi\rangle$ that belongs to a given Hilbert space.^[57] In a measurement of a physical observable, the eigenvalues ε of a corresponding Hermitian operator with eigenstates $|\varepsilon\rangle$ are measured with the probability^[57]

$$P(\varepsilon) = |\langle\varepsilon|\Psi\rangle|^2. \quad (2.1)$$

$|\Psi\rangle$ may be expanded in an orthonormal set of position-spin kets $|n\rangle$

$$|\Psi\rangle = \sum_n |n\rangle \langle n|\Psi\rangle = \sum_n \Psi_n |n\rangle, \quad (2.2)$$

which in the limiting case of infinitesimally spaced position-spin kets becomes the integral

$$|\Psi\rangle = \int \Psi(\mathbf{x}) |\mathbf{x}\rangle d\mathbf{x} , \quad (2.3)$$

where \mathbf{x} is the collective variable for the position \mathbf{r} and spin projection σ of the particle, implying $\int d\mathbf{x} \equiv \sum_{\sigma} \int d\mathbf{r}$.^[57] The continuous function $\Psi(\mathbf{x})$ is called the wave function of the particle. Using eq. 2.1 for the probability of finding the particle at position \mathbf{x}' yields

$$P(\mathbf{x}') = |\langle \mathbf{x}' | \Psi \rangle|^2 = \left| \int \Psi(\mathbf{x}) \langle \mathbf{x}' | \mathbf{x} \rangle d\mathbf{x} \right|^2 = \left| \int \Psi(\mathbf{x}) \delta(\mathbf{x}' - \mathbf{x}) d\mathbf{x} \right|^2 = |\Psi(\mathbf{x}')|^2 \quad (2.4)$$

and therefore allows the interpretation of the wave function as a probability amplitude with its squared absolute value $|\Psi(\mathbf{x})|^2$ being the probability density at position \mathbf{x} .^[57] The extension to many-particle systems is straightforward, i.e.

$$|\Psi\rangle = \int \Psi(\mathbf{x}_1, \dots, \mathbf{x}_N) |\mathbf{x}_1\rangle \dots |\mathbf{x}_N\rangle d\mathbf{x}_1 \dots d\mathbf{x}_N , \quad (2.5)$$

where $\Psi(\mathbf{x}_1, \dots, \mathbf{x}_N)$ is the N -particle wave function. For the special case of indistinguishable particles, the position-spin kets may be denoted as $|\mathbf{x}_1 \dots \mathbf{x}_N\rangle$. Because the particles are indistinguishable, the ket $|\mathbf{x}_1 \mathbf{x}_2 \dots \mathbf{x}_N\rangle$ has to correspond to the same state as $|\mathbf{x}_2 \mathbf{x}_1 \dots \mathbf{x}_N\rangle$.^[57] Exploiting that the ket of any physical state is uniquely defined up to a phase factor $e^{i\alpha}$

$$|\mathbf{x}_1 \mathbf{x}_2 \dots \mathbf{x}_N\rangle = e^{i\alpha} |\mathbf{x}_2 \mathbf{x}_1 \dots \mathbf{x}_N\rangle = e^{i\alpha} e^{i\alpha} |\mathbf{x}_1 \mathbf{x}_2 \dots \mathbf{x}_N\rangle = e^{2i\alpha} |\mathbf{x}_1 \mathbf{x}_2 \dots \mathbf{x}_N\rangle \quad (2.6)$$

yields $e^{2i\alpha} = 1$ or $e^{i\alpha} = \pm 1$, so that for any N -particle state

$$|\mathbf{x}_1 \mathbf{x}_2 \dots \mathbf{x}_N\rangle = \pm |\mathbf{x}_2 \mathbf{x}_1 \dots \mathbf{x}_N\rangle \quad (2.7)$$

holds.^[57] Hence, the ket $|\mathbf{x}_1 \mathbf{x}_2 \dots \mathbf{x}_N\rangle$ is either symmetric or antisymmetric with respect to the interchange of the particle positions and the corresponding particles are called bosons and fermions, respectively. For fermions, the observation $|\mathbf{x}_1 \mathbf{x}_1 \dots \mathbf{x}_N\rangle = -|\mathbf{x}_1 \mathbf{x}_1 \dots \mathbf{x}_N\rangle$ implies that $|\mathbf{x}_1 \mathbf{x}_1 \dots \mathbf{x}_N\rangle$ is not a valid state, i.e. two fermions cannot take the same position and spin.^[57] For electrons, this is known as the Pauli exclusion principle.^[58] A fermionic N -particle state may be constructed as an antisymmetrized product of one-particle kets

$$|\mathbf{x}_1 \dots \mathbf{x}_N\rangle = \frac{1}{\sqrt{N!}} \sum_P (-1)^P |\mathbf{x}_{P(1)}\rangle \dots |\mathbf{x}_{P(N)}\rangle , \quad (2.8)$$

where the sum runs over all permutations P and the sign $(-1)^P$ gets positive for even numbers of interchanges in the permutation and negative for odd numbers of interchanges.^[57] Projection of a given state $|\Psi\rangle$ on this ansatz for the position-spin ket gives the corresponding antisymmetrized wave function.

2.1.2 The Schrödinger Equation

The time evolution of a quantum state $|\Psi(t)\rangle$ is described by the time-dependent Schrödinger equation

$$\hat{H}(t) |\Psi(t)\rangle = i \frac{\partial}{\partial t} |\Psi(t)\rangle , \quad (2.9)$$

where \hat{H} is the system's Hamiltonian. For this work, it seems natural to think of the system as some molecule exposed to an external time-dependent scalar potential $V_{\text{ext}}(t)$. The Hamiltonian may then be split up according to

$$\hat{H}(t) = \hat{T}_e + \hat{V}_{ee} + \hat{V}_{eN} + \hat{T}_N + \hat{V}_{NN} + \hat{V}_{\text{ext}}(t) , \quad (2.10)$$

into the operators for the kinetic energy of the electrons (\hat{T}_e) and nuclei (\hat{T}_N), the electron-electron (\hat{V}_{ee}), nucleus-nucleus (\hat{V}_{NN}) and electron-nucleus (\hat{V}_{eN}) potential operators and some external time-dependent scalar potential operator $\hat{V}_{\text{ext}}(t)$. Due to the substantial difference in the mass, and hence velocity, of electrons and atomic nuclei, their motions may be separated, i.e. the electrons can be imagined to move in a potential of fixed nuclei. This is known as the Born–Oppenheimer approximation.^[59,60] The total state $|\Psi(t)\rangle$ may be separated in an electronic $|\Psi_e(t)\rangle$ and a nuclear $|\Psi_N(t)\rangle$ state. Likewise, the nuclear part $\hat{T}_N + \hat{V}_{NN}$ of the Hamiltonian is separated out. The remaining electronic Hamiltonian reads

$$\begin{aligned} \hat{H}_e(t) &= \hat{T}_e + \hat{V}_{ee} + \hat{V}_{eN} + \hat{V}_{\text{ext}}(t) \\ &= - \sum_i \frac{1}{2} \nabla_i^2 + \sum_{i,j>i} \frac{1}{|\mathbf{r}_i - \mathbf{r}_j|} - \sum_{i,A} \frac{Z_A}{|\mathbf{R}_A - \mathbf{r}_i|} + \hat{V}_{\text{ext}}(t) , \end{aligned} \quad (2.11)$$

where the explicit form in the second line uses the iterator A for nuclei with coordinates \mathbf{R}_A and charge Z_A and i, j for electrons with coordinates \mathbf{r}_i and \mathbf{r}_j .^[61]

Restricting the external potential to a time-independent potential makes the Hamiltonian time-independent $\hat{H}_e(t) = \hat{H}_e(t_0)$ and eq. 2.9 is solved by

$$|\Psi(t)\rangle = e^{-i\hat{H}_e(t_0)(t-t_0)} |\Psi(t_0)\rangle , \quad (2.12)$$

where $|\Psi(t_0)\rangle$ is the state of interest at a fixed point in time t_0 .^[62] The time-evolution of a molecular system will be reconsidered in Section 2.4 and the focus here is on time-independent states $|\Psi\rangle := |\Psi(t_0)\rangle$, which are obtained as eigenstates of $\hat{H}_e := \hat{H}_e(t_0)$, i.e. from the time-independent Schrödinger equation

$$\hat{H}_e |\Psi\rangle = E |\Psi\rangle , \quad (2.13)$$

with the eigenvalue E corresponding to the energy of the state. The ground state (GS) of a system is the state $|\Psi_0\rangle$ which yields the smallest eigenvalue E_0 . Inserting $|\Psi_0\rangle$ in eq. 2.13 and multiplying from the left with the GS bra vector $\langle\Psi_0|$ leads to an expression for the ground state energy E_0

$$E_0 = \frac{\langle\Psi_0|\hat{H}_e|\Psi_0\rangle}{\langle\Psi_0|\Psi_0\rangle} . \quad (2.14)$$

Eq. 2.14 also defines the lower bound of the energy, i.e. inserting any trial state $|\Psi_{\text{trial}}\rangle$ will always yield a higher energy $E_{\text{trial}} \geq E_0$, which is known as the variational principle.^[63,64] A rather direct implementation of this trial-and-error idea is seen in variational quantum Monte-Carlo methods^[65] but the variational principle is also deeply ingrained in other quantum chemical methods that are based on the idea of expanding the wave function in a suitable subset.

2.1.3 The Hartree–Fock Method

One of the simplest of such expansion approaches is the Hartree–Fock (HF) method, where the N -electron wave function is constructed from N one-electron wave functions $\phi(\mathbf{x})$, also called spin orbitals, from a set of orthonormal functions $\{\phi_i\}$. They may be split into a spin function $\sigma(s)$ which itself is an eigenfunction of the \hat{s}_z operator with possible eigenvalues $\frac{1}{2}$ and $-\frac{1}{2}$, labeled as $\alpha(s)$ and $\beta(s)$ respectively, and a spatial (molecular) orbital $\varphi_\sigma(\mathbf{r})$

$$\phi(\mathbf{x}) = \sigma(s)\varphi_\sigma(\mathbf{r}) . \quad (2.15)$$

Using a simple product of N such spin orbitals and the ansatz for a fermionic state from eq. 2.8 leads to the HF ground state

$$|\Psi_0^{\text{HF}}\rangle = \int \left(\prod_{i=1}^N \phi_i(\mathbf{x}_i) \right) \frac{1}{\sqrt{N!}} \sum_P (-1)^P |\mathbf{x}_{P(1)}\rangle \dots |\mathbf{x}_{P(N)}\rangle d\mathbf{x}_1 \dots d\mathbf{x}_N . \quad (2.16)$$

To simplify notations, it is common practice in quantum chemistry to deal with an equivalent wave function instead of the state itself. To incorporate the antisymmetry of the state in the N -electron wave function, eq. 2.16 is projected onto the product of involved one-particle position-spin kets yielding the Hartree–Fock wave function, written here as a Slater determinant^[66]

$$\Psi_0^{\text{HF}}(\mathbf{x}_1, \dots, \mathbf{x}_N) = \frac{1}{\sqrt{N!}} \begin{vmatrix} \phi_1(\mathbf{x}_1) & \phi_1(\mathbf{x}_2) & \cdots & \phi_1(\mathbf{x}_N) \\ \phi_2(\mathbf{x}_1) & \phi_2(\mathbf{x}_2) & \cdots & \phi_2(\mathbf{x}_N) \\ \vdots & \vdots & \ddots & \vdots \\ \phi_N(\mathbf{x}_1) & \phi_N(\mathbf{x}_2) & \cdots & \phi_N(\mathbf{x}_N) \end{vmatrix}. \quad (2.17)$$

Using this wave function to calculate the energy expectation value of the electronic (time-independent) Hamiltonian from eq. 2.11 by following eq. 2.14 gives^[67]

$$E^{\text{HF}} = \sum_{\sigma} \sum_{pq} \left[h_{pq}^{\sigma} + \frac{1}{2} \sum_{\sigma'} \sum_{rs} \left[v_{pqrs}^{\sigma\sigma'} - v_{psrq}^{\sigma\sigma'} \delta_{\sigma\sigma'} \right] D_{rs}^{\sigma'} \right] D_{pq}^{\sigma}, \quad (2.18)$$

where h_{pq}^{σ} are elements of the core Hamilton matrix, given by the one-electron integrals

$$h_{pq}^{\sigma} = -\frac{1}{2} \int \varphi_{p,\sigma}^*(\mathbf{r}) \nabla^2 \varphi_{q,\sigma}(\mathbf{r}) d\mathbf{r} - \sum_A Z_A \int \frac{\varphi_{p,\sigma}^*(\mathbf{r}) \varphi_{q,\sigma}(\mathbf{r})}{|\mathbf{R}_A - \mathbf{r}|} d\mathbf{r}, \quad (2.19)$$

and where $v_{pqrs}^{\sigma\sigma'}$ are two-electron integrals defined as

$$v_{pqrs}^{\sigma\sigma'} = \iint \frac{\varphi_{p,\sigma}^*(\mathbf{r}) \varphi_{q,\sigma}(\mathbf{r}) \varphi_{r,\sigma'}^*(\mathbf{r}') \varphi_{s,\sigma'}(\mathbf{r}')}{|\mathbf{r} - \mathbf{r}'|} d\mathbf{r} d\mathbf{r}'. \quad (2.20)$$

In eq. 2.18, these two- and four-index quantities are contracted with elements of the one-electron density matrix \mathbf{D} ^[67,68] given in the MO basis as

$$D_{ij}^{\sigma} = \delta_{ij}, \quad D_{ia}^{\sigma} = 0, \quad D_{ai}^{\sigma} = 0, \quad D_{ab}^{\sigma} = 0, \quad (2.21)$$

where the convention is used that indices i, j, \dots refer to occupied and a, b, \dots to virtual (unoccupied) orbitals. Inserting the definition of the density matrix elements into eq. 2.18 generates a more commonly seen form of this equation, where the summations run over occupied orbitals only.^[69] The density matrix based notation, however, offers a general framework to take derivatives w.r.t. the GS density or orbitals by rewriting them as derivative w.r.t. the density matrix itself. This concept will be extended in Sections 2.2.2 and 3.2.1.

Using the energy expression from eq. 2.18, the optimal set of spin orbitals that minimizes the energy can be determined using the variational principle.^[70] In the notation of density matrices, this means that the Fock matrix \mathbf{F} that represents the change of the energy E^{HF} w.r.t. the density matrix

$$F_{pq}^{\sigma} = \frac{\partial E^{\text{HF}}}{\partial D_{pq}^{\sigma}} = h_{pq}^{\sigma} + \sum_{\sigma'} \sum_{rs} \left[v_{pqrs}^{\sigma\sigma'} - v_{psrq}^{\sigma\sigma'} \delta_{\sigma\sigma'} \right] D_{rs}^{\sigma'} \quad (2.22)$$

has non-zero entries only in the occupied-occupied block, which is expressed in the Hartree–Fock equations^[71]

$$\mathbf{F}^{\sigma} \mathbf{D}^{\sigma} = \mathbf{D}^{\sigma} \mathbf{F}^{\sigma} . \quad (2.23)$$

In other words, interchanging the occupations among occupied and virtual orbitals does not lower the energy, i.e. the optimal set of orbitals has been found. Computationally, finding the optimal set of spin orbitals has to be done in an iterative fashion because the Fock matrix, in turn, depends on the orbitals and the density matrix. Note, that the set of spin orbitals that makes the energy stationary is not unique^[72] and that by convention, the condition $F_{pq}^{\sigma} = \epsilon_p^{\sigma} \delta_{pq}$ is used to derive such a unique set, called the canonical HF spin orbitals, for which the values ϵ_p^{σ} are interpreted as the orbital energies.^[67,73]

2.1.4 Basis Sets and Integral Evaluation

Up to this point, the orbitals and the way in which they may change during optimization were not specified. The customary solution is expanding the molecular orbitals in a linear combination of atomic orbitals (LCAO)^[74]

$$\varphi_{p,\sigma}(\mathbf{r}) = \sum_{\mu}^{N_b} C_{\mu p \sigma} \chi_{\mu}(\mathbf{r}) , \quad (2.24)$$

where the expansion coefficients $C_{\mu p \sigma}$ are flexible and the atomic orbitals $\chi_{\mu}(\mathbf{r})$ are from a set of N_b basis functions. Applying the LCAO ansatz from eq. 2.24 to the equations from HF theory yields the Roothaan–Hall equations,^[74–76] which are the common working equations for a HF computer program.

The most common choice of basis functions for molecular systems are atom-centered Gaussian-type orbitals. For an atom positioned at $\mathbf{R}_A = (x_A \ y_A \ z_A)^{\text{T}}$, they have the form

$$\chi_{\mu}(\mathbf{r}) = (x - x_A)^{l_{\mu,x}} (y - y_A)^{l_{\mu,y}} (z - z_A)^{l_{\mu,z}} \cdot \exp \left\{ -\alpha_{\mu} |\mathbf{r} - \mathbf{R}_A|^2 \right\} , \quad (2.25)$$

where $l_\mu = l_{\mu,x} + l_{\mu,y} + l_{\mu,z}$ is the angular quantum number of the basis function determining the spatial shape of the basis function and where the exponent α_μ defines its radial drop-off.^[77] All required matrix elements are calculated within the AO basis and the results are then back-transformed to the MO basis using the coefficients $C_{\mu p \sigma}$. There exist well-established strategies to calculate typically occurring matrix elements like the two-center one-electron integrals $h_{\mu\nu}$ (eq. 2.19) or the four-center two-electron integrals $v_{\mu\nu\kappa\lambda}$ (eq. 2.20) analytically within a Gaussian basis set. Typical examples for such integral algorithms include the Gauss–Rys quadrature,^[78] the Obara–Saika scheme,^[79] and the McMurchie–Davidson scheme.^[80] The calculation of four-center two-electron integrals within these analytical schemes scales as N_b^4 making it the most time-consuming part of a HF calculation. A common strategy to accelerate these computation steps is the use of prescreening techniques that calculate a computationally inexpensive estimate of the integral, compare this estimate to a predefined threshold, and decide if the integral is neglected and the more demanding exact computation can be skipped. Equations for such estimates can, for example, be derived using the Cauchy–Schwarz inequality.^[81,82] Another approach is the resolution of the identity (RI) method,^[83] where one basis function pair of a four-center integral is approximated within an auxiliary basis set of size N_{aux} . The coefficients for this expansions are obtained by fitting, where typically the Coulomb or overlap norm is minimized. Using the RI method for the Coulomb four-center integrals (RI-J) reduces the N_b^4 scaling to a $N_b^2 \cdot N_{\text{aux}}$ scaling and thus gives an appreciable speed-up.^[83] For the application of the RI to the exchange four-center integral (RI-K), an improved scaling is not obtained due to increased complexity of the transformations required for the fitting process, but reduced prefactors can be achieved nonetheless.^[84,85]

2.1.5 Post Hartree–Fock Methods

The electron-electron interaction operator in the definition of \hat{H}_e covers all interactions between electrons explicitly. In HF theory, the energy contributions from this term (eq. 2.18 and eq. 2.20) describe the interaction of an electron only with the spatial distribution of electrons as specified by set of occupied orbitals. That is, the HF methods is a mean-field approximation, where the electron-electron interactions are only considered in an averaged way.^[73] The difference of the exact energy E_0 resulting from an exact treatment of the electron-electron interaction and the HF energy is called the electron correlation energy^[86,87]

$$E_{\text{corr.}} = E_0 - E_{\text{HF}}. \quad (2.26)$$

Although the correlation energy makes up only about 1% of the total energy of a molecule, large parts of the correlation energy have to be accounted for if chemical accuracy, typically defined as 1 kcal/mol (~ 0.04 eV) accuracy, is targeted. Although no clear-cut partitioning has been established, it is common to distinguish two kinds of contributions to the correlation energy that have different physical origins.^[88,89] Effects of the explicit electron-electron repulsion, which is not considered in the mean-field approximation, are declared as dynamical correlation. In contrast, nondynamical (or static) correlation is associated with effects of near-degeneracy of different HF determinants for the same system. While some static correlation effects can already be captured by an unrestricted HF calculation that introduces the required flexibility in the wave function via the additional spin functions (“absolute near-degeneracy”), other static correlation effects cannot (“relative near-degeneracy”).^[90]

There exist various strategies to account for electron correlation and to systematically improve on a converged HF wave function. One route of methods builds upon a single HF determinant and introduces additional excited determinants constructed from the occupied and virtual orbitals of the reference HF state. Pictorially speaking, electrons gain more flexibility to avoid each other by populating virtual orbitals associated with some excited determinant. Mathematical implementations of this concept were realized in different fashions with configuration interaction (CI),^[91,92] Møller–Plesset (MP) perturbation theory,^[93,94] and coupled-cluster (CC) theory^[95,96] being the most prominent variants. Depending on the number of excited electrons, the excited determinants used in expansion methods like CI or CC are referred to as singles, doubles, etc., where inclusion up to N -tuple excited determinants corresponds to a complete expansion for a given N -electron system and would yield the exact energy within a given basis set. Hence, such expansion methods are in principle able to restore the full electron correlation including static correlation. However, a full expansion is computationally unfeasible for all but the smallest molecules. In situations where static correlation effects are mild, single-reference CI or CC methods may recover sufficient amounts of static correlation already at computationally accessible, truncated expansion levels. In more severe cases of near-degeneracy, commonly referred to as multi-reference cases, it is a useful strategy to start from a multi-configurational self-consistent field (MCSCF) calculation,^[97] where in addition to the expansion coefficients also the orbital coefficients are optimized for the many-determinant wave function thereby accounting for static correlation. Additional correction schemes like perturbation theory, CI or CC may be applied on top to recover dynamical correlation. A common strategy to balance computational cost and accuracy is the restriction to a space of active orbitals in the initial MCSCF calculation, in which

a full CI is performed. This method is called complete active space self-consistent field (CASSCF) and is often combined with second-order perturbation theory leading to the CASPT2 method.^[97] Typically, the active orbitals are those close to the HOMO-LUMO gap of a HF reference but the decision which and how many orbitals and electrons are to be included is often not straightforward^[98] making this method more of an expert’s method rather than a “black-box” tool.

2.2 Density Functional Theory

The *ab initio* post-HF wave function methods described above provide clearly defined routes to systematically improve on the results from HF theory. A crucial drawback is their scaling with system size which limits the applicability of the higher-order methods to relatively small systems. As an alternative approach to wave function based methods, density functional theory (DFT) is introduced.

2.2.1 The Electron Density as the Central Quantity

While the N -electron wave function Ψ generally depends on $3N$ position variables and N spin variables, the electron density

$$\rho(\mathbf{r}) := \rho(\mathbf{r}_1) = N \int |\Psi(\mathbf{x}_1, \dots, \mathbf{x}_N)|^2 ds_1 d\mathbf{x}_2 \dots d\mathbf{x}_N \quad (2.27)$$

depends on only three spatial variables where s_1 is used to denote integration over spin for electron 1. The multiplication of the integral in eq. 2.27 with N ensures that $\rho(\mathbf{r})$ integrates to the total number of electrons

$$\int \rho(\mathbf{r}) d\mathbf{r} = N. \quad (2.28)$$

The significantly smaller number of variables makes the electron density an attractive quantity for electronic structure calculations. If it was possible to obtain the energy expectation value of the N -electron wave function from just knowing the electron density, exact results would be accessible potentially at a fraction of the cost of methods dealing with the N -electron wave function itself.

The theoretical foundation for this idea was laid by Hohenberg and Kohn in 1964.^[2] They proved that there exists a one-to-one mapping between an external potential $V(\mathbf{r})$ (defined, e.g., by the nuclei of a molecule) and the electron density ρ and that therefore

the energy is an unique functional of the density (up to an additive constant). The general form of this functional reads^[2]

$$E[\rho] = \int V(\mathbf{r})\rho(\mathbf{r}) \, d\mathbf{r} + F[\rho]. \quad (2.29)$$

Additionally, they showed that only the true GS electron density, i.e. the electron density associated with the wave function that yields the exact energy expectation value (eq. 2.14), minimizes that functional such that E_0 is obtained

$$E_0 = E[\tilde{\rho}] \Big|_{\tilde{\rho}=\rho_0} \leq E[\tilde{\rho}], \quad (2.30)$$

where $\tilde{\rho}$ is a test density. The first term on the RHS of eq. 2.29 is system dependent and describes the interaction of the density with a given external potential, which for molecules is simply the Coulomb attraction from the nuclei. The second term $F[\rho]$ is universally valid and has to cover the remaining energy contributions, i.e. the sum of the electron-electron repulsion E_{ee} and the kinetic energy of the electrons T . With this partition, the GS energy may be written as

$$E_0 = E[\rho_0] = E_{eN}[\rho_0] + E_{ee}[\rho_0] + T[\rho_0]. \quad (2.31)$$

While the electron-nuclei attraction functional

$$E_{eN}[\rho] = - \sum_A Z_A \int \frac{\rho(\mathbf{r})}{|\mathbf{R}_A - \mathbf{r}|} \, d\mathbf{r} \quad (2.32)$$

is known exactly, the other two functionals $E_{ee}[\rho]$ and $T[\rho]$ are not. Therefore, the idea by Hohenberg and Kohn shifts the problem of minimizing the energy expectation value of a N -electron wave function to finding the universal functional $F[\rho] = E_{ee}[\rho] + T[\rho]$. If this expression was found (and simple enough for evaluation), the remaining process of minimizing the electron density would be comparatively straightforward.^[2] As a matter of fact, such a universal functional has not been found to date. As a practical solution, approximations have been put forward but it was also realized that good approximations for the kinetic energy were difficult to obtain in the original, orbital-free framework by Hohenberg and Kohn.^[99–101]

2.2.2 Kohn–Sham Density Functional Theory

That is why Kohn and Sham have brought the concept of molecular orbitals familiar from HF theory to DFT.^[3] Their idea was to start from a fictitious non-interacting reference systems for which the exact wave function is a single Slater determinant. The kinetic energy of this Slater determinant is readily accessible from the MOs

$$T_S[\{\varphi\}] = -\frac{1}{2} \sum_{\sigma} \sum_{pq} D_{pq}^{\sigma} \int \varphi_{p,\sigma}^*(\mathbf{r}) \nabla^2 \varphi_{q,\sigma}(\mathbf{r}) d\mathbf{r} , \quad (2.33)$$

where here and below the density-matrix notation from ref. 67 is used instead of a summation over occupied orbitals to simplify notations in upcoming chapters. By definition, it is enforced that the electron density of the fictitious non-interacting reference system is equal to the density of the real, interacting system $\rho(\mathbf{r}) = \rho_S(\mathbf{r})$ and hence may also be calculated from the MOs^[67]

$$\rho(\mathbf{r}) = \sum_{\sigma} \rho_{\sigma}(\mathbf{r}) = \sum_{\sigma} \sum_{pq} D_{pq}^{\sigma} \varphi_{p,\sigma}^*(\mathbf{r}) \varphi_{q,\sigma}(\mathbf{r}) . \quad (2.34)$$

The two densities can only be equal if the external potential for the fictitious reference system adapts accordingly. This effective potential is called the Kohn–Sham (KS) potential. The idea of KS-DFT is to calculate the kinetic energy as if the system was in this KS potential and later correct for the difference from the true kinetic energy T . Similarly (but independent from the idea of a non-interacting reference system) the electron-electron repulsion functional $E_{ee}[\rho]$ may be split into a classical part $J[\rho]$ that covers the Coulomb repulsion energy of two charge densities

$$J[\rho] = \frac{1}{2} \iint \frac{\rho(\mathbf{r})\rho(\mathbf{r}')}{|\mathbf{r} - \mathbf{r}'|} d\mathbf{r} d\mathbf{r}' \quad (2.35)$$

and some correction term that accounts for all non-classical effects of the electron-electron interaction. With the correction terms for the kinetic energy and the electron-electron interaction collected in the exchange-correlation (XC) functional

$$E_{xc}[\rho] = T[\rho] - T_S[\{\varphi\}] + E_{ee}[\rho] - J[\rho] , \quad (2.36)$$

the total energy functional may be expressed as

$$E[\rho] = T_S[\{\varphi\}] + E_{eN}[\rho] + J[\rho] + E_{xc}[\rho] . \quad (2.37)$$

Compared to conventional DFT, the challenge of finding a universal functional $F[\rho]$ for the total kinetic and total electron-electron interaction energy is shifted to finding the correction functional $E_{\text{xc}}[\rho]$, while about 99% of the energy is already covered by the first three functionals on the RHS of eq. 2.37, whose exact forms are known. However, just like for $F[\rho]$, the exact form of $E_{\text{xc}}[\rho]$ is unknown and approximations have to be made (see below).

To minimize the energy functional eq. 2.37, the optimal set of KS orbitals has to be found. The corresponding KS equation is formally identical to eq. 2.23 except that the Fock matrix is replaced by the KS matrix \mathbf{F} . Its matrix elements are obtained by inserting the definitions from eq. 2.34-2.35 in eq. 2.37 and taking the derivative w.r.t. the density matrix

$$F_{pq}^{\sigma} = \frac{\delta E[\rho]}{\delta D_{pq}^{\sigma}} = h_{pq}^{\sigma} + \sum_{\sigma'} \sum_{rs} v_{pqrs}^{\sigma\sigma'} D_{rs}^{\sigma'} + V_{pq,\sigma}^{\text{xc}}, \quad (2.38)$$

where $V_{pq,\sigma}^{\text{xc}}$ are matrix elements of the XC potential which may be expressed as the derivative of the XC energy

$$V_{pq,\sigma}^{\text{xc}} = \frac{\delta E_{\text{xc}}}{\delta D_{pq}^{\sigma}}. \quad (2.39)$$

The somewhat non-standard notation as a density matrix derivative^[67] is used to conveniently cover the more general case of orbital-dependent XC functionals to be introduced below (Sections 2.2.4 and 2.3). For a pure density functional, invoking the functional chain-rule and inserting the definition of the density (eq. 2.34) recovers the more commonly seen notation of $V_{pq,\sigma}^{\text{xc}}$ as the matrix element of a functional derivative

$$V_{pq,\sigma}^{\text{xc}} = \frac{\delta E_{\text{xc}}}{\delta D_{pq}^{\sigma}} = \int \frac{\delta E_{\text{xc}}[\rho_{\sigma}(\mathbf{r})]}{\delta \rho_{\sigma}(\mathbf{r})} \frac{\delta \rho_{\sigma}(\mathbf{r})}{\delta D_{pq}^{\sigma}} d\mathbf{r} = \int \frac{\delta E_{\text{xc}}}{\delta \rho_{\sigma}(\mathbf{r})} \varphi_{p,\sigma}^*(\mathbf{r}) \varphi_{q,\sigma}(\mathbf{r}) d\mathbf{r}. \quad (2.40)$$

2.2.3 The Quest for the Exact Exchange-Correlation Functional

Over half a century after the original paper by Kohn and Sham,^[3] the exact XC functional remains unknown and the success of KS-DFT is due to the pragmatic approach of using approximated XC functionals (see Section 2.2.4). Likewise, considerable effort was devoted to illuminating the nature of the exact XC functional and several lines of thinking, mathematical formalisms, and exact constraints were derived.^[102]

One important such concept is the hole formalism. Pictorially speaking, each electron digs a hole around itself so that the probability of finding another electron in its vicinity is reduced and the exchange and correlation effects may be expressed as the interaction of an electron density with a hole function $h(\mathbf{r}_1, \mathbf{r}_2)$.^[103] The electron-electron interaction

energy is then obtained as^[104]

$$E_{\text{ee}} = J[\rho] + \frac{1}{2} \sum_{\sigma\sigma'} \iint \frac{\rho_{\sigma}(\mathbf{r}_1) h_{\sigma\sigma'}(\mathbf{r}_1, \mathbf{r}_2)}{|\mathbf{r}_1 - \mathbf{r}_2|} d\mathbf{r}_1 d\mathbf{r}_2, \quad (2.41)$$

i.e. as the sum of the classical Coulomb interaction, which misses all quantum mechanical effects and contains unphysical self-interaction (see below), and a correcting term governed by the hole function $h_{\sigma\sigma'}(\mathbf{r}_1, \mathbf{r}_2)$, which is formally obtained from the pair density^[71,104]

$$P_2^{\sigma\sigma'}(\mathbf{r}_1, \mathbf{r}_2) := P_2(\mathbf{x}_1, \mathbf{x}_2) = N(N-1) \int |\Psi(\mathbf{x}_1, \mathbf{x}_2, \dots, \mathbf{x}_N)|^2 d\mathbf{x}_3 \dots d\mathbf{x}_N \quad (2.42)$$

as

$$h_{\sigma\sigma'}(\mathbf{r}_1, \mathbf{r}_2) = \frac{P_2^{\sigma\sigma'}(\mathbf{r}_1, \mathbf{r}_2)}{\rho_{\sigma}(\mathbf{r}_1)} - \rho_{\sigma'}(\mathbf{r}_2). \quad (2.43)$$

To transfer the hole function formalism to KS-DFT, the Adiabatic Connection (AC) is introduced.^[105] The AC builds on the fact that in KS-DFT, the density of the non-interacting reference system is the same as for the real, interacting system, while the external potential V_{ext} is thought to adapt accordingly. The AC generalizes this idea by introducing a coupling parameter λ that moderates the transition between the non-interacting (fictitious) reference system ($\lambda = 0$) and the real system ($\lambda = 1$) while the density remains unchanged along this line giving rise to the term “adiabatic” connection. The idea is expressed in the λ -dependent Hamiltonian^[105]

$$\hat{H}^{\lambda} = \hat{T} + \lambda \hat{V}_{\text{ee}} + \hat{V}_{\text{ext}}^{\lambda}, \quad 0 \leq \lambda \leq 1, \quad (2.44)$$

which enters the Schrödinger equation $\hat{H}^{\lambda} \Psi^{\lambda} = E^{\lambda} \Psi^{\lambda}$, where all wave functions Ψ^{λ} yield the same density ρ if plugged into eq. 2.27. The energy E^{λ} will also change depending on λ with the difference in energy of the interacting and non-interacting being simply^[106]

$$E^{\lambda=1} - E^{\lambda=0} = \int_0^1 dE^{\lambda}. \quad (2.45)$$

Proceeding from this equation using the hole formalism from eq. 2.41 for V_{ee} as well as the KS kinetic energy density for T in the limiting case for $\lambda = 0$ in eq. 2.44, eventually leads to the following energy expression for the interacting system^[106]

$$E^{\lambda=1} = T_{\text{S}}[\{\varphi\}] + E_{\text{eN}}[\rho] + J[\rho] + \sum_{\sigma\sigma'} \frac{1}{2} \iint \int_0^1 \frac{\rho_{\sigma}(\mathbf{r}_1) h_{\sigma\sigma'}^{\lambda}(\mathbf{r}_1, \mathbf{r}_2)}{|\mathbf{r}_1 - \mathbf{r}_2|} d\lambda d\mathbf{r}_1 d\mathbf{r}_2, \quad (2.46)$$

so that by comparison with eq. 2.37, the XC functional is identified to be

$$E_{\text{xc}} = \frac{1}{2} \sum_{\sigma\sigma'} \iint \frac{\rho_{\sigma}(\mathbf{r}_1) h_{\text{xc}}^{\sigma\sigma'}(\mathbf{r}_1, \mathbf{r}_2)}{|\mathbf{r}_1 - \mathbf{r}_2|} d\mathbf{r}_1 d\mathbf{r}_2, \quad (2.47)$$

where the XC hole

$$h_{\text{xc}}^{\sigma\sigma'}(\mathbf{r}_1, \mathbf{r}_2) = \int_0^1 h_{\sigma\sigma'}^{\lambda}(\mathbf{r}_1, \mathbf{r}_2) d\lambda \quad (2.48)$$

is defined as the coupling-strength integrated hole function.^[104,106] Although $h_{\text{xc}}^{\sigma\sigma'}(\mathbf{r}_1, \mathbf{r}_2)$ can be expected to be a rather complicated function, the $1/|\mathbf{r}_1 - \mathbf{r}_2|$ term in eq. 2.47 implies that at least its angular dependence is unimportant and only its spherical average has to be considered.^[104] With that, the problem of the unknown universal functional has been once more shifted to a new quantity. The advantage of this formalism is that exact constraints known for the hole function^[104] transfer to the XC hole, as they are unaffected by the integration over λ .^[106] First, the XC hole follows the simple integration rule

$$\int h_{\text{xc}}^{\sigma\sigma'}(\mathbf{r}_1, \mathbf{r}_2) d\mathbf{r}_2 = -\delta_{\sigma\sigma'} \quad (2.49)$$

for any position of the reference point \mathbf{r}_1 , i.e. it integrates to -1 for the same-spin case and vanishes for the opposite-spin case.^[104] For the special case of $\mathbf{r}_2 = \mathbf{r}_1$, the so called “on-top” values^[106] of the same-spin XC hole are obtained as

$$h_{\text{xc}}^{\sigma\sigma}(\mathbf{r}_1, \mathbf{r}_1) = -\rho_{\sigma}(\mathbf{r}_1), \quad (2.50)$$

which is an immediate consequence of the antisymmetry built into $P_2^{\sigma\sigma'}(\mathbf{r}_1, \mathbf{r}_2)$. Also, it is customary to split the XC hole into a Fermi hole h_{x} , which is known exactly from the one-body spin-density matrix (see ref. 104) and a correlation hole h_{c} , defined as the difference $h_{\text{c}}^{\sigma\sigma'} = h_{\text{xc}}^{\sigma\sigma'} - h_{\text{x}}^{\sigma\sigma'}$. Because the same-spin Fermi hole $h_{\text{x}}^{\sigma\sigma}$ is known to contain exactly one electron,^[104] the integration rules for the separate holes read

$$\int h_{\text{x}}^{\sigma\sigma}(\mathbf{r}_1, \mathbf{r}_2) d\mathbf{r}_2 = -1 \quad (2.51a)$$

$$\int h_{\text{c}}^{\sigma\sigma'}(\mathbf{r}_1, \mathbf{r}_2) d\mathbf{r}_2 = 0. \quad (2.51b)$$

Like the same-spin XC hole (eq. 2.50), the Fermi hole has the on-top value $h_{\text{x}}^{\sigma\sigma}(\mathbf{r}_1, \mathbf{r}_1) = -\rho_{\sigma}(\mathbf{r}_1)$ and takes only negative values $h_{\text{x}}^{\sigma\sigma}(\mathbf{r}_1, \mathbf{r}_1) < 0$.^[107] Note, however, that the on-top value of the total XC hole is not known.

Besides the conditions implied by the XC, Fermi and correlation holes, several other exact constraints and desirable properties are known for the exact XC functional.^[108,109] Of particular importance in the context of this work is the requirement that the functional has to be self-interaction free. This means that in a one-electron system, the unphysical interaction of a density with itself (as obtained from $J[\rho]$, eq. 2.35) has to be corrected for by the XC functional^[110]

$$J[\rho^{1-\text{El.}}] = -E_{\text{xc}}[\rho^{1-\text{El.}}]. \quad (2.52)$$

2.2.4 Exchange-Correlation Functional Approximations

As outlined above, the exact XC functional is not known and approximations have to be made for practical applications of KS-DFT. For convenience, these approximations are nonetheless referred to as “XC functionals” within this work. In the development of such functionals, it is customary to a) split the XC functional into an exchange and a correlation part and b) deal with spatially resolved X/C energy densities $e_{\text{x/c}}(\mathbf{r})$ instead of total energies

$$E_{\text{xc}} = E_{\text{x}} + E_{\text{c}} = \int e_{\text{x}}(\mathbf{r}) \, d\mathbf{r} + \int e_{\text{c}}(\mathbf{r}) \, d\mathbf{r}, \quad (2.53)$$

where the energy densities $e_{\text{x/c}}(\mathbf{r})$ must not be confused with the per-electron energy densities, which would require multiplication with the density under the integrals in eq. 2.53. The separation into an exchange and a correlation part is to some degree arbitrary for approximate functionals, i.e. the exchange functional may cover effects that could also be viewed as correlation.^[111]

Over the past decades, several hundred XC functionals have been put forward.^[7] A popular way to systematize these developments is expressed in the metaphorical Jacob’s Ladder of density functional approximations suggested by Perdew and Schmidt.^[112] Stepping up from the “Hartree world” (where no XC functional is used), additional quantities are introduced as inputs to the XC functional at each rung of the ladder. In principle, the larger input of information allows to satisfy more of the exact constraints at each rung, potentially leading to improved accuracy and ultimately to the “heaven of chemical accuracy”.^[112] Below, some of the most important developments are outlined. The selection of representatives for each rung is based on general popularity as well as usage within this work and is by no means exhaustive.

Local (Spin-)Density Approximation

The local density approximation (LDA) and local spin-density approximation (LSDA) constitute the lowest rung (rung 1) of the Jacob’s Ladder and solely depend on the density and spin-density, respectively. They assume that at each point in space, the density is a slowly varying function and may be treated as a uniform electron gas (UEG).^[113] Hence, the LDA expression for the exchange term is equivalent to an expression by Dirac for the UEG,^[113] which was later taken up by Slater^[114] as an approximation to the exchange-term in HF theory. For LDA, it reads

$$e_x^{\text{LDA}}(\mathbf{r}) = -C_x \rho^{4/3}(\mathbf{r}) = -C_x \left(\sum_{\sigma} \rho_{\sigma}(\mathbf{r}) \right)^{4/3}, \quad (2.54)$$

where $C_x = \frac{3}{4} \left(\frac{3}{\pi} \right)^{1/3}$ is a constant. As opposed to LDA, LSDA is not based on the total density but is formulated for individual spin-channels, so that the total exchange energy density is obtained as the sum of both spin channels

$$e_x^{\text{LSDA}}(\mathbf{r}) = \sum_{\sigma} e_{x,\sigma}^{\text{LSDA}}(\mathbf{r}) = -2^{1/3} C_x \sum_{\sigma} \rho_{\sigma}^{4/3}(\mathbf{r}). \quad (2.55)$$

As this makes LSDA better suited for unrestricted calculations and situations where symmetry breaking has to be described, it is usually preferred over LDA.^[115] For the correlation part of the UEG, no exact formula is known. Instead, the respective LSDA correlation functionals were obtained by fitting to highly accurate quantum Monte Carlo results.^[113] Popular fits are those by Vosko, Wilk and Nusair (VWN),^[116] and by Perdew and Wang (PW92).^[117] LSDA is (essentially) an exact method for the model system of an UEG and therefore very successful for comparable real systems, i.e. systems with a rather slowly varying electron density such as simple metals.^[113] Molecules, on the other hand, are clearly distinct from this situation because of the steep increase of the density around individual atomic nuclei. Nonetheless, LSDA provides some benefits over HF, e.g., for atomization energies, ionization potentials, and electron affinities.^[118] Barrier heights, on the other hand, are notably deteriorated,^[118] which is related to the strong overbinding observed for LSDA and limits applicability for chemical reactions.^[115]

Generalized Gradient Approximation

To account for more rapid changes in the density of molecules, a natural extension of the LSDA is the inclusion of the density’s spatial derivatives, first and foremost its gradient.

The basic idea of a gradient expansion of the density has already been introduced by Kohn and Sham^[3] and pursued for some time also by others,^[119] until eventually, clear pitfalls were noticed^[120] and developments shifted to the related ansatz of a generalized gradient approximation (GGA) that restores theoretical constraints violated by the simpler gradient expansions.^[121] GGAs constitute the second rung of the Jacob’s Ladder, and since they include information beyond the local density, they are classified as semilocal functionals. Among many other variants, some of the most popular GGA functionals for the exchange part are those by Becke from 1988 (B88)^[122] and by Perdew, Burke and Ernzerhof (PBE).^[123] Both functionals may be expressed as corrections to the LSDA exchange energy density where the correction terms depend on the reduced spin density gradient for which two forms are in common use

$$x_\sigma(\mathbf{r}) = \frac{|\nabla \rho_\sigma(\mathbf{r})|}{\rho_\sigma^{4/3}(\mathbf{r})}, \quad (2.56a)$$

$$s_\sigma(\mathbf{r}) = \frac{x_\sigma(\mathbf{r})}{2(3\pi^2)^{1/3}}. \quad (2.56b)$$

Also note that the absolute value of the density gradient $|\nabla \rho_\sigma(\mathbf{r})|$ is typically implemented as $\gamma_{\sigma\sigma}^{1/2}(\mathbf{r})$, where

$$\gamma_{\sigma\sigma'}(\mathbf{r}) = \nabla^\top \rho_\sigma(\mathbf{r}) \nabla \rho_{\sigma'}(\mathbf{r}) \quad (2.57)$$

is the squared density gradient and where here and below the transpose notation from ref. 67 is adopted to simplify notations in upcoming chapters. With that, the exchange energy density for the B88 model reads

$$e_{x,\sigma}^{\text{B88}}(\mathbf{r}) = e_{x,\sigma}^{\text{LSDA}}(\mathbf{r}) - \rho_\sigma^{4/3}(\mathbf{r}) \cdot \frac{\beta x_\sigma^2(\mathbf{r})}{1 + 6\beta x_\sigma(\mathbf{r}) \operatorname{asinh}(x_\sigma(\mathbf{r}))}, \quad (2.58)$$

where $\beta = 0.0042$ was found by fitting to exact values for the exchange energies of the noble gas atoms (He–Rn).^[122] The PBE exchange energy density has a similar form and is typically written as the LSDA exchange energy density multiplied by an enhancement factor

$$e_{x,\sigma}^{\text{PBE}}(\mathbf{r}) = e_{x,\sigma}^{\text{LSDA}}(\mathbf{r}) \cdot \left(1 + \kappa - \frac{\kappa}{1 + \mu s_\sigma^2(\mathbf{r})/\kappa} \right). \quad (2.59)$$

In contrast to B88, the parameters $\kappa = 0.804$ and $\mu = 0.21951$ are nonempirical.^[123] They were derived from theoretical constraints, i.e. the value of κ ensures that the Lieb–Oxford bound is satisfied and μ was chosen such that the LSDA linear response is recovered.^[123] For the correlation part, again, many different GGA functionals were developed. The popular LYP functional^[124] was derived by Lee, Yang and Parr from the Colle-Salvetti

formula^[125] that approximates the correlation energy starting from the one and two-electron density matrix of a HF wave function. The performance of GGA functionals is generally superior to LSDA functionals and has led to a major breakthrough of DFT in chemistry.^[121] In particular, GGAs were shown to significantly reduce the problem of overbinding inherent to LSDA functionals.^[126]

Meta Generalized Gradient Approximation

Considering the improvements seen with the inclusion of density gradient terms in GGAs it seems natural to also include higher-order derivatives of the density such as its Laplacian.^[127] It turned out, however, that it is numerically more stable to use the orbital kinetic energy density τ which is directly related to the Laplacian via the effective potential and the orbitals of the KS system.^[127] Functionals that include τ or the Laplacian represent the third rung of the Jacob's Ladder and are termed meta-GGAs (mGGAs). The orbital kinetic energy density is defined from the gradient of the occupied KS orbitals

$$\tau_{\sigma}(\mathbf{r}) = \frac{1}{2} \sum_{pq} D_{pq}^{\sigma} \nabla^{\mathbf{T}} \varphi_{p,\sigma}^*(\mathbf{r}) \nabla \varphi_{q,\sigma}(\mathbf{r}). \quad (2.60)$$

In the case of a one-orbital system, it is easy to show that the kinetic energy density may be expressed in terms of the density and its gradient (assuming a real-valued orbital)

$$\tau_{\sigma}^{1\text{-Orb.}} = \frac{1}{2} \nabla^{\mathbf{T}} \varphi_{1,\sigma} \nabla \varphi_{1,\sigma} = \frac{1}{2} \nabla^{\mathbf{T}} \varphi_{1,\sigma} \nabla \varphi_{1,\sigma} \cdot \frac{4\varphi_{1,\sigma} \varphi_{1,\sigma}}{4\varphi_{1,\sigma} \varphi_{1,\sigma}} = \frac{\nabla^{\mathbf{T}} \rho_{\sigma}^{1\text{-Orb.}} \nabla \rho_{\sigma}^{1\text{-Orb.}}}{8\rho_{\sigma}^{1\text{-Orb.}}}, \quad (2.61)$$

where the last term is equivalent to the von Weizsäcker kinetic energy density

$$\tau_{\text{W},\sigma}(\mathbf{r}) = \frac{\gamma_{\sigma\sigma}(\mathbf{r})}{8\rho_{\sigma}(\mathbf{r})}. \quad (2.62)$$

For systems with multiple orbitals, this observation suggests that comparison of $\tau_{\sigma}(\mathbf{r})$ and $\tau_{\text{W},\sigma}(\mathbf{r})$ allows to identify one-orbital regions which is useful to address the self-interaction problem. Both, the difference of the kinetic energy densities^a

$$D_{\sigma}(\mathbf{r}) = 2 \cdot [\tau_{\sigma}(\mathbf{r}) - \tau_{\text{W},\sigma}(\mathbf{r})] \quad (2.63)$$

and their ratio

$$t_{\sigma}(\mathbf{r}) = \frac{\tau_{\text{W},\sigma}(\mathbf{r})}{\tau_{\sigma}(\mathbf{r})} \quad (2.64)$$

^aThe prefactor of 2 in eq. 2.63 is introduced for consistency with the definition by Becke in ref. 128.

are in common use in mGGAs.^[128,129]

An early attempt for a mGGA exchange functional is the non-empirical ansatz by Becke and Roussel^[130] that uses both Laplacian and τ terms to model the exchange hole within an iterative procedure proceeding from the exactly known exchange hole of a hydrogen-like system. The model provides significantly improved atomic exchange energies when compared to LSDA but lags behind the GGA functional B88 described above.^[131] In 1995, Becke also suggested a mGGA correlation functional (B95)^[128] that uses the quantity D_σ defined above and its uniform gas limit $D_\sigma^{\text{UEG}} = \frac{3}{5}(6\pi^2)^{2/3}\rho_\sigma^{5/3}$ to construct a functional that is free from one-electron self-interaction.^[128] Dropping the spatial variable \mathbf{r} for brevity, the B95 correlation energy density reads^[17,128]

$$e_c^{\text{B95}} = d_{\text{opp}} [1 + c_{\text{opp}} (x_\alpha^2 + x_\beta^2)]^{-1} e_{c, \text{opp}}^{\text{PW92}} + \sum_\sigma d_{\sigma\sigma} [1 + c_{\sigma\sigma} x_\sigma^2]^{-2} \frac{D_\sigma}{D_\sigma^{\text{UEG}}} e_{c, \sigma\sigma}^{\text{PW92}}, \quad (2.65)$$

where $e_{c, \sigma\sigma}^{\text{PW92}} = e_c^{\text{PW92}}(\rho_\sigma, 0)$ is either one of the same-spin parts of the PW92 LSDA correlation energy density and the remaining opposite-spin correlation is defined by subtracting the same-spin correlation parts, i.e. $e_{c, \text{opp}}^{\text{PW92}}(\rho_\alpha, \rho_\beta) = e_c^{\text{PW92}}(\rho_\alpha, \rho_\beta) - \sum_\sigma e_c^{\text{PW92}}(\rho_\sigma, 0)$.^[128]

Perdew, Kurth, Zupan and Blaha (PKZB) presented another mGGA in which they systematically improved the PBE model by including τ terms in the enhancement factor.^[129] In the correlation part, the ratio $t_\sigma(\mathbf{r})$ defined in eq. 2.64 is used to construct a self-interaction free version of the PBE correlation functional.^[129] This led to improvements compared to PBE for surface and atomization energies, but other properties like bond-lengths or binding energies in hydrogen-bonded complexes were deteriorated.^[132] Building on PKZB, Tao, Perdew, Staroverov and Scuseria (TPSS) developed a mGGA that fulfills additional exact constraints.^[132] The TPSS functional cured its predecessor problems with bond lengths and hydrogen-bonded complexes while maintaining good atomization energies.^[132] Perdew and co-workers continued the strategy of satisfying more of the known exact constraints introducing a strongly constrained and appropriately normed (SCAN) mGGA functional that fulfills all 17 known constraints for a mGGA functional and gives particularly good results for weak interactions and lattice constants.^[133]

Hybrid Functionals

The fourth rung of the Jacob's Ladder is held by functionals that explicitly depend on the occupied KS orbitals. The motivation for this step can be understood within the AC formalism described in section Section 2.2.3. Rearranging the definitions from eq. 2.47 and eq. 2.48, the XC functional is obtained as an integral over the coupling strength

dependent XC functional

$$E_{\text{xc}} = \int_0^1 U_{\text{xc}}^\lambda d\lambda, \quad (2.66)$$

where U_{xc}^λ is the potential energy part of the XC energy at intermediate coupling strength λ .^[10] Note that the kinetic energy part of the XC energy is obtained by integration over λ .^[10] Considering first the $\lambda = 0$ limit, it is clear that correlation is absent and that only exchange has to be considered. Because the exact wave function is a single Slater determinant in the non-interacting limit, the exchange energy can be expressed as in HF theory but using the KS orbitals $\{\varphi\}$, which is referred to as exact exchange (EXX)

$$E_{\text{x}}^{\text{ex}} = -\frac{1}{2} \sum_{\sigma} \sum_{pqrs} D_{pq}^{\sigma} D_{rs}^{\sigma} \iint \frac{\varphi_{p,\sigma}^*(\mathbf{r}) \varphi_{s,\sigma}(\mathbf{r}) \varphi_{r,\sigma}^*(\mathbf{r}') \varphi_{q,\sigma}(\mathbf{r}')}{|\mathbf{r} - \mathbf{r}'|} d\mathbf{r} d\mathbf{r}', \quad (2.67)$$

where the density matrix elements are non-zero only for occupied-occupied orbital indices (cf. eq. 2.21). For the other limit of the AC, namely the fully interacting, $\lambda = 1$ limit, $U_{\text{xc}}^{\lambda=1}$ has to cover both exchange and correlation. For the correlation, the simplest approach is to use the potential energy part from LSDA functionals $U_{\text{c}}^{\text{LSDA}}$. Opposed to the exact correlation hole, the correlation hole from LSDA is localized around the reference electron. Combining it with the correct, non-local exact-exchange hole would not give the correct, rather localized XC hole structure but a too delocalized hole.^[9,134] Therefore, the exchange part in the $\lambda = 1$ limit must not be E_{x}^{ex} but has to be more localized, so that if combined with LSDA correlation the qualitatively correct XC hole is obtained.^[9,134] Of course, this requirement is fulfilled if the exchange part is also LSDA exchange. If the connection between the two limits U_{xc}^λ was assumed to be linear in λ , solving the integral in eq. 2.66 is straightforward

$$E_{\text{xc}}^{\text{H\&H}} = \frac{1}{2} E_{\text{x}}^{\text{ex}} + \frac{1}{2} U_{\text{xc}}^{\text{LSDA}}, \quad (2.68)$$

which is exactly the half-and-half (H&H) theory by Becke.^[9] The inclusion of HF like EXX makes the functional explicitly orbital dependent and gives rise to the term “hybrid functional”. Soon after the original H&H theory, hybrid functionals with other fractions a of EXX and any desired (semi)local exchange and correlation functionals were suggested. Their general form may be denoted as

$$E_{\text{xc}}^{\text{GH}} = a E_{\text{x}}^{\text{ex}} + (1 - a) E_{\text{x}}^{\text{sl}} + E_{\text{c}}^{\text{sl}}, \quad (2.69)$$

and they are referred to in this work as global hybrid functionals (global hybrids, GHs) because $0 < a \leq 1$ is constant in space. Becke extended the hybrid concept by intro-

ducing additional semi-empirical parameters fitted to various properties, which became known as the Becke3 (B3) parameterization and substantially improved the performance for atomization energies.^[10] Using the same fitting parameters but employing the LYP functional^[124] in the correlation part instead of LSDA,^[135] has led to the well-known B3LYP functional

$$E_{xc}^{\text{B3LYP}} = aE_x^{\text{ex}} + (1 - a)E_x^{\text{LSDA}} + b\Delta E_x^{\text{B88}} + cE_c^{\text{LYP}} + (1 - c)E_c^{\text{VWN}}, \quad (2.70)$$

where $a = 0.2$, $b = 0.72$, and $c = 0.81$. Overall, B3LYP provided substantial improvements over rung 1–3 functionals at the time for thermochemistry and barriers,^[118] which caused unprecedented popularity of this functional in chemistry.^[136,137]

Over time, numerous other GHs were developed and two major design philosophies can be identified. One strategy is starting from an existing non-empirical GGA or mGGA functional like PBE or SCAN and then identify a suitable amount of EXX following theoretical arguments leading to functionals like PBE0^[138] or SCAN0.^[139] Another strategy is to determine the optimal amount of EXX empirically by fitting to some dataset as done in TPSSH,^[140] B97,^[141] PW6B95,^[142] or many of the functionals from the Minnesota class of functionals by Truhlar^[143] to name only a few.

A major reason for the success of GHs is the mitigation of the self-interaction error inherent in the classical Coulomb term $J[\rho]$ (eq. 2.35). If J is expressed as a four-center integral $J = \frac{1}{2} \sum_{pqrs\sigma\sigma'} v_{pqrs}^{\sigma\sigma'} D_{pq}^{\sigma} D_{rs}^{\sigma'}$, comparison with eq. 2.67 illustrates that for same-electron interactions, i.e. identical density matrix elements and spin-indices, the EXX term from GHs compensates the artificial repulsive term from J just as it does in HF theory (cf. eq. 2.18). The extent of this effect depends, of course, on the prefactor a in eq. 2.69. However, as outlined above, 100% EXX ($a = 1$) is typically not desirable as it gives a qualitatively incorrect XC hole when combined with conventional (semi)local correlation functionals. Developments of compatible non-local correlation functionals like the B05 functional by Becke aim at solving this problem.^[144,145] Apart from that, (semi)local exchange functionals emulate some effects of static correlation^[111] and can therefore be preferable over a complete cancellation of self-interaction.^[18,146]

As EXX admixture has revealed to cut both ways, more flexible approaches than a globally constant admixture are a natural extension. One such approach are local hybrid functionals, which are central to this work and will be discussed in detail in Section 2.3. Another popular scheme are range-separated hybrid (RSH) functionals. Their basic idea is the range-separation (RS) of the interelectronic interaction operator $1/r_{12} = 1/|\mathbf{r}_1 - \mathbf{r}_2|$

into a short-range part and a long-range part using the error-function^[131]

$$\frac{1}{r_{12}} = \frac{1 - \text{erf}(\omega r_{12})}{r_{12}} + \frac{\text{erf}(\omega r_{12})}{r_{12}}, \quad (2.71)$$

where ω is the RS parameter. The inverse of ω corresponds to the characteristic length at which the second term (long-range) in eq. 2.71 starts to dominate, i.e. small values ω give an extended short-range contribution, and larger values of ω lead to an earlier onset of the long-range part along the interelectronic coordinate. In RSHs, this separation scheme is used for a mixing of exact and (semi)local exchange. For functionals devoted to the application in molecular systems, the common choice is to use EXX in the long-range part and some suitably modified (semi)local exchange functional in the short-range part. 100% EXX for $r_{12} \rightarrow \infty$ ensures the correct asymptotic $-1/r$ increase of the exchange potential, which is required to compensate the $+1/r$ drop-off of the Coulomb potential and thus avoids self-interaction at large r_{12} .^[147] This behavior makes RSHs particularly successful for situations where charge-separation has to be described as it is the case with charge-transfer excitations or zwitterionic electronic structures.^[148–150] An early RSH that is based on the PBE model is LC- ω PBE,^[148] which uses a range-separation parameter of $\omega = 0.4$ and proved to be suitable for the description of charge-separation phenomena while providing moderate performance for thermochemistry, barrier heights, and bond lengths.^[148] Based on B3LYP, the RSH CAM-B3LYP has been developed, where the range separation ($\omega = 0.33$) is not between 0% and 100% EXX but between a constant fraction of EXX at SR (19%) and long range (65%), which was termed the 'Coulomb-attenuating method'.^[151] Other popular RSHs are the more parametrized functionals from the ω B97 family developed by Head-Gordon.^[152–155] Notably, three of those functionals hold the top 3 of best performing rung 4 functionals for the extensive and diverse GMTKN55 main group energetics test suite which, however, cannot be attributed to the RS scheme exclusively.^[6] It has also been realized that the optimal RS parameter ω exhibits a significant system dependence.^[156,157] This has led to the development of optimally tuned RSHs,^[158] which derive this optimal parameter from the IP theorem.^[159] Although this approach can give superior results, it lacks size-consistency and the tuning-process makes practical applications somewhat cumbersome.^[158] As a strategy to overcome the system-dependency of the RS parameter, the idea of local range-separation has been put forward^[160] and has recently been advanced with the first self-consistent implementation of these functionals becoming available.^[161] The idea here is to replace the constant RS parameter in RSHs by a real-space dependent RS function. The approach was particularly successful and

competitive with optimally tuned RSHs for the prediction of outer-valence spectra but does not have the pitfalls associated with the tuning process.^[161]

Virtual Orbital Dependent Functionals

While the explicit orbital-dependence of rung 4 hybrid functionals is limited to occupied orbitals, functionals from the fifth and topmost rung of the Jacob’s Ladder also depend on virtual orbitals. The subclass of double hybrid (DH) functionals extend the hybrid scheme, previously used exclusively for exchange, to the correlation part. A certain fraction b of (semi)local correlation is replaced by a perturbative MP2-like term E_c^{PT2} ^[162]

$$E_{\text{xc}}^{\text{DH}} = aE_{\text{x}}^{\text{ex}} + (1 - a)E_{\text{x}}^{\text{sl}} + cE_c^{\text{PT2}} + (1 - c)E_c^{\text{sl}}. \quad (2.72)$$

A popular DH is B2PLYP by Grimme,^[162] which was at the time of its development claimed to be the best general purpose XC functional and delivered significant improvements over rung 4 functionals for thermochemistry and barriers.^[162] However, the inclusion of the virtual orbital space increases the formal N_{b}^4 scaling of rung 4 functionals to a formal N_{b}^5 scaling, which somewhat limits the applicability. However, applying a spin-opposite scaled scheme for the perturbative part and combining this ansatz with a Laplace transformation algorithm,^[163] reduces the scaling of energy calculations to N_{b}^4 .^[164,165] Over the past years, several other DHs have been developed^[165] including functionals that apply the RS scheme to the correlation part,^[166] the exchange part,^[167] or both.^[168]

A different ansatz to include virtual orbitals for the description of correlation is the Random Phase Approximation (RPA), which deduces the correlation energy from a response treatment of the density.^[169,170] The quality is comparable to the MP2-like approach used in DHs but the computational cost and sensitivity to small differences in the orbital energies are reduced.^[171]

2.3 Local Hybrid Functionals

The admixture of EXX has proven useful both in the GH, RSH, and DH scheme to mitigate the self-interaction error and for (partly) satisfying theoretical constraints (cf. Section 2.2.4). Another natural extension of the hybrid concept is the real-space dependent admixture of EXX. This idea was originally envisaged by Burke and co-workers in 1998^[172] and the first explicit functional was specified by Jaramillo, Scuseria and Ernzerhof in 2003^[11] and the corresponding class of functionals is called local hybrid functionals (local hybrids, LHs).

2.3.1 General Formulation

To accomplish the desired real-space mixing of EXX, the fixed hybrid parameter a in the definition of a GH (eq. 2.69) has to be replaced by a position-dependent function $a_\sigma(\mathbf{r})$, termed local mixing function (LMF) that is bound to $0 \leq a_\sigma(\mathbf{r}) \leq 1$. The choice of this LMF is crucial and possible forms are discussed in Section 2.3.2. While GHs are conveniently denoted as a mixing of exchange energies (cf. eq. 2.69), the concept of real-space mixing can only be formulated as a mixing of exchange energy-densities. For EXX, this energy density is simply the integrand from eq. 2.67^[67]

$$e_{x,\sigma}^{\text{ex}}(\mathbf{r}) = -\frac{1}{2} \sum_{pqrs} D_{pq}^\sigma D_{rs}^\sigma \int \frac{\varphi_{p,\sigma}^*(\mathbf{r}) \varphi_{s,\sigma}(\mathbf{r}) \varphi_{r,\sigma}^*(\mathbf{r}') \varphi_{q,\sigma}(\mathbf{r}')}{|\mathbf{r} - \mathbf{r}'|} d\mathbf{r}' . \quad (2.73)$$

However, exchange energy-densities, and energy densities in general, are not unambiguously defined,^[172,173] i.e. it is always possible to add some gauge function $\tilde{G}(\mathbf{r})$ that integrates to zero without changing the integrated energy

$$E_x = \int e_x(\mathbf{r}) d\mathbf{r} = \int e_x(\mathbf{r}) d\mathbf{r} + \underbrace{\int \tilde{G}(\mathbf{r}) d\mathbf{r}}_{=0} = \int [e_x(\mathbf{r}) + \tilde{G}(\mathbf{r})] d\mathbf{r} = \int \tilde{e}_x(\mathbf{r}) d\mathbf{r} . \quad (2.74)$$

If two different exchange energies are mixed, differences in their gauges have to be corrected for, which is accomplished by a calibration function (CF) $G_\sigma(\mathbf{r})$, which will be discussed in more detail in Section 2.3.3. With these definitions, the general form of a local hybrid reads

$$E_{xc}^{\text{LH}} = \sum_\sigma \int a_\sigma(\mathbf{r}) \cdot e_{x,\sigma}^{\text{ex}}(\mathbf{r}) d\mathbf{r} + \sum_\sigma \int [1 - a_\sigma(\mathbf{r})] \cdot [e_{x,\sigma}^{\text{sl}}(\mathbf{r}) + G_\sigma(\mathbf{r})] d\mathbf{r} + E_c^{\text{sl}} . \quad (2.75)$$

This formulation of LHs is closely related to the GH scheme from eq. 2.69 and gives some intuition of the underlying hybrid concept. By minor rearrangements, the alternative formulation

$$E_{xc}^{\text{LH}} = E_x^{\text{ex}} + \sum_\sigma \int [1 - a_\sigma(\mathbf{r})] \cdot [e_{x,\sigma}^{\text{sl}}(\mathbf{r}) - e_{x,\sigma}^{\text{ex}}(\mathbf{r}) + G_\sigma(\mathbf{r})] d\mathbf{r} + E_c^{\text{sl}} \quad (2.76)$$

is obtained.^[174] Since exchange is accounted for by E_x^{ex} and because the correlation functional E_c can be assumed to mainly capture dynamical correlation, the middle term in eq. 2.76 can be interpreted as a non-dynamical correlation term.

It is also possible to combine the real-space dependent mixing concept of local hybrids with the range-separation idea. One such approach is local range-separation discussed in the context of RSHs in Section 2.2.4 above. Another ansatz are functionals that mix range-separated exchange energy densities via a LMF, which are called range-separated local hybrids.^[175,176]

2.3.2 Local Mixing Functions

The LMF is central to the LH concept. It controls how much of the EXX energy-density and (semi)local exchange energy-density, respectively, is used in different regions of the system. The basic motivation to use different amounts of EXX is the following: While 100% EXX ($a_\sigma(\mathbf{r}) = 1$) is desirable in one-electron regions to counteract the problem of self-interaction, it is rather undesirable in other regions like the valence or bonding region. There, the use of a (semi)local functional can help to describe non-dynamical correlation.^[111] Compared to the constant mixing parameter in GHs, the LMF in LHs provides this additional flexibility.

Aside from this basic construction principle, other constraints and guidelines for the development of LMFs were identified.^[12] Consider first the real-space asymptotic region of a molecule. An electron in this region is infinitely separated from all other electrons, which makes this a one-electron region and requires an LMF value of 1 to cancel self-interaction.^[12] Secondly, at and around the nuclei the density is distinctly larger than in the rest of the molecule. In these high-density regions, the correlation energy becomes negligible compared to the exchange energy.^[12] With correlation being relatively unimportant, (semi)local exchange does not provide any benefits and it is favorable to use EXX, and hence, $a_\sigma(\mathbf{r}) = 1$ is required.^[12] A third construction principle for LMFs is obtained by considering the homogeneous limit, i.e. the limit of uniform electron density. Here, most (semi)local functionals as well as EXX are exact, but the (semi)local exchange has the aforementioned advantage of emulating effects of non-dynamical correlation.^[12] This makes (semi)local exchange desirable in this regions and implies $a_\sigma(\mathbf{r}) = 0$. The discussed constraints give guidance on how to construct LMFs but their exact fulfillment is not necessarily required to yield useful functionals.^[12] For some constraints, such as the one-electron limit, certain LMF models (e.g., the t-LMF, see below) perform better for general thermochemistry, if the exact constraint is lifted and a scaled version is used.^[13] Also, apart from the correct height of the LMF in different regions, its shape in these regions and the transition between different regions has to be taken into account.^[12]

One of the simplest LMFs is based on the inhomogeneity parameter $t_\sigma(\mathbf{r})$ introduced in the context of mGGA functionals (eq. 2.64). It takes values of 1 in iso-orbital regions and is therefore capable to determine one-electron regions. It is also bound to $0 \leq t_\sigma(\mathbf{r}) \leq 1$ and hence can be used as is as an LMF, which has been done in the first local hybrid by Jaramillo *et al.*^[11] Although this LMF satisfies the one-electron, homogenous, and asymptotic limit^[12] and gives promising results for reaction barriers and dissociation curves,^[11] it was realized by Bahmann *et al.*^[13] that a linear down-scaling of $t_\sigma(\mathbf{r})$ by a prefactor b as in

$$a_\sigma(\mathbf{r}) = b \cdot t_\sigma(\mathbf{r}) = b \cdot \frac{\tau_{W,\sigma}}{\tau_\sigma} \quad (2.77)$$

gives improved performance for thermochemistry when combined with LSDA exchange and correlation. The LMF in eq. 2.77 is referred to as “t-LMF”. With $b = 0.48$, the performance for the G2-1 set of atomization energies was shown to be competitive with contemporary GGA based GHs.^[13]

Another early LMF is based on the reduced spin-density gradient $s_\sigma(\mathbf{r})$ as defined in eq. 2.56b. This quantity is commonly used in (m)GGAs as a measure of inhomogeneity. For vanishing density gradients $|\nabla\rho_\sigma(\mathbf{r})|$ it goes to 0 thus indicating a region of homogeneous electron density.^[177] However, it diverges for vanishing densities which prevents a direct use as an LMF. Instead, it has to be mapped from the interval $[0;\infty)$ to the interval $[0;1]$, which can be achieved with various functions^[177] of which a simple error-function prevailed. This LMF is called “s-LMF” and reads

$$a_\sigma(\mathbf{r}) = \text{erf}(\beta \cdot s_\sigma(\mathbf{r})), \quad (2.78)$$

where the empirical parameter β was optimized for the G2-1 test set of atomization energy yielding an optimal value of $\beta = 0.22$ when the s-LMF is combined with LSDA exchange and correlation.^[177] The s-LMF fulfills the homogeneous limit because just like the original quantity $s_\sigma(\mathbf{r})$, it vanishes for uniform electron densities ($|\nabla\rho_\sigma(\mathbf{r})| = 0$).^[12] The mapping function also ensures that in asymptotic regions where $\rho_\sigma(\mathbf{r}) \rightarrow 0$, i.e. $s_\sigma(\mathbf{r}) \rightarrow \infty$, the LMF will approach 1 independent of the scaling factor β .^[12]

Important variants of the t- and s-LMF are the so-called “common” versions,^[178] which are obtained by replacing the spin-resolved quantities in the definition of $t_\sigma(\mathbf{r})$ and $s_\sigma(\mathbf{r})$ by the spin-summed quantities, i.e.

$$t(\mathbf{r}) = \frac{\tau_W(\mathbf{r})}{\tau(\mathbf{r})} = \frac{\gamma_{\alpha\alpha}(\mathbf{r}) + 2\gamma_{\alpha\beta}(\mathbf{r}) + \gamma_{\beta\beta}(\mathbf{r})}{8(\tau_\alpha(\mathbf{r}) + \tau_\beta(\mathbf{r}))(\rho_\alpha(\mathbf{r}) + \rho_\beta(\mathbf{r}))}, \quad (2.79a)$$

$$s(\mathbf{r}) = \frac{2^{1/3}}{k} \frac{(\gamma_{\alpha\alpha}(\mathbf{r}) + 2\gamma_{\alpha\beta}(\mathbf{r}) + \gamma_{\beta\beta}(\mathbf{r}))^{1/2}}{(\rho_{\alpha}(\mathbf{r}) + \rho_{\beta}(\mathbf{r}))^{4/3}}, \quad (2.79b)$$

where the factor of $2^{1/3}$ in the definition of the reduced density gradient ensures $s(\mathbf{r}) = s_{\sigma}(\mathbf{r})$ for spin-restricted calculations.^[67] To distinguish the standard LMFs from their common variants, the former are also referred to as spin-channel LMFs. While the two forms are identical for the spin-restricted case, the common LMF versions bring in additional opposite-spin terms in unrestricted calculations of open-shell systems or in the case of triplet excitations.^[178] It is assumed that these cross-terms help with the description of non-dynamical correlation.^[24,178]

Apart from the simple t-LMF and s-LMF, several other LMF models have been suggested such as an LMF by Kümmel and co-workers^[179] that depends on the spin-polarization, an LMF by de Silva and Corminbeuf^[180] that uses an ingredient from the density overlap region indicator,^[181] LMFs that are constructed as perturbations to a constant EXX mixing factor by Haunschild *et al.*,^[182] an LMF based on a density-matrix similarity metric suggested by Janesko *et al.*,^[183] or LMF models by Arbuznikov and Kaupp^[184] derived from the AC formalism.^[12]

2.3.3 Calibration Functions

As mentioned in Section 2.3.1, the ambiguity in the definition of energy densities leads to the problem of possibly incompatible gauges of the (semi)local and exact exchange energy-densities. Because the exchange energy density is multiplied with an LMF within the LH scheme, an additive gauge function does not integrate to zero but gives rise to an additional term

$$\int a(\mathbf{r})e_x(\mathbf{r}) \, d\mathbf{r} \neq \int a(\mathbf{r}) \left[e_x(\mathbf{r}) + \tilde{G}(\mathbf{r}) \right] \, d\mathbf{r} = \int a(\mathbf{r})e_x(\mathbf{r}) \, d\mathbf{r} + \underbrace{\int a(\mathbf{r})\tilde{G}(\mathbf{r}) \, d\mathbf{r}}_{\neq 0}. \quad (2.80)$$

This circumstance is known as the “gauge problem” and presents a major challenge in the development of LHs.^[12,15] As this problem affects both the exact and the (semi)local exchange energy-density, it is sufficient to correct for the difference of the individual gauge functions. This is the purpose of the CF $G_{\sigma}(\mathbf{r}) = \tilde{G}_{\sigma}^{\text{sl}}(\mathbf{r}) - \tilde{G}_{\sigma}^{\text{ex}}(\mathbf{r})$, which, by definition, is required to integrate to zero

$$\int G_{\sigma}(\mathbf{r}) \, d\mathbf{r} = 0. \quad (2.81)$$

Apart from that, several other requirements for suitable CFs were deduced,^[14,15] of which the condition of being totally symmetric, having the same uniform coordinate scaling as an exchange energy density, featuring an asymptotic decay and vanishing in the homogeneous limit are most important.^[15] Tao *et al.*^[14] suggested a CF that fulfills all these requirements, but due to its dependence on the Laplacian of the exact exchange energy-density, an efficient implementation seems elusive.^[15] Following Tao's basic ansatz of constructing the CF as the divergence of some vector field $\mathbf{W}_\sigma(\mathbf{r})$

$$G_\sigma(\mathbf{r}) = \nabla \cdot \mathbf{W}_\sigma(\mathbf{r}), \quad (2.82)$$

a related approach was followed by Arbuznikov *et al.*^[15] and later generalized by Maier *et al.*^[16] Importantly, their ansatz for \mathbf{W} exclusively uses (semi)local quantities and dispenses with the exact exchange energy-density used by Tao, which facilitates efficient implementation. The scheme by Maier is derived using a partial integration formula and was thus termed partial integration gauge (pig).^[16] The general expression for the N th-order CF reads^[16]

$$G_\sigma = \sum_{m=1}^N \left[\prod_{n=1}^m f_n \right] \nabla \cdot \left[\frac{\nabla \rho_\sigma s_\sigma^{m-1}}{\rho_\sigma^{1/3}} \frac{d^{m-1} F(s_\sigma)}{ds_\sigma^{m-1}} \right], \quad (2.83)$$

where dependence on \mathbf{r} was dropped for clarity, and where f_n are flexible parameters, and $F(s_\sigma)$ is some damping function that can be of the same type as GGA damping functions or also a simple Gaussian damping.^b As these CFs were deduced for the GGA case, they might be less compatible with mGGA exchange energy-densities, which led to the development of a related scheme that explicitly includes the kinetic energy density.^[16] The first ($N = 1$) and second ($N = 2$) order versions of eq. 2.83 are labeled pig1 and pig2, respectively, and are used in recent LHs.^[15,17] The flexible prefactors f_1 (and f_2) are typically optimized so that the middle term on the RHS of eq. 2.76 is minimized for systems where non-dynamical correlation should be absent.^[16] In such cases, the CF has to cancel any spurious non-dynamical correlation that arises from an incompatibility of the exact and (semi)local exchange energy density.^[16] A convenient approach is the fitting of dissociation curves of weakly bound noble gas dimers using HF as a reference.^[12,15–17,185] While (semi)local functionals give a much too attractive potential, increasing amounts of EXX in GHs brings the curve closer to the HF reference. LHs would be expected to fall somewhere in between the curves of (semi)local functionals and GHs. However,

^bNote that in ref. 16, s_σ was defined with a slightly different prefactor than in this work (eq. 2.56b), which has to be accounted for in the definition of $F(s_\sigma)$.

uncalibrated LHs were found to give a much too repulsive curve due to positive spurious non-dynamical correlation contributions.^[15] Calibration diminishes these terms yielding weakly bound dissociation curves in excellent agreement with the HF reference.^[16,185] Note that for the calibration of a more recent LH, the reference calculation is HF plus B95 correlation to account for attractive contributions from the B95 correlation functional used for this LH.^[17] Calibration also improves the compatibility of LHs with dispersion corrections like Grimme’s D3^[186] or D4^[187] corrections because these corrections no longer have to correct for gauge artifacts as they do in uncalibrated LHs.^[17,185]

2.3.4 Established Local Hybrids Used in this Work

Although the LMF and CF are clearly the characteristic features of LHs, the choice of the (semi)local exchange and correlation energy densities considerably affects the performance of a LH as well. In this section, some successful combinations of LMFs, CFs and (semi)local energy densities are reviewed. They are summarized in Table 2.1. All of these LHs are implemented in the quantum chemistry program package TURBOMOLE^[36,37] and are part of the investigations in later chapters.

LH07t-SVWN^[13] and LH07s-SVWN^[177] are based on LSDA (Slater) exchange and VWN correlation. Despite not using gradient corrections in the (semi)local exchange and correlation energy densities, they showed results for thermochemistry and barriers competitive with standard GHs.^[13,177] They use a scaled spin-channel t-LMF and s-LMF, respectively, which are plotted in Figure 2.1 along the bonding axis of the carbon monoxide molecule for demonstration. The LMFs look somewhat similar in the bonding and valence region but the behavior around the cores and in the asymptotics is distinctly different. While the t-LMF rapidly approaches the value of its prefactor as $\tau_{W,\sigma}/\tau_\sigma$ approaches 1

Table 2.1: Overview of the local hybrids used in this work.

Functional	LMF	Scal.	Exchange	Calib.	Correlation	Ref.
LH07t-SVWN	t_σ	0.480	LSDA	—	VWN	[13]
LH07s-SVWN	s_σ	0.220	LSDA	—	VWN	[177]
LH12ct-SsirPW92	t	0.646	LSDA	—	sir-PW92 ^a	[178]
LH12ct-SsifPW92	t	0.709	LSDA	—	sif-PW92 ^b	[178]
LH14t-calPBE	t_σ	0.500	0.49·LSDA + 0.51·PBE	pig1	0.55·PW92 + 0.45·PBE	[15]
LH20t	t	0.715	0.22·LSDA + 0.78·PBE	pig2	modified B95 ^c	[17]
LH20t*	t	0.715	0.22·LSDA + 0.78·PBE	—	modified B95 ^c	[17]

^a Short-range self-interaction-reduced PW92 correlation functional.^[178]

^b Short-range self-interaction-free PW92 correlation functional.^[178]

^c With parameters $d_{\text{opp}} = 1.23$, $c_{\text{opp}} = 0.00499$, $d_{\sigma\sigma} = 0.82$, and $c_{\sigma\sigma} = 0.0954$ (cf. eq. 2.65).^[17]

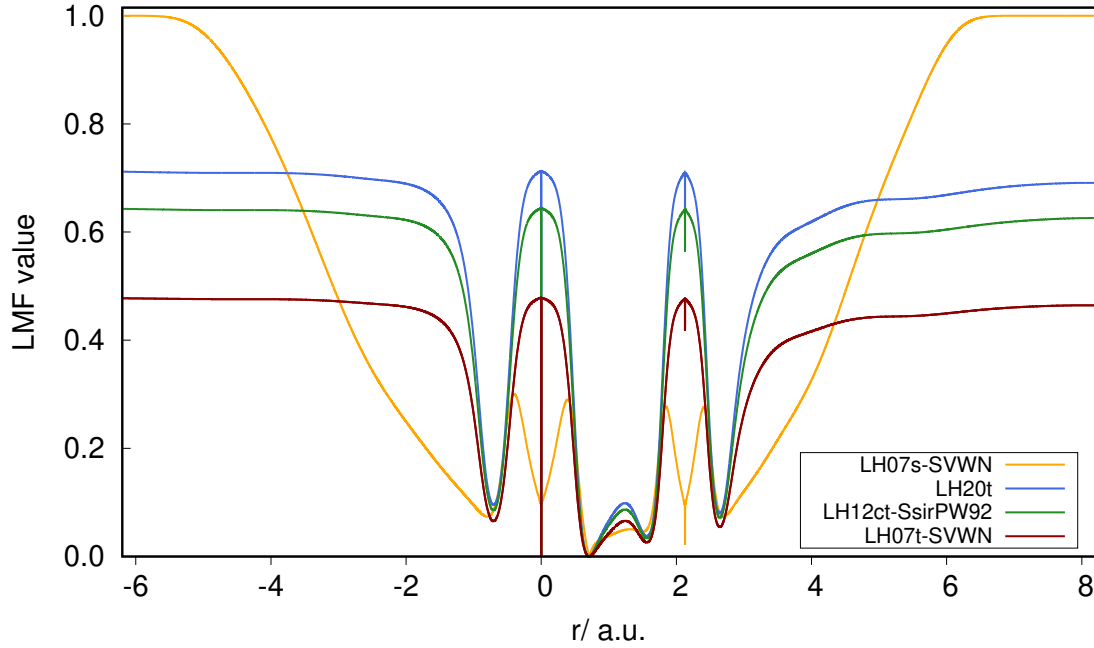


Figure 2.1: Plot of the LMFs used in some of the LHs studied in this work along the bonding axis of the carbon monoxide molecule with the carbon atom positioned at 0. Calculations were performed with TURBOMOLE 7.5 using the aug-cc-pVQZ basis set. Spikes at the positions of the nuclei are related to vanishing density gradients at nuclei within Gaussian basis sets.

in these one-electron regions, the s-LMF shows a rather slow increase towards 1 in the asymptotics and has a minimum instead of a maximum at the position of the nuclei.

LH12ct-SsirPW92 and LH12ct-SsifPW92^[178] are both based on a common t-LMF with prefactors of 0.646 and 0.709, respectively. For LH12ct-SsirPW92, this LMF is plotted in Figure 2.1 which is simply a scaled version of the t-LMF from LH07t-SVWN for this closed-shell molecule. These two LHs use a short-range self-interaction reduced (sir) and short-range self-interaction free (sif) version of the PW92 correlation functional.^[178] It is constructed by subtracting the short range part $e_{c,\mu}^{\text{SR-PW92}}$ of the PW92 correlation energy density from the conventional PW92 correlation energy density

$$e_{c,\mu,\lambda}^{\text{sir-PW92}}(\mathbf{r}) = e_c^{\text{PW92}}[\rho_\alpha(\mathbf{r}), \rho_\beta(\mathbf{r})] - \lambda \sum_{\sigma} t_{\sigma}(\mathbf{r}) e_{c,\mu}^{\text{SR-PW92}}[\rho_{\sigma}(\mathbf{r}), 0], \quad (2.84)$$

where a t-LMF with prefactor λ is used to concentrate this effect around one-electron regions and the parameter μ tunes the range-separation of the PW92 functional.^[178] Choosing $\mu = 0.8$ and enforcing $\lambda = b$, where b is the prefactor of the common t-LMF from the exchange part, LH12ct-SsirPW92 was obtained by optimizing the free parameter b

w.r.t. atomization energies. By enforcing $\lambda = b$, the short-range self-interaction is reduced by the same amount of which Coulomb self-interaction is reduced by the exchange part. Compared to LH07t-SVWN, this allows the use of larger LMF prefactors, which help with the description of barriers, without loss in accuracy for atomization energies.^[178] LH12ct-SsifPW92 also uses $\mu = 0.8$ but enforces $\lambda = 1$, which makes the correlation part short-range self-interaction free in one-electron regions. The optimal LMF prefactor of 0.709 in LH12ct-SsifPW92 is a bit larger than the 0.646 prefactor found for LH12ct-SsirPW92. Likewise, atomization energies are deteriorated very slightly with LH12ct-SsifPW92 when compared to LH12ct-SsirPW92 but barrier heights are further improved.^[178]

The LHs presented so far do not use GGA components in the (semi)local parts because these increase the sensitivity to the gauge problem. With the use of a pig1 CF in LH14t-calPBE, inclusion of PBE exchange and correlation became feasible.^[15] This t-LMF based LH was found to give excellent performance for the GMTKN30 test suite^[164] competitive with PW6B95 (both including D3^[186] dispersion corrections), which is one of the best performing GHs.^[185] Further improvements were achieved with the recent LH20t, which utilizes a common t-LMF, a larger fraction of PBE exchange in the (semi)local exchange energy density, a pig2 CF and a modified B95 correlation functional.^[17] The overall nine empirical parameters were optimized in a multistep procedure for atomization energies and barrier heights as well as for noble gas dimer curves to adjust the pig2 CF as outlined in Section 2.3.3. LH20t shows excellent performance for the GMTKN55 test suite^[6] which is further improved when the functional is combined with D4^[187] dispersion corrections. With a WTMAD-1 of 2.64 kcal/mol and a WTMAD-2 of 4.74 kcal/mol (both including D4 dispersion corrections)^[17] its performance surpasses all GHs and puts LH20t among the best rung 4 functionals,^[17] i.e. the range-separated, dispersion corrected hybrids ω B97X-D3 (WTMAD-1 = 2.71 kcal/mol, WTMAD-2 = 4.77 kcal/mol),^[6] ω B97X-V (2.32 kcal/mol, 3.98 kcal/mol),^[6] and ω B97M-V (2.01 kcal/mol, 3.53 kcal/mol).^[188] With that, LH20t is the so far most successful of all LHs. It is also particularly well suited for the description of mixed-valence compounds,^[17] which often require a fine balance of avoiding delocalization errors and correctly simulating left-right correlation.^[189] The additional flexibility in EXX admixture governed by the LMF makes LHs particularly suited for this challenge.^[18,190] For a demanding test set of mixed-valence oxide systems (MVO-10),^[18] LH20t is the only investigated XC functional that simultaneously describes the most localized case (Al_2O_4^-) and delocalized case ($\text{V}_4\text{O}_{10}^-$) correctly.^[17] In addition to the excellent performance for ground state properties, LH20t also proved to be accurate for excited state calculations.^[17]

2.4 Excited State Theory

DFT, both in its original formulation by Hohenberg and Kohn (cf. Section 2.2.1) and in the KS formalism (cf. Section 2.2.2), is strictly a GS theory. That is, even with knowledge of the exact functional, the theory provides no universal access to the energy or properties of electronically excited states (ESs). A pragmatic and often successful^[25] approach is the Δ SCF method^[191,192] that treats ESs as if they were GSs. Excitation energies are obtained as the difference of the minimized ES energy and that of the true GS. To achieve converged solutions for the ES, collapse to the GS or lower-energy ESs has to be precluded, e.g. by (spin-)symmetry, which limits the applicability of the original Δ SCF method. This limitation has been overcome with the development of constricted variational DFT,^[193–197] which mixes a fraction of every virtual GS orbital into each of the occupied GS orbitals to create a new set of occupied ES orbitals.^[194] The additional constraints enforced on the involved mixing coefficients prevent the variational collapse of higher lying ESs in SCF calculations.^[194] Besides, other approaches like the generalized adiabatic connection KS formalism were developed and allow a DFT treatment of specific ESs.^[198]

Despite these developments, the more widespread theory for the treatment of excited states within DFT is time-dependent density functional theory (TDDFT). Just like DFT is an exact theory to solve the stationary Schrödinger equation (eq. 2.13), TDDFT is a formally exact theory to solve the time-dependent Schrödinger equation (eq. 2.9). And while DFT uses the GS electron density $\rho(\mathbf{r})$, the central quantity in TDDFT is the time-dependent electron density

$$\rho(\mathbf{r}, t) := \rho(\mathbf{r}_1, t) = N \int |\Psi(\mathbf{x}_1, \dots, \mathbf{x}_N, t)|^2 ds_1 d\mathbf{x}_2 \dots d\mathbf{x}_N \quad (2.85)$$

derived from the time-dependent N -electron wave function $\Psi(\mathbf{x}_1, \dots, \mathbf{x}_N, t)$, the latter denoted below as $\Psi(\mathbf{r}, t)$ to simplify notations. Although it is possible to propagate the time-dependent density in real-time,^[199,200] the more widespread approach^[21] is linear response TDDFT^[22] (LR-TDDFT) that extracts excitation energies and ES properties from the linear response function of the density in frequency space. For a comprehensible derivation of the relevant equations, the foundations of response theory are introduced in a general scheme first (Section 2.4.1). In this context, the important special case of the dynamic polarizability tensor is derived as well. Next, the time-dependent Kohn–Sham (TDKS) framework is introduced, and eventually, the linear response scheme is

applied within TDKS to derive Casida's equations,^[22] which are the working equations of LR-TDDFT.

2.4.1 Response Theory

Derivation of the Linear Response Function

The basic idea of response theory is to express the response of a system to some time-dependent perturbation using a response function χ . Consider, for example, the response of the time-dependent density $\delta\rho(\mathbf{r}, t)$ to a change in the external potential $\delta v_{\text{ext}}(\mathbf{r}, t)$ which is formally obtained as

$$\delta\rho(\mathbf{r}, t) = \int dt' \int d\mathbf{r}' \underbrace{\frac{\delta\rho(\mathbf{r}, t)}{\delta v_{\text{ext}}(\mathbf{r}', t')}\bigg|_{v_{\text{ext},0}}}_{\chi(\mathbf{r}, \mathbf{r}', t-t')} \delta v_{\text{ext}}(\mathbf{r}', t'), \quad (2.86)$$

where the response function $\chi(\mathbf{r}, \mathbf{r}', t-t')$ is simply the functional derivative.^[201] Using the convolution theorem,^c an equivalent representation of eq. 2.86 in the frequency domain reads

$$\delta\rho(\mathbf{r}, \omega) = \int d\mathbf{r}' \chi(\mathbf{r}, \mathbf{r}', \omega) \delta v_{\text{ext}}(\mathbf{r}', \omega). \quad (2.87)$$

To determine the response function, the change in the density $\delta\rho(\mathbf{r}, \omega)$ is derived from time-dependent perturbation theory and later compared to eq. 2.87.

In general, a quantum chemical system with Hamilton operator \hat{H}^0 that is perturbed by a small, time-dependent perturbation $\delta\hat{H}(t)$ obeys the time-dependent Schrödinger equation

$$i \frac{\partial}{\partial t} |\Psi(\mathbf{r}, t)\rangle = [\hat{H}^0 + \delta\hat{H}(t)] |\Psi(\mathbf{r}, t)\rangle. \quad (2.88)$$

The time-dependency of the state $|\Psi(\mathbf{r}, t)\rangle$ can be expanded in terms of eigenstates of the unperturbed, time-independent Schrödinger equation $\hat{H}^0 |\Psi_n^0\rangle = E_n |\Psi_n^0\rangle$ and a time-dependent function $a_n(t)$ as^[202]

$$|\Psi(t)\rangle = \sum_n a_n(t) e^{-iE_n t} |\Psi_n^0\rangle. \quad (2.89)$$

^cThis work uses the Fourier convention from ref. 22: $f(\omega) = \int_{-\infty}^{+\infty} dt e^{+i\omega t} f(t)$, $f(t) = \int_{-\infty}^{+\infty} \frac{d\omega}{2\pi} e^{-i\omega t} f(\omega)$ and the convolution theorem: $h(t) = \int_{-\infty}^{+\infty} dt' g(t-t') f(t') \Leftrightarrow h(\omega) = g(\omega) \cdot f(\omega)$

Inserting this ansatz into eq. 2.88, left-multiplying with $\langle \Psi_k^0 |$ and exploiting the orthonormality condition $\langle \Psi_k^0 | \Psi_n^0 \rangle = \delta_{kn}$ gives^[202]

$$\frac{\partial a_k(t)}{\partial t} = -i \sum_n \langle \Psi_k^0 | \delta \hat{H}(t) | \Psi_n^0 \rangle a_n(t) e^{+i(E_k - E_n)t}. \quad (2.90)$$

Next, the time-dependent function $a_k(t)$ is expanded in a power series^[202]

$$a_k(t) = a_k^0(t) + \lambda a_k^{(1)}(t) + \lambda^2 a_k^{(2)}(t) + \dots, \quad (2.91)$$

where λ determines the strength of the perturbation. Inserting this ansatz into eq. 2.90 and collecting only terms up to first order gives after time-integration^[202]

$$a_k^{(1)}(t) = -i \int_{-\infty}^t dt' \langle \Psi_k^0 | \delta \hat{H}(t') | \Psi_0^0 \rangle e^{+i\Omega_k t'}, \quad (2.92)$$

where $\Omega_k = E_k - E_0$ is the excitation energy for the state with energy E_k and where it was assumed that the system was at the unperturbed state at $t = -\infty$. To relate this general scheme to the response of the density which is of interest here, an explicit ansatz for the perturbing term $\delta \hat{H}(t)$ has to be made

$$\delta \hat{H}(t) = e^{\eta t} \sum_{q=1}^{N_e} \delta v_{\text{ext}}(\mathbf{r}_q, t). \quad (2.93)$$

Here, the exponential with $0 < \eta \ll 1$ is used to guarantee a slow switch-on of the perturbation and the external potential is written as the sum of all individual one-body terms (in the simplest case, electron-nuclei interactions).^[201] Introducing now the density operator

$$\hat{\rho}(\mathbf{r}) = \sum_{q=1}^{N_e} \delta(\mathbf{r}_q - \mathbf{r}) \quad (2.94)$$

and writing $\delta v_{\text{ext}}(\mathbf{r}_q, t)$ in the frequency domain gives^[201]

$$\delta \hat{H}(t) = \int d\mathbf{r} \int \frac{d\omega}{2\pi} e^{-i(\omega + i\eta)t} \delta v_{\text{ext}}(\mathbf{r}, \omega) \hat{\rho}(\mathbf{r}). \quad (2.95)$$

This expression may now be inserted in eq. 2.92, which after time integration yields^[201]

$$a_n^{(1)}(t) = - \int d\mathbf{r} \int \frac{d\omega}{2\pi} \langle \Psi_n^0 | \hat{\rho}(\mathbf{r}) | \Psi_0^0 \rangle \delta v_{\text{ext}}(\mathbf{r}, \omega) \frac{e^{+i(\Omega_n - \omega - i\eta)t}}{\Omega_n - \omega - i\eta}, \quad (2.96)$$

which may be used to get a first-order approximation of the time-dependent wave function^[201]

$$|\Psi(t)\rangle = e^{-iE_0t} |\Psi_0^0\rangle + \sum_{n \neq 0} a_n^{(1)}(t) e^{-iE_nt} |\Psi_n^0\rangle. \quad (2.97)$$

With this expression for the wave function, the linear change in the density may be written as

$$\begin{aligned} \delta\rho(\mathbf{r}, t) &= \langle \Psi(t) | \hat{\rho}(\mathbf{r}) | \Psi(t) \rangle - \langle \Psi_0^0 | \hat{\rho}(\mathbf{r}) | \Psi_0^0 \rangle \\ &= \sum_{n \neq 0} [a_n^{(1)}(t) e^{-i\Omega_nt} \langle \Psi_0^0 | \hat{\rho}(\mathbf{r}) | \Psi_n^0 \rangle + a_n^{(1)*}(t) e^{+i\Omega_nt} \langle \Psi_n^0 | \hat{\rho}(\mathbf{r}) | \Psi_0^0 \rangle] \\ &= \int d\mathbf{r}' \int \frac{d\omega}{2\pi} \delta v_{\text{ext}}(\mathbf{r}', \omega) e^{-i(\omega+i\eta)t} \sum_{n \neq 0} \left[\frac{\langle \Psi_n^0 | \hat{\rho}(\mathbf{r}') | \Psi_0^0 \rangle \langle \Psi_0^0 | \hat{\rho}(\mathbf{r}) | \Psi_n^0 \rangle}{\omega + i\eta - \Omega_n} \right. \\ &\quad \left. - \frac{\langle \Psi_0^0 | \hat{\rho}(\mathbf{r}') | \Psi_n^0 \rangle \langle \Psi_n^0 | \hat{\rho}(\mathbf{r}) | \Psi_0^0 \rangle}{\omega + i\eta + \Omega_n} \right], \quad (2.98) \end{aligned}$$

where second-order terms were neglected and terms were rearranged so that the Fourier transformation is easy to see^[201]

$$\begin{aligned} \delta\rho(\mathbf{r}, \omega) &= \int d\mathbf{r}' \delta v_{\text{ext}}(\mathbf{r}', \omega) \sum_{n \neq 0} \left[\frac{\langle \Psi_n^0 | \hat{\rho}(\mathbf{r}') | \Psi_0^0 \rangle \langle \Psi_0^0 | \hat{\rho}(\mathbf{r}) | \Psi_n^0 \rangle}{\omega + i\eta - \Omega_n} \right. \\ &\quad \left. - \frac{\langle \Psi_0^0 | \hat{\rho}(\mathbf{r}') | \Psi_n^0 \rangle \langle \Psi_n^0 | \hat{\rho}(\mathbf{r}) | \Psi_0^0 \rangle}{\omega + i\eta + \Omega_n} \right]. \quad (2.99) \end{aligned}$$

Comparison of this expression with eq. 2.87 gives the density response function^[201]

$$\chi(\mathbf{r}, \mathbf{r}', \omega) = \sum_{n \neq 0} \left[\frac{\langle \Psi_n^0 | \hat{\rho}(\mathbf{r}') | \Psi_0^0 \rangle \langle \Psi_0^0 | \hat{\rho}(\mathbf{r}) | \Psi_n^0 \rangle}{\omega + i\eta - \Omega_n} - \frac{\langle \Psi_0^0 | \hat{\rho}(\mathbf{r}') | \Psi_n^0 \rangle \langle \Psi_n^0 | \hat{\rho}(\mathbf{r}) | \Psi_0^0 \rangle}{\omega + i\eta + \Omega_n} \right]. \quad (2.100)$$

Response to an External Electric Field

Equation 2.100 gives the general response function of the density under the influence of a (time-dependent) change in the external potential. As a first concrete example, the response of the dipole moment

$$\boldsymbol{\mu} = \int \mathbf{r} \cdot \rho(\mathbf{r}) d\mathbf{r} \quad (2.101)$$

to an external electric field \mathcal{E} with field strength $\mathcal{E}(t)$ is considered. From the time-independent case it is known that the Taylor expansion of the dipole moment

$$\boldsymbol{\mu} = \boldsymbol{\mu}_0 + \boldsymbol{\alpha}\mathcal{E} + \frac{1}{2}\mathcal{E}^\top\boldsymbol{\beta}\mathcal{E} + \dots \quad (2.102)$$

can be used to express its change under the influence of an electric field in terms of its polarizability $\boldsymbol{\alpha}$, hyperpolarizability $\boldsymbol{\beta}$, and higher-order terms, where

$$\alpha_{ij} = \left. \frac{\partial \mu_i}{\partial \mathcal{E}_j} \right|_{\mathcal{E}=0}, \quad \beta_{ijk} = \left. \frac{\partial^2 \mu_i}{\partial \mathcal{E}_j \partial \mathcal{E}_k} \right|_{\mathcal{E}=0}, \quad i, j, k \in \{x, y, z\}. \quad (2.103)$$

The extension to the time-dependent case requires an appropriate time-integration

$$\begin{aligned} \mu_x(t) &= \mu_x^0 + \int_{-\infty}^{+\infty} dt' \left. \frac{\delta \mu_x(t)}{\delta \mathcal{E}_z(t')} \right|_{\mathcal{E}_z=0} \mathcal{E}_z(t) + \dots \\ &= \mu_x^0 + \int_{-\infty}^{+\infty} dt' \alpha_{xz}(t-t') \mathcal{E}_z(t) + \dots, \end{aligned} \quad (2.104)$$

where, without loss of generality, the field is assumed to be oriented in z -direction and the response of the dipole moment is considered in x -direction to simplify notations.^[22] Subtracting μ_x^0 from both sides of eq. 2.104 and applying the convolution theorem yields

$$\delta \mu_x(\omega) = \alpha_{xz}(\omega) \cdot \mathcal{E}_z(\omega). \quad (2.105)$$

Alternatively, the change in the dipole moment can be calculated from the density following eq. 2.101

$$\delta \mu_x(\omega) = - \int d\mathbf{r} \hat{r}_x \cdot \delta \rho(\mathbf{r}, \omega), \quad (2.106)$$

where the minus sign accounts for the negative charge of the electron density and the position in x -direction is written as a position operator \hat{r}_x . Inserting the definition of $\delta \rho(\mathbf{r}, \omega)$ from eq. 2.87 and the ansatz $\delta v_{\text{ext}}(t) = \hat{r}_z \mathcal{E}_z(t)$ for the change in the external potential gives

$$\delta \mu_x(\omega) = - \int d\mathbf{r} \int d\mathbf{r}' \hat{r}_x \cdot \chi(\mathbf{r}, \mathbf{r}', \omega) \cdot \hat{r}'_z \mathcal{E}_z(\omega) \quad (2.107)$$

Comparison of this equation with eq. 2.105 gives the frequency-dependent (dynamic) polarizability^[203]

$$\alpha_{xz}(\omega) = - \int d\mathbf{r} \int d\mathbf{r}' \hat{r}_x \cdot \chi(\mathbf{r}, \mathbf{r}', \omega) \cdot \hat{r}_z \quad (2.108)$$

expressed in terms of the general density response function $\chi(\mathbf{r}, \mathbf{r}', \omega)$. Using the explicit expression for $\chi(\mathbf{r}, \mathbf{r}', \omega)$ (eq. 2.100), considering the $\eta \rightarrow 0^+$ limit and exploiting symmetry of the position operators finally yields^[22]

$$\alpha_{xz}(\omega) = \sum_{n \neq 0} \frac{2\Omega_n \langle \Psi_0^0 | \hat{r}_x | \Psi_n^0 \rangle \langle \Psi_n^0 | \hat{r}_z | \Psi_0^0 \rangle}{\Omega_n^2 - \omega^2}. \quad (2.109)$$

Of particular interest is the mean polarizability

$$\bar{\alpha}(\omega) = \frac{1}{3} \text{tr}(\boldsymbol{\alpha}(\omega)) = \frac{2}{3} \sum_{k \in \{x,y,z\}} \sum_{n \neq 0} \frac{\Omega_n |\langle \Psi_0^0 | \hat{r}_k | \Psi_n^0 \rangle|^2}{\Omega_n^2 - \omega^2}, \quad (2.110)$$

which by comparison with the definition of spectroscopic oscillator strengths

$$f_n = \frac{2}{3} \Omega_n \sum_{k \in \{x,y,z\}} |\langle \Psi_0^0 | \hat{r}_k | \Psi_n^0 \rangle|^2 \quad (2.111)$$

is transformed to the simple expression^[22]

$$\bar{\alpha}(\omega) = \sum_{n \neq 0} \frac{f_n}{\Omega_n^2 - \omega^2}. \quad (2.112)$$

Two basic conclusions can be drawn from this equation. First, excitation energies are associated with poles of the mean dynamic polarizability as can be seen from the denominator in eq. 2.112 which gets zero if the irradiated frequency ω equals an excitation energy Ω_n .^[22] Second, the residues at these poles correspond to the oscillator strength of the respective excitation.^[22] In the limiting case of $\omega \rightarrow 0$, eq. 2.112 yields the mean static polarizability. This goes to show that the mean static polarizability can be interpreted as the oscillator-strength weighted sum of the reciprocal squares of all (single) excitation energies. Just like the dipole moment obtained from an approximate method can be viewed as a globally averaged measure of the method's accuracy for predicting GS densities,^[204] the static polarizability can be considered as a state-averaged^d measure of a method's accuracy for predicting excitation energies and oscillator strengths.^[205]

^dStrictly speaking, this only includes dipole-allowed transitions where $f_n \neq 0$.

2.4.2 Time-Dependent Density Functional Theory

With the basic working equations of response theory at hand, their application to DFT is discussed in this section. As a first step, the formal justification of TDDFT is presented and the TDKS equations are derived.

Runge–Gross Theorems and Formal Foundations

As a time-dependent analogue to the first Hohenberg–Kohn theorem, Runge and Gross proved^[206] that the time-dependent electron density $\rho(\mathbf{r}, t)$ uniquely determines the time-dependent external potential $v(\mathbf{r}, t)$ up to a time-dependent function.^[207] In other words, if two time-dependent densities are equivalent $\rho(\mathbf{r}, t) = \rho'(\mathbf{r}, t) + C(t)$ and have evolved from the same initial state, the underlying potentials have to be equivalent, $v(\mathbf{r}, t) = v'(\mathbf{r}, t)$. An analogue to the second Hohenberg–Kohn theorem was developed by Runge and Gross starting from the quantum chemical action integral

$$\mathcal{A} = \int_{t_0}^{t_1} dt \left\langle \Psi(\mathbf{r}, t) \left| i \frac{\partial}{\partial t} - \hat{H}(\mathbf{r}, t) \right| \Psi(\mathbf{r}, t) \right\rangle, \quad (2.113)$$

which is immediately obtained by left-multiplying the time-dependent Schrödinger equation (eq. 2.9) with $\langle \Psi(\mathbf{r}, t) |$ and performing a time-integration over the interval of interest. According to the Runge–Gross theorem, \mathcal{A} is a functional of the density $\mathcal{A} = \mathcal{A}[\rho]$. Thus, the time-dependent electron density $\rho(\mathbf{r}, t)$ is obtained from the stationarity condition

$$\frac{\delta \mathcal{A}[\rho]}{\delta \rho(\mathbf{r}, t)} = 0. \quad (2.114)$$

Note that there have been some discussions if the action integral (eq. 2.113) and stationarity condition (eq. 2.114) present an adequate formalism.^[208] However, ultimately, it was shown by Vignale,^[209] that enforcing proper boundary conditions on eq. 2.114 restores the previously violated causality relation.^[208] Also, he showed that the original formulation by Runge and Gross leads to the same results for the cases relevant to this work and hence, eq. 2.114 is kept for simplicity.^[208,209]

To proceed, the Hamilton Operator from eq. 2.11 is inserted into the action functional from eq. 2.113, which is then split according to

$$\mathcal{A}[\rho] = \mathcal{B}[\rho] - \int_{t_0}^{t_1} dt \int d\mathbf{r} \rho(\mathbf{r}, t) v_{\text{ext}}(\mathbf{r}, t) \quad (2.115)$$

into a universal functional

$$\mathcal{B}[\rho] = \int_{t_0}^{t_1} dt \left\langle \Psi(\mathbf{r}, t) \left| i \frac{\partial}{\partial t} - \hat{T}(\mathbf{r}) - \hat{V}_{\text{ee}}(\mathbf{r}) \right| \Psi(\mathbf{r}, t) \right\rangle \quad (2.116)$$

independent from the external potential, and a part dependent on the external potential (second term of the RHS in eq. 2.115), where the external potential is typically $v_{\text{ext}}(\mathbf{r}, t) = \hat{V}_{\text{eN}}(\mathbf{r}) + \hat{V}_{\text{ext}}(t)$.^[207]

Time-Dependent Kohn–Sham Theory

In analogy to the procedure by Kohn and Sham for GS DFT (cf. Section 2.2.2), a time-dependent non-interacting reference system is introduced, for which the external potential $v_{\text{S}}(\mathbf{r}, t)$ adapts so that the time-dependent density of the real interacting system is equal to that of the non-interacting one. Accordingly, the time-dependent electron density may be expanded in a one-particle basis of time-dependent KS orbitals^[207]

$$\rho(\mathbf{r}, t) = \rho_{\text{S}}(\mathbf{r}, t) = \sum_i^{\text{occ}} |\varphi_i(\mathbf{r}, t)|^2. \quad (2.117)$$

These orbitals are solutions of the simple one-particle time-dependent Schrödinger equation^[207]

$$i \frac{\partial}{\partial t} \varphi_i(\mathbf{r}, t) = \left[\hat{T}(\mathbf{r}) + v_{\text{S}}(\mathbf{r}, t) \right] \varphi_i(\mathbf{r}, t), \quad (2.118)$$

with the kinetic energy operator for the one-particle case being simply $\hat{T}(\mathbf{r}) = -\frac{1}{2} \nabla^2$. For the non-interacting system, the action functional becomes

$$\mathcal{A}_{\text{S}}[\rho] = \mathcal{B}_{\text{S}}[\rho] - \int_{t_0}^{t_1} dt \int d\mathbf{r} \rho(\mathbf{r}, t) v_{\text{S}}(\mathbf{r}, t), \quad (2.119)$$

where the functional

$$\mathcal{B}_{\text{S}}[\rho] = \int_{t_0}^{t_1} dt \left\langle \Psi(\mathbf{r}, t) \left| i \frac{\partial}{\partial t} - \hat{T}(\mathbf{r}) \right| \Psi(\mathbf{r}, t) \right\rangle \quad (2.120)$$

is exactly known and may be calculated by inserting a single Slater determinant for $\Psi(\mathbf{r}, t)$.^[207] Applying the stationarity condition from eq. 2.114 to eq. 2.119 yields^[207]

$$v_{\text{S}}(\mathbf{r}, t) = \left. \frac{\delta \mathcal{B}_{\text{S}}[\rho]}{\delta \tilde{\rho}(\mathbf{r}, t)} \right|_{\tilde{\rho}(\mathbf{r}, t) = \rho(\mathbf{r}, t)}. \quad (2.121)$$

Turning back to the functional \mathcal{A} of the interacting system (eq. 2.115) and rewriting it as

$$\mathcal{A}[\rho] = \mathcal{B}_S[\rho] - \int_{t_0}^{t_1} dt \int d\mathbf{r} \rho(\mathbf{r}, t) v_{\text{ext}}(\mathbf{r}, t) - \frac{1}{2} \int_{t_0}^{t_1} dt \int d\mathbf{r} \int d\mathbf{r}' \frac{\rho(\mathbf{r}, t) \rho(\mathbf{r}', t)}{|\mathbf{r} - \mathbf{r}'|} - \mathcal{A}_{\text{xc}}[\rho] \quad (2.122)$$

with

$$\mathcal{A}_{\text{xc}}[\rho] = \mathcal{B}_S[\rho] - \frac{1}{2} \int_{t_0}^{t_1} dt \int d\mathbf{r} \int d\mathbf{r}' \frac{\rho(\mathbf{r}, t) \rho(\mathbf{r}', t)}{|\mathbf{r} - \mathbf{r}'|} - \mathcal{B}[\rho], \quad (2.123)$$

gives after application of the stationarity condition and comparison with eq. 2.121

$$v_S(\mathbf{r}, t) = v_{\text{ext}}(\mathbf{r}, t) + \underbrace{\int d\mathbf{r}' \frac{\rho(\mathbf{r}', t)}{|\mathbf{r} - \mathbf{r}'|}}_{v_H(\mathbf{r}, t)} + \underbrace{\frac{\delta \mathcal{A}_{\text{xc}}[\rho]}{\delta \rho(\mathbf{r}, t)}}_{v_{\text{xc}}(\mathbf{r}, t)} \quad (2.124)$$

for the time-dependent single-particle potential.^[207] Inserting this expression into eq. 2.118 finally yields the time-dependent Kohn–Sham (TDKS) equations^[206]

$$i \frac{\partial}{\partial t} \varphi_i(\mathbf{r}, t) = \left[-\frac{1}{2} \nabla_i^2 + v_{\text{ext}}(\mathbf{r}, t) + v_H(\mathbf{r}, t) + v_{\text{xc}}(\mathbf{r}, t) \right] \varphi_i(\mathbf{r}, t). \quad (2.125)$$

The computation of $v_{\text{xc}}(\mathbf{r}, t)$ is complicated by the fact that \mathcal{A}_{xc} depends on the changes in the density within the time interval $[t_0; t_1]$ (cf. eq. 2.123). As an approximate solution, the limiting case of a slowly varying external potential

$$\mathcal{A}_{\text{xc}} = \int_{t_0}^{t_1} dt E_{\text{xc}}[\rho_t] \quad (2.126)$$

is considered,^[22] where the conventional XC functional from GS KS-DFT is evaluated at the density ρ at time t (ρ_t). Since E_{xc} is always evaluated for densities fixed in time, this ansatz eliminates the time-dependence and is hence known as the “adiabatic approximation” (AA) or “adiabatic local density approximation” because the density is treated as local in time.^[22] The derivative $v_{\text{xc}}(\mathbf{r}, t)$ then becomes^[22]

$$v_{\text{xc}}[\rho](\mathbf{r}, t) = \frac{\delta \mathcal{A}_{\text{xc}}[\rho]}{\delta \rho(\mathbf{r}, t)} \approx \frac{\delta E_{\text{xc}}[\rho_t]}{\delta \rho_t(\mathbf{r})} = v_{\text{xc}}[\rho_t](\mathbf{r}). \quad (2.127)$$

Linear Response TDDFT

The introduction of a non-interacting reference system in TDKS theory having at each point in time the same density as the true, interacting system allows to rewrite the density

response from eq. 2.86 using the time-dependent single-particle potential (eq. 2.124)^[201]

$$\begin{aligned}\delta\rho(\mathbf{r}, t) &= \int dt' \int d\mathbf{r}' \left. \frac{\delta\rho(\mathbf{r}, t)}{\delta v_S(\mathbf{r}', t')} \right|_{v_S[\rho_0]} \delta v_S(\mathbf{r}', t') \\ &= \int dt' \int d\mathbf{r}' \chi_{KS}(\mathbf{r}, \mathbf{r}', t - t') \delta v_S(\mathbf{r}', t') \\ &= \int dt' \int d\mathbf{r}' \chi_{KS}(\mathbf{r}, \mathbf{r}', t - t') [\delta v_{\text{ext}}(\mathbf{r}', t') + \delta v_H(\mathbf{r}', t') + \delta v_{xc}(\mathbf{r}', t')] .\end{aligned}\quad (2.128)$$

While the variation $\delta v_H(\mathbf{r}, t)$ is straightforward to calculate,^e the variation $\delta v_{xc}(\mathbf{r}, t)$ requires the use of the AA, which eliminates the time-dependence in the second derivative^[22]

$$\frac{\delta v_{xc}[\rho](\mathbf{r}, t)}{\delta\rho(\mathbf{r}', t')} \approx \delta(t - t') \frac{\delta v_{xc}[\rho_t](\mathbf{r}, t)}{\delta\rho_t(\mathbf{r}')} \quad (2.129)$$

encoded here by a Dirac δ function. This allows to express the variation in the XC potential as an ordinary second functional derivative of the XC functional^[201]

$$\delta v_{xc}(\mathbf{r}, t) = \int d\mathbf{r}' \int dt' \frac{\delta v_{xc}[\rho](\mathbf{r}, t)}{\delta\rho(\mathbf{r}', t')} \delta\rho(\mathbf{r}', t') \approx \int d\mathbf{r}' f_{xc}(\mathbf{r}, \mathbf{r}') \delta\rho(\mathbf{r}', t), \quad (2.130)$$

where

$$f_{xc}(\mathbf{r}, \mathbf{r}') = \frac{\delta^2 E_{xc}[\rho_0]}{\delta\rho_0(\mathbf{r})\delta\rho_0(\mathbf{r}')} \quad (2.131)$$

is called the XC kernel. Resubstituting the explicit expressions for δv_H and δv_{xc} back into eq. 2.128 and using the convolution theorem gives^[201,210]

$$\delta\rho(\mathbf{r}, \omega) = \int d\mathbf{r}' \chi_{KS}(\mathbf{r}, \mathbf{r}', \omega) \left[\delta v_{\text{ext}}(\mathbf{r}', \omega) + \int d\mathbf{r}'' \left(\frac{1}{|\mathbf{r}' - \mathbf{r}''|} + f_{xc}(\mathbf{r}', \mathbf{r}'') \right) \delta\rho(\mathbf{r}'', \omega) \right]. \quad (2.132)$$

For future discussions, extension to the spin-resolved case is required and achieved by minor modifications

$$\begin{aligned}\delta\rho_\sigma(\mathbf{r}, \omega) &= \sum_{\sigma'} \int d\mathbf{r}' \chi_{\sigma\sigma'}^{KS}(\mathbf{r}, \mathbf{r}', \omega) \\ &\quad \left[\delta v_{\text{ext}}(\mathbf{r}', \omega) + \sum_{\sigma''} \int d\mathbf{r}'' \left(\frac{1}{|\mathbf{r}' - \mathbf{r}''|} + f_{xc}^{\sigma'\sigma''}(\mathbf{r}', \mathbf{r}'') \right) \delta\rho_{\sigma''}(\mathbf{r}'', \omega) \right],\end{aligned}\quad (2.133)$$

where the external potential was assumed to be spin-independent.^[201,210]

^eUsing the functional chain rule gives: $\delta v_H(\mathbf{r}, t) = \int d\mathbf{r}' \frac{\delta v_H(\mathbf{r}, t)}{\delta\rho(\mathbf{r}', t)} \delta\rho(\mathbf{r}', t) = \int d\mathbf{r}' \frac{1}{|\mathbf{r} - \mathbf{r}'|} \delta\rho(\mathbf{r}', t)$.^[201]

Next, the density response function of the KS system $\chi_{\text{KS}}(\mathbf{r}, \mathbf{r}', \omega)$ has to be determined. It is obtained by inserting the KS Slater determinant as an ansatz for the wave function Ψ_0^0 into the general response function from eq. 2.100. Because the density operator $\hat{\rho} = \sum_{i=1}^{N_e} \delta(\mathbf{r}_i - \mathbf{r})$ is a one-body operator, matrix elements of type $\langle \Psi_0^0 | \hat{\rho}(\mathbf{r}) | \Psi_n^0 \rangle$ in eq. 2.100 are non-zero only if the ES determinant is singly excited, i.e. constructed from promoting one electron from an occupied orbital φ_i to a virtual orbital φ_a .^[201] Hence, the sum of matrix elements $\sum_{n \neq 0} \langle \Psi_0^0 | \hat{\rho}(\mathbf{r}) | \Psi_n^0 \rangle$ reduces to a summation over orbital pairs $\varphi_a^*(\mathbf{r})\varphi_i(\mathbf{r})$ and the energy difference $\Omega_n = E_n - E_0$ has to be replaced by the difference in orbital energies $(\epsilon_a - \epsilon_i)$ ^[201,203]

$$\chi_{\text{KS}}(\mathbf{r}, \mathbf{r}', \omega) = \sum_i^{N_{\text{occ}}} \sum_a^{N_{\text{virt}}} \left[\frac{\varphi_a^*(\mathbf{r}')\varphi_i(\mathbf{r}')\varphi_i^*(\mathbf{r})\varphi_a(\mathbf{r})}{\omega + i\eta - (\epsilon_a - \epsilon_i)} - \frac{\varphi_i^*(\mathbf{r}')\varphi_a(\mathbf{r}')\varphi_a^*(\mathbf{r})\varphi_i(\mathbf{r})}{\omega + i\eta + (\epsilon_a - \epsilon_i)} \right]. \quad (2.134)$$

Again, the spin-resolved generalization is straightforward^[201,210]

$$\chi_{\sigma\sigma'}^{\text{KS}}(\mathbf{r}, \mathbf{r}', \omega) = \delta_{\sigma\sigma'} \sum_i^{N_{\text{occ}}} \sum_a^{N_{\text{virt}}} \left[\frac{\varphi_{a\sigma}^*(\mathbf{r}')\varphi_{i\sigma}(\mathbf{r}')\varphi_{i\sigma}^*(\mathbf{r})\varphi_{a\sigma}(\mathbf{r})}{\omega + i\eta - (\epsilon_{a\sigma} - \epsilon_{i\sigma})} - \frac{\varphi_{i\sigma}^*(\mathbf{r}')\varphi_{a\sigma}(\mathbf{r}')\varphi_{a\sigma}^*(\mathbf{r})\varphi_{i\sigma}(\mathbf{r})}{\omega + i\eta + (\epsilon_{a\sigma} - \epsilon_{i\sigma})} \right]. \quad (2.135)$$

As an ansatz for the left-hand-side of eq. 2.133, the density response is expanded in the change in occupation of occupied and virtual orbitals^[201,210]

$$\delta\rho_{\sigma}(\mathbf{r}, \omega) = \sum_i^{N_{\text{occ}}} \sum_a^{N_{\text{virt}}} [P_{ia\sigma}(\omega)\varphi_{a\sigma}^*(\mathbf{r})\varphi_{i\sigma}(\mathbf{r}) + P_{ai\sigma}(\omega)\varphi_{i\sigma}^*(\mathbf{r})\varphi_{a\sigma}(\mathbf{r})], \quad (2.136)$$

with the expansion coefficients $P_{ia\sigma}(\omega)$ and $P_{ai\sigma}(\omega)$ being elements of the transition density matrix $\mathbf{P}(\omega)$. Combining equations 2.133, 2.135 and 2.136 eventually gives the set of equations^[201,210]

$$\begin{aligned} \sum_{jb\sigma'} \left[\left(\delta_{\sigma\sigma'}\delta_{ij}\delta_{ab}(\epsilon_{a\sigma} - \epsilon_{i\sigma} + \omega + i\eta) + v_{iabj}^{\sigma\sigma'} + f_{iabj}^{\sigma\sigma'} \right) P_{jb\sigma'} + \left(v_{iajb}^{\sigma\sigma'} + f_{iajb}^{\sigma\sigma'} \right) P_{bj\sigma'} \right] &= -\delta V_{ia\sigma}^{\text{ext}} \\ \sum_{jb\sigma'} \left[\left(\delta_{\sigma\sigma'}\delta_{ij}\delta_{ab}(\epsilon_{a\sigma} - \epsilon_{i\sigma} - \omega - i\eta) + v_{aijb}^{\sigma\sigma'} + f_{aijb}^{\sigma\sigma'} \right) P_{bj\sigma'} + \left(v_{aibj}^{\sigma\sigma'} + f_{aibj}^{\sigma\sigma'} \right) P_{jb\sigma'} \right] &= -\delta V_{ai\sigma}^{\text{ext}}, \end{aligned} \quad (2.137)$$

in which

$$\delta V_{ia\sigma}^{\text{ext}} = \int \varphi_{i\sigma}^*(\mathbf{r})\delta v_{\text{ext}}(\mathbf{r}, \omega)\varphi_{a\sigma}(\mathbf{r}) d\mathbf{r} \quad (2.138)$$

are matrix elements of the change in the external potential, $v_{pqrs}^{\sigma\sigma'}$ are usual four-center Coulomb integrals (cf. eq. 2.20) and $f_{pqrs}^{\sigma\sigma'}$ are matrix elements of the XC kernel

$$f_{pqrs}^{\sigma\sigma'} = \frac{\delta^2 E_{\text{xc}}}{\delta D_{pq}^{\sigma} \delta D_{rs}^{\sigma'}} = \iint \varphi_{p,\sigma}^*(\mathbf{r}) \varphi_{q,\sigma}(\mathbf{r}) f_{\text{xc}}^{\sigma\sigma'}(\mathbf{r}, \mathbf{r}') \varphi_{r,\sigma'}^*(\mathbf{r}') \varphi_{s,\sigma'}(\mathbf{r}') d\mathbf{r} d\mathbf{r}' . \quad (2.139)$$

In eq. 2.139, the density-matrix derivative notation from ref. 67 is used in addition to the standard matrix-element notation to cover explicitly orbital-dependent functionals like LHs. It is customary to set $X_{ia\sigma} = P_{ai\sigma}$ and $Y_{ia\sigma} = P_{ia\sigma}$ and to introduce the matrices **A** and **B** given by^f

$$A_{ia\sigma j b \sigma'} = \delta_{\sigma\sigma'} \delta_{ij} \delta_{ab} (\epsilon_{a\sigma} - \epsilon_{i\sigma}) + v_{iabj}^{\sigma\sigma'} + f_{iabj}^{\sigma\sigma'} \quad (2.140a)$$

$$B_{ia\sigma j b \sigma'} = v_{iajb}^{\sigma\sigma'} + f_{iajb}^{\sigma\sigma'} . \quad (2.140b)$$

For non-relativistic calculations and in the absence of magnetic fields, it is common to assume that real orbitals are used and thus $A_{ia\sigma j b \sigma'} = A_{ia\sigma j b \sigma'}^*$ and $B_{ia\sigma j b \sigma'} = B_{ia\sigma j b \sigma'}^*$. Using the matrices **X**, **Y**, **A**, **B**, and **V**^{ext} as elements within a 2×2 super vector space, leads to a compact reformulation of eq. 2.137^[201,210]

$$\left[\begin{pmatrix} \mathbf{A} & \mathbf{B} \\ \mathbf{B} & \mathbf{A} \end{pmatrix} - (\omega + i\eta) \begin{pmatrix} \mathbf{1} & 0 \\ 0 & -\mathbf{1} \end{pmatrix} \right] \begin{pmatrix} \mathbf{X} \\ \mathbf{Y} \end{pmatrix} = - \begin{pmatrix} \delta \mathbf{V}_{\text{ext}} \\ \delta \mathbf{V}_{\text{ext}}^* \end{pmatrix} , \quad (2.141)$$

typically written with suppressed spin-indices for clarity. As known from the discussion of general response theory (cf. Section 2.4.1), the poles of the response function in the limit $\eta \rightarrow 0^+$ are related to excitation energies $\omega = \Omega_n$. Because poles in the response function are associated with an infinite density response for an arbitrarily small change $\delta v_{\text{ext}}(\mathbf{r}, \omega)$ in the external potential,^[201] eq. 2.141 takes the schematic form $\square \cdot (+\infty) = 0$,^[208] which can be interpreted as \square , i.e. the term in square brackets in eq. 2.141, having a zero eigenvalue,^[201] which yields the well-known Casida's equations,^[22,208]

$$\begin{pmatrix} \mathbf{A} & \mathbf{B} \\ \mathbf{B} & \mathbf{A} \end{pmatrix} \begin{pmatrix} \mathbf{X} \\ \mathbf{Y} \end{pmatrix} = \Omega \begin{pmatrix} \mathbf{1} & 0 \\ 0 & -\mathbf{1} \end{pmatrix} \begin{pmatrix} \mathbf{X} \\ \mathbf{Y} \end{pmatrix} , \quad (2.142)$$

which, without loss of generality, consider only one excitation with excitation energy $\Omega = \Omega_n$ and transition matrices $\mathbf{X} = \mathbf{X}_n, \mathbf{Y} = \mathbf{Y}_n$ to further simplify notations.^g Another common notation of eq. 2.142 is via the (anti)symmetrized matrices $(\mathbf{A} \pm \mathbf{B})$ and

^fNote that **A** and **B** must not be confused with the functionals of the same name from the above discussion of TDKS theory.

^gAlternatively, the quantities Ω , **X** and **Y** may be viewed as sets holding all excitations.

$(\mathbf{X} \pm \mathbf{Y})$; it reads

$$(\mathbf{A} \pm \mathbf{B})(\mathbf{X} \pm \mathbf{Y}) = \Omega(\mathbf{X} \mp \mathbf{Y}). \quad (2.143)$$

The matrices $(\mathbf{A} \pm \mathbf{B})$ are obtained from the definitions of \mathbf{A} and \mathbf{B} in eq. 2.140a and eq. 2.140b and by using the symmetry properties of the Coulomb-Integral

$$(A + B)_{ia\sigma jb\sigma'} = \delta_{\sigma\sigma'} \delta_{ij} \delta_{ab} (\epsilon_{a\sigma} - \epsilon_{i\sigma}) + 2v_{iajb}^{\sigma\sigma'} + f_{+iajb}^{\sigma\sigma'} \quad (2.144a)$$

$$(A - B)_{ia\sigma jb\sigma'} = \delta_{\sigma\sigma'} \delta_{ij} \delta_{ab} (\epsilon_{a\sigma} - \epsilon_{i\sigma}) + f_{-iajb}^{\sigma\sigma'}, \quad (2.144b)$$

where the XC kernel notation from ref. 211 is introduced

$$f_{\pm iajb}^{\sigma\sigma'} = f_{iabj}^{\sigma\sigma'} \pm f_{iajb}^{\sigma\sigma'}. \quad (2.145)$$

For (semi)local XC functionals, the orbital index interchange in eq. 2.145 does not affect the value of the kernel integrals, hence the relations $f_{+iajb}^{\sigma\sigma'} = 2f_{iajb}^{\sigma\sigma'}$ and $f_{-iajb}^{\sigma\sigma'} = 0$ hold, leading to convenient simplifications in eq. 2.144a and eq. 2.144b. However, this is not the case for LHs where generally $f_{+iajb}^{\sigma\sigma'} \neq 2f_{iajb}^{\sigma\sigma'}$ and $f_{-iajb}^{\sigma\sigma'} \neq 0$. This is because the real-space dependence of the LMF prevents the required interchange of orbital indices and their associated integration variables of EXX-like integrals.^[67,212]

If the XC kernel was replaced with that derived from exact exchange, i.e. $f_{\pm iajb}^{\sigma\sigma'} = -\delta_{\sigma\sigma'} (v_{ijba}^{\sigma\sigma'} \pm v_{ibja}^{\sigma\sigma'})$, eq. 2.142 recovers the equation from time-dependent Hartree–Fock (TDHF) theory, also referred to as RPA^h in the literature.^[207] Another notable relationship is revealed when the \mathbf{B} matrix is set to zero, which results in a simplified eigenvalue problem

$$\mathbf{A}\mathbf{X} = \Omega\mathbf{X}, \quad (2.146)$$

which is known as the Tamm–Dancoff approximation (TDA).^[213] Applying the TDA to the TDHF method results in equations equivalent to the Configuration Interaction with Singles (CIS) method.^[207]

To obtain frequency dependent (dynamic) polarizabilities within LR-TDDFT, the general expression for the polarizability (eq. 2.108) is evaluated for the KS response function from eq. 2.134. The final result for the elements of the polarizability tensor α with $k, l \in \{x, y, z\}$ reads^[214,215]

$$\alpha_{kl}(\omega) = -2 \begin{pmatrix} \mathbf{M}_k & -\mathbf{M}_k \end{pmatrix} \begin{pmatrix} \omega \mathbf{1} - \mathbf{A} & \mathbf{B} \\ \mathbf{B} & -\omega \mathbf{1} - \mathbf{A} \end{pmatrix}^{-1} \begin{pmatrix} \mathbf{M}_l \\ -\mathbf{M}_l \end{pmatrix}, \quad (2.147)$$

^hNote that the term RPA is used for various methods^[170] and must not be confused with RPA correlation functionals discussed in Section 2.2.4 (although the methods are related).

where \mathbf{M}_k is the matrix of transition dipole moments in k -direction with elements $M_{k,ia} = \langle \varphi_i | \hat{\mu}_k | \varphi_a \rangle$. This result was obtained within the AA (eq. 2.129). If a frequency-dependent XC kernel was used, the frequency dependency would transfer to the matrices \mathbf{A} and \mathbf{B} .^[215] Note that computing the inverse matrix from eq. 2.147 can be impractical for larger vector spaces. Hence, in practice, polarizabilities are not obtained via eq. 2.147 but by solving the eigenvalue problem eq. 2.141 for $\delta \mathbf{V}_{\text{ext}} = \mathbf{M}_k$ in the $\eta \rightarrow 0^+$ limit and projecting the solution vector on the matrix of transition dipole moments^[214]

$$\alpha_{kl}(\omega) = - \begin{pmatrix} \mathbf{X}_{k,\omega} & \mathbf{Y}_{k,\omega} \end{pmatrix} \begin{pmatrix} \mathbf{M}_l \\ \mathbf{M}_l \end{pmatrix} = -2\mathbf{M}_l(\mathbf{X} + \mathbf{Y})_{k,\omega}. \quad (2.148)$$

Variational Formulation of LR-TDDFT

To prepare the way for the derivation of ES gradients (Section 3.1), the variational formulation of LR-TDDFT suggested by Furche^[215] is introduced. Within this formalism, excitation energies Ω are stationary points of the functional

$$\begin{aligned} G[\mathbf{X}, \mathbf{Y}, \Omega] = & \frac{1}{2} \sum_{ia\sigma j b \sigma'} (X + Y)_{ia\sigma} (A + B)_{ia\sigma j b \sigma'} (X + Y)_{j b \sigma'} \\ & + \frac{1}{2} \sum_{ia\sigma j b \sigma'} (X - Y)_{ia\sigma} (A - B)_{ia\sigma j b \sigma'} (X - Y)_{j b \sigma'} \\ & - \Omega \left[\sum_{ia\sigma} (X + Y)_{ia\sigma} (X - Y)_{ia\sigma} - 1 \right]. \end{aligned} \quad (2.149)$$

While variation of G w.r.t. $(X \pm Y)_{ia\sigma}$

$$\frac{\delta G}{\delta (X \pm Y)_{ia\sigma}} = \sum_{j b \sigma'} (A \pm B)_{ia\sigma j b \sigma'} (X \pm Y)_{j b \sigma'} - \Omega (X \mp Y)_{ia\sigma} = 0 \quad (2.150)$$

leads back to eq. 2.143, variation with respect to Ω

$$\frac{\delta G}{\delta \Omega} = \sum_{ia\sigma} (X + Y)_{ia\sigma} (X - Y)_{ia\sigma} - 1 = 0, \quad (2.151)$$

recovers the normalization constraint enforced on the matrices \mathbf{X} and \mathbf{Y} ^[35]

$$\sum_{ia\sigma} (X + Y)_{ia\sigma} (X - Y)_{ia\sigma} = 1. \quad (2.152)$$

Note, however, that G is not fully variational. In particular, it is not variational w.r.t. the coefficients of molecular orbitals involved in the calculation of $(\mathbf{A} \pm \mathbf{B})$. A suitable extension was suggested by Furche and Ahlrichs in ref. 35 and is presented in Section 3.1.

2.4.3 Vibrational Corrections

So far, molecules were treated within the Born–Oppenheimer (BO) approximation introduced in Section 2.1.2, which is founded on the large difference in the velocities of electrons and nuclei and has allowed to treat the nuclei as if they were fixed in space. The energy of a quantum state then depends parametrically on the positions of the nuclei. Plotting the energy within this parameter space yields the potential energy surface (PES), which can be intuitively interpreted as an ”energy landscape” a molecule is moving on when the positions of the nuclei are changed.

Molecular Vibrations

The fact that the nuclei are treated as fixed in space from the perspective of the electrons is, of course, not supposed to say that the nuclei are at rest in reality. They are constantly moving having $3N$ degrees of freedom, where N is the number of nuclei. It is customary to separate the translational and rotational movements of the entire molecule as they do not affect the distances between individual nuclei leaving $3N - 6$ degrees of freedom (or $3N - 5$ for linear molecules). Those are described in terms of molecular vibrations. There is no unique way of defining a vibration in a molecule but it is helpful to use mass-weighted coordinates $\mathbf{q}_i = m_i^{1/2} \mathbf{R}_i$ and constructing linear combination of the individual nuclear coordinates.^[216] If these combinations are chosen such that a) no cross-terms contribute to the potential energy within an harmonic ansatz and b) translations and rotations can be separated out, the coordinates are called normal coordinates \mathbf{Q} .^[216] The vibrations along these normal coordinates are the normal modes θ , which are eigenfunctions of the (harmonic) vibrational Hamilton operator

$$\hat{H}_j^{\text{vib}} = -\frac{1}{2} \frac{\partial^2}{\partial Q_j^2} + \frac{1}{2} k_j Q_j^2, \quad (2.153)$$

with eigenvalues

$$E_{\nu_j} = \left(\nu_j + \frac{1}{2} \right) \omega_j \quad (2.154)$$

where k_j is the force constant, $\omega_j = k_j^{1/2}$ the vibrational frequency and $\nu_j = 0, 1, \dots$ a quantum number for the j -th normal mode.ⁱ[216] The total vibrational wave function Θ is the eigenfunction of the total vibrational operator $\hat{H}^{\text{vib}} = \sum_j \hat{H}_j^{\text{vib}}$. Since \hat{H}^{vib} is sum of independent Hamiltonians, the total vibrational energy is simply the sum of the energies of all individual normal modes within their quantum states ν_j

$$E^{\text{vib}} = \sum_j^{3N-6} \left(\nu_j + \frac{1}{2} \right) \omega_j \quad (2.155)$$

and the total vibrational wave function is the product of all $3N - 6$ normal modes^[216]

$$\Theta_{\boldsymbol{\nu}}(\mathbf{Q}) = \prod_j^{3N-6} \theta_{\nu_j}(Q_j), \quad (2.156)$$

where $\boldsymbol{\nu}$ is a vector that collects the vibrational quantum numbers of the individual modes.^[217]

Vibronic Transitions

In previous sections, expressions derived for excitation energies, like those from linear response TDDFT, always corresponded to vertical excitation energies (VEEs). That is, the positions of the nuclei do not change during the excitation process, which corresponds to drawing a vertical line between two PESs as schematically represented by the blue and red arrows in Figure 2.2. For the absorption process (blue arrow), the VEE is obtained as

$$\Delta E^{\text{abs}} = E_{\text{ES}}(\mathbf{R}_{\text{GS}}) - E_{\text{GS}}(\mathbf{R}_{\text{GS}}), \quad (2.157)$$

i.e. at the GS structure, where for the emission process (red arrow), the VEE is obtained as

$$\Delta E^{\text{emi}} = E_{\text{ES}}(\mathbf{R}_{\text{ES}}) - E_{\text{GS}}(\mathbf{R}_{\text{ES}}), \quad (2.158)$$

i.e. at the ES structure. It is common practice to use these VEEs (possibly for more than one ES) to generate absorption and emission spectra either as line spectra or using an empirical Gaussian broadening to obtain a continuous line shape with maxima at the VEEs. However, even when using an exact electronic structure method, these VEEs generally do not coincide with the maxima of experimental (gas phase) spectra. This is because the energy of the absorbed or emitted photon will not only depend on the electronic state of

ⁱNote that the value of j does *not* fix ν_j to a value from the set $\{0, 1, \dots\}$ but is just an index that counts over all $3N - 6$ normal modes.

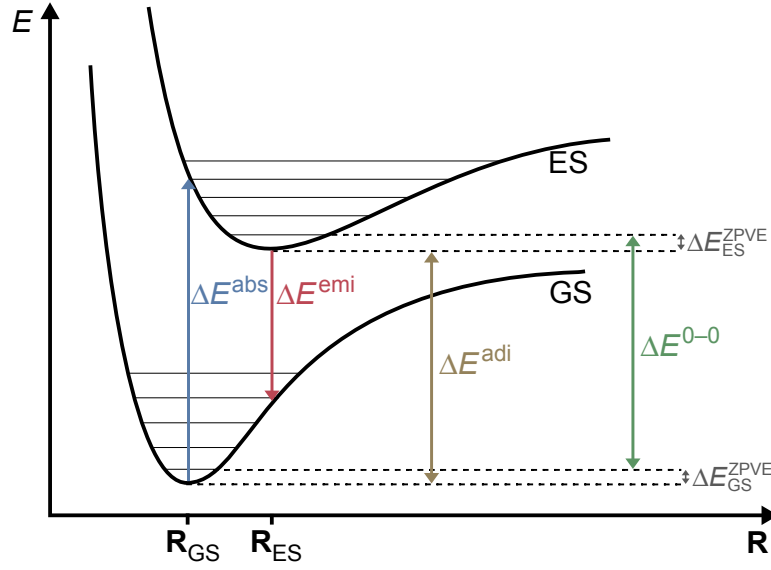


Figure 2.2: Schematic diagram of GS and ES potential energy curves with their vibrational energy levels. Characteristic energies are marked and explained in the text.

the GS and ES but also on their vibrational states (see Figure 2.2 for a schematic representation). Instead of one excitation with a fixed energy, several other excitations shifted by the energy difference of the respective vibrational levels are in principle possible. The combined transition process among electronic and vibrational levels is called a vibronic transition. The intensity of the associated absorption or emission bands is obtained from the transition probability of these vibronic excitations. According to Fermi's golden rule, the transition probability is (considering only one-photon transitions) proportional to the square of the absolute value of the transition dipole moment $|\mu_{fi}|^2$,^[31] which are the matrix elements of the dipole moment operator μ

$$\mu_{fi} = \langle \Phi_f | \mu | \Phi_i \rangle, \quad (2.159)$$

where indices i and f indicate the initial and final state, respectively. The total wave function Φ of a vibronic state is obtained as the product of the electronic wave function Ψ and the nuclear vibrational wave function $\Theta_\nu(\mathbf{Q})$, i.e. $|\Phi\rangle = |\Psi\Theta_\nu\rangle$. The total dipole moment is the sum of the nuclear dipole moment μ^N caused by the positively charged nuclei and the electronic dipole moment μ^{el} from the negative charge density of the electrons. Substitution in eq. 2.159 gives^[218]

$$\begin{aligned} \mu_{fi} &= \langle \Psi_f \Theta_{\nu_f} | \mu^{el} + \mu^N | \Psi_i \Theta_{\nu_i} \rangle \\ &= \langle \Psi_f \Theta_{\nu_f} | \mu^{el} | \Psi_i \Theta_{\nu_i} \rangle + \langle \Psi_f \Theta_{\nu_f} | \mu^N | \Psi_i \Theta_{\nu_i} \rangle \end{aligned}$$

$$\begin{aligned}
 &= \langle \Theta_{\nu_f} | \Theta_{\nu_i} \rangle \langle \Psi_f | \boldsymbol{\mu}^{\text{el}} | \Psi_i \rangle + \underbrace{\langle \Psi_f | \Psi_i \rangle}_{=0} \langle \Theta_{\nu_f} | \boldsymbol{\mu}^{\text{N}} | \Theta_{\nu_i} \rangle \\
 &= \langle \Theta_{\nu_f} | \Theta_{\nu_i} \rangle \mu_{\text{fi}}^{\text{el}}, \tag{2.160}
 \end{aligned}$$

where $\langle \Psi_f | \Psi_i \rangle$ is zero due to the orthonormality of the electronic states. The integral $\langle \Theta_{\nu_f}(\mathbf{Q}_f) | \Theta_{\nu_i}(\mathbf{Q}_i) \rangle$ gives the overlap of the vibrational wave functions of the initial and final states and is called the Franck–Condon (FC) factor.^[219] Note that this integral is generally not zero because the final state has an equilibrium structure displaced by some vector \mathbf{D} from that of the initial state. This also affects the normal coordinates of the final state which are related to the initial state via the Duschinsky transformation^[217,220]

$$\mathbf{Q}_f = \mathbf{J}\mathbf{Q}_i + \mathbf{D}, \tag{2.161}$$

with \mathbf{J} being a rotation matrix. Note that eq. 2.160 gives the transition dipole moment for just one specific excitation, where the initial (final) vibronic state is defined by a set of normal modes depending on normal coordinates \mathbf{Q}_i (\mathbf{Q}_f) in vibrational quantum states defined by quantum numbers collected in $\boldsymbol{\nu}_i$ ($\boldsymbol{\nu}_f$). To obtain the complete spectrum, all possible FC factors have to be obtained. This is summarized in the expression for the absorption/ emission cross-section^[217]

$$\sigma(\omega) = \frac{4\pi^2\omega}{3c} |\mu_{\text{fi}}^{\text{el}}|^2 \sum_{\boldsymbol{\nu}_i} \sum_{\boldsymbol{\nu}_f} |\langle \Theta_{\nu_f}(\mathbf{Q}_f) | \Theta_{\nu_i}(\mathbf{Q}_i) \rangle|^2 \delta(\Delta E_{\text{if}}^{\text{adi}} + E_{\nu_f}^{\text{vib}} - E_{\nu_i}^{\text{vib}} - \omega), \tag{2.162}$$

where c is the speed of light and the δ function is used generate peaks at frequencies $\omega = \Delta E_{\text{if}}^{\text{adi}} + E_{\nu_f}^{\text{vib}} - E_{\nu_i}^{\text{vib}}$ with the height of the peak given by the respective prefactor of the δ function. $\Delta E_{\text{if}}^{\text{adi}}$ is the adiabatic excitation energy (AEE) defined as the energy difference of the final and initial states at their respective equilibrium structures (see Figure 2.2 for illustration)

$$\Delta E_{\text{if}}^{\text{adi}} = E_f(\mathbf{R}_f) - E_i(\mathbf{R}_i). \tag{2.163}$$

Assuming that the initial state is in its ground electronic and vibrational state (i.e. $\boldsymbol{\nu}_i = \mathbf{0}$), the absorption cross-section is given by^[217]

$$\sigma_{\text{abs}}(\omega) = \frac{4\pi^2\omega}{3c} |\mu_{\text{f0}}^{\text{el}}|^2 \sum_{\boldsymbol{\nu}_f} |\langle \Theta_{\nu_f}(\mathbf{Q}_f) | \Theta_0(\mathbf{Q}_i) \rangle|^2 \delta(\Delta E_{\text{if}}^{\text{adi}} + E_{\nu_f}^{\text{vib}} - E_{\mathbf{0}_i}^{\text{vib}} - \omega), \tag{2.164}$$

with $E_{\mathbf{0}_i}^{\text{vib}} = \sum_j^{3N-6} \frac{1}{2} \omega_j$ being the GS vibrational energy. The computation of FC factors is theoretically quite involved already for the simple case of a diatomic molecule where only one normal mode has to be considered. Matters are further complicated for polyatomic molecules, both theoretically and computationally.^[221,222] Consider, e.g., the glucose molecule with 24 atoms and thus 66 vibrational degrees of freedom. Already when considering just three vibrational levels (i.e. $\nu \in \{0, 1, 2\}$) for the final state and assuming that the initial state is always in its vibrational ground state $3^{66} = 3.1 \cdot 10^{31}$ FC factors have to be calculated.^[223] However, although the FC factors are generally not exactly zero, the overlap of two vibrational wave functions might in fact be negligible. Hence it is possible to use selection schemes that only calculate the most important FC factors and check for the completeness of this selection using sum rules.^[224] Another strategy is to use a real-time generating function approach.^[217,225] It allows to replace the summation over vibrational states and the FC integrals so that after expressing the δ function in eq. 2.164 in terms of its Fourier transform, the absorption cross-section reads^[226]

$$\sigma_{\text{abs}}(\omega) = \frac{4\pi^2\omega}{3c} |\mu_{f0}^{\text{el}}|^2 \frac{1}{2\pi} \int_{-\infty}^{\infty} dt \exp \left\{ -it \left(\Delta E_{\text{if}}^{\text{adi}} - E_{\mathbf{0}_i}^{\text{vib}} - \omega \right) \right\} G(t), \quad (2.165)$$

where $G(t)$ is the generating function derived by Etinski, Tatchen and Marian^[225] using Mehler's formula;^[227] it reads^[217]

$$G(t) = 2^{(3N-6)/2} \left(\frac{\det(\mathbf{S}^{-1} \mathbf{\Omega}_i \mathbf{\Omega}_f)}{\det(\mathbf{L}) \det(\mathbf{M})} \right)^{1/2} \exp \left(\mathbf{D}^T (\mathbf{\Omega}_f \mathbf{B} \mathbf{J} \mathbf{M}^{-1} \mathbf{J}^T \mathbf{\Omega}_f \mathbf{B} - \mathbf{\Omega}_f \mathbf{B}) \mathbf{D} \right), \quad (2.166)$$

where $\mathbf{M} = \mathbf{J}^T \mathbf{\Omega}_f \mathbf{B} \mathbf{J} + \mathbf{\Omega}_i$ and $\mathbf{L} = \mathbf{J}^T \mathbf{\Omega}_f \mathbf{B}^{-1} \mathbf{J} + \mathbf{\Omega}_i$ with $\mathbf{\Omega}_i$, $\mathbf{\Omega}_f$, \mathbf{S} , and \mathbf{B} being diagonal matrices with matrix elements $(\Omega_i)_{kk} = \omega_k^i$, $(\Omega_f)_{kk} = \omega_k^f$, $S_{kk} = \sinh(i\omega_k^f t)$, and $B_{kk} = \tanh(i\omega_k^f t/2)$.^[217] For an implementation, the integral over $G(t)$ in eq. 2.165 has to be solved, which is done numerically with $G(t)$ being truncated after a maximum time t_{max} .^[217] Multiplication of $G(t)$ by a damping function $\exp(-t/\tau)$ with lifetime τ allows to introduce an empirical Lorentzian line broadening of the spectrum.^[217] For the emission process, an analogous equation to that of eq. 2.165 can be derived.^[228]

When the absorption and emission spectra are calculated (or measured), the spectra intersect at some specific energy, which is identified to coincide with the 0–0 transition, i.e. the transition where the initial and final states are in their ground vibrational state ($\nu_{i/f} = \mathbf{0}$). For illustration, computed absorption and fluorescence spectra for the $1^1\text{A}_g \rightarrow 1^1\text{B}_{2u}$ transition of anthracene are shown in Figure 2.3. The 0–0 energy is formally obtained as the adiabatic energy corrected by the difference in the zero-point vibrational

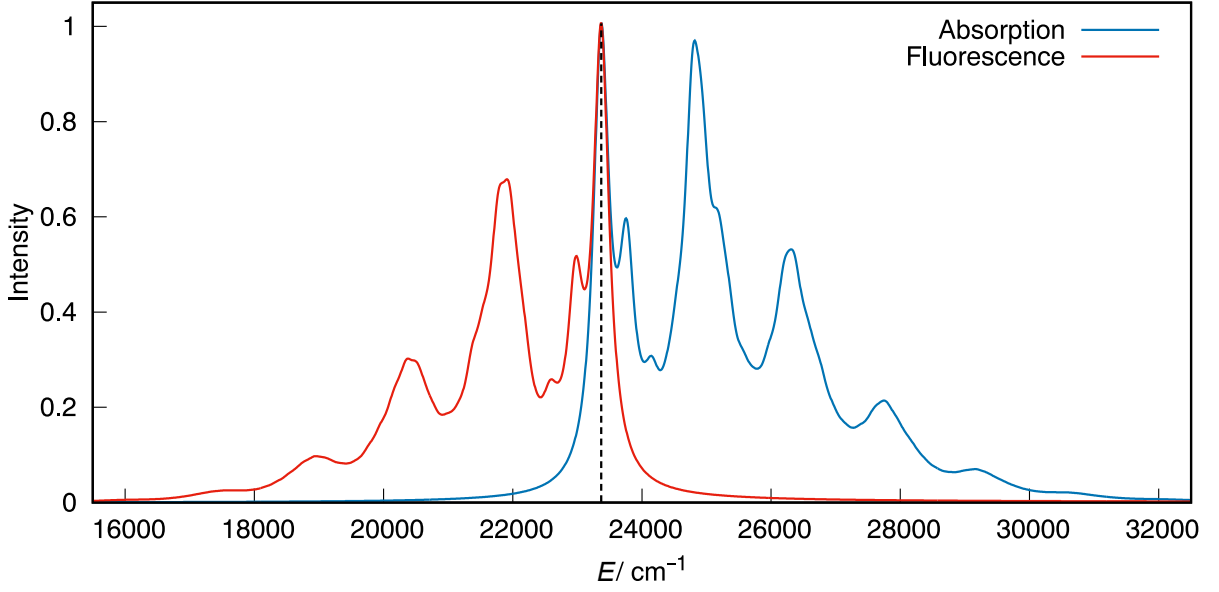


Figure 2.3: Normalized vibronic absorption and fluorescence spectra for the $1^1A_g \rightarrow 1^1B_{2u}$ transition of anthracene computed using the generating function approach as implemented in TURBOMOLE’s `radless` module. The dashed line at the intersection of both spectra corresponds to the 0–0 energy. A lifetime of 36.3 fs was used for the line broadening and the maximum integration time was set to $t_{\max} = 2^{17} \text{ au} = 131072 \text{ au}$. Electronic structure calculations were performed at the B3LYP/ def2-TZVP level.

energy (ZPVE) of the ground and excited state (see Figure 2.2 for energy levels)

$$\Delta E^{0-0} = \Delta E^{\text{adi}} + (\Delta E_{\text{ES}}^{\text{ZPVE}} - \Delta E_{\text{GS}}^{\text{ZPVE}}) . \quad (2.167)$$

Since this quantity is in fact measurable it is often preferred over VEEs to benchmark the quality of computational methods.^[31,229–232]

It should be noted that the FC approximation assumes that the dipole moment operator is not changed during the excitation, which is only true to the zero-th order, i.e. in a Taylor expansion of the dipole moment as a function of normal coordinates \mathbf{Q}

$$\boldsymbol{\mu}(\mathbf{Q}) = \boldsymbol{\mu}_0 + \sum_j^{3N-6} \left(\frac{\partial \boldsymbol{\mu}}{\partial Q_j^i} \right)_{\mathbf{Q}^i} Q_j^i + \dots \quad (2.168)$$

only the zero-th order term $\boldsymbol{\mu}_0$ has been considered in eq. 2.160.^[31] The first-order terms that cover the linear dependency of the dipole moment on the change in normal coordinates, are called the Herzberg–Teller contributions.^[31] They can become important if the structural differences of the GS and ES are substantial, e.g., when a bulky substituent

is rotated. Other effects that have to be considered in the simulation of experimental spectra include anharmonicity and solvent effects.^[233]

3 Development of Excited-State Gradients for Local Hybrid Functionals

Nuclear gradients are important quantities for optimizations and simulations on a molecule's PES. For any given configuration of nuclei in a molecule, the gradient vector points in the direction of the largest slope on the multidimensional PES. This information can be used in an optimization algorithm to move the nuclei in the opposite direction until, after several iterations, a stationary point with a vanishing gradient is found. Analysis of the nuclear Hessian then clarifies if a local maximum, saddle-point or local minimum has been found. Nuclear gradients may be calculated either numerically from a finite-difference approximation using the energy at multiple displaced structures, or analytically, i.e. from the analytical expression for the first derivative of the energy w.r.t. the nuclear coordinates. While numerical gradients require no additional method development when energies are available, they require a significant amount of single-point calculations, which makes this approach computationally costly for larger molecules. Analytical gradients are typically favorable in terms of computational cost, but require additional development and implementation steps for the respective method. For LHs, self-consistent GS energies,^[234] GS gradients,^[47] and ES energies within LR-TDDFT^[23] have already been implemented. Building on the implementation by Furche and Ahlrichs for GH ES gradients,^[35] the formal derivation of LH ES gradients is presented in this chapter. It has been published as part of ref. 212 and is reproduced in this chapter with some additional explanations and details. Reprinted (adapted) with permission from R. Grotjahn, F. Furche, M. Kaupp, *J. Chem. Theory Comput.* **2019**, *15*, 5508. Copyright 2019 American Chemical Society.

3.1 Derivation of TDDFT Excited State Gradients

The ES gradients are the derivatives of the ES energy w.r.t. all nuclear coordinates. Since the ES energy is the sum of the GS energy and the excitation energy Ω of the state of interest, the ES gradients are the sum of the gradients of these energies. Since GS

gradients for LHs are readily accessible from the existing implementation^[47] only the gradients of the excitation energy are discussed and loosely referred to as ES gradients. They are denoted as Ω^ξ or equivalently $\nabla_\xi \Omega$ where the super/subscript ξ is used to indicate a set of coordinates with respect to which the gradients are calculated. The derivation of Ω^ξ for LHs^[212] uses the the variational formulation of TDDFT (Section 2.4.2) and follows the strategy by Furche and Ahlrichs for the ES gradients of conventional (hybrid) functionals.^[35] The ES gradients may be calculated from the functional G defined in eq. 2.149 as

$$\Omega^\xi = G^\xi[\mathbf{X}, \mathbf{Y}, \Omega]. \quad (3.1)$$

Since G is variational w.r.t. the matrices $(\mathbf{X} \pm \mathbf{Y})$, the calculation of this first-order property does not require derivatives of G w.r.t. $(\mathbf{X} \pm \mathbf{Y})$.^[35] However, the derivatives of the matrices $(\mathbf{A} \pm \mathbf{B})$ require derivatives of the molecular orbitals $\varphi_{p\sigma}(\mathbf{r})$. As usual, the MOs are expanded in a LCAO as given by eq. 2.24, rewritten here for convenience

$$\varphi_{p\sigma}(\mathbf{r}) = \sum_{\mu}^{N_b} C_{\mu p\sigma} \chi_{\mu}(\mathbf{r}). \quad (3.2)$$

While derivatives of the basis functions $\chi_{\mu}(\mathbf{r})$ are straightforward to calculate and are non-zero only for those nuclear coordinates from the set ξ associated with a nucleus a given basis function is centered at, the derivatives of the MO coefficients $C_{\mu p\sigma}$ are more involved.^[35] Compared to the unperturbed MO coefficients, the computational effort for all $C_{\mu p\sigma}^\xi$ would be larger by a factor equivalent to the degrees of freedom in the molecule.^[35] It is possible to circumvent the need to calculate $C_{\mu p\sigma}^\xi$ by eliminating them via the introduction of relaxed densities and use of the Z vector method.^[235] Although this strategy has been successfully applied to TDDFT^[34] it remains a rather cumbersome method.^[35] The strategy by Furche and Ahlrichs,^[35] also used here, avoids derivatives of MO coefficients from the beginning by starting from a fully variational functional L that is made stationary w.r.t. the MO coefficients,

$$\frac{\partial L}{\partial C_{\mu p\sigma}} = 0, \quad (3.3)$$

so that the associated derivatives of the MO coefficients are no longer required

$$\Omega^\xi = \frac{dL}{d\xi} = \frac{\partial L}{\partial \xi} + \underbrace{\frac{\partial L}{\partial C_{\mu p\sigma}}}_{=0} \frac{\partial C_{\mu p\sigma}}{\partial \xi}. \quad (3.4)$$

The ES gradients are then obtained as an explicit derivative $\Omega^\xi = \frac{\partial L}{\partial \xi} = L^{(\xi)}$ (indicated by the superscript (ξ)). A suitable ansatz for L reads^[35]

$$L[\mathbf{X}, \mathbf{Y}, \Omega, \mathbf{C}, \mathbf{Z}, \mathbf{W}] = G[\mathbf{X}, \mathbf{Y}, \Omega] + \sum_{ia\sigma} Z_{ia\sigma} F_{ia\sigma} - \sum_{\substack{pq\sigma \\ p \leq q}} W_{pq\sigma} (S_{pq\sigma} - \delta_{pq}) , \quad (3.5)$$

where $F_{ia\sigma}$ are matrix elements of the occupied-virtual block of the KS matrix defined in eq. 2.38. Via the Lagrange multiplier \mathbf{Z} , these elements are enforced to be zero

$$\frac{\partial L}{\partial Z_{ia\sigma}} = F_{ia\sigma} = 0 , \quad (3.6)$$

which ensures that the GS KS equations are always satisfied.^[35] In eq. 3.5, the additional Lagrange multiplier \mathbf{W} fixes the elements of the overlap matrix $S_{pq\sigma}$ such that orthonormality of the MOs is preserved^[35]

$$\frac{\partial L}{\partial W_{pq\sigma}} = S_{pq\sigma} - \delta_{pq} = 0 . \quad (3.7)$$

Further note that for L being fully variational, the orbital energy difference term in the definition of the matrix elements of $(\mathbf{A} \pm \mathbf{B})$ in eq. 2.144a has to be expressed in terms of the KS matrix

$$\delta_{\sigma\sigma'} \delta_{ij} \delta_{ab} (\epsilon_{a\sigma} - \epsilon_{i\sigma}) = \delta_{\sigma\sigma'} (F_{ab\sigma} \delta_{ij} - F_{ij\sigma} \delta_{ab}) , \quad (3.8)$$

which corresponds to lifting the (basically arbitrary) choice of canonical KS MOs.^[35] After \mathbf{Z} and \mathbf{W} are calculated, the ES gradients are obtained as^[35]

$$\begin{aligned} L^\xi[\mathbf{X}, \mathbf{Y}, \Omega, \mathbf{C}, \mathbf{Z}, \mathbf{W}] = & \frac{1}{2} \sum_{ia\sigma jb\sigma'} (X + Y)_{ia\sigma} (A + B)_{ia\sigma jb\sigma'}^{(\xi)} (X + Y)_{jb\sigma'} \\ & + \frac{1}{2} \sum_{ia\sigma jb\sigma'} (X - Y)_{ia\sigma} (A - B)_{ia\sigma jb\sigma'}^{(\xi)} (X - Y)_{jb\sigma'} \\ & + \sum_{ia\sigma} Z_{ia\sigma} F_{ia\sigma}^{(\xi)} - \sum_{\substack{pq\sigma \\ p \leq q}} W_{pq\sigma} S_{pq\sigma}^{(\xi)} , \end{aligned} \quad (3.9)$$

i.e. as an explicit derivative w.r.t. ξ without the need to calculate MO coefficient derivatives. Expressions for the additional matrices \mathbf{Z} and \mathbf{W} are derived from the stationarity condition (eq. 3.3). For this purpose, the first step is to explicitly denote the derivative

w.r.t. MO coefficients $C_{\mu p \sigma}$ for each term in L that depends on $C_{\mu p \sigma}$

$$\frac{\partial G}{\partial C_{\mu p \sigma}} + \sum_{ia \sigma'} Z_{ia \sigma'} \frac{\partial F_{ia \sigma'}}{\partial C_{\mu p \sigma}} - \sum_{\substack{rs \sigma' \\ r \leq s}} W_{rs \sigma'} \frac{\partial S_{rs \sigma'}}{\partial C_{\mu p \sigma}} = 0. \quad (3.10)$$

The last term is transferred to the RHS, the total equation is multiplied by $C_{\mu q \sigma}$, and a summation over all AO indices μ is performed^[35]

$$Q_{pq \sigma} + \sum_{ia \sigma'} Z_{ia \sigma'} \sum_{\mu} \frac{\partial F_{ia \sigma'}}{\partial C_{\mu p \sigma}} C_{\mu q \sigma} = \sum_{\substack{rs \sigma' \\ r \leq s}} W_{rs \sigma'} \sum_{\mu} \frac{\partial S_{rs \sigma'}}{\partial C_{\mu p \sigma}} C_{\mu q \sigma}, \quad (3.11)$$

where

$$Q_{pq \sigma} = \sum_{\mu} \frac{\partial G}{\partial C_{\mu p \sigma}} C_{\mu q \sigma}. \quad (3.12)$$

Next, the derivatives w.r.t. $C_{\mu p \sigma}$ are evaluated. For this purpose, each matrix element is transformed from the MO to the AO basis, the derivative is carried out, and the result is back-transformed to the MO basis. Detailed steps are provided in Appendix A.3 using the XC potential as an example. In the derivation, the block-shape of the matrices in eq. 3.11 is exploited and hence a separate equation is obtained for each block, which are the occupied-occupied (indices ij), occupied-virtual (ia), virtual-occupied (ai), and virtual-virtual (ab) blocks. Also, some additional notation is required to compactly note the following equations. The linear transformations^[35,212]

$$H_{pq \sigma}^+[\mathbf{M}] = \sum_{rs \sigma'} \left[2 v_{pqrs}^{\sigma \sigma'} + f_{+pqrs}^{\sigma \sigma'} \right] M_{rs \sigma'}, \quad (3.13a)$$

$$H_{pq \sigma}^-[\mathbf{M}] = \sum_{rs \sigma'} f_{-pqrs}^{\sigma \sigma'} M_{rs \sigma'}, \quad (3.13b)$$

are applied at various points to some matrix \mathbf{M} . The unrelaxed difference density matrix \mathbf{T} is used and defined as^[35]

$$T_{ij \sigma} = -\frac{1}{2} \sum_c [(X + Y)_{ic \sigma} (X + Y)_{jc \sigma} + (X - Y)_{ic \sigma} (X - Y)_{jc \sigma}] \quad (3.14a)$$

$$T_{ab \sigma} = \frac{1}{2} \sum_k [(X + Y)_{ka \sigma} (X + Y)_{kb \sigma} + (X - Y)_{ka \sigma} (X - Y)_{kb \sigma}] \quad (3.14b)$$

$$T_{ia \sigma} = T_{ai \sigma} = 0. \quad (3.14c)$$

Derivatives of G w.r.t. to MO coefficients involve derivatives of the XC kernel w.r.t. to MO coefficients. These derivatives are expressed in terms of the XC hyper-kernel $g_{xc}^{\sigma\sigma'\sigma''}(\mathbf{r}, \mathbf{r}', \mathbf{r}'')$, i.e. the third functional derivative of the XC energy. Its matrix elements are expressed using the density-matrix derivative notation

$$g_{pqrstu}^{\sigma\sigma'\sigma''} = \frac{\delta^3 E_{xc}}{\delta D_{pq}^{\sigma} \delta D_{rs}^{\sigma'} \delta D_{tu}^{\sigma''}}, \quad (3.15)$$

where, similar to the XC kernel, the convention

$$g_{\pm pqrstu}^{\sigma\sigma'\sigma''} = g_{pqrsut}^{\sigma\sigma'\sigma''} \pm g_{pqrstu}^{\sigma\sigma'\sigma''} \quad (3.16)$$

is used. Returning now to the four different equations resulting from eq. 3.11 for the different blocks, they read^[35]

$$Q_{ij\sigma} + H_{ij\sigma}^+[\mathbf{Z}] = (1 + \delta_{ij})W_{ij\sigma} \quad (3.17a)$$

$$Q_{ia\sigma} + \epsilon_a^{\sigma} Z_{ia\sigma} + H_{ia\sigma}^+[\mathbf{Z}] = W_{ia\sigma} \quad (3.17b)$$

$$Q_{ai\sigma} + \epsilon_i^{\sigma} Z_{ia\sigma} = W_{ia\sigma} \quad (3.17c)$$

$$Q_{ab\sigma} = (1 + \delta_{ab})W_{ab\sigma}, \quad (3.17d)$$

where the matrix elements of \mathbf{Q} are different for each block

$$Q_{ij\sigma} = \sum_a \Omega [(X + Y)_{ia\sigma}(X - Y)_{ja\sigma} + (X - Y)_{ia\sigma}(X + Y)_{ja\sigma}] \quad (3.18a)$$

$$\begin{aligned} & - \sum_a \epsilon_a^{\sigma} [(X + Y)_{ia\sigma}(X + Y)_{ja\sigma} + (X - Y)_{ia\sigma}(X - Y)_{ja\sigma}] + H_{ij\sigma}^+[\mathbf{T}] \\ & + \sum_{ka\sigma'lb\sigma''} \left[g_{+ijkalb}^{\sigma\sigma'\sigma''}(X + Y)_{ka\sigma'}(X + Y)_{lb\sigma''} + g_{-ijkalb}^{\sigma\sigma'\sigma''}(X - Y)_{ka\sigma'}(X - Y)_{lb\sigma''} \right] \end{aligned}$$

$$Q_{ia\sigma} = \sum_c [(X + Y)_{ic\sigma} H_{ac\sigma}^+[(\mathbf{X} + \mathbf{Y})] + (X - Y)_{ic\sigma} H_{ac\sigma}^-[(\mathbf{X} - \mathbf{Y})]] + H_{ia\sigma}^+[\mathbf{T}] \quad (3.18b)$$

$$+ \sum_{kc\sigma'ld\sigma''} \left[g_{+iakcld}^{\sigma\sigma'\sigma''}(X + Y)_{kc\sigma'}(X + Y)_{ld\sigma''} + g_{-iakcld}^{\sigma\sigma'\sigma''}(X - Y)_{kc\sigma'}(X - Y)_{ld\sigma''} \right]$$

$$Q_{ai\sigma} = \sum_k [(X + Y)_{ka\sigma} H_{ki\sigma}^+[(\mathbf{X} + \mathbf{Y})] + (X - Y)_{ka\sigma} H_{ki\sigma}^-[(\mathbf{X} - \mathbf{Y})]] \quad (3.18c)$$

$$Q_{ab\sigma} = \sum_i \Omega [(X + Y)_{ia\sigma}(X - Y)_{ib\sigma} + (X - Y)_{ia\sigma}(X + Y)_{ib\sigma}] \quad (3.18d)$$

$$+ \sum_i \epsilon_i^{\sigma} [(X + Y)_{ia\sigma}(X + Y)_{ib\sigma} + (X - Y)_{ia\sigma}(X - Y)_{ib\sigma}].$$

Comparison of the above equations with those derived by Furche and Ahlrichs^[35] reveals that the more general LH scheme leads to additional antisymmetric kernel and hyperkernel terms that vanish for GHs and (semi)local XC functionals. To solve for the different blocks, eq. 3.17c is subtracted from eq. 3.17b yielding^[35]

$$(\epsilon_a^\sigma - \epsilon_i^\sigma) Z_{ia\sigma} + H_{ia\sigma}^+[\mathbf{Z}] = -(Q_{ia\sigma} - Q_{ai\sigma}) \quad (3.19)$$

Writing out the explicit terms for the transformation $H_{ia\sigma}^+[\mathbf{Z}]$, combining it with the orbital energy difference term, and comparing everything to the definition of the matrix elements of the $(\mathbf{A} + \mathbf{B})$ matrix (eq. 2.144a) leads to the so-called Z vector equation^[35]

$$\sum_{jb\sigma'} (A + B)_{ia\sigma jb\sigma'} Z_{jb\sigma'} = -R_{ia\sigma}, \quad (3.20)$$

where the RHS $R_{ia\sigma}$ is the difference $Q_{ia\sigma} - Q_{ai\sigma}$ reading

$$\begin{aligned} R_{ia\sigma} = & \sum_b [(X + Y)_{ib\sigma} H_{ab\sigma}^+[(\mathbf{X} + \mathbf{Y})] + (X - Y)_{ib\sigma} H_{ab\sigma}^-[(\mathbf{X} - \mathbf{Y})]] \\ & - \sum_j [(X + Y)_{ja\sigma} H_{ji\sigma}^+[(\mathbf{X} + \mathbf{Y})] + (X - Y)_{ja\sigma} H_{ji\sigma}^-[(\mathbf{X} - \mathbf{Y})]] + H_{ia\sigma}^+[\mathbf{T}] \\ & + \sum_{jb\sigma' kc\sigma''} \left[g_{+iajbkc}^{\sigma\sigma'\sigma''} (X + Y)_{jb\sigma'} (X + Y)_{kc\sigma''} + g_{-iajbkc}^{\sigma\sigma'\sigma''} (X - Y)_{jb\sigma'} (X - Y)_{kc\sigma''} \right]. \end{aligned} \quad (3.21)$$

After the RHS has been calculated from the transition density matrices $(\mathbf{X} \pm \mathbf{Y})$, the Z vector equation can be solved iteratively for \mathbf{Z} , where the occupied-occupied and virtual-virtual blocks of \mathbf{Z} are zero. Having solved for \mathbf{Z} allows to calculate the elements of \mathbf{W} via eq. 3.17a-d and eq. 3.18a-d. For this purpose, it is convenient to define the one-particle difference density matrix \mathbf{P} as^a

$$\mathbf{P} = \mathbf{Z} + \mathbf{T}. \quad (3.22)$$

Explicit expressions for the different blocks of \mathbf{W} are given in Appendix A.1.

With solutions for \mathbf{Z} and \mathbf{W} , all that remains for the evaluation of the ES gradients in eq. 3.9 is taking all derivatives w.r.t. ξ . This step is straightforward after the definitions of $(\mathbf{A} \pm \mathbf{B})$ (eq. 2.144a-b, eq. 3.8) and of the KS matrix \mathbf{F} (eq. 2.38) are inserted into eq. 3.9. After transformation from the MO to the AO basis (cf. also Section 3.2.1), the

^a \mathbf{P} must not be confused with the same-named general transition density matrix from Section 2.4.2.

final equation for the ES gradients reads

$$\begin{aligned}
 \Omega^\xi = & \sum_{\mu\nu\sigma} h_{\mu\nu}^\xi P_{\mu\nu\sigma} - \sum_{\mu\nu\sigma} S_{\mu\nu\sigma}^\xi W_{\mu\nu\sigma} + \sum_{\mu\nu\sigma} V_{\mu\nu\sigma}^{xc(\xi)} P_{\mu\nu\sigma} \\
 & + \sum_{\mu\nu\sigma\kappa\lambda\sigma'} v_{\mu\nu\kappa\lambda}^\xi [P_{\mu\nu\sigma} D_{\kappa\lambda\sigma'} + (X + Y)_{\mu\nu\sigma} (X + Y)_{\kappa\lambda\sigma'}] \\
 & + \frac{1}{2} \sum_{\mu\nu\sigma\kappa\lambda\sigma'} f_{+\mu\nu\sigma\kappa\lambda\sigma'}^{(\xi)} (X + Y)_{\mu\nu\sigma} (X + Y)_{\kappa\lambda\sigma'} \\
 & + \frac{1}{2} \sum_{\mu\nu\sigma\kappa\lambda\sigma'} f_{-\mu\nu\sigma\kappa\lambda\sigma'}^{(\xi)} (X - Y)_{\mu\nu\sigma} (X - Y)_{\kappa\lambda\sigma'} .
 \end{aligned} \tag{3.23}$$

To summarize, the calculation of ES gradients requires three steps subsequent to a converged solution of the GS KS equations.^[35]

1. Solve the Casida's equations to obtain $(\mathbf{X} \pm \mathbf{Y})$ and Ω (eq. 2.143).
2. Obtain \mathbf{Z} and \mathbf{W} by solving the Z vector equation (eq. 3.20).
3. Calculate the ES gradient from eq. 3.23.

The first step is an ordinary LR-TDDFT calculation of a VEE. All LH specific developments for this step have been previously reported by Maier *et al.*^[23] The second step requires the development of the LH hyper-kernel $g_{pqrstu}^{\sigma\sigma'\sigma''}$. However, it is in fact preferable in terms of performance to never actually calculate and store this six-index quantity as it is always contracted with two transition density matrices anyway.^[35] Hence, the more relevant quantities are the contracted (anti)symmetric LH hyper-kernel elements. For the third step, the LH potential gradients $V_{\mu\nu\sigma}^{xc(\xi)}$ and kernel gradients $f_{\pm\mu\nu\sigma\kappa\lambda\sigma'}^{(\xi)}$ are required. Again, these quantities are directly contracted with other matrices.

3.2 Derivation of the LH Hyper-Kernel and Potential/ Kernel Gradients

The derivation of the aforementioned quantities for the LH case is the subject of this section. Compared to the expressions for (semi)local functionals and GHs, LHs require a special treatment because they feature additional LMF derivative terms. The LMF derivatives by themselves are treated just like a (semi)local energy density and do not present a major problem for an implementation. However, due to the product rule of differentiation, each derivative of the LMF or of the LMF complement is multiplied with

the derivatives of the exact-exchange energy density or of the (semi)local exchange energy density, respectively. This significantly increases the complexity of higher-order derivatives like the third-order derivatives needed for the hyper-kernel. To make the vast amount of terms more manageable, various shorthand notations are introduced, which were previously developed in the context of the SCF,^[234] GS gradients,^[47] and VEE LR-TDDFT^[23] implementations and extended here for use within the LR-TDDFT ES gradients implementation. Furthermore, the LMF weighted EXX-like integrals are non-standard integrals and thus require an adequate integration scheme. On that account, the seminumerical integration scheme is introduced^[48] and its particularities for the use with LHs are discussed.

3.2.1 Formalism and Notation

This work uses the density matrix derivative notation from ref. 67 and 23. It has been used in previous sections to denote general expressions for the XC potential (eq. 2.39), XC kernel (eq. 2.139) and XC hyper-kernel (eq. 3.15). It is generally valid in the sense that it allows denoting derivatives of explicitly orbital dependent terms and (semi)local (implicitly orbital dependent) terms, alike.

Derivatives of the Exact Exchange Energy Density

First, it is demonstrated how the density matrix derivative scheme can be used to calculate derivatives of the EXX energy density defined in eq. 2.73, rewritten here for convenience

$$e_{x,\sigma}^{\text{ex}}(\mathbf{r}) = -\frac{1}{2} \sum_{pqrs} D_{pq}^{\sigma} D_{rs}^{\sigma} \int w_{psrq}^{\sigma\sigma}(\mathbf{r}, \mathbf{r}') d\mathbf{r}' , \quad (3.24)$$

where the short-hand notation

$$w_{psrq}^{\sigma\sigma'}(\mathbf{r}, \mathbf{r}') = \frac{\varphi_{p,\sigma}^*(\mathbf{r}) \varphi_{s,\sigma}(\mathbf{r}) \varphi_{r,\sigma'}^*(\mathbf{r}') \varphi_{q,\sigma'}(\mathbf{r}')}{|\mathbf{r} - \mathbf{r}'|} \quad (3.25)$$

is used. The first derivative w.r.t. some density matrix element D_{mn}^{ς} , where ς is used as a spin-index, is obtained as an explicit derivative

$$\begin{aligned} \frac{\partial e_{x,\sigma}^{\text{ex}}(\mathbf{r})}{\partial D_{mn}^{\varsigma}} &= -\frac{1}{2} \sum_{rs} D_{rs}^{\sigma} \delta_{\sigma\varsigma} \int w_{msrn}^{\sigma\sigma}(\mathbf{r}, \mathbf{r}') d\mathbf{r}' - \frac{1}{2} \sum_{pq} D_{pq}^{\sigma} \delta_{\sigma\varsigma} \int w_{pnmq}^{\sigma\sigma}(\mathbf{r}, \mathbf{r}') d\mathbf{r}' \\ &= -\frac{1}{2} \sum_{pq} D_{pq}^{\sigma} \delta_{\sigma\varsigma} \int [w_{mqpn}^{\sigma\sigma}(\mathbf{r}, \mathbf{r}') + w_{pnmq}^{\sigma\sigma}(\mathbf{r}, \mathbf{r}')] d\mathbf{r}' , \end{aligned} \quad (3.26)$$

where in the first line, the product rule of differentiation has been applied and summation indices were relabeled in the second line.^[67] If the derivative of the EXX energy density $e_{x,\sigma}^{\text{ex}}(\mathbf{r})$ was integrated over \mathbf{r} to yield the derivative of the EXX energy $E_{x,\sigma}^{\text{ex}}$, it would be possible to summarize the two four-center integrals in the second line of eq. 3.26 by interchanging the integration variables \mathbf{r} and \mathbf{r}' . Importantly, this is not possible when dealing with the EXX energy density itself and also for the situation where $e_{x,\sigma}^{\text{ex}}(\mathbf{r})$ is multiplied by an LMF $a_\sigma(\mathbf{r})$ before it is integrated over \mathbf{r} .^b The second derivative is obtained in the same manner and reads

$$\frac{\partial^2 e_{x,\sigma}^{\text{ex}}(\mathbf{r})}{\partial D_{mn}^\varsigma \partial D_{tu}^{\varsigma'}} = -\frac{1}{2} \delta_{\sigma\varsigma} \delta_{\sigma\varsigma'} \int [w_{mutn}^{\sigma\sigma}(\mathbf{r}, \mathbf{r}') + w_{tnmu}^{\sigma\sigma}(\mathbf{r}, \mathbf{r}')] d\mathbf{r}' . \quad (3.27)$$

Note that the second derivative vanishes if $\varsigma \neq \varsigma'$, i.e. second partial derivatives of EXX energy densities are only non-zero if both differentiation variables have the same spin.^[67] The third derivative of the EXX energy density w.r.t. the density matrix is always zero because the second derivative does not depend on the density matrix

$$\frac{\partial^3 e_{x,\sigma}^{\text{ex}}(\mathbf{r})}{\partial D_{mn}^\varsigma \partial D_{tu}^{\varsigma'} \partial D_{vw}^{\varsigma''}} = 0 . \quad (3.28)$$

Semilocal Potential Operator

The density matrix derivative scheme can also be applied to the (semi)local energy densities $e^{\text{sl}}(\mathbf{r})$ of a functional or the LMF in a LH. In this case, the dependence of the density matrix is not explicit (as for the EXX energy density) but implicit through the definitions of the (semi)local quantities, i.e. the spin density, squared spin density gradient and the spin resolved kinetic energy density. Their definitions are repeated here for convenience

$$\rho_\sigma(\mathbf{r}) = \sum_{pq} D_{pq}^\sigma \varphi_{p\sigma}^*(\mathbf{r}) \varphi_{q\sigma}(\mathbf{r}) \quad (3.29)$$

$$\gamma_{\sigma\sigma'}(\mathbf{r}) = \nabla^\top \rho_\sigma(\mathbf{r}) \nabla \rho_{\sigma'}(\mathbf{r}) \quad (3.30)$$

$$\tau_\sigma(\mathbf{r}) = \frac{1}{2} \sum_{pq} D_{pq}^\sigma \nabla^\top \varphi_{p\sigma}^*(\mathbf{r}) \nabla \varphi_{q\sigma}(\mathbf{r}) . \quad (3.31)$$

The derivative $\frac{\delta e^{\text{sl}}(\mathbf{r})}{\delta D_{pq}^\sigma}$ is obtained by applying the functional chain rule for each (semi)local quantity \mathcal{Q} that appears in the definition of $e^{\text{sl}}(\mathbf{r})$. As a short hand notation for this

^bAt least not without introducing an additional dependence of the LMF on \mathbf{r}' .

procedure, the semilocal potential operator $\hat{d}_{pq\sigma}$ is introduced^[23,67]

$$\hat{d}_{pq\sigma} = \sum_{\mathbb{Q} \in \mathbb{Q}} \int \frac{\partial \mathcal{Q}(\mathbf{r}')}{\partial D_{pq}^\sigma} \frac{\delta}{\delta \mathcal{Q}(\mathbf{r}')} d\mathbf{r}' , \quad \mathbb{Q} = \{\rho_\alpha, \rho_\beta, \gamma_{\alpha\alpha}, \gamma_{\alpha\beta}, \gamma_{\beta\beta}, \tau_\alpha, \tau_\beta\} . \quad (3.32)$$

Within this notation, the derivative of some (semi)local energy density w.r.t. a density matrix element reads^[67]

$$\begin{aligned} \frac{\delta e^{\text{sl}}(\mathbf{r})}{\delta D_{pq}^\sigma} &= \hat{d}_{pq\sigma} e^{\text{sl}}(\mathbf{r}) \\ &= \int \frac{\partial \rho_\sigma(\mathbf{r}')}{\partial D_{pq}^\sigma} \frac{\delta e^{\text{sl}}(\mathbf{r})}{\delta \rho_\sigma(\mathbf{r}')} d\mathbf{r}' + \int \frac{\partial \tau_\sigma(\mathbf{r}')}{\partial D_{pq}^\sigma} \frac{\delta e^{\text{sl}}(\mathbf{r})}{\delta \tau_\sigma(\mathbf{r}')} d\mathbf{r}' \\ &\quad + \int \frac{\partial \gamma_{\sigma\sigma}(\mathbf{r}')}{\partial D_{pq}^\sigma} \frac{\delta e^{\text{sl}}(\mathbf{r})}{\delta \gamma_{\sigma\sigma}(\mathbf{r}')} d\mathbf{r}' + \int \frac{\partial \gamma_{\sigma\sigma'}(\mathbf{r}')}{\partial D_{pq}^\sigma} \frac{\delta e^{\text{sl}}(\mathbf{r})}{\delta \gamma_{\sigma\sigma'}(\mathbf{r}')} d\mathbf{r}' \\ &= \varphi_{p\sigma}^*(\mathbf{r}) \varphi_{q\sigma}(\mathbf{r}) \frac{\delta e^{\text{sl}}(\mathbf{r})}{\delta \rho_\sigma(\mathbf{r})} + \frac{1}{2} \nabla^\top \varphi_{p\sigma}^*(\mathbf{r}) \nabla \varphi_{q\sigma}(\mathbf{r}) \frac{\delta e^{\text{sl}}(\mathbf{r})}{\delta \tau_\sigma(\mathbf{r})} \\ &\quad + 2 \nabla^\top [\varphi_{p\sigma}^*(\mathbf{r}) \varphi_{q\sigma}(\mathbf{r})] \nabla \rho_\sigma(\mathbf{r}) \frac{\delta e^{\text{sl}}(\mathbf{r})}{\delta \gamma_{\sigma\sigma}(\mathbf{r})} + \nabla^\top [\varphi_{p\sigma}^*(\mathbf{r}) \varphi_{q\sigma}(\mathbf{r})] \nabla \rho_{\sigma'}(\mathbf{r}) \frac{\delta e^{\text{sl}}(\mathbf{r})}{\delta \gamma_{\sigma\sigma'}(\mathbf{r})} . \end{aligned} \quad (3.33)$$

Repeated application of the semilocal potential operator gives the corresponding higher derivatives. The semilocal kernel operator was derived by Maier^[67] and reads

$$\begin{aligned} \hat{d}_{pq\sigma} \hat{d}_{rs\sigma'} &= \sum_{\mathbb{Q} \in \mathbb{Q}} \sum_{\mathbb{Q}' \in \mathbb{Q}} \iint \frac{\partial \mathcal{Q}(\mathbf{r})}{\partial D_{pq}^\sigma} \frac{\partial \mathcal{Q}'(\mathbf{r}')}{\partial D_{rs}^{\sigma'}} \frac{\delta^2}{\delta \mathcal{Q}(\mathbf{r}) \delta \mathcal{Q}'(\mathbf{r}')} d\mathbf{r} d\mathbf{r}' \\ &\quad + \sum_{\mathbb{Q} \in \mathbb{Q}} \int \frac{\partial^2 \mathcal{Q}(\mathbf{r})}{\partial D_{pq}^\sigma \partial D_{rs}^{\sigma'}} \frac{\delta}{\delta \mathcal{Q}(\mathbf{r})} d\mathbf{r} . \end{aligned} \quad (3.34)$$

In the context of this work, the semilocal hyper-kernel operator is required, which is obtained by applying the semilocal potential operator three times^[212]

$$\begin{aligned} \hat{d}_{pq\sigma} \hat{d}_{rs\sigma'} \hat{d}_{tu\sigma''} &= \sum_{\mathbb{Q} \in \mathbb{Q}} \sum_{\mathbb{Q}' \in \mathbb{Q}} \sum_{\mathbb{Q}'' \in \mathbb{Q}} \iiint \frac{\partial \mathcal{Q}(\mathbf{r})}{\partial D_{pq}^\sigma} \frac{\partial \mathcal{Q}'(\mathbf{r}')}{\partial D_{rs}^{\sigma'}} \frac{\partial \mathcal{Q}''(\mathbf{r}'')}{\partial D_{tu}^{\sigma''}} \frac{\delta^3}{\delta \mathcal{Q}(\mathbf{r}) \delta \mathcal{Q}'(\mathbf{r}') \delta \mathcal{Q}''(\mathbf{r}'')} d\mathbf{r} d\mathbf{r}' d\mathbf{r}'' \\ &\quad + \sum_{\mathbb{Q} \in \mathbb{Q}} \sum_{\mathbb{Q}' \in \mathbb{Q}} \iint \left[\frac{\partial^2 \mathcal{Q}(\mathbf{r})}{\partial D_{rs}^{\sigma'} \partial D_{tu}^{\sigma''}} \frac{\partial \mathcal{Q}'(\mathbf{r}')}{\partial D_{pq}^\sigma} + \frac{\partial^2 \mathcal{Q}(\mathbf{r})}{\partial D_{pq}^\sigma \partial D_{tu}^{\sigma''}} \frac{\partial \mathcal{Q}'(\mathbf{r}')}{\partial D_{rs}^{\sigma'}} \right. \\ &\quad \left. + \frac{\partial^2 \mathcal{Q}(\mathbf{r})}{\partial D_{pq}^\sigma \partial D_{rs}^{\sigma'}} \frac{\partial \mathcal{Q}'(\mathbf{r}')}{\partial D_{tu}^{\sigma''}} \right] \frac{\delta^2}{\delta \mathcal{Q}(\mathbf{r}) \delta \mathcal{Q}'(\mathbf{r}')} d\mathbf{r} d\mathbf{r}' \\ &\quad + \sum_{\mathbb{Q} \in \mathbb{Q}} \int \frac{\partial^3 \mathcal{Q}(\mathbf{r})}{\partial D_{pq}^\sigma \partial D_{rs}^{\sigma'} \partial D_{tu}^{\sigma''}} \frac{\delta}{\delta \mathcal{Q}(\mathbf{r})} d\mathbf{r} . \end{aligned} \quad (3.35)$$

Note, that the last term in eq. 3.35 vanishes for the set of (semi)local quantities considered in this work (cf. eq. 3.32) because all third derivatives of ρ_σ , $\gamma_{\sigma\sigma}$, $\gamma_{\sigma\sigma'}$ and τ_σ w.r.t. density matrices are zero. To cover the most general case, the term is nonetheless included here and below.

Transformation to the Atomic Orbital Basis

Except for eq. 3.23, all equations relevant for the calculation of ES gradients and the associated derivatives are written in the MO basis. However, for an implementation, the MOs are typically expanded in an AO basis (cf. eq. 3.2)

$$\varphi_{p\sigma}(\mathbf{r}) = \sum_{\mu}^{N_b} C_{\mu p\sigma} \chi_{\mu}(\mathbf{r}). \quad (3.36)$$

Conveniently, the density matrix formalism developed within the MO basis, also transfers to the AO basis, where

$$D_{\mu\nu}^{\sigma} = \sum_{pq} C_{p\mu\sigma}^* C_{q\nu\sigma} D_{pq}^{\sigma} \quad (3.37)$$

defines the transformation between the MO and AO density matrices. A derivative w.r.t. an MO density matrix element D_{pq}^{σ} is transferred via

$$\frac{\partial}{\partial D_{pq}^{\sigma}} = \sum_{\mu\nu} \frac{\partial D_{\mu\nu}^{\sigma}}{\partial D_{pq}^{\sigma}} \frac{\partial}{\partial D_{\mu\nu}^{\sigma}} = \sum_{\mu\nu} C_{p\mu\sigma}^* C_{q\nu\sigma} \frac{\partial}{\partial D_{\mu\nu}^{\sigma}} \quad (3.38)$$

to the AO basis. Hence, all derivative schemes denoted above in the MO basis are straightforwardly transferred to the AO basis by formally replacing Roman letters (MO indices) with Greek letters (AO indices). This also holds for the semilocal potential operator, which is abbreviated as $\hat{\partial}_{\mu\nu\sigma}$ in the AO basis.

Numerical Integration

Standard AO matrix elements in (TD)DFT are calculated as outlined in Section 2.1.4 for HF theory. For the XC energy and its derivatives, an analytical integration is not reasonably possible and the integrals are evaluated using numerical integration. The integral over some energy density $e(\mathbf{r})$ is approximated as the sum over N_g grid points positioned at \mathbf{r}_i with associated grid weights q_i

$$E = \int e(\mathbf{r}) d\mathbf{r} \approx \sum_i^{N_g} q_i e(\mathbf{r}_i). \quad (3.39)$$

The grids are typically constructed based on atomic grids distributed around each atom,^[236] where the atomic grids are separated into a spherical and a radial grid. For the spherical grid, schemes by Lebedev^[237] and Gauss-Lobatto^[238,239] are in common use. For the radial integration, a popular choice are Chebychev grids, which are mapped from their originally defined interval $[0, 1]$ onto the interval $[0, \infty)$.^[240] To evaluate eq. 3.39, $e(\mathbf{r}_i)$ has to be calculated from the values of the (semi)local quantities at any given grid point. In the AO basis, their values are obtained as

$$\rho_\sigma(\mathbf{r}_i) = \sum_{\mu\nu} D_{\mu\nu}^\sigma \chi_\mu(\mathbf{r}_i) \chi_\nu(\mathbf{r}_i) = \mathbf{X}_i^\top \mathbf{D}^\sigma \mathbf{X}_i \quad (3.40a)$$

$$\nabla \rho_\sigma(\mathbf{r}_i) = \sum_{\mu\nu} D_{\mu\nu}^\sigma \nabla [\chi_\mu(\mathbf{r}_i) \chi_\nu(\mathbf{r}_i)] = 2 \mathbf{X}_i^\top \mathbf{D}^\sigma \nabla \mathbf{X}_i \quad (3.40b)$$

$$\gamma_{\sigma\sigma'}(\mathbf{r}_i) = \nabla^\top \rho_\sigma(\mathbf{r}_i) \nabla \rho_{\sigma'}(\mathbf{r}_i) \quad (3.40c)$$

$$\tau_\sigma(\mathbf{r}_i) = \frac{1}{2} \sum_{\mu\nu} D_{\mu\nu}^\sigma \nabla^\top \chi_\mu(\mathbf{r}_i) \nabla \chi_\nu(\mathbf{r}_i) = \frac{1}{2} \nabla^\top \mathbf{X}_i^\top \mathbf{D}^\sigma \nabla \mathbf{X}_i, \quad (3.40d)$$

where the basis function vector at grid point \mathbf{r}_i

$$\mathbf{X}_i := \begin{pmatrix} \chi_1(\mathbf{r}_i) \\ \chi_2(\mathbf{r}_i) \\ \vdots \\ \chi_{N_b}(\mathbf{r}_i) \end{pmatrix} \quad (3.41)$$

is introduced to express summations over AO indices as matrix-vector products.^c

If numerical integration is used for the calculation of the gradient of an energy E , applying the product rule of differentiation to eq. 3.39 gives two terms

$$\nabla E \approx \sum_i^{N_g} [\nabla q_i \cdot e(\mathbf{r}_i) + q_i \cdot \nabla e(\mathbf{r}_i)] . \quad (3.42)$$

The first term including the derivatives of the quadrature weights ∇q_i (weight derivatives, WD) arises because the quadrature weights depend on the position of the nuclei. This first term is usually small, in particular when fine quadrature grids are used, which is why they are often neglected and only the second term is implemented.^[241] However, if accurate gradients are needed (e.g. for numerical frequency calculations) or coarse grids are used, it is advisable to include WDs. Because energy densities are a necessity for the

^cThe basis function vector \mathbf{X}_i must not be confused with the same-named transition density matrix (cf., e.g., eq. 2.142), which is relabeled further below (eq. 3.51).

development of gradients, the WD term $\nabla q_i \cdot e(\mathbf{r}_i)$ requires only minor development work for the ∇q_i part^[241] and causes negligible extra computational cost.

Seminumerical Integration

The functional form of LHs (eq. 2.75) requires the calculation of integrals where the EXX energy density (or one of its derivatives) is weighted by an LMF (or one of its derivatives). In the AO basis, the simplest of these integrals reads

$$\int a_\sigma(\mathbf{r}) \cdot e_\sigma^{\text{ex}}(\mathbf{r}) \, d\mathbf{r} = -\frac{1}{2} \sum_{\mu\nu\kappa\lambda} D_{\mu\nu}^\sigma D_{\kappa\lambda}^\sigma \int a_\sigma(\mathbf{r}) \chi_\mu(\mathbf{r}) \chi_\lambda(\mathbf{r}) \int \frac{\chi_\kappa(\mathbf{r}') \chi_\nu(\mathbf{r}')}{|\mathbf{r} - \mathbf{r}'|} \, d\mathbf{r}' \, d\mathbf{r} . \quad (3.43)$$

Multiplication of the four-center two-electron integral with the position-dependent LMF $a_\sigma(\mathbf{r})$ prevents the use of standard analytical techniques to calculate the EXX integral (cf. Section 2.1.4). Instead, a seminumerical integration scheme^[48] inspired by Friesner's pseudospectral method^[242] is followed, where one integration is done analytically, while the second integral is solved via numerical quadrature. In eq. 3.43, it is sensible to perform the integral over \mathbf{r} on a numerical quadrature grid, because the LMF $a_\sigma(\mathbf{r})$ depends on this coordinate. The remaining integral defines the **A** matrix^d

$$A_{\kappa\nu}(\mathbf{r}_i) = \int \frac{\chi_\kappa(\mathbf{r}') \chi_\nu(\mathbf{r}')}{|\mathbf{r}_i - \mathbf{r}'|} \, d\mathbf{r}' , \quad (3.44)$$

which is evaluated analytically at each grid point \mathbf{r}_i . Since the values of \mathbf{r}_i are fixed, the integral in eq. 3.44 has the same structure as a nuclear-electron interaction integral for which efficient evaluation schemes are well established (cf. Section 2.1.4). With the above definition of the **A** matrix, the integral from eq. 3.43 is obtained as^[234]

$$\begin{aligned} \int a_\sigma(\mathbf{r}) \cdot e_\sigma^{\text{ex}}(\mathbf{r}) \, d\mathbf{r} &= -\frac{1}{2} \sum_i^{N_g} q_i \sum_{\mu\nu\kappa\lambda} D_{\mu\nu}^\sigma D_{\kappa\lambda}^\sigma a_\sigma(\mathbf{r}_i) \chi_\mu(\mathbf{r}_i) \chi_\lambda(\mathbf{r}_i) A_{\kappa\nu}(\mathbf{r}_i) \\ &= -\frac{1}{2} \sum_i^{N_g} q_i a_\sigma(\mathbf{r}_i) \cdot \sum_\lambda \chi_\lambda(\mathbf{r}_i) \sum_\kappa D_{\kappa\lambda}^\sigma \sum_\nu A_{\kappa\nu}(\mathbf{r}_i) \sum_\mu D_{\mu\nu}^\sigma \chi_\mu(\mathbf{r}_i) \\ &= -\frac{1}{2} \sum_i^{N_g} q_i a_\sigma(\mathbf{r}_i) \cdot \mathbf{X}_i^\top \mathbf{D}^\sigma \mathbf{A}_i \mathbf{D}^\sigma \mathbf{X}_i \\ &= -\frac{1}{2} a_\sigma \cdot \mathbf{X}^\top \mathbf{D}^\sigma \mathbf{A} \mathbf{D}^\sigma \mathbf{X} , \end{aligned} \quad (3.45)$$

^dNote that **A** must not be confused with the matrix of identical name from eq. 2.142.

where the summations over AO indices were expressed as matrix-vector products and where in the last line, the convention was introduced that suppressed grid indices imply a q_i -weighted summation over all grid points. Also note that the symmetry of the GS density matrix \mathbf{D}^σ was exploited. Overall, a formal scaling of $N_g \cdot N_b^2$ is obtained, which makes the seminumerical scheme superior for calculations with large basis sets compared to an analytical implementation (as often used for GHs) that scales as N_b^4 . Of course, the seminumerical scheme is not exclusively suited for LHs^[23,47,234,243–246] and it has been implemented also for GHs before.^[45,48,247] A convenient side effect of the seminumerical scheme is that it is well suited for parallelization because the loop over grid points (or batches of grid points) can be spread effectively over multiple processors without causing significant overheads.^[244,248] Because the bottle-neck of the seminumerical scheme is the calculation of the \mathbf{A} matrix, it is desirable to avoid any unnecessary calculations of elements of this matrix. For this purpose, various prescreening techniques may be used that identify negligible or non-contributing matrix elements. One such technique is adopted from the chain-of-spheres exchange (COSX) method^[48] and aims at identifying basis function shell pairs that have negligible overlap at a given grid point and thus result in negligible \mathbf{A} matrix elements (S-junctions). Another technique tries to identify negligible elements of the vector $\mathbf{D}^\sigma \mathbf{X}$, which allows to skip not only the multiplication with the \mathbf{A} matrix but also the calculation of the \mathbf{A} matrix elements this vector is contracted with (P-junctions).^[234] It is also possible to exploit the asymptotic decay of the Coulomb operator in the definition of the \mathbf{A} matrix as done in the recently suggested F-junctions.^[249] For this method, a sphere^e with minimal radius is constructed around all grid points of a given grid batch and, based on an asymptotic integral estimate,^[249] an upper bound of the respective \mathbf{A} matrix element is determined for any basis function pair which center lies outside this sphere. If the contraction of this estimate with the maximum values of the $\mathbf{D}^\sigma \mathbf{X}$ vector leads to negligible contributions, the exact evaluation of the \mathbf{A} matrix for this basis function pair can be skipped for the complete grid batch.

For the evaluation of LH GS/ES gradients, integrals where the gradient of the EXX energy density is weighted by an LMF (or derivative versions of the same general form)

^eTo avoid the mathematical problem of finding such a sphere, a cuboid is used in practice.^[249]

have to be calculated. Following again the idea of seminumerical integration gives

$$\begin{aligned}
 & \int a_\sigma(\mathbf{r}) \cdot \nabla_\xi e_\sigma^{\text{ex}}(\mathbf{r}) \, d\mathbf{r} \\
 &= -\frac{1}{2} \sum_i^{N_g} q_i \sum_{\mu\nu\kappa\lambda} D_{\mu\nu}^\sigma D_{\kappa\lambda}^\sigma a_\sigma(\mathbf{r}_i) \nabla_\xi \left[\chi_\mu(\mathbf{r}_i) \chi_\lambda(\mathbf{r}_i) \int \frac{\chi_\kappa(\mathbf{r}') \chi_\nu(\mathbf{r}')}{|\mathbf{r}_i - \mathbf{r}'|} \, d\mathbf{r}' \right] \\
 &= -\sum_i^{N_g} q_i \sum_{\mu\nu\kappa\lambda} D_{\mu\nu}^\sigma D_{\kappa\lambda}^\sigma a_\sigma(\mathbf{r}_i) \left[\nabla_\xi \chi_\mu(\mathbf{r}_i) \chi_\lambda(\mathbf{r}_i) A_{\kappa\nu}(\mathbf{r}_i) + \chi_\mu(\mathbf{r}_i) \chi_\lambda(\mathbf{r}_i) A_{\kappa\nu}^\xi(\mathbf{r}_i) \right] \\
 &= a_\sigma \cdot \left[\mathbf{X}^\top \mathbf{D}^\sigma \mathbf{A} \mathbf{D}^\sigma \nabla_\xi \mathbf{X} + \mathbf{X}^\top \mathbf{D}^\sigma \mathbf{A}^\xi \mathbf{D}^\sigma \mathbf{X} \right] , \tag{3.46}
 \end{aligned}$$

with

$$A_{\kappa\nu}^\xi(\mathbf{r}_i) = \int \frac{\nabla_\xi \chi_\kappa(\mathbf{r}') \chi_\nu(\mathbf{r}')}{|\mathbf{r}_i - \mathbf{r}'|} \, d\mathbf{r}' , \tag{3.47}$$

being a derivative version of the \mathbf{A} matrix.^[47] In the third line of eq. 3.46, the fact that the matrix \mathbf{D}^σ , the basis function pair $\chi_\mu \chi_\lambda$ and the \mathbf{A} matrix are symmetric was exploited, which has allowed to summarize a total of four gradient terms resulting from the product rule of differentiation to two gradient terms. If no LMF was used, the second term in the last line of eq. 3.46 could be brought into the same form as the first term thus avoiding the need to calculate \mathbf{A}^ξ . In the case of GHs, this is indeed a valid step and leads to significant savings in computation time because opposed to \mathbf{A} , the matrix \mathbf{A}^ξ is not symmetric and, in fact, represents a set of three matrices with one matrix for each direction in space.^[212] Hence, computing and storing \mathbf{A}^ξ takes about six times the amount of memory and computation time as it does for \mathbf{A} while the overall scaling remains unaffected.^[47] Since the real-space dependence of the LMF precludes this summation for LHs, algorithms for calculating \mathbf{A}^ξ have been developed in the context of the implementation of GS gradients.^[47]

3.2.2 The LH Hyper-Kernel

For the calculation of the RHS of the Z vector equation (eq. 3.21) as well as for some of the blocks of \mathbf{W} (cf. Appendix A.1), the matrix elements of the XC hyper-kernel $g_{pqrstu}^{\sigma\sigma'\sigma''}$ are needed. Using the density matrix derivative scheme and the semilocal potential operator, these matrix elements are derived in Appendix A.2 and the result is given below

$$\begin{aligned}
g_{pqrstu}^{\sigma\sigma'\sigma''} = & -\frac{1}{2} \iint \hat{d}_{rs\sigma'} a_{\sigma}(\mathbf{r}) \cdot \delta_{\sigma\sigma''} \cdot [w_{tqpu}^{\sigma\sigma}(\mathbf{r}, \mathbf{r}') + w_{putq}^{\sigma\sigma}(\mathbf{r}, \mathbf{r}')] d\mathbf{r} d\mathbf{r}' \\
& -\frac{1}{2} \iint \hat{d}_{tu\sigma''} a_{\sigma}(\mathbf{r}) \cdot \delta_{\sigma\sigma'} \cdot [w_{rqp\sigma}^{\sigma\sigma}(\mathbf{r}, \mathbf{r}') + w_{psrq}^{\sigma\sigma}(\mathbf{r}, \mathbf{r}')] d\mathbf{r} d\mathbf{r}' \\
& -\frac{1}{2} \iint \hat{d}_{rs\sigma'} \hat{d}_{tu\sigma''} a_{\sigma}(\mathbf{r}) \cdot \sum_{mn} D_{mn}^{\sigma} [w_{mqpn}^{\sigma\sigma}(\mathbf{r}, \mathbf{r}') + w_{pnmq}^{\sigma\sigma}(\mathbf{r}, \mathbf{r}')] d\mathbf{r} d\mathbf{r}' \\
& -\frac{1}{2} \iint \hat{d}_{pq\sigma'} a_{\sigma'}(\mathbf{r}) \cdot \delta_{\sigma'\sigma''} \cdot [w_{tsru}^{\sigma'\sigma'}(\mathbf{r}, \mathbf{r}') + w_{ruts}^{\sigma'\sigma'}(\mathbf{r}, \mathbf{r}')] d\mathbf{r} d\mathbf{r}' \\
& -\sum_{\zeta} \int \hat{d}_{pq\sigma'} a_{\zeta}(\mathbf{r}) \cdot \hat{d}_{rs\sigma'} \hat{d}_{tu\sigma''} e_{x,\zeta}^{\text{sl}}(\mathbf{r}) d\mathbf{r} - \sum_{\zeta} \int \hat{d}_{pq\sigma} e_{x,\zeta}^{\text{sl}}(\mathbf{r}) \cdot \hat{d}_{rs\sigma'} \hat{d}_{tu\sigma''} a_{\zeta}(\mathbf{r}) d\mathbf{r} \\
& -\frac{1}{2} \iint \hat{d}_{pq\sigma} \hat{d}_{rs\sigma'} a_{\sigma''}(\mathbf{r}) \cdot \sum_{mn} D_{mn}^{\sigma''} [w_{mutn}^{\sigma''\sigma''}(\mathbf{r}, \mathbf{r}') + w_{tnmu}^{\sigma''\sigma''}(\mathbf{r}, \mathbf{r}')] d\mathbf{r} d\mathbf{r}' \\
& -\frac{1}{2} \iint \hat{d}_{pq\sigma} \hat{d}_{tu\sigma''} a_{\sigma'}(\mathbf{r}) \cdot \sum_{mn} D_{mn}^{\sigma'} [w_{msrn}^{\sigma'\sigma'}(\mathbf{r}, \mathbf{r}') + w_{rnms}^{\sigma'\sigma'}(\mathbf{r}, \mathbf{r}')] d\mathbf{r} d\mathbf{r}' \\
& -\sum_{\zeta} \int \hat{d}_{pq\sigma} \hat{d}_{rs\sigma'} a_{\zeta}(\mathbf{r}) \cdot \hat{d}_{tu\sigma''} e_{x,\zeta}^{\text{sl}}(\mathbf{r}) d\mathbf{r} - \sum_{\zeta} \int \hat{d}_{pq\sigma} \hat{d}_{tu\sigma''} a_{\zeta}(\mathbf{r}) \cdot \hat{d}_{rs\sigma'} e_{x,\zeta}^{\text{sl}}(\mathbf{r}) d\mathbf{r} \\
& -\sum_{\zeta} \int \hat{d}_{rs\sigma'} a_{\zeta}(\mathbf{r}) \cdot \hat{d}_{pq\sigma} \hat{d}_{tu\sigma''} e_{x,\zeta}^{\text{sl}}(\mathbf{r}) d\mathbf{r} - \sum_{\zeta} \int \hat{d}_{tu\sigma''} a_{\zeta}(\mathbf{r}) \cdot \hat{d}_{pq\sigma} \hat{d}_{rs\sigma'} e_{x,\zeta}^{\text{sl}}(\mathbf{r}) d\mathbf{r} \\
& -\sum_{\zeta} \iint \hat{d}_{pq\sigma} \hat{d}_{rs\sigma'} \hat{d}_{tu\sigma''} a_{\zeta}(\mathbf{r}) \cdot \left[\frac{1}{2} \sum_{mnkl} D_{mn}^{\zeta} D_{kl}^{\zeta} w_{mlkn}^{\zeta\zeta}(\mathbf{r}, \mathbf{r}') + e_{x,\zeta}^{\text{sl}}(\mathbf{r}) \right] d\mathbf{r} d\mathbf{r}' \\
& + \sum_{\zeta} \int [1 - a_{\zeta}(\mathbf{r})] \cdot \hat{d}_{pq\sigma} \hat{d}_{rs\sigma'} \hat{d}_{tu\sigma''} e_{x,\zeta}^{\text{sl}}(\mathbf{r}) d\mathbf{r} + \int \hat{d}_{pq\sigma} \hat{d}_{rs\sigma'} \hat{d}_{tu\sigma''} e_c^{\text{sl}}(\mathbf{r}) d\mathbf{r} . \quad (3.48)
\end{aligned}$$

This expression looks rather intimidating, especially when compared to the matrix elements of the GH hyper-kernel, which is simply the last line of the above equation. All other terms include derivatives of the LMF $a_{\sigma}(\mathbf{r})$ that vanish in the GH case, where $a_{\sigma}(\mathbf{r}) = \text{const}$. However, ultimately, the LH expression is nothing but the result of subsequently applying the product rule of differentiation to the LH energy expression (eq. 2.75) and utilizing the rules and notations outline in Section 3.2.1. Note that the CF $G_{\sigma}(\mathbf{r})$ is not explicitly shown in eq. 3.48 for clarity. Formally, it can be thought of as being part of $e_{x,\sigma}^{\text{sl}}(\mathbf{r})$. For reasons outlined below, the CF is nonetheless neglected within this work.

As mentioned in Section 3.1, setting up and storing this six-index quantity explicitly would be excessively expensive. Fortunately, however, this can be avoided because the matrix elements are always contracted with two transition density matrices resulting in an overall two-index quantity. Hence, the actual LH hyper-kernel does not have to be implemented. Instead, what is needed for an implementation are the quantities

$$\sum_{jb\sigma'kc\sigma''} g_{\pm iajbkc}^{\sigma\sigma'\sigma''} (X \pm Y)_{jb\sigma'} (X \pm Y)_{kc\sigma''} , \quad (3.49)$$

which are calculated in the AO basis and transformed with the respective MO coefficients to the MO basis. In the AO basis, these terms read

$$\sum_{\kappa\lambda\eta\iota} \sum_{\sigma'\sigma''} g_{\pm\mu\nu\kappa\lambda\eta\iota}^{\sigma\sigma'\sigma''} U_{\kappa\lambda\sigma'}^{\pm} U_{\eta\iota\sigma''}^{\pm} , \quad (3.50)$$

where the transition density matrices $(\mathbf{X} \pm \mathbf{Y})$ are relabeled according to

$$\mathbf{U}^+ = (\mathbf{X} + \mathbf{Y}) , \quad \mathbf{U}^- = (\mathbf{X} - \mathbf{Y}) \quad (3.51)$$

to avoid confusion with the basis function vector \mathbf{X} . Since these transition matrices are either symmetric (\mathbf{U}^+) or antisymmetric (\mathbf{U}^-), it is possible to summarize several terms that appear in the definition of the LH hyper-kernel (eq. 3.48) with flipped index order. Also, recall that the definition of $g_{\pm\mu\nu\kappa\lambda\eta\iota}^{\sigma\sigma'\sigma''}$ includes two hyper-kernel terms as indicated by the \pm sign (cf. eq. 3.16). To condense the summation over AO indices, additional (partly) contracted versions of the semilocal potential operator are introduced.^[212] Their effect is demonstrated below for the LMF $a(\mathbf{r})$ but the effect is equivalent for a (semi)local energy density; the space variable \mathbf{r} (or \mathbf{r}_i if evaluated on a grid point) is dropped for brevity

$$\widehat{\partial}_{\mu\nu\sigma} a = \sum_{Q \in \mathbb{Q}} \int d\mathbf{r}' \frac{\partial Q(\mathbf{r}')}{\partial D_{\mu\nu}^{\sigma}} \frac{\delta}{\delta Q(\mathbf{r}')} a , \quad (3.52a)$$

$$\widehat{\partial}^+ a = \sum_{\kappa\lambda\sigma'} \widehat{\partial}_{\kappa\lambda\sigma'} a \cdot U_{\kappa\lambda\sigma'}^+ , \quad (3.52b)$$

$$\widehat{\partial\partial}_{\mu\nu\sigma}^+ a = \sum_{\kappa\lambda\sigma'} \widehat{\partial}_{\mu\nu\sigma} \widehat{\partial}_{\kappa\lambda\sigma'} a \cdot U_{\kappa\lambda\sigma'}^+ , \quad (3.52c)$$

$$\widehat{\partial\partial}^{++} a = \sum_{\eta\epsilon\sigma'\kappa\lambda\sigma''} \widehat{\partial}_{\eta\epsilon\sigma'} \widehat{\partial}_{\kappa\lambda\sigma''} a \cdot U_{\eta\epsilon\sigma'}^+ U_{\kappa\lambda\sigma''}^+ , \quad (3.52d)$$

$$\widehat{\partial\partial\partial}_{\mu\nu\sigma}^{++} a = \sum_{\eta\epsilon\sigma'\kappa\lambda\sigma''} \widehat{\partial}_{\mu\nu\sigma} \widehat{\partial}_{\eta\epsilon\sigma'} \widehat{\partial}_{\kappa\lambda\sigma''} a \cdot U_{\eta\epsilon\sigma'}^+ U_{\kappa\lambda\sigma''}^+ . \quad (3.52e)$$

Explicitly expanded expressions for these terms are given in Appendix A.4. Note that for the XC hyper-kernel of a global hybrid or purely semilocal functional, only the $\widehat{\partial\partial\partial}_{\mu\nu\sigma}^{++}$ operator is required. It has been reported, e.g., in ref. 41 using a different notation but yields the same terms as given in Appendix A.4. With the above notations, the symmetric LH hyper-kernel contracted with two symmetric transition-density matrices is finally obtained as^[212]

$$\begin{aligned}
 & \sum_{\kappa\lambda\eta\iota} \sum_{\sigma'\sigma''} g_{+\mu\nu\kappa\lambda\eta\iota}^{\sigma\sigma'\sigma''} U_{\kappa\lambda\sigma'}^+ U_{\eta\iota\sigma''}^+ \\
 &= -2 \widehat{\partial}^+ a_\sigma \cdot [X_\mu (\mathbf{A} \mathbf{U}_\sigma^+ \mathbf{X})_\nu + (\mathbf{A} \mathbf{U}_\sigma^+ \mathbf{X})_\mu X_\nu] \\
 & \quad - \widehat{\partial\partial}^{++} a_\sigma \cdot [X_\mu (\mathbf{A} \mathbf{D}^\sigma \mathbf{X})_\nu + (\mathbf{A} \mathbf{D}^\sigma \mathbf{X})_\mu X_\nu] \\
 & \quad - 2 \sum_{\sigma'} \widehat{\partial}_{\mu\nu\sigma} a_{\sigma'} \cdot [\mathbf{X}^\top \mathbf{U}_{\sigma'}^+ \mathbf{A} \mathbf{U}_{\sigma'}^+ \mathbf{X} + \widehat{\partial\partial}^{++} e_{\mathbf{x},\sigma'}^{\text{sl}}] - 2 \sum_{\sigma'} \widehat{\partial}_{\mu\nu\sigma} e_{\mathbf{x},\sigma'}^{\text{sl}} \cdot \widehat{\partial\partial}^{++} a_{\sigma'} \\
 & \quad - 4 \sum_{\sigma'} \widehat{\partial\partial}^+ a_{\sigma'} \cdot [\mathbf{X}^\top \mathbf{D}^{\sigma'} \mathbf{A} \mathbf{U}_{\sigma'}^+ \mathbf{X} + \widehat{\partial}^+ e_{\mathbf{x},\sigma'}^{\text{sl}}] - 4 \sum_{\sigma'} \widehat{\partial\partial}^+ e_{\mathbf{x},\sigma'}^{\text{sl}} \cdot \widehat{\partial}^+ a_{\sigma'} \\
 & \quad - 2 \sum_{\sigma'} \widehat{\partial\partial\partial}^{++} a_{\sigma'} \cdot \left[\frac{1}{2} \mathbf{X}^\top \mathbf{D}^{\sigma'} \mathbf{A} \mathbf{D}^{\sigma'} \mathbf{X} + e_{\mathbf{x},\sigma'}^{\text{sl}} \right] + 2 \sum_{\sigma'} [1 - a_{\sigma'}] \cdot \widehat{\partial\partial\partial}^{++} e_{\mathbf{x},\sigma'}^{\text{sl}} \\
 & \quad + 2 \widehat{\partial\partial\partial}^{++} e_{\mathbf{c}}^{\text{sl}}, \tag{3.53}
 \end{aligned}$$

where grid indices are suppressed and an implicit summation over all grid points is assumed. For the antisymmetric LH hyper-kernel, a much simpler expression is obtained^[212]

$$\sum_{\kappa\lambda\eta\iota} \sum_{\sigma'\sigma''} g_{-\mu\nu\kappa\lambda\eta\iota}^{\sigma\sigma'\sigma''} U_{\kappa\lambda\sigma'}^- U_{\eta\iota\sigma''}^- = -2 \sum_{\sigma'} \widehat{\partial}_{\mu\nu\sigma} a_{\sigma'} \cdot [\mathbf{X}^\top \mathbf{U}_{\sigma'}^- \mathbf{A} \mathbf{U}_{\sigma'}^- \mathbf{X}]. \tag{3.54}$$

The main reason for this simple structure is the assumption that the semilocal potential operator is symmetric w.r.t. to the interchange of basis function indices, i.e. $\widehat{\partial}_{\kappa\lambda\sigma} - \widehat{\partial}_{\lambda\kappa\sigma} = 0$. This assumption is in fact valid for the set of (semi)local quantities considered in this work (cf. eq. 3.32). However, this symmetry property would get lost, if the paramagnetic current-density

$$\mathbf{j}_\sigma(\mathbf{r}) = \frac{1}{2} \sum_{\mu\nu} D_{\mu\nu}^\sigma [\nabla \chi_\mu(\mathbf{r}) \chi_\nu(\mathbf{r}) - \chi_\mu(\mathbf{r}) \nabla \chi_\nu(\mathbf{r})] \tag{3.55}$$

was included as part of a modified kinetic-energy term suggested for ensuring gauge invariance of τ -dependent functionals.^[211] LR-TDDFT implementations of excitation energies including the response of the current-density were reported by Bates and Furche^[211] for mGGAs and mGGA based GHs as well as by Maier *et al.* for LHs.^[23] Given that only

minor effects on excitation energies were found^[24,211] and that a full inclusion of the current terms would result in a severely more complicated equation for the antisymmetric part, the current-density response is neglected in the equations for ES gradients within this work. The validity of this approximation is analyzed in Section 4.3.3.

The equations above are given for the most general case of spin-unrestricted calculations. For closed-shell GSs, it is customary to perform spin-restricted calculations that exploit symmetry of the GS density matrix ($\mathbf{D}^\alpha = \mathbf{D}^\beta$) and consider singlet excitations ($\mathbf{U}_\alpha^\pm = \mathbf{U}_\beta^\pm$) and triplet excitations ($\mathbf{U}_\alpha^\pm = -\mathbf{U}_\beta^\pm$) separately. The respective transition-density matrix contracted hyper-kernels are obtained by inserting these spin relations into eq. 3.53-3.54 and executing all spin summations explicitly.

3.2.3 The LH Potential and Kernel Gradients

For the evaluation of the final ES gradients (eq. 3.23), the gradients of the XC potential contracted with the relaxed one-particle difference-density matrix

$$\sum_{\mu\nu\sigma} V_{\mu\nu\sigma}^{\text{xc}(\xi)} P_{\mu\nu\sigma} \quad (3.56)$$

and the gradients of the (anti)symmetric XC kernel contracted with two (anti)symmetric transition density matrices

$$\frac{1}{2} \sum_{\mu\nu\sigma\kappa\lambda\sigma'} f_{\pm\mu\nu\sigma\kappa\lambda\sigma'}^{(\xi)} U_{\mu\nu\sigma}^\pm U_{\kappa\lambda\sigma'}^\pm \quad (3.57)$$

are required. Both terms have to be derived for the LH case. For the (semi)local parts, derivatives w.r.t. nuclear coordinates (ξ) are easily transformed to conventional derivatives w.r.t. (semi)local quantities. In analogy to the semilocal potential operator, the semilocal gradient operator $\hat{\nabla}_\xi$ is introduced

$$\hat{\nabla}_\xi = \sum_{\mathbf{Q} \in \mathbf{Q}} \int \frac{\partial \mathcal{Q}(\mathbf{r}')}{\partial \xi} \frac{\delta}{\delta \mathcal{Q}(\mathbf{r}')} d\mathbf{r}' , \quad (3.58)$$

where $\frac{\partial \mathcal{Q}(\mathbf{r}')}{\partial \xi}$ is used to denote the gradients of the (semi)local quantities. Exploiting that the nuclear gradient of a Gaussian basis function is equivalent to the negative of the gradient w.r.t. electronic coordinates, i.e. $\nabla_\xi \chi = -\nabla \chi$, these derivatives read

$$\frac{\partial \rho_\sigma}{\partial \xi} = -2\mathbf{X}^\top \mathbf{D}^\sigma \nabla \mathbf{X} \quad (3.59a)$$

$$\begin{aligned} \frac{\partial \gamma_{\sigma\sigma'}}{\partial \xi} = & -2 [\nabla \mathbf{X}^\top \mathbf{D}_\sigma \nabla^\top \mathbf{X} + \nabla \nabla^\top \mathbf{X}^\top \mathbf{D}_\sigma \mathbf{X}] \nabla \rho_{\sigma'} \\ & -2 [\nabla \mathbf{X}^\top \mathbf{D}_{\sigma'} \nabla^\top \mathbf{X} + \nabla \nabla^\top \mathbf{X}^\top \mathbf{D}_{\sigma'} \mathbf{X}] \nabla \rho_\sigma \end{aligned} \quad (3.59b)$$

$$\frac{\partial \tau_\sigma}{\partial \xi} = -\nabla \nabla^\top \mathbf{X}^\top \mathbf{D}^\sigma \nabla \mathbf{X}. \quad (3.59c)$$

Additionally, two transition-density matrix contracted operators are defined as

$$\widehat{\nabla_\xi \partial^+} a = \sum_{\kappa\lambda\sigma'} \widehat{\nabla_\xi \partial_{\kappa\lambda\sigma'}} a \cdot U_{\kappa\lambda\sigma'}^+, \quad (3.60a)$$

$$\widehat{\nabla_\xi \partial \partial^{++}} a = \sum_{\eta\epsilon\sigma'\kappa\lambda\sigma''} \widehat{\nabla_\xi \partial_{\eta\epsilon\sigma'}} \widehat{\partial_{\kappa\lambda\sigma''}} a \cdot U_{\eta\epsilon\sigma'}^+ U_{\kappa\lambda\sigma''}^+ \quad (3.60b)$$

acting here on the LMF a for demonstration. Their explicitly expanded forms are given in Appendix A.4. Proceeding from the LH kernel^[23] as given in Appendix A.2 and using these notations, the symmetric contracted kernel gradients read^[212]

$$\begin{aligned} & \frac{1}{2} \sum_{\mu\nu\sigma\kappa\lambda\sigma'} f_{+\mu\nu\sigma\kappa\lambda\sigma'}^{(\xi)} U_{\mu\nu\sigma}^+ U_{\kappa\lambda\sigma'}^+ \\ = & -2 \sum_{\sigma} a_\sigma [\mathbf{X}^\top \mathbf{U}_\sigma^+ \mathbf{A} \mathbf{U}_\sigma^+ \nabla_\xi \mathbf{X} + \mathbf{X}^\top \mathbf{U}_\sigma^+ \mathbf{A}^\xi \mathbf{U}_\sigma^+ \mathbf{X}] \\ & -2 \sum_{\sigma} \widehat{\partial^+} a_\sigma [\mathbf{X}^\top \mathbf{D}^\sigma \mathbf{A} \mathbf{U}_\sigma^+ \nabla_\xi \mathbf{X} + \nabla_\xi \mathbf{X}^\top \mathbf{D}^\sigma \mathbf{A} \mathbf{U}_\sigma^+ \mathbf{X} + \mathbf{X}^\top \mathbf{D}^\sigma \mathbf{A}^\xi \mathbf{U}_\sigma^+ \mathbf{X} + \mathbf{X}^\top \mathbf{D}^\sigma \mathbf{A}^{\xi\top} \mathbf{U}_\sigma^+ \mathbf{X}] \\ & - \sum_{\sigma} \widehat{\partial \partial^{++}} a_\sigma [\mathbf{X}^\top \mathbf{D}^\sigma \mathbf{A} \mathbf{D}^\sigma \nabla_\xi \mathbf{X} + \mathbf{X}^\top \mathbf{D}^\sigma \mathbf{A}^\xi \mathbf{D}^\sigma \mathbf{X}] \\ & - \sum_{\sigma} \widehat{\nabla_\xi} a_\sigma [\mathbf{X}^\top \mathbf{U}_\sigma^+ \mathbf{A} \mathbf{U}_\sigma^+ \mathbf{X} + \widehat{\partial \partial^{++}} e_{\mathbf{x},\sigma}^{\text{sl}}] - \sum_{\sigma} \widehat{\nabla_\xi} e_{\mathbf{x},\sigma}^{\text{sl}} \widehat{\partial \partial^{++}} a_\sigma \\ & -2 \sum_{\sigma} \widehat{\nabla_\xi \partial^+} a_\sigma [\mathbf{X}^\top \mathbf{D}^\sigma \mathbf{A} \mathbf{U}_\sigma^+ \mathbf{X} + \widehat{\partial^+} e_{\mathbf{x},\sigma}^{\text{sl}}] -2 \sum_{\sigma} \widehat{\nabla_\xi \partial^+} e_{\mathbf{x},\sigma}^{\text{sl}} \widehat{\partial^+} a_\sigma \\ & - \sum_{\sigma} \widehat{\nabla_\xi \partial \partial^{++}} a_\sigma \left[\frac{1}{2} \mathbf{X}^\top \mathbf{D}^\sigma \mathbf{A} \mathbf{D}^\sigma \mathbf{X} + e_{\mathbf{x},\sigma}^{\text{sl}} \right] \\ & + \sum_{\sigma} [1 - a_\sigma] \widehat{\nabla_\xi \partial \partial^{++}} e_{\mathbf{x},\sigma}^{\text{sl}} + \widehat{\nabla_\xi \partial \partial^{++}} e_{\mathbf{c}}^{\text{sl}}. \end{aligned} \quad (3.61)$$

From this equation, the GH case is formally recovered by setting the LMF to a constant value ($a_\sigma = \text{const.}$), which zeros out all LMF derivative terms leaving only the first and last line of the RHS of eq. 3.61. Just like the antisymmetric contracted hyper-kernel, the antisymmetric contracted kernel gradients have a much simpler form than their symmetric

counterparts; they read^[212]

$$\begin{aligned} & \frac{1}{2} \sum_{\mu\nu\sigma\kappa\lambda\sigma'} f_{-\mu\nu\sigma\kappa\lambda\sigma'}^{(\xi)} U_{\mu\nu\sigma}^- U_{\kappa\lambda\sigma'}^- \\ &= - \sum_{\sigma} \widehat{\nabla}_{\xi} a_{\sigma} \mathbf{X}^{\top} \mathbf{U}_{\sigma}^- \mathbf{A} \mathbf{U}_{\sigma}^- \mathbf{X} - 2 \sum_{\sigma} a_{\sigma} [\mathbf{X}^{\top} \mathbf{U}_{\sigma}^- \mathbf{A} \mathbf{U}_{\sigma}^- \nabla_{\xi} \mathbf{X} + \mathbf{X}^{\top} \mathbf{U}_{\sigma}^- \mathbf{A}^{\xi} \mathbf{U}_{\sigma}^- \mathbf{X}] . \end{aligned} \quad (3.62)$$

The first term of this equation vanishes for the GH case due to multiplication with a LMF derivative. The second term does, however, remain also for the GH case. Note however, that in the work by Furche and Ahlrichs^[35] this term it is not written as an additional kernel gradient but instead included in a matrix Γ that collects all four-center two-electron contributions. This also holds for the equivalent symmetric contracted kernel gradient term (first line of the RHS of eq. 3.61).

For the LH potential gradients contracted with the relaxed one-particle difference density matrix \mathbf{P}^{σ} , the formalism is completely analogous. Proceeding from the LH potential^[234] given in Appendix A.2 the application of the gradient operator and contraction with \mathbf{P}^{σ} yields^[212]

$$\begin{aligned} & \sum_{\mu\nu\sigma} V_{\mu\nu\sigma}^{xc(\xi)} P_{\mu\nu\sigma} \\ &= - \sum_{\sigma} a_{\sigma} \cdot [\mathbf{X}^{\top} \mathbf{D}^{\sigma} \mathbf{A} \mathbf{P}^{\sigma} \nabla_{\xi} \mathbf{X} + \nabla_{\xi} \mathbf{X}^{\top} \mathbf{D}^{\sigma} \mathbf{A} \mathbf{P}^{\sigma} \mathbf{X} + \mathbf{X}^{\top} \mathbf{D}^{\sigma} \mathbf{A}^{\xi} \mathbf{P}^{\sigma} \mathbf{X} + \mathbf{X}^{\top} \mathbf{D}^{\sigma} \mathbf{A}^{\xi \top} \mathbf{P}^{\sigma} \mathbf{X}] \\ & \quad - \sum_{\sigma} \widehat{\partial}^P a_{\sigma} \cdot [\mathbf{X}^{\top} \mathbf{D}^{\sigma} \mathbf{A} \mathbf{D}^{\sigma} \nabla_{\xi} \mathbf{X} + \mathbf{X}^{\top} \mathbf{D}^{\sigma} \mathbf{A}' \mathbf{D}^{\sigma} \mathbf{X}] \\ & \quad - \sum_{\sigma} \nabla_{\xi} a_{\sigma} \cdot [\mathbf{X}^{\top} \mathbf{D}^{\sigma} \mathbf{A} \mathbf{P}^{\sigma} \mathbf{X} + \widehat{\partial}^P e_{\mathbf{x},\sigma}^{\text{sl}}] - \sum_{\sigma} \widehat{\partial}^P a_{\sigma} \cdot \nabla_{\xi} e_{\mathbf{x},\sigma}^{\text{sl}} \\ & \quad - \sum_{\sigma} \widehat{\nabla}_{\xi} \widehat{\partial}^P a_{\sigma} \cdot \left[\frac{1}{2} \mathbf{X}^{\top} \mathbf{D}^{\sigma} \mathbf{A} \mathbf{D}^{\sigma} \mathbf{X} + e_{\mathbf{x},\sigma}^{\text{sl}} \right] \\ & \quad + \sum_{\sigma} [1 - a_{\sigma}] \cdot \widehat{\nabla}_{\xi} \widehat{\partial}^P e_{\mathbf{x},\sigma}^{\text{sl}} + \widehat{\nabla}_{\xi} \widehat{\partial}^P e_{\mathbf{c}}^{\text{sl}} , \end{aligned} \quad (3.63)$$

where the operators $\widehat{\partial}^P$ and $\widehat{\nabla}_{\xi} \widehat{\partial}^P$ are defined analogous to those given in eq. 3.52b and eq. 3.60a, respectively, but using \mathbf{P}^{σ} instead of \mathbf{U}_{σ}^+ .

4 Implementation

This chapter describes the implementation of ES gradients for LHs in the **egrad** program of the quantum chemical software package TURBOMOLE.^[36,37] The implementation is included in the official 7.5 version released in 2020.^[36] First, a brief review of the existing program structure of TURBOMOLE, the **egrad** program, and the LH specific software infrastructure is given. Next, the details of the new implementation are presented and connected challenges are discussed. In the technical evaluation, it is explained how the correctness of the implementation was ensured and the performance of the implementation is analyzed. Finally, the influence of the current-density response on the ES gradients is assessed to judge the validity of its neglect in the present implementation. The second half of Section 4.3.2 (starting from the second paragraph) and Section 4.3.3 are reproduced (adapted) and reprinted with permission from ref. 212 [R. Grotjahn, F. Furche, M. Kaupp, *J. Chem. Theory Comput.* **2019**, *15*, 5508]. Copyright 2019 American Chemical Society.

4.1 Existing Program Structure

4.1.1 The Software Package TURBOMOLE

The development of TURBOMOLE dates back to 1987, where Häser and Ahlrichs initiated the project^[250] intending to deliver a quantum chemical program with industry-standard robustness and efficiency.^[37] Starting with HF and MP2, numerous methods were added over time to the package such as CC2, KS-DFT, and LR-TDDFT. The different functionalities were added in the form of separate programs and scripts. For this work, the most relevant programs for GS calculations are the **dscf** program, which facilitates HF and KS-DFT calculations, and the **grad** program, which features gradient calculations as well as the **ridft** and **rdgrad** programs, which do the same within the RI approximation. For ES calculations, the **escf** program is used for LR-TDDFT energy, oscillator strength, and polarizability calculations, and the **egrad** program facilitates the calculation of ES gradients and some other ES properties. For structure optimizations, the script **jobex** can be used to perform subsequent runs of one of the energy programs,

one of the gradient programs, and a program for approximate Hessians and structural displacements (**statpt**) until convergence w.r.t. to a given criterium (typically the gradient norm **gcart**) is reached. The stationary points may then be further characterized by calculating the Hessian matrix, which can be done via **aoforce** for GS stationary points (excluding LH functionals) or via the script **NumForce** for both GS and ES stationary points. This script performs gradient calculations (either via **grad**/**rdgrad** or **egrad**) for a set of displaced coordinates (in C_1 symmetry) to calculate the Hessian as a numerical first derivative of the gradients. Accurate gradient calculations are important here to avoid numerical noise.

4.1.2 The **egrad** Program

The **egrad** program was developed by Furche and Ahlrichs in 2002 and originally contained their implementation of LR-TDDFT ES gradients for (semi)local and global hybrid XC functionals.^[35] Other features like non-adiabatic coupling matrix elements^[251] or polarizability derivatives^[252] were added later on as they require many of the steps and routines already available from the ES gradients implementation. As these are not relevant to this work, they are disregarded in the following explanation of the program structure.

In Figure 4.1, a simplified overview of the main routines of the **egrad** program is given. In addition, the most important matrices from the Z vector equation (eq. 3.20) and the final ES gradients equation (eq. 3.23) are given. It is assumed that a KS-DFT calculation was performed with either **dscf** or **ridft** so that the GS density matrix **D** is readily available from the MOs stored on disk. After an input processing section (not shown in Figure 4.1), the routine **respon** is called. The general purpose of this routine is to find the lowest eigenvalues and eigenvectors of a given matrix using the Davidson algorithm.^[253] This first call of **respon** serves to solve Casida's equations (eq. 2.143), yielding the excitation vectors ($\mathbf{U}^\pm = (\mathbf{X} \pm \mathbf{Y})$) and excitation energies Ω . Solving Casida's equation involves setting up the matrix-vector product $(\mathbf{A} \pm \mathbf{B})(\mathbf{X} \pm \mathbf{Y})$ which is done in the subroutine **mvproduct**. First, it transforms the excitation vector obtained in the previous iteration (or as a start guess) from the MO to the AO basis (**tramocao**), calculates the Coulombic contributions in **colrsp** and all XC kernel contributions in **df2nd**, and finally back transforms the result to the MO basis (**tracaomo**). For GHs, additional routines handle the analytical EXX evaluation (not shown). The EXX contributions featured by LHs are accounted for as part of the XC kernel in **df2nd**. Depending on the DFT level, i.e. the rung of the functional, the appropriate subroutine is called. The corresponding

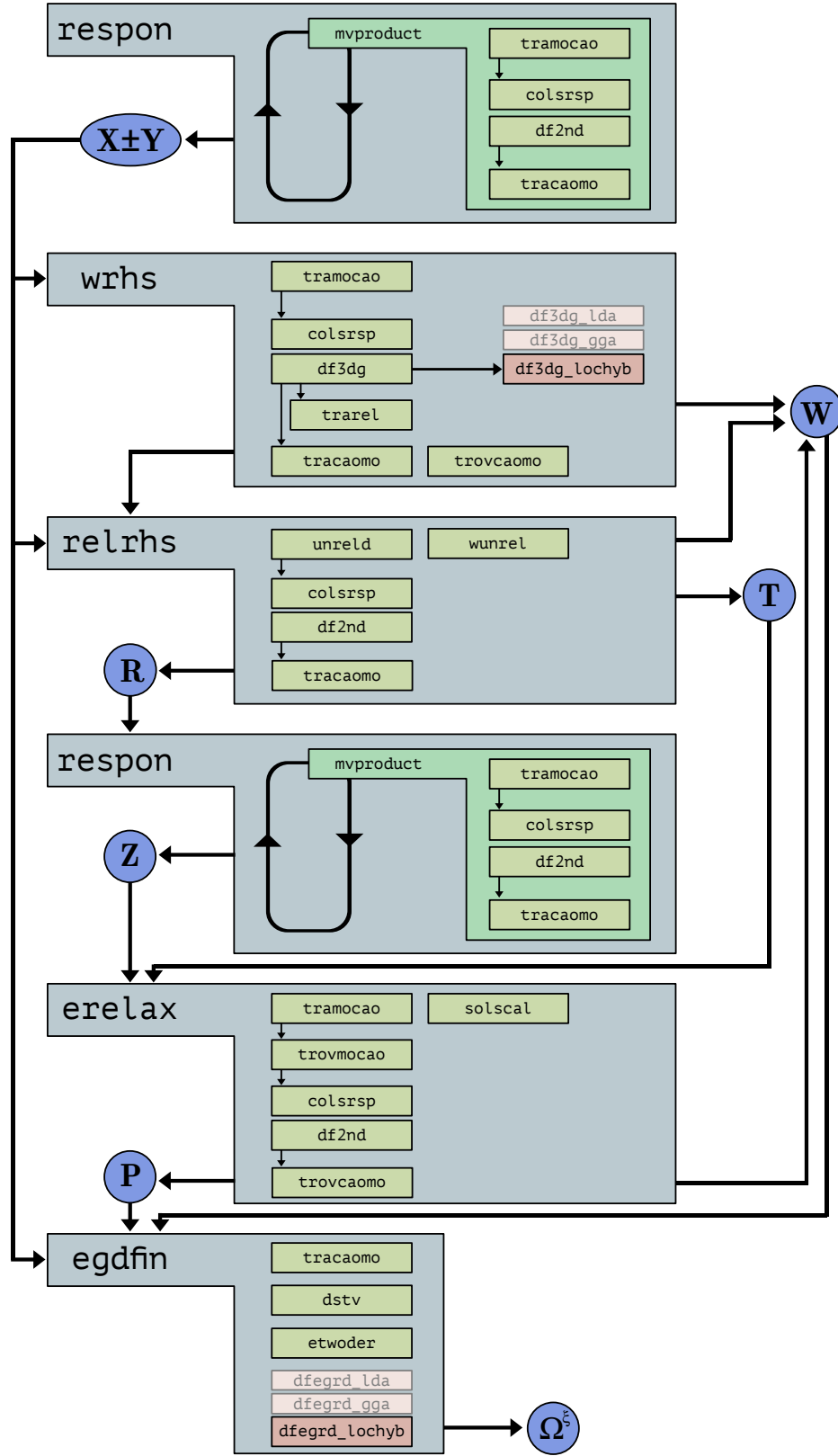


Figure 4.1: Simplified scheme of the **egrad** program and its main routines. Routines in dark red boxes were added as part of this work.

LH routine has been implemented by Maier as part of the LR-TDDFT excitation energy implementation in the `escf` program that uses the same routines.^[23] Only one of the excitation vectors that corresponds to the state of interest is needed in subsequent routines but if this state is not the lowest ES in a given irreducible representation, all lower excitation vectors will have to be calculated initially to access the state of interest. The next step is setting up the RHS \mathbf{R} (eq. 3.21) of the \mathbf{Z} vector equation (eq. 3.20). Except for the contribution $H_{ia\sigma}^+[\mathbf{T}]$, which is calculated separately in `relrhs`, this is done in `whrs`. This includes the calculation of the XC hyper-kernel contributions given by eq. 3.61 and 3.62 for the LH case. The kernel and hyper-kernel contributions are obtained in `df3dg`, which calls either one of the routines `df3dg_*` depending on the chosen XC functional (red boxes in Figure 4.1). The functionality of the new `df3dg_lochyb` routine is described in detail in Section 4.2. As side products, some of the blocks of the energy-weighted difference density matrix \mathbf{W} as well as the unrelaxed difference density matrix \mathbf{T} are obtained in the routines `wrhs` and `relrhs` and stored on disk for later usage. Subsequently, the RHS \mathbf{R} is passed to the `respon` routine that now serves as a solver for the \mathbf{Z} vector equation. After convergence, \mathbf{Z} is passed to `erelax` where it is added to \mathbf{T} to form the relaxed one-particle difference density matrix \mathbf{P} . Moreover, the remaining parts of \mathbf{W} are calculated, in particular the contribution $H_{ij\sigma}^+[\mathbf{P}]$ which requires another call to `colrsp` and `df2nd` for the linear-transformations defined in eq. 3.13a-b. Now, all matrices required for the final evaluation of ES gradients are available and passed to the `egdfin` routine or are read from disk. The one-electron contributions from the final ES gradients expression (eq. 3.23) are calculated in `dstv`, while the Coulomb-like two-electron parts are obtained via `etwoder` for the case of a RI-J calculation^[39] and are otherwise obtained via a separate routine (not shown). In a last step, the XC potential and kernel contributions to the ES gradients are calculated in either one of the routines `dfegrd_*` depending on the chosen XC functional (red boxes in Figure 4.1). The new `dfegrd_lochyb` routine is described in detail in Section 4.2.

To simplify the above explanations, the calculation of the GS gradients has been omitted. They are calculated on the fly using the respective GS density matrices and are added to the gradients of the excitation energy (loosely referred to "ES gradients" above) to yield the true ES gradients. After some minor finalizing steps, the ES gradients are written to the `gradient` file for subsequent usage by other programs such as those called by `jobex` as part of a structure optimization.

4.1.3 Local Hybrid Specific Software Infrastructure

On account of previous implementations of LH SCF energies in `ridft`,^[234] GS gradients in `rdgrad`,^[47] and LR-TDDFT excitation energies in `escf`,^[23] several LH specific routines required for the calculation of ES gradients are already available. In particular, the calculation of the \mathbf{A} and \mathbf{A}^ξ matrices required for the seminumerical integration scheme has been implemented in routines named `a_matrix` and `a_matrices`, respectively. Routines for the calculation of matrix-vector products and (contracted) semilocal quantities \mathcal{Q} named `ondes_ks` and a general matrix-vector multiplication routine `onval_1` are also available.

Partial derivatives of various LMFs and typically used (semi)local exchange and correlation energy densities are already implemented up to second derivatives and accessed via the routines `lmf_u2` and `fdiff_u2`. Extension to third partial derivatives is straightforward and can be assisted by computer algebra systems and code generation for more intricate derivatives. Note that these partial derivatives alone do not constitute the XC potential, contracted kernel, or contracted hyper-kernel matrix elements. It is required to appropriately combine the various terms derived from the product rule of differentiation and multiply with the contracted transition density matrix quantities if applicable. For the existing SCF and LR-TDDFT implementations, the routines `lochyb_u1` and `lochyb_u2` handle these steps. The resulting contributions are stored on a variable array named `oper` for the (semi)local parts and `adx_s/as` for the non-local contributions. Their addition to the KS matrix (SCF, `ridft`) or the $(\mathbf{A} \pm \mathbf{B})(\mathbf{X} \pm \mathbf{Y})$ matrix-vector product (LR-TDDFT, `escf`) is handled by the routine `onf_k` for the (semi)local parts and by `onfx_1/1as` for the non-local parts. In `onf_k`, the density matrix derivatives of the quantities $\mathcal{Q} \in \mathbb{Q}^a$ are multiplied with the respective contributions stored previously on `oper`, the summation over grid points of the current grid batch is performed, and the result is put on the global KS matrix or the $(\mathbf{A} \pm \mathbf{B})(\mathbf{X} \pm \mathbf{Y})$ matrix-vector product. In the case of GS gradients (`rdgrad`), a similar routine `ongrd_k` handles the multiplication of the values stored on `oper` with the spatial derivatives of the quantities $\mathcal{Q} \in \mathbb{Q}^b$, summation over basis functions and grid points, and writing to the gradient vector.

^aConsider the basis function pairs $X_\mu X_\nu$ for $\mathcal{Q} = \rho$ as an example.

^bConsider the basis function pairs $X_\mu \nabla X_\nu$ for $\mathcal{Q} = \rho$ as an example.

```

subroutine df3dg_lochyb
  for n = 1 to Ng do
    call funct           ▷ Evaluate basis function vector X
    call ondes_ks         ▷ Perform matrix-vector multiplication  $\mathbf{B}^\sigma = \mathbf{D}^\sigma \mathbf{X}$ 
                        ▷ Determine GS quantities  $\mathcal{Q}$ 
    call lmf_u3           ▷ Evaluate LMF derivatives
    call fdiff_u3         ▷ Evaluate (semi)local energy density derivatives
    call a_matrix         ▷ Calculate A Matrix
    call onval_1          ▷ Perform matrix-vector multiplication  $\mathbf{G}^\sigma = \mathbf{A}\mathbf{B}^\sigma$ 
    for i = 1 to Nexi do (Loop over Excitations)
      call ondes_ks/2as   ▷ Perform matrix-vector multiplication  $\mathbf{B}_\sigma^\pm = \mathbf{U}_\sigma^\pm \mathbf{X}$ 
                        ▷ Determine ES quantities  $\mathcal{Q}^\pm$ 
      call onval_1        ▷ Perform matrix-vector multiplication  $\mathbf{G}_\sigma^\pm = \mathbf{A}\mathbf{B}_\sigma^\pm$ 
      call lochyb_u3       ▷ Calculate non-local parts  $\mathbf{G}_{\sigma, \text{nl}}^\pm$ 
                        ▷ Calculate (semi)local parts  $\mathbf{G}_{\sigma, \text{sl}}^\pm$ 
      call onfx_1/1as     ▷ Finish calculation of non-local parts
      call onf_k/kas_rg   ▷ Finish calculation of (semi)local parts
    end
  end
end
end subroutine

```

Algorithm 4.1: Simplified pseudocode and explanations for the new subroutine `df3dg_lochyb` in TURBOMOLE’s `egrad` program.

4.2 Implementation of ES Gradients for Local Hybrids

4.2.1 Implementation of the Contracted LH Hyper-Kernel

The implementation of the contracted LH hyper-kernel can be broken down into the same basic steps as required for the contracted LH kernel implemented in `df2nd_lochyb`. The new routine is called `df3dg_lochyb` and presented in Algorithm 4.1. It starts with a loop over grid points in which all other routines are called. In practice, this loop is organized as a loop over batches of grid points. These batches may be distributed over multiple CPU cores by a parallelization wrapper-routine (not shown). In a first step, the basis function vector \mathbf{X} is calculated (`funct`) as well as its derivatives ($\nabla \mathbf{X}$, $\nabla^T \nabla \mathbf{X}$). Then, \mathbf{X} is contracted with the GS density matrix \mathbf{D}^σ to yield the \mathbf{B} vector (`ondes_ks`, cf. also ref. 67)

$$\mathbf{B}^\sigma = \mathbf{D}^\sigma \mathbf{X}. \quad (4.1)$$

In the same routine, the basis function vector and its derivatives are used to evaluate the (semi)local quantities $\mathcal{Q} \in \mathbb{Q}$. The results are used in `lmf_3` and `fdiff_3` to determine the partial derivatives of the LMF and X/C energy densities up to third derivatives. While

these derivatives are easily obtained for simple quantities like the t-LMF, computer algebra and code generation were used for more intricate cases such as the s-LMF or the B95 correlation energy density. Next, the \mathbf{A} matrix is calculated in `a_matrix` and multiplied with the \mathbf{B}^σ vector in `onval_1` to yield the \mathbf{G}^σ vector (cf. also ref. 67)

$$\mathbf{G}^\sigma = \mathbf{A}\mathbf{B}^\sigma. \quad (4.2)$$

The setup and storing of the \mathbf{B}^σ and \mathbf{G}^σ serves to calculate many of the EXX related terms from the contracted hyper-kernel as given in eq. 3.53. For example, the contribution $X_\mu(\mathbf{A}\mathbf{D}^\sigma\mathbf{X})_\nu$ from the second line of the RHS of eq. 3.53 can be formed by multiplying the μ -th element of the basis function vector \mathbf{X} with the ν -th element of the \mathbf{G}^σ vector, and the EXX energy density $\frac{1}{2}\mathbf{X}^\top\mathbf{D}^\sigma\mathbf{A}\mathbf{D}^\sigma\mathbf{X}$ as required in the fifth line of the RHS of eq. 3.53 is obtained as the dot product of \mathbf{B}^σ and \mathbf{G}^σ . Next, a loop over excitation vectors is entered. However, since `egrad` handles only the state of interest, this loop is usually terminated after one iteration. An exception to this occurs if symmetry is used and the state of interest is described by a degenerate irreducible representation, which is internally handled via multiple excitation vectors. Within this loop, the same steps as for the GS density matrix are performed using the transition density matrices \mathbf{U}_σ^\pm . Instead of the GS quantities \mathcal{Q} , `ondes_ks` now calculates the analogous transition density quantities

$$Q^\pm = \sum_{\kappa\lambda\sigma'} \frac{\partial Q}{\partial D_{\kappa\lambda}^{\sigma'}} U_{\kappa\lambda\sigma'}^\pm \quad (4.3)$$

as occurring in the definitions of the contracted semilocal potential operators (eq. 3.52b-d and eq. A.9). All intermediate quantities calculated so far are passed to the `lochyb_u3` routine that handles the combination of partial derivatives, (semi)local quantities $\mathcal{Q}^{(\pm)}$, $\mathbf{B}_\sigma^{(\pm)}$ vectors and $\mathbf{G}_\sigma^{(\pm)}$ vectors as expressed by eq. 3.53-3.54. For the symmetric non-local part, the vector

$$\mathbf{G}_{\sigma,\text{nl}}^+ = -2\widehat{\partial}^+ a_\sigma \mathbf{G}_\sigma^+ - \widehat{\partial}\widehat{\partial}^{++} a_\sigma \mathbf{G}_\sigma \quad (4.4)$$

is constructed and stored on the variable `gadx_s`, while for the antisymmetric part, there are no non-local contributions to the contracted hyper-kernel. For the (semi)local part, the numerous terms generated by the (contracted) semilocal potential operators are collected on different vectors depending on the required basis function pair

$$\mathbf{G}_{\sigma,\text{sl}}^\pm = \mathbf{G}_{\sigma,\text{xx}}^\pm + \mathbf{G}_{\sigma,\text{dxx}}^\pm + \mathbf{G}_{\sigma,\text{dxdx}}^\pm, \quad (4.5)$$

where $\mathbf{G}_{\sigma,xx}^{\pm}$ is intended for multiplication with the basis function pair $X_{\mu}X_{\nu}$, $\mathbf{G}_{\sigma,dxx}^{\pm}$ with $\nabla^T(X_{\mu}X_{\nu})$, and $\mathbf{G}_{\sigma,dxdx}^{\pm}$ with $\nabla^T X_{\mu} \nabla X_{\nu}$. These contributions are collectively stored on an array called **goper** for the symmetric part and **goper_as** for the antisymmetric part. The calculation of the kernel contributions to the $(\mathbf{A} \pm \mathbf{B})(\mathbf{X} \pm \mathbf{Y})$ matrix-vector product also required in the superordinated **wrhs** routine (cf. Figure 4.1), is handled on the fly in **lochyb_u3** using the same code as in **lochyb_u2** and the results are stored on **adx_s/as** and **oper**. Finally, the non-local contributions stored on **gadx_s** are passed to **onfx_1**, where they are multiplied with the basis function vector \mathbf{X} . A summation over all grid points of the grid batch is performed and the results are written to the final contracted hyper-kernel. Similarly, the (semi)local contributions stored on **goper** and **goper_as** are processed by **onf_k** using the appropriate basis function pair for each contribution.

4.2.2 Implementation of the LH Potential and Kernel Gradients

The implementation of the LH potential gradients (eq. 3.63) and the (anti)symmetric kernel gradients (eq. 3.61-3.62) is realized in the routine **dfegrd_lochyb** which is called by **egdfin** as the last step of the ES gradients calculation in **egrad** (cf. Figure 4.1). A simplified overview of the routine is given in Algorithm 4.2. Many of the steps are similar to those explained for the **df3dg_lochyb** routine in Section 4.2.1 and not discussed again. Note that an additional call to **ondes_ks** is invoked passing the relaxed one-particle difference density matrix \mathbf{P} instead of the GS density matrix to obtain the respective \mathbf{B}_{σ}^P vector and contracted quantities \mathcal{Q}^P . Additionally, a derivative analog of the \mathbf{B} vector is calculated (cf. also ref. 47)

$$\mathbf{B}_{\sigma}^{\xi} = \mathbf{D}^{\sigma} \nabla \mathbf{X}. \quad (4.6)$$

The calculation of the \mathbf{A} and \mathbf{A}^{ξ} matrices is handled by the routine **a_matrices** that directly contracts these matrices with each of the \mathbf{B} vectors yielding the respective \mathbf{G} and \mathbf{G}^{ξ} vectors (multiplications yielding \mathbf{G}^{ξ} are not shown in Algorithm 4.2).^[47] All terms are combined in **lochyb_gradfx_u** according to eq. 3.61-3.62 for the kernel gradients and in **lochyb_gradvp_u** according to eq. 3.63 for the potential gradients. Similar to the **onf_k** routine used in **df3dg_lochyb**, the routine **ongrd_k** handles the processing of the (semi)local contributions, performs the final grid summation and writes the contributions to the gradient vector. The non-local contributions $\mathbf{G}_{\sigma,nl}$, $\mathbf{G}_{\sigma,nl}^{\pm}$, and $\mathbf{G}_{\sigma,nl}^P$ are multiplied with the appropriate \mathbf{B}^{ξ} vectors in **get_hfx1_rg**, while **get_hfx2_rg**, is used to multiply $\mathbf{G}_{\sigma,nl}^{\xi}$, $\mathbf{G}_{\sigma,nl}^{\pm\xi}$, and $\mathbf{G}_{\sigma,nl}^{P\xi}$ with the appropriate \mathbf{B} vectors (cf. also ref. 47). Derivatives of the quadrature weights (cf. eq. 3.42) are calculated at several points on the fly. Some of the remaining contributions are added in a final step using the routine **wmgrd**.

```
subroutine dfegrd_lochyb
```

```
  for  $n = 1$  to  $N_g$  do
```

```
    call funct
```

▷ Evaluate basis function vector \mathbf{X}

```
    call ondes_ks
```

▷ Perform matrix-vector multiplication $\mathbf{B}^\sigma = \mathbf{D}^\sigma \mathbf{X}$

▷ Determine GS quantities \mathcal{Q}

```
    call ondes_ks
```

▷ Perform matrix-vector multiplication $\mathbf{B}_\sigma^P = \mathbf{P}^\sigma \mathbf{X}$

▷ Determine P contracted quantities \mathcal{Q}^P

```
    call lmf_u3
```

▷ Evaluate LMF derivatives

```
    call fdiff_u3
```

▷ Evaluate (semi)local energy density derivatives

```
    for  $i = 1$  to  $N_{\text{exi}}$  do (Loop over Excitations)
```

```
      call ondes_ks/2as
```

▷ Perform matrix-vector multiplication $\mathbf{B}_\sigma^\pm = \mathbf{U}_\sigma^\pm \mathbf{X}$

▷ Determine ES quantities \mathcal{Q}^\pm

```
      call a_matrices
```

▷ Calculate \mathbf{A} and \mathbf{A}^ξ Matrix

▷ Perform matrix-vector multiplication $\mathbf{G}^\sigma = \mathbf{A} \mathbf{B}^\sigma$

▷ Perform matrix-vector multiplication $\mathbf{G}_\sigma^\pm = \mathbf{A} \mathbf{B}_\sigma^\pm$

▷ Perform matrix-vector multiplication $\mathbf{G}_\sigma^P = \mathbf{A} \mathbf{B}_\sigma^P$

```
      call lochyb_gradfx_u
```

▷ Calculate non-local kernel parts $\mathbf{G}_{\sigma,\text{nl}}^{(\pm)}$, $\mathbf{G}_{\sigma,\text{nl}}^{(\pm)\xi}$

▷ Calculate (semi)local kernel parts $\mathbf{G}_{\sigma,\text{sl}}^\pm$

```
      call ongrd_k
```

▷ Finish calculation of (semi)local parts $\mathbf{G}_{\sigma,\text{sl}}^\pm$

```
      call get_hfx1_rg
```

▷ Finish calculation of non-local parts $\mathbf{G}_{\sigma,\text{nl}}^{(\pm)}$

```
      call get_hfx2_rg
```

▷ Finish calculation of non-local parts $\mathbf{G}_{\sigma,\text{nl}}^{(\pm)\xi}$

```
    end
```

```
    call lochyb_gradvp_u
```

▷ Calculate non-local potential parts $\mathbf{G}_{\sigma,\text{nl}}^P$, $\mathbf{G}_{\sigma,\text{nl}}^{P,\xi}$

▷ Calculate (semi)local potential parts $\mathbf{G}_{\sigma,\text{sl}}^P$

```
    call ongrd_k
```

▷ Finish calculation of (semi)local parts $\mathbf{G}_{\sigma,\text{sl}}^P$

```
    call get_hfx1_rg
```

▷ Finish calculation of non-local parts $\mathbf{G}_{\sigma,\text{nl}}^P$

```
    call get_hfx2_rg
```

▷ Finish calculation of non-local parts $\mathbf{G}_{\sigma,\text{nl}}^{P,\xi}$

```
    call wmgrd
```

▷ Add weight derivatives

```
  end
```

```
end subroutine
```

Algorithm 4.2: Simplified pseudocode and explanations for the new subroutine `dfegrd_lochyb` in TURBOMOLE's `egrad` program.

4.3 Technical Evaluation

4.3.1 Numerical Validation

The intricate form of the contracted LH hyper-kernel, kernel gradients, and potential gradients makes their implementation very prone to man-made errors. To check the correctness of the implementation, the ES gradients calculated using `egrad` are compared to numerical gradients calculated using ES energies from `escf`. Importantly, such numerical

tests require that the ES energies from **escf** are correct, i.e. the LH XC kernel has been correctly implemented. This was verified by comparing static polarizabilities from LR-TDDFT calculations (**escf**) with numerical results obtained within a finite-field ansatz using an external electric field and GS energies calculated with **dscf** (cf. Section 6.3.2 for details). Numerical gradients can be calculated with finite-difference (FD) formulas for the first derivative using energies obtained at structures displaced along a Cartesian coordinate by a step size δ . The three-point formula

$$\left. \frac{\partial E(z)}{\partial z} \right|_{z=z_0} \approx \frac{E(z_0 + \delta) - E(z_0 - \delta)}{2\delta} + \mathcal{O}(\delta^2) \quad (4.7)$$

is commonly used for this purpose and gives reasonably accurate results with an error term quadratic in δ .^[254] Even better accuracy can be achieved using the five-point formula

$$\left. \frac{\partial E(z)}{\partial z} \right|_{z=z_0} \approx \frac{-E(z_0 + 2\delta) + 8E(z_0 + \delta) - 8E(z_0 - \delta) + E(z_0 - 2\delta)}{12\delta} + \mathcal{O}(\delta^4) \quad (4.8)$$

for which the error term is quartic in δ .^[254]

Test calculations using these FD formulas have been performed for various molecules, functionals, and excitation types (singlet, triplet, and closed-shell/open-shell unrestricted). As an illustrative example, results are presented here for the first singlet ES of the carbon monoxide (CO) molecule using the LH07t-SVWN functional. The def2-TZVP^[255] basis set was used and very strict convergence criteria were set for all calculation steps (GS energy convergence: **scfconv** 12, GS density matrix convergence: **denconv** 1d-10, excitation vector convergence: **rpaconv** 10). For the DFT part, very fine quadrature grids (**gridsize** 7, **radsize** 14) and tight numerical cutoffs were enabled using the **reference** keyword. The RI-J approximation and S- and P-junctions were not used. To judge the accuracy of the **egrad** gradients, two comparisons are made. On the one hand, GS gradients were calculated using the **grad** program to test the consistency of errors among GS and ES gradients. On the other hand, gradient calculations were repeated with the PBE0 functional using the standard analytical EXX implementation to ensure that the seminumerical implementation does not introduce any additional errors.

All results for energies and gradients are reported in Table 4.1. The deviation of the gradient components obtained with **grad** or **egrad** from those obtained using a three-point FD formula are on the order of 10^{-6} au. Although this is already a good agreement, it does not rule out the possibility of minor bugs in the implementation in parts that marginally contribute to the final gradients. However, when comparing to the results

Table 4.1: GS and ES energies for the CO molecules at different internuclear separations (top) and z -components of the GS and ES gradient for the oxygen atom (O) evaluated with different methods (see text) at $R = 2.000$ (bottom). All values in au.

$R(\text{C-O})$	LH07t-SVWN		PBE0	
	E_{GS}	E_{ES}	E_{GS}	E_{ES}
2.002	-112.934775540	-112.592270075	-113.219903624	-112.883241109
2.001	-112.934567601	-112.591867220	-113.219705174	-112.882849554
2.000	-112.934357634	-112.591462321	-113.219504708	-112.882455974
1.999	-112.934145631	-112.591055371	-113.219302219	-112.882060362
1.998	-112.933931586	-112.590646365	-113.219097700	-112.881662711
Method	$\frac{\partial E_{\text{GS}}}{\partial z_{\text{O}}}$	$\frac{\partial E_{\text{ES}}}{\partial z_{\text{O}}}$	$\frac{\partial E_{\text{GS}}}{\partial z_{\text{O}}}$	$\frac{\partial E_{\text{ES}}}{\partial z_{\text{O}}}$
FD-3 (eq. 4.7) ^a	-0.210984920	-0.405924226	-0.201477515	-0.394596092
FD-5 (eq. 4.8)	-0.210983741	-0.405923128	-0.201476337	-0.394595013
grad/ egrad	-0.210983776	-0.405923100	-0.201476335	-0.394594955
Deviation (FD-3)	$1.1 \cdot 10^{-6}$	$1.1 \cdot 10^{-6}$	$1.2 \cdot 10^{-6}$	$1.1 \cdot 10^{-6}$
Deviation (FD-5)	$-3.6 \cdot 10^{-8}$	$2.8 \cdot 10^{-8}$	$2.1 \cdot 10^{-9}$	$5.8 \cdot 10^{-8}$

^a Using a step size of 0.001 au.

obtained with the five-point FD formula, deviations drop by almost two orders of magnitude to about 10^{-8} au, which approaches the convergence settings chosen for the energy calculations. Considering that the errors are consistent among different programs (**grad/ egrad**) and different implementations (seminumerical/ analytical EXX), the correctness of the implementation can be considered as given.

4.3.2 Grid Dependence

For the numerical validation of the implementation presented above, very fine numerical quadrature grids were used for the seminumerical integration scheme. Due to the formal $N_{\text{g}} \cdot N_{\text{b}}^2$ scaling of the \mathbf{A} matrix evaluation, the grid size directly affects the time-critical step of the seminumerical scheme. For practical applications, it is therefore desirable to keep the grid size as small as tolerable with regard to accuracy. As a first assessment, the $1^1\text{A}''$ excited state of the HCN molecule is studied. It was optimized with the PBE0 functional using the new seminumerical implementation of EXX integrals as well as the standard analytical implementation for comparison. The def2-QZVPPD basis set^[256,257] was used and strict convergence criteria were applied (GS energy convergence: **scfconv** 10, GS density matrix convergence: **denconv** 1d-9, excitation vector convergence: **rpaconv** 7). The RI-J approximation^[39] was used to reduce the computational

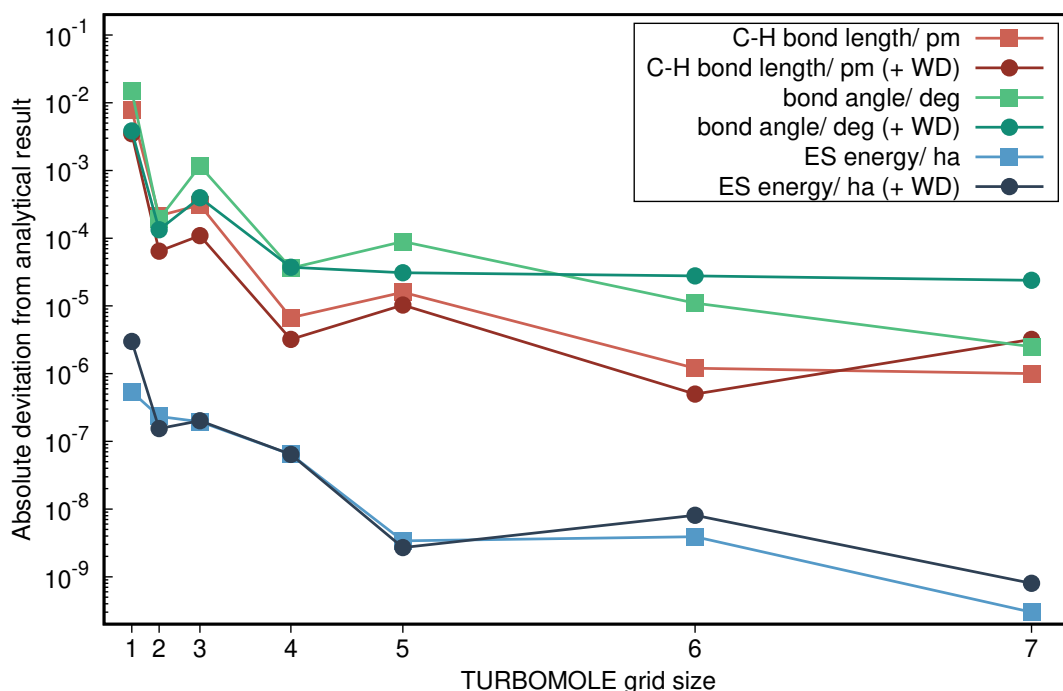


Figure 4.2: Deviation of seminumerical PBE0 results from the corresponding analytical results for the C–H bond length, the $\angle(\text{HCN})$ bond angle and the energy of the optimized $1^1\text{A}''$ excited state of HCN for different grid sizes. Underlying numerical data and total number of grid points are provided in Table A.3.

costs.^c The influence of including quadrature weight derivatives has also been studied. Deviations from the analytical results for TURBOMOLE grid sizes between 1 and 7 are plotted in Figure 4.2 and numerical data is provided in Table A.3. Note that the analytical PBE0 result were calculated using the same grid settings for the DFT part as for the seminumerical PBE0 results. Hence, the deviations do not reflect the total grid error but the additional grid error from the seminumerical EXX evaluation.^d Already for the smallest grid, errors are below 0.01 pm for the C–H bond length, below 0.1 deg for the bond angle, and below 10^{-5} ha for the ES energy. Inclusion of WDs has almost no influence on the absolute errors for energies, which is as expected since WDs affect the energy only indirectly via changes in the structures and these structural changes are minor. WDs help, however, to reach excellent accuracy already at small and medium-sized grids for the bond length and bond angle without adding much to the computational costs. Errors for TURBOMOLE grid sizes above 4 are extremely small. In fact, they are too small to be detected with sufficient accuracy compared to the reached convergence for

^cErrors from the RI-J approximation are grid independent and indirect changes in errors for the RI-J part via structural changes are negligible in this comparison.

^dA plot that reflects the total grid error is included in Appendix A.6 (Figure A.1).

the residual gradient vector norms, which is why the trends seen in Figure 4.2 for these low-error regimes are of no significance.

The above example indicates that the additional grid errors from the seminumerical EXX evaluation should be negligible even with the smallest grid. To confirm the generality of this observation, a broader test set of molecules and ESs has been considered. The test set includes several ESs of small molecules for which high-resolution experimental gas phase data was available. It was compiled by Furche and Ahlrichs^[35,39] and is also used to benchmark different XC functionals as part of this work (cf. Section 5.3.1, 5.4.1 and 5.5.1). To study the influence of ES parameters on the grid size, the ESs were optimized at the PBE0/ def2-QZVPPD level of theory, where either the new seminumerical EXX evaluation was used or the standard analytical EXX integration scheme. Two TURBO-MOLE grid settings were tested, i.e. the smallest grid size 1 as well as grid size 2 with diffuse 1 option for additional radial grid points further away from the nuclei. Reference values were obtained at grid size 5, diffuse 2 using the analytical EXX implementation. Convergence thresholds were the same as above. Deviations of ES structural parameters for the smaller grid sizes from the reference calculations are plotted in Figure 4.3 for those 25 parameters where deviations larger than 0.1 pm or 0.1 deg at grid size 1 were determined. The remaining 38 parameters evaluated for the test set showed smaller deviations already at grid size 1 and are not plotted (see Table A.4 for numerical data). While the deviation of the data points from the zero line in Figure 4.3 is related to the total grid error, differences between the conventional and seminumerical results at the same grid size (squares and crosses in Figure 4.3) reveal the additional error introduced by the seminumerical scheme.

No systematic over- or underestimation of structural parameters is observed when using smaller grids. For the small grid (red labels), several parameters show notable but small total absolute deviations of around 0.5 pm or 0.5 deg. Somewhat larger effects include a distinct 3.0 deg deviation for the out-of-plane dihedral angle in the $1^3A''$ state of CH_2S and a 1.8 pm deviation for the bond length in the $1^1\Sigma_u^+$ state of Mg_2 . These deviations have to be put into perspective since the potential energy surfaces of these states are very flat along the respective coordinates. Nonetheless, these cases expose the limitations of the small grid. However, even a moderate increase of the grid size (green labels) eliminates almost all deviations. Note that diffuse grids are of course only required for diffuse states (ESs with notable Rydberg character) and do not necessarily entail an increased number of grid points as a tuning of the radial mapping parameter is often sufficient.^[23] Errors introduced by the seminumerical scheme are mostly small with the largest deviation being

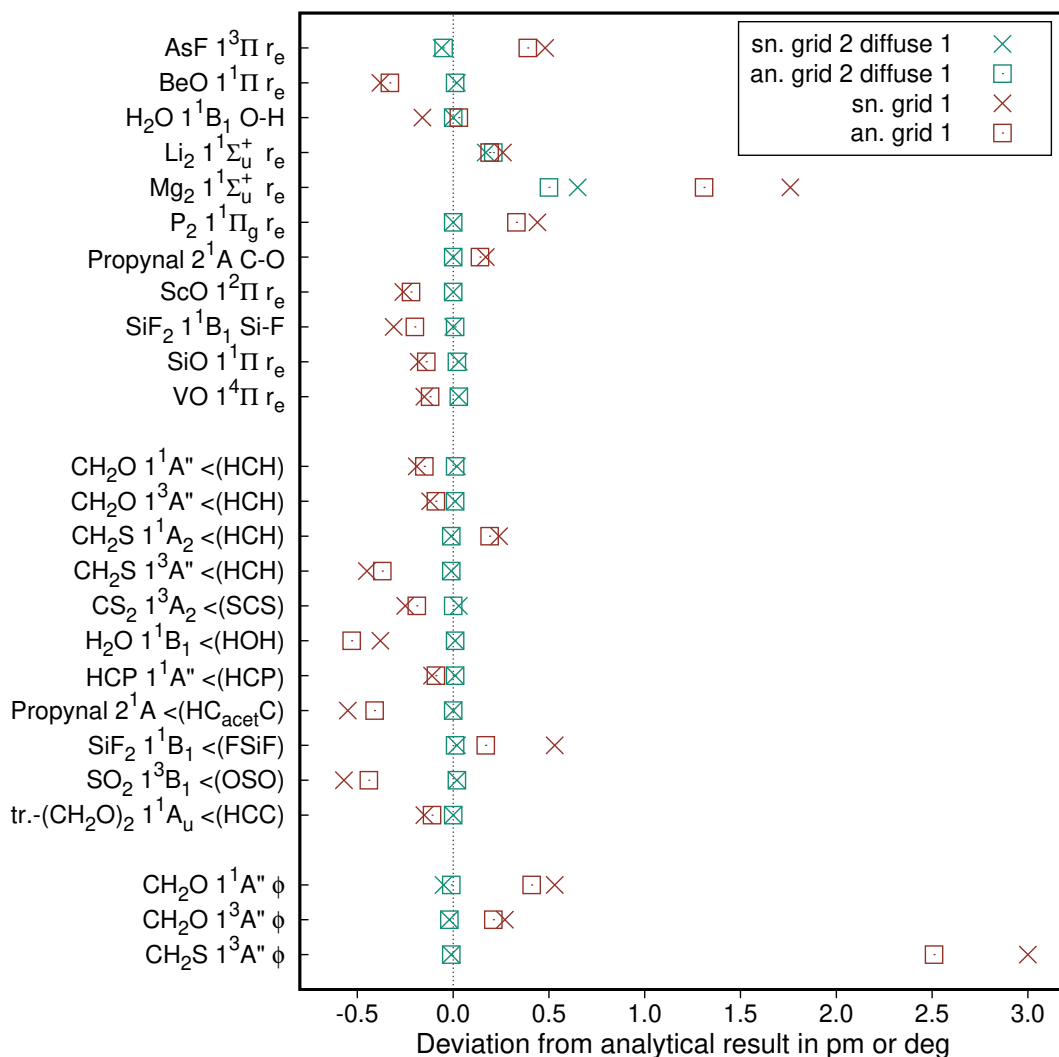


Figure 4.3: Dependence of the ES structures on the grid size for the analytical and the seminumerical implementation, respectively (PBE0/ def2-QZVPPD level). Datapoints indicate deviations for smaller grid sizes (see key) from analytical results obtained with a large diffuse grid (TURBOMOLE: grid size 5 diffuse 2). From a total of 63 parameters in the test set only those parameters with a deviation larger than 0.1 pm or 0.1 deg at grid size 1 (25 parameters) were plotted for clarity.

0.4 deg for the 1^1B_1 state of SiF₂ for the small grid (excluding here the two most severe absolute outliers). They are further reduced when switching to the medium-sized grid.

In conclusion, errors of the seminumerical scheme are well controlled and the choice of grid requires no particular additional care for LHs compared to standard DFT functionals. For most applications, the smallest grid (TURBOMOLE grid size 1) is expected to deliver sufficient accuracy. Potentially more demanding cases such as Rydberg states should be checked for grid convergence especially for the radial grid.

4.3.3 Neglect of the Current Density Response

As discussed in Section 3.2.2, the neglect of the current-density response for τ -dependent functionals considerably reduces the theoretical and computational complexity of the antisymmetric XC hyper-kernel and XC kernel-gradient terms. An ad-hoc test of the validity of this approximation can be performed for the diatomic molecules from the test set by Furche and Ahlrichs^[35,39] by scanning the potential energy curves of the ESs for their minima. This was done using the LH implementation of ES energies in **escf**, which fully considers the current-density response.^[23] Minimum bond lengths are then compared against those obtained from the gradient-based optimization using **egrad**. The results in Table 4.2 indicate that the effects of the current-density response are rather

Table 4.2: Effects of the current-density response on ES bond lengths (in pm) for diatomic molecules at the LH07t-SVWN/ def2-QZVPPD level of theory. Optimizations without inclusion of the current-density response ($r_e^{\text{no cur}}$) were performed using the new gradient implementation, while optimizations with inclusion of the current-density response (r_e^{cur}) were performed using a linear-search algorithm for ES single-point energies.

Mol.	State	k^a	$r_e^{\text{no cur}}$	r_e^{cur}	Δr_e	$\Delta r_e / r_e^{\text{cur}}$
AsF	1 $^3\Pi$	149	197.70	197.08	0.62	0.31%
BeH	1 $^2\Pi$	249	133.10	133.10	0.00	0.00%
BeO	1 $^1\Pi$	501	144.35	143.88	0.47	0.32%
BF	1 $^1\Pi$	673	130.68	130.33	0.35	0.27%
BH	1 $^1\Pi$	316	121.47	121.23	0.24	0.20%
CO	1 $^1\Pi$	996	122.91	122.62	0.29	0.24%
CO	1 $^3\Pi$	1334	119.94	119.80	0.14	0.12%
CuH	2 $^1\Sigma^+$	173	158.44	158.03	0.41	0.26%
Li ₂	1 $^1\Sigma_u^+$	13	313.20	307.64	5.56	1.81%
Mg ₂	1 $^1\Sigma_u^+$	17	323.08	325.82	-2.74	-0.84%
N ₂	1 $^1\Delta_u$	1074	127.38	127.27	0.11	0.09%
N ₂	1 $^1\Pi_g$	1291	121.16	121.06	0.10	0.09%
N ₂	1 $^1\Sigma_u^-$	1020	126.57	126.47	0.10	0.08%
N ₂	1 $^3\Pi_g$	1409	120.20	120.10	0.10	0.08%
NH	1 $^3\Pi$	561	104.42	104.21	0.21	0.20%
NO	1 $^2\Sigma^+$	2904	104.92	104.67	0.25	0.24%
P ₂	1 $^1\Pi_g$	374	198.37	198.23	0.14	0.07%
SiO	1 $^1\Pi$	513	160.17	159.91	0.26	0.16%
ScO	1 $^2\Pi$	520	168.33	168.19	0.14	0.08%
VO	1 $^4\Pi$	664	163.03	163.10	-0.07	-0.05%
MAE					0.62	0.28%
MAE* ^b					0.22	0.16%

^a ES force constants (in kg s^{-2}) from calculations without current-density response are given as an estimate of the steepness of the potential-energy curves.

^b Calculated excluding Li₂ and Mg₂.

small and in most cases on the order of 0.2 pm. A notable deviation of 5.6 pm (2%) is found for the $1^1\Sigma_+^u$ state of Li_2 and a -2.7 pm (-0.8%) deviation for the $1^1\Sigma_+^u$ state of Mg_2 . These deviations can be attributed to the flatness of the ES potential-energy surfaces (weak partial M-M bonds) in those two cases, where small changes in the energy can cause drastic changes in the minimum bond lengths. Moreover, the unoccupied orbitals involved in this excitation are comparatively diffuse. For VEEs of low-lying Rydberg states, it is known that the steep change of the LMF in the intermediate valence/asymptotic region of the molecule has a large impact.^[24] This is because the LMF controls the amount of locally admixed EXX, which predominantly affects Rydberg excitations. This explanation is supported by the results for the $1^1\Sigma_+^u$ state of Li_2 obtained with the mGGA functional TPSSh. While this functional is τ -dependent as well, optimized bond lengths including and neglecting the current-density response deviate by only 0.9 pm (305.6 pm vs. 304.7 pm). Overall, the neglect of the current-density response appears to be well justified for ES gradients with the exception of extremely weak (stretched) bonds in Rydberg ESs.

4.3.4 Timings

Computational Details

To analyze the efficiency of the new implementation, two scaling tests are performed. First, the scaling w.r.t. system size is determined and compared to that of the standard analytical implementation used for GHs. For this purpose, the lowest singlet ESs of conjugated all-*trans* polyene chains with an increasing number of carbon atoms are considered. These systems were previously studied for the LH implementation in `escf`.^[23] Limiting the increase of the system size to one dimension benefits the efficiency of the overlap prescreening used in the conventional analytical implementation of EXX integrals (cf. Section 2.1.4).^[23] While the choice of the smallest grid (TURBOMOLE grid size 1) avoids large prefactors for the seminumerical scheme, the use of the only medium-sized def2-TZVP basis set somewhat hinders to see the profits expected from the improved formal scaling w.r.t. basis set size of the seminumerical implementation. However, both choices seem realistic if calculations are envisaged for molecules with a hundred or more atoms, which is a typical field of application for (TD)DFT methods. Because the analytical implementation of EXX integrals uses a prescreening for non-overlapping basis function pairs, an S-junction-based prescreening was used for the seminumerical scheme as well, where the same threshold (`scftol`) is used and left at its default value ($10^{-(\text{scfconv}+1)}/(3 \cdot N_{\text{BF}})$). Thus, overall, the setup makes for a fair and realistic comparison.

As a second analysis, the scaling w.r.t. basis-set size was studied for the BODIPY molecule and its first singlet ES. The same settings as described above were used and calculations with various basis sets were performed including the STO-3G basis set,^[258] the Karlsruhe basis sets (def2-SV(P), def2-SVP, def2-SVPD, def2-TZVP, def2-TZVPP, def2-TZVPD, def2-QZVP, def2-QZVPD),^[255–257] the Dunning basis sets (cc-pVXZ, where X=D,T,Q),^[259] augmented Dunning basis sets (aug-cc-pVXZ, where X=D,T,Q),^[259,260] and the Jensen basis sets (pc-1, pc-2, pc-3).^[261,262]

For both setups, the LH07t-SVWN and PBE0 functional were used for (seminumerical) LH and (analytical) GH calculations, respectively. The RI-J approximation was used and standard convergence criteria were set (GS energy convergence: `scfconv` 9, GS density matrix convergence: `denconv` 1d-7, excitation vector convergence: `rpaconv` 5). In addition to timings for `egrad`, timings for the calculation of GS gradients (`rdgrad`) and ES energies (`escf`) are determined for comparison. Linear fits were determined on double-logarithmic scales using the number of primitive basis functions and the total wall time, which is virtually identical to the total CPU time with differences not exceeding 1 second for the largest systems.

Scaling w.r.t. System Size

The timings for the calculations on polyene chains obtained with the def2-TZVP basis set at grid size 1 are given in Table A.2 (Appendix A.5) and are plotted in Figure 4.4 along with linear equations for fits on the double-logarithmic scales. For both the seminumerical LH and the analytical GH implementation, the `rdgrad` program requires the least computation time followed by `escf` and `egrad`. This is as expected because a GS gradients calculation in `rdgrad` does not require an iterative procedure. An `escf` run requires one call to the iterative `respon` routine, whereas `egrad` requires two such iterative steps as well as additional steps for intermediate quantities and the final gradient step (cf. Section 4.1.2). For all system sizes, the seminumerical LH implementation is slower than the analytical GH implementation. This finding contradicts that from ref. 23, where the seminumerical `escf` implementation was found to be faster than the analytical implementation for all studied polyene chains. The reason for that is massive improvements in the analytical routines of the `escf` program in the more recent TURBOMOLE version used here. The introduction of nonorthonormal Krylov space methods^[263] and the RI-J approximation^[263] has enabled to reduce the computational cost for GH calculations considerably compared to that of the conventional implementation used before TURBOMOLE V7.2 and in the investigations by Maier *et al.*^[23] Also note, that the seminumerical

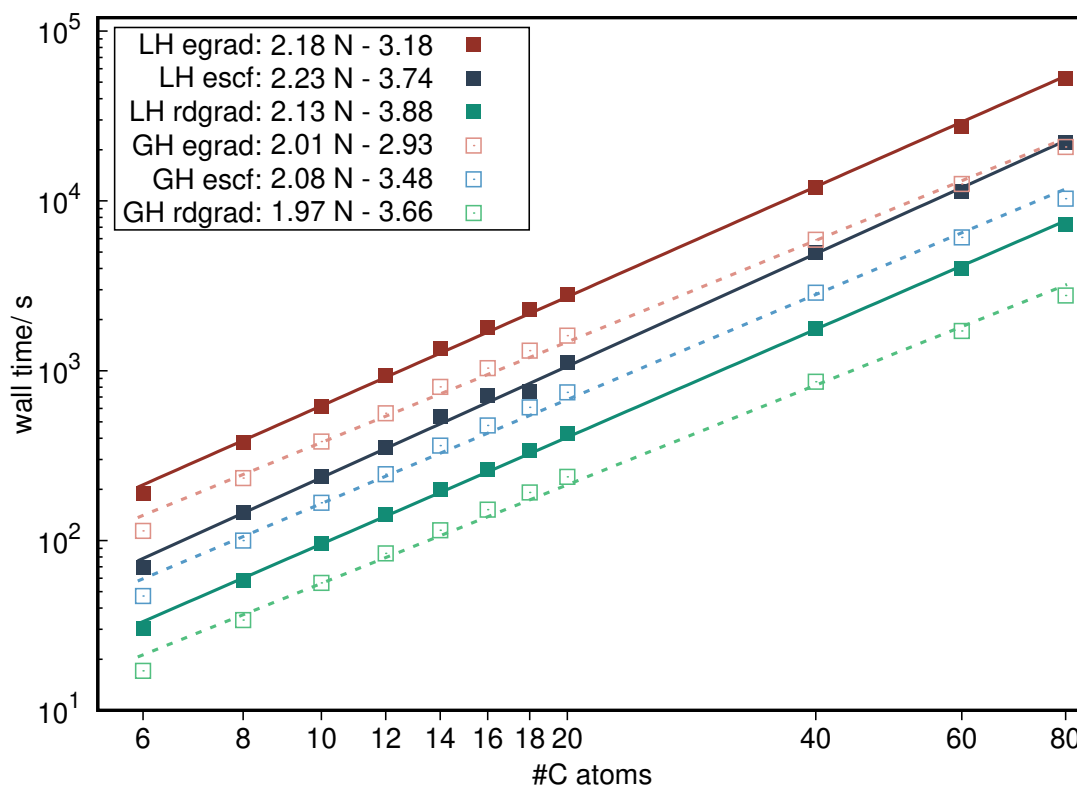


Figure 4.4: Double-logarithmic plot of the wall times and the system size of polyene chains for calculations with different TURBOMOLE programs using the def2-TZVP basis set and a small grid (grid size 1). The number of primitive basis functions is used for the horizontal axis with the number of carbon atoms marked for illustration. Linear fits are shown for LH calculations (solid lines) using the seminumerical implementation and GH calculations (dashed lines) using the standard analytical implementation of EXX integrals.

implementation can be considerably faster than the analytical implementation for larger basis sets (see also below) while this comparison uses the medium-sized def2-TZVP basis set.

Overall, all programs show a scaling that is roughly quadratic with system size with moderate advantages for the analytical GH implementations. Notably, the new seminumerical **egrad** implementation of LHs does not show significantly deteriorated scaling. As expected, the prefactor is notably increased by a factor of $10^{-3.18}/10^{-3.74} \approx 3.63$ compared to the seminumerical **escf** implementation. Considering the additional iterative step for solving the Z vector equation, the setup of intermediate quantities that also involve the costly **A** matrix evaluation, and the final ES gradients step involving the **A** and **A**^ξ matrices, such additional costs are inevitable. The increase of the prefactor is virtually identical

to that for the same comparison of the respective analytical GH implementations, where it amounts to $10^{-2.93}/10^{-3.48} \approx 3.55$.

The timings presented so far only include an overlap prescreening (via S-junctions) using the rather tight default threshold. This was done for better comparison with the analytical implementation which uses the same threshold for the overlap prescreening. Previous investigations for the LH implementation in `escf`^[23] and `rdgrad`^[47] revealed that looser thresholds can be applied without significant loss in accuracy. Besides, P-Junctions (cf. Section 3.2.1) can be applied to screen for non-contributing elements of the $\mathbf{B}_\sigma^{(\pm)}$ vectors. However, a test calculation revealed only a moderate additional reduction in computation time of about 4% in an `escf` run for the $\text{C}_{40}\text{H}_{42}$ molecule using the fairly loose threshold of 10^{-6} for S- and P-junctions. Moreover, for some systems such as the $\text{C}_{60}\text{H}_{62}$ molecule, the `escf` calculations no longer converge if the default convergence criterium (`rpaconv 5`) is applied. Slightly tightening the thresholds for S- and P-junctions to 10^{-8} gives converged results but leads to a 0.7% increase in computation time compared to calculations where no P-junctions are used (and the prescreening routines can be skipped) and only default S-junctions are applied. Of course, such problems transfer to the `egrad` implementation. Despite that, it should be noted that S- and P-junctions can still be useful for practical applications where convergence criteria can be loosened, which was not reasonable within the formal comparison intended here. However, even with a loosened convergence threshold, a calculation may take more iterations to converge when loose S- and P-junctions are used which might lead to overall longer wall times than accepting slightly longer computation times per iteration at tighter S- and P-junction thresholds. Predicting upfront what is favorable for a particular case is hardly possible. Also, the risk of unconverged calculations that require additional human work in adapting the settings and restarting has to be weighed against the moderate (relative) savings in computation time.

Scaling w.r.t. Basis-Set Size

The increasing length of the polyene chain in the setup described above does not only entail an increased number of basis functions, but also an increased number of grid points. While the increase in grid size hardly affects the analytical GH implementation, it linearly increases the computation time for the seminumerical LH implementation. For an isolated investigation of the scaling w.r.t. basis-set size, one given molecule (BODIPY) was studied at the same grid size using various basis sets. The results for these calculations are given in Table A.1 (Appendix A.5) and are plotted in Figure 4.5 along with linear equations

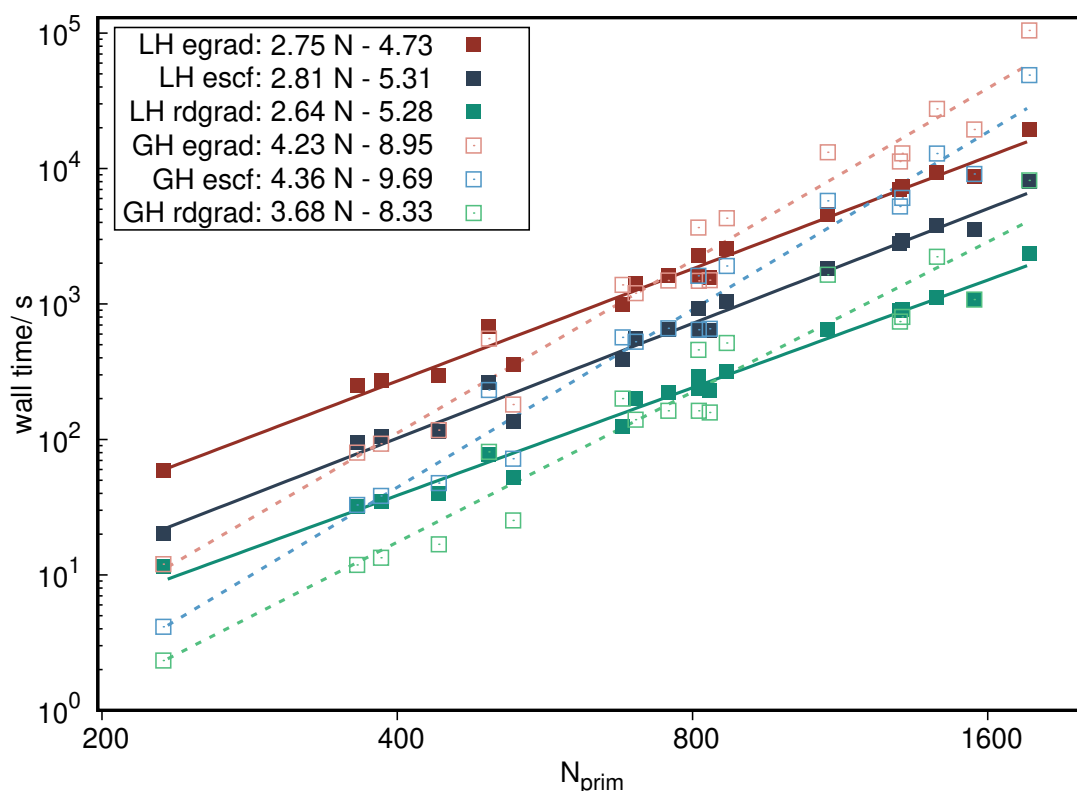


Figure 4.5: Double logarithmic plot of the wall times and the number of primitive basis functions N_{prim} for calculations with different TURBOMOLE programs for the BODIPY molecule using various basis sets (see text). Linear fits are shown for LH calculations (solid lines) using the seminumerical implementation and GH calculations (dashed lines) using the standard analytical implementation of EXX integrals.

for fits on the double-logarithmic scales. The analytical GH implementations exhibit a roughly quartic scaling w.r.t. basis-set size as expected from the formal N_b^4 scaling of the EXX integral evaluation scheme. The formal quadratic (N_b^2) scaling of the seminumerical implementation is reached in neither of the three investigated programs. The reason for that is the dependence of the scaling of the integral calculations on the angular-momentum quantum number l (cf. eq. 2.25), which scales as l^5 and l^{10} for two-center and four-center integrals, respectively.^[23] The theoretically expected advantage of the seminumerical implementation over the analytical implementation for larger basis sets arises at around 800 primitive basis functions^e consistent among the investigated programs. This cross-over depends on the number of grid points and therefore on the grid size setting and system size.

^eThis corresponds to the def2-TZVPD or cc-pVTZ basis set for the BODIPY molecule.

The linear fits for the scaling w.r.t. basis-set size in Figure 4.5 are less accurate than those for the scaling w.r.t. system size from Figure 4.4. This has to do with the different types of basis sets investigated in the former case. In particular, augmentation with diffuse functions entails a less effective overlap prescreening and thus increases computational cost compared to a non-augmented basis set with the same number of primitive basis functions.

As a final remark, note that all benefits seen for the LH implementation will transfer to calculations with GHs if the same seminumerical implementation is used.^f In fact, the performance for seminumerical GH calculations can be expected to be even better than for LHs because \mathbf{A}^ξ matrices do not have to be calculated (cf. Section 3.2.1).

^fThis is feasible in TURBOMOLE either by specifying a constant LMF (c-LMF) in the LH input or by using the separate **senex** implementation.

5 Validation of Local Hybrids for Excited-State Properties

The presented implementation of ES gradients for LHs facilitates for the first time the efficient optimization of ES structures with this class of functionals. Besides obtaining structural parameters of ESs, it is now possible to determine emission energies at relaxed structures as well as adiabatic excitation energies (AEEs). Via numerical differentiation of ES gradients, harmonic ES vibrational frequencies can be computed which allows to simulate absorption and emission spectra within the Franck–Condon approximation and provides access to 0–0 energies (cf. Section 2.4.3). In contrast to absorption VEEs that were already investigated with LHs,^[17,24,25] 0–0 energies are experimentally measurable and are thus interesting quantities for benchmarking LHs. In this chapter, LHs are investigated for ES structural parameters, fluorescence and phosphorescence emission energies, AEEs and 0–0 energies, harmonic ES vibrational frequencies, and the emulation of vibrationally resolved spectra. The studies were originally published in ref. 212 and ref. 264 and are reproduced here in a new order (refer to the front matter for details). Parts from ref. 212 are reprinted with permission from R. Grotjahn, F. Furche, M. Kaupp, *J. Chem. Theory Comput.* **2019**, *15*, 5508. Copyright 2019 American Chemical Society. Parts from ref. 264 are reprinted with permission from R. Grotjahn, M. Kaupp, *J. Chem. Theory Comput.* **2020**, *16*, 5821. Copyright 2020 American Chemical Society.

5.1 Introduction

The significance of benchmark studies crucially depends on the selection of test sets and the quality of the underlying reference data. While gas phase experimental data are closest to the real value of a quantity of interest, they also contain contributions not covered by the electronic structure method under investigation. For the LR-TDDFT methods to be evaluated here, this includes, e.g., effects of higher-order excitations, non-Born-Oppenheimer effects, anharmonicity effects, and relativistic effects. Given that such contributions are small relative to the expected error of the electronic structure method (here, mainly the XC functional error), gas-phase experimental data can still be used for benchmarking

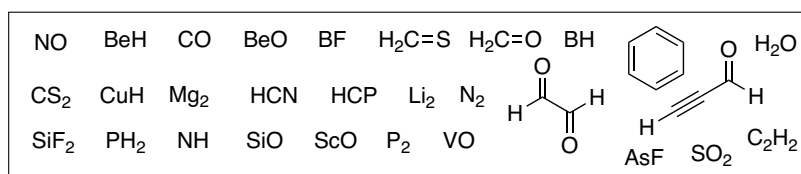


Figure 5.1: Chemical formulas of the molecules included in the Furche and Ahlrichs test set.^[35,39]

purposes. Also note that the accuracy at which molecular parameters can be deduced from experimental data varies. While ES bond lengths of diatomic molecules and AEEs can usually be deduced from experimental spectra with great accuracy, structural parameters of polyatomic molecules can be more problematic.^[212] They are typically obtained from vibronic spectra via complex fitting procedures (cf., e.g., ref. 265) and are thus more prone to errors.^[212] Reference values determined by an accurate electronic structure method such as correlated wave-function methods are more closely related to the quantity calculated with the method under investigation but do not necessarily correspond to an experimentally measured quantity.

The first test set under investigation here has been compiled by Furche and Ahlrichs^[35,39] and uses gas-phase experimental data as reference values. The molecules under investigation are shown in Figure 5.1 and are mainly small inorganic molecules, but some organic molecules are also included. The test set covers ES structural parameters for different bond types, harmonic ES vibrational frequencies, and a mixture of AEEs (diatomic molecules) and 0–0 energies (polyatomic molecules) for a variety of ESs with a different character (valence and Rydberg) and spin multiplicity. For some molecules, two or more ESs are considered. The experimental reference values are mostly in satisfactory agreement with available theoretical reference values,^[266,267] except for the 1¹A_u state of acetylene. For this state, the reference values were updated to more recent experimental values,^[268] which improves the agreement with the high-level computational results.^[266,269,270]

A larger test set containing small and medium-sized organic and inorganic molecules has been compiled from several works by Jacquemin and coworkers^[266,267,271–273] and is shown in Figure 5.2. It is used here to benchmark the performance for ES bond lengths for different bond types as well as for fluorescence energies. The reference values are coupled-cluster results obtained at different levels of theory. Results obtained at the CC3/aug-cc-pVTZ level of theory are the most trusted, but structure optimizations at this level are prohibitively expensive for all but the smallest molecules.^[264] The (slightly) lower computational levels used for the reference values are CC3/def2-TZVPP, CCSDR(3)/aug-cc-pVTZ, and CCSDR(3)/def2-TZVPP.^[264] Compared to CC3/aug-cc-

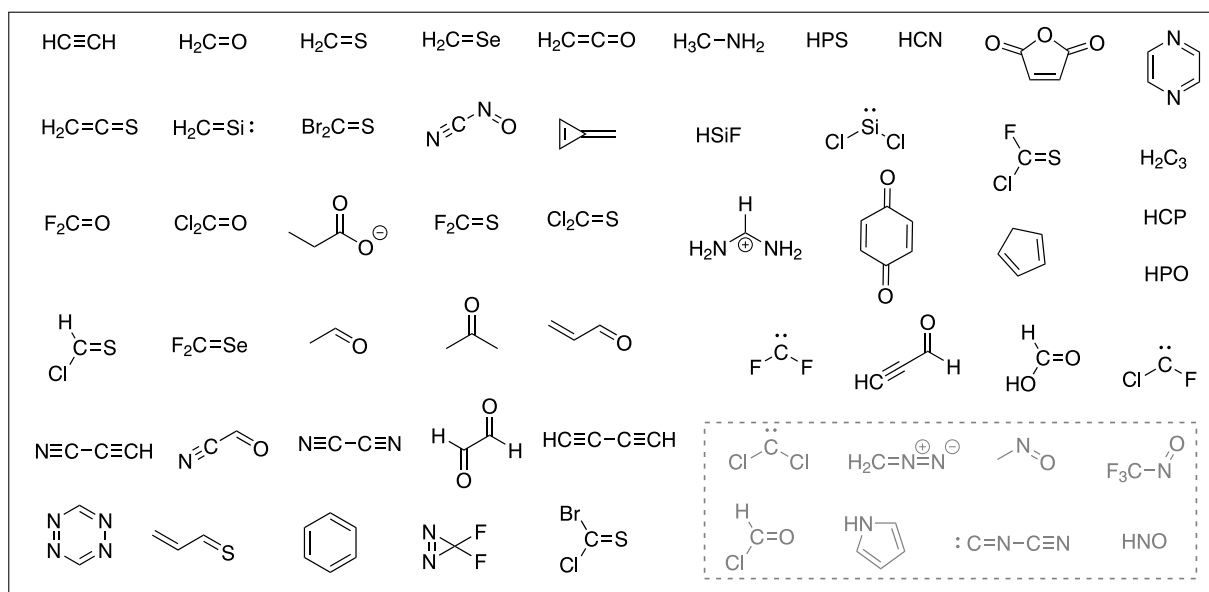


Figure 5.2: Chemical formulas of the molecules included in the Jacquemin test set.^[266,267,271–273] Molecules shown in gray were excluded from the statistical analysis because of convergence problems with several functionals.

pVTZ or CASPT2/aug-cc-pVTZ reference values, the latter gives an average error of 0.3 pm (MAE) for bond lengths.^[264,266]

For the assessment of phosphorescence energies, a set of medium-sized organic molecules previously studied by Adamo, Ehara, and coworkers^[274] at the SAC-CI and PBE0 level of theory is considered. Additionally, three smaller molecules from ref. 271 were added to the test set. The molecules are shown in Figure 5.3 and one or more triplet ESs are studied for each molecule. For the triplet states previously studied at the SAC-CI level, improved reference values for the phosphorescence energies were obtained at the CC3 level using a basis set extrapolation at the CC2 level (cf. Section 5.2.3 for details), all at the SAC-CI structures from ref. 274.

While ES structural parameters, vertical fluorescence energies, and vertical phosphorescence energies are undoubtedly valuable quantities for benchmarking TDDFT methods,

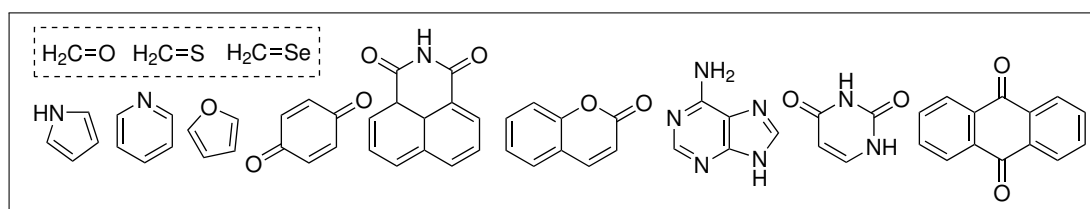


Figure 5.3: Chemical formulas of the molecules included in the Adamo and Ehara test set^[274] and additional molecules studied alongside (dashed box) from ref. 271.

they are either difficult to measure and therefore rarely reported (ES structural parameters) or not at all measurable (vertical transition energies). By contrast, absorption and emission spectra are routinely recorded and frequently published. Computationally, the position of absorption or emission bands are often approximated as the vertical absorption or emission energies and empirically broadened using Gaussian line shapes. While this approach is often successful, especially when thermal averaging conceals details in the shape of the experimental spectrum, it cannot recover vibronic effects typically observed in the fine structure of high-resolution spectra at low temperatures (cf. Section 2.4.3 for theoretical details).

For vibronically resolved absorption spectra, the performance of the XC functionals BP86, B3LYP, and BHLYP has been previously studied for 43 transitions of organic molecules by Dierksen and Grimme.^[275] The amount of EXX admixture affects the shape of these spectra significantly, but a generally optimal value could not be established.^[275,276] Besides evaluating the general performance of LHs for the emulation of vibronic spectra, it is therefore also interesting to analyze if the more flexible mixing scheme used in LHs provides a more uniform behavior among different systems compared to GHs that use a constant admixture of EXX.

5.2 Computational Details

5.2.1 Furche and Ahlrichs Test Set

The 1^1B_1 ES of CCl_2 was excluded from the Furche and Ahlrichs test set here, as it showed non-real instabilities for all considered LH functionals. Pyridine and porphyrin were excluded from the test set because reference data was not available for all investigated properties. Note that pyridine is contained in the test set of phosphorescence energies from ref. 274 also discussed within this chapter. In ref. 39, the $1^4\Pi$ state of VO, the $1^3\Pi$ state of AsF, and the 2^1A state of propynal were added to the test set and are included here as well.

If not stated otherwise, all calculations have been performed using the def2-QZVPPD basis set.^[257] Compared to the aug-TZVPP basis set used in ref. 35, this basis set is of quadruple- ζ quality and has been optimized for the calculation of molecular properties. While impractically large for many applications, this basis set is feasible for the given test set and is used here to essentially work at the orbital-basis limit. The 2^1B_1 ES of the H_2O molecule exhibits distinct Rydberg character and thus required additional diffuse f - and g -functions. The corresponding exponents were taken from Dunning’s aug-cc-pVQZ basis

set.^[260] Although investigations in Section 4.3.2 suggest that smaller grids are sufficient, large and diffuse integration grids (TURBOMOLE grid size 5, diffuse 2) were used in producing the benchmark results, to preclude any errors from the seminumerical integration. Additionally, neither S- nor P-junctions were used for an integral prescreening in the seminumerical scheme. For the optimization of the GS and ES structures, very tight convergence criteria were used, i.e. GS calculations were converged to energy changes $\leq 10^{-10}$ ha (`scfconv 10`) and density-matrix changes $\leq 10^{-9}$ a.u (`denconv 1d-9`). Excitation vectors were converged to residual excitation-vector norms $\leq 10^{-7}$ a.u (`rpaconv 7`). The maximum gradient norms were converged to $\leq 10^{-4}$ a.u (`gcart 4`). Harmonic vibrational frequencies of the ground and excited states were calculated using the TURBOMOLE `NumForce` script, i.e. by means of numerical differentiation (first derivative, central differences) of the gradients. The displacement of the atoms generally breaks the molecular symmetry, and calculations were thus performed in C_1 . However, this led to non-real instabilities for the displaced structure with some functionals. Since this was only observed for the $1^2\Sigma^+$ state of NO, the $1^2\Pi$ state of ScO, and the $1^4\Pi$ state of VO, i.e. some linear molecules, the calculation of the corresponding harmonic vibrational frequencies was carried out by manually displacing one atom along the molecular axis and exploiting full point group symmetry. Weight derivatives were used to improve the numerical accuracy of gradients in displaced structures during frequency calculations and to improve the convergence of structure optimizations. In general, the resolution of the identity (RI-J)^[39] approximation was used for the Coulomb part, with the only exceptions being ES gradients calculations of triplet ESs, which were empirically found to be unstable with RI-J. The standard TURBOMOLE auxiliary basis sets (def2-universal) was used.^[277] The LHs LH07t-SVWN, LH07s-SVWN, LH12ct-SsirPW92, and LH12ct-SsifPW92 were investigated (see Section 2.3.4 for a detailed description). Additionally, the LSDA functional SVWN,^[114,116] the GGA functional PBE,^[123] the mGGA functional TPSS,^[109,132] and the GHs PBE0^[138] and TPSSh^[140] were studied for comparison.

5.2.2 Jaquemin Test Set

All (TD)DFT calculations for this test set used the def2-TZVPD basis set^[257] and fairly large and diffuse integration grids (TURBOMOLE grid size 3, diffuse 1) were employed to preclude any errors from the (semi)numerical integration. Derivatives of the quadrature weights were included to improve the numerical accuracy of gradients. Neither S- nor P-junctions were used for an integral prescreening in the seminumerical scheme. The resolution of the identity (RI-J)^[39] approximation was used for the Coulomb part, with the

exception of gradient calculations of triplet ESs (see above). Standard TURBOMOLE auxiliary basis sets (def2-universal) were used for the RI.^[277] Tight convergence criteria were applied, i.e. GS calculations were typically converged to energy changes of $\leq 10^{-9}$ ha (`scfconv 9`) and density-matrix root mean squares of $\leq 10^{-8}$ au (`denconv 1d-8`). Excitation vectors were converged to residual excitation-vector norms of $\leq 10^{-5}$ au (`rpaconv 5`). The maximum gradient norms were converged to $\leq 10^{-4}$ au (`gcart 4`).

The LHs LH07t-SVWN, LH07s-SVWN, LH12ct-SsirPW92, and LH12ct-SsifPW92 were investigated (see Section 2.3.4 for a detailed description). In addition, the new LH20t^[17] functional (cf. Section 2.3.4) was investigated, where the pig2 calibration function was neglected as it depends on the density Laplacian and Hessian, for which third derivatives are not included in the `egrad` implementation. To distinguish this functional from the original, it is termed LH20t*. The CF’s relatively small importance for the target ES structures and emission energies is supported by a comparison of numerically optimized ES structures with and without CF for the diatomic molecules from the Furche and Ahlrichs test set (cf. Table A.5 in Appendix A.7 for details). For comparison, the popular XC functionals BLYP,^[122,124] B3-LYP,^[10,124] BLYP35,^[122,124,146] PBE0,^[123,138] TPSSh,^[140] M06,^[143] M06-2X,^[143] ω B97X,^[153] and CAM-B3LYP^[151] were tested as well.

5.2.3 Adamo and Ehara Test Set

For the study of phosphorescence energies, new reference values were calculated as single-point excitation energies using the SAC-CI structures from ref 274. To that end, CC2 results extrapolated to the complete basis set limit (CBS) were combined with a high-level CC3/cc-pVDZ correction

$$\Delta E_{\text{CBS}}^{\text{CC3}} \approx \Delta E_{\text{CBS}}^{\text{CC2}} + (\Delta E_{\text{DZ}}^{\text{CC3}} - \Delta E_{\text{DZ}}^{\text{CC2}}) . \quad (5.1)$$

Comparison with CC3/aug-cc-pVTZ results for small molecules (cf. Table A.7 in Appendix A.10) shows that the composite CC2/CBS+CC3 values deviate by less than 0.02 eV from these data, which is clearly sufficient for the purposes of the present work. CC3 calculations were performed with the Dalton package^[278–280] using default convergence settings and the frozen-core approximation. Dunning’s correlation-consistent cc-pVDZ basis set was used for this step.^[259] CC2 calculations were performed within the RI approximation using TURBOMOLE’s `ricc2` module,^[281–283] again using default settings and the frozen-core approximation. For the basis-set extrapolation of excitation energies, the same 2-3-4 approach^[284] as described in detail in ref. 25 using Dunning’s augmented aug-cc-pVXZ (X=D,T,Q) basis sets^[259,260] was employed. To this set, three

triplet ES structures from ref. 271 obtained at the CC3/aug-cc-pVTZ level were added and phosphorescence energies were calculated at the CC3/aug-cc-pVQZ level for these smaller molecules. The (TD)DFT calculations used the same settings and functionals as described in Section 5.2.2 above.

5.2.4 Dierksen and Grimme Test Set

The performance of the LHs LH07t-SVWN and LH12ct-SsifPW92 is studied for a sizeable subset of the 43 spectra compiled in ref. 275 along with B3LYP and BLYP35 for comparison. Vibronic spectra were simulated with the **radless** module of TURBOMOLE, i.e. within the real-time generating function approach described in Section 2.4.3.^[217] For better comparability, the intensities of the experimental and calculated spectra are scaled to a maximum of 1.0 and the frequencies were shifted so that the first maximum occurs at 0 cm^{-1} . The lifetimes used for the broadening of the spectra were adjusted to match the experimental spectra and are typically on the order of 10^3 au ($\sim 24\text{ fs}$). The maximum integration time was set to $2^{17}\text{ au} = 131072\text{ au}$ with a sample rate of 1.0 au .

Harmonic vibrational frequencies of the ground and excited states were calculated using TURBOMOLE’s **NumForce** script. These calculations take up considerable computational resources for large molecules. Hence, a mindful choice of the basis set is important. The influence of the basis set on the shape of vibronic spectra has already been tested by Grimme and coworkers.^[275] The (shifted and scaled) spectrum of the $1^1\text{A}_g \rightarrow 1^1\text{B}_{2u}$ transition of tetracene calculated with the SVP basis set using B3LYP was qualitatively correct but noticeably deviated from the one generated with the QZVP basis set. With the TZVP basis set, the spectrum was almost indistinguishable from the QZVP result. For the spectra of anionic species, a rather strong influence of diffuse functions might be suspected. But their impact was in fact found to be negligible for the spectral shapes of the studied systems.^[275] Hence, the TZVP basis set was used in this study but updated to the more recent def2-TZVP version.^[255] The associated less diffuse basis set also rendered the diffuse option for the DFT quadrature grid unnecessary. Otherwise, the (TD)DFT calculations used the same settings as described in Section 5.2.2 above.

Note that most experimental reference spectra were recorded in a solvent or an organic glass matrix. As in ref. 275, effects from these environments were neglected. As a molecule’s polarizability is typically larger in its ES than in its GS, the ES is stabilized on a relative basis in solution, leading to a red-shift in the absorption spectrum. Such effects can be quite large and were estimated to be 0.15 eV for the molecules under investigation in ref. 275. However, such shifts are obviously irrelevant in the zero-shifted spectra con-

sidered here. Possible more intricate solvent effects on the band shapes are missing in the calculated spectra presented here. Although these effects are expected to be more or less similar for different XC functionals, this makes it harder to decide if subtle differences between two spectra are actually favorable or not if both spectra are already close to the experimental spectrum.

5.3 Results for Excited-State Structures

5.3.1 Furche and Ahlrichs Test Set

As discussed in ref. 35, the significance of a statistical analysis in terms of MAEs is limited for this test set due to the different nature of the ESs and differences in the practical significance of the individual molecular parameters. Nonetheless, this test set gives a first impression of the performance of LHs and is discussed first before proceeding with a more in-depth analysis. All raw data and the gas-phase experimental reference data as well as optimized structures are provided in ref. 212 as Supporting Information.

In Table 5.1, MAEs for ES structural parameters are given for all XC functionals evaluated. The $1^1\Sigma_u^+$ states of Li_2 and Mg_2 were excluded from the statistical analysis

Table 5.1: Mean absolute errors for bond lengths (R in pm), bond angles (\angle in deg), and out-of-plane angles (ϕ in deg) from the Furche and Ahlrichs test set^[35,39] calculated with various standard functionals and four LHs. The number of parameters for each subset is given in parentheses in the header line. 'Total' also contains unrestricted calculations not falling into the 'Singlet' or 'Triplet' categories.

Functional	Total			Singlet			Triplet		
	R (43)	\angle (15)	ϕ (3)	R (28)	\angle (10)	ϕ (1)	R (10)	\angle (4)	ϕ (2)
SVWN	1.4 ^a	3.9	5.1	1.4	4.3	0.4	1.5	3.8	7.4
PBE	1.2 ^b	2.2 ^b	6.3	1.3 ^b	1.5 ^b	1.1	1.3	3.9	8.9
TPSS	1.2 ^{b,c}	1.6 ^{b,c}	10.0 ^c	1.2 ^b	1.4 ^b	1.4	1.3 ^c	2.2 ^c	18.6 ^c
TPSSh	1.1	2.4	10.5	1.2	1.3	2.2	0.9	5.4	14.7
PBE0	1.4	2.3	4.4	1.5	1.6	3.3	1.4	4.2	4.9
LH07s-SVWN	1.1	2.1	5.5	1.2	1.5	2.3	1.3	3.7	7.2
LH07t-SVWN	1.1	1.9	6.6	1.2	1.2	6.7	1.3	3.7	6.6
LH12ct-SsirPW92	1.2	1.8	7.2	1.2	1.3	8.4	1.3	3.4	6.6
LH12ct-SsifPW92	1.2	1.9	7.6	1.2	1.4	9.0	1.3	3.4	6.9

Due to instabilities of the reference state, the statistics exclude:

^a $1^2\Sigma^+$ state of NO.

^b 2^1A state of propynal.

^c $1^3A''$ state of CH_2O .

because the large absolute deviations would otherwise distort the overall evaluation. With the exception of the somewhat poorer performance of the LDA functional SVWN for bond angles, all MAEs for bond lengths and bond angles are essentially on par. EXX admixture in the GHs TPSSh and PBE0 tends to shorten bond lengths compared to their non-hybrid counterparts leading to left-shifted error histograms (cf. Figure A.2 in Appendix A.8). Among the LHs, no clear trends are observed, i.e. neither the underlying LMF model nor the LMF prefactor significantly alters the averaged results. Moderate prefactors as in LH07t-SVWN tend to deliver somewhat more uniform performance for bond lengths as can be seen from Figure A.2. Out-of-plane angles show significantly larger MAEs than bond angles for all functionals, but the low number of values in the test set prevents a more definite analysis. No major differences between singlet and triplet ESs are observed for bond lengths indicating that structures of the considered triplet ESs are not particularly more challenging than the singlet ESs included in the test set. The distinctly larger MAEs for bond angles of triplet ESs presumably are a statistical artifact of the small number of values for the triplet case.

5.3.2 Jacquemin Test Set

Compared to the smaller Furche and Ahlrichs test set discussed above, the larger sample size of the Jacquemin test set permits a more differentiated analysis, e.g. regarding bond types. The raw data for this test set and a set of optimized coordinates is contained in ref. 264 as Supporting Information. For the investigated standard functionals, the results presented here are in line with those by Jacquemin and coworkers (see ref. 267 for a more detailed discussion). Results obtained within the present study are nonetheless included for comparison with the LH data. Overall, TPSSh shows the best performance (MAE 1.1 pm) closely followed by LH07t-SVWN (MAE 1.2 pm) and by BLYP, LH07s-SVWN, LH12ct-SsirPW92 and LH20t* (MAEs 1.3 pm). The total MAEs of LH12ct-SsifPW92 (1.4 pm) and PBE0 (1.5 pm) are slightly larger. The MAEs of M06 (1.6 pm), CAM-B3LYP (1.7 pm), and particularly ω B97X and M06-2X (1.8 pm) are noticeably larger. The absolute results and relative performance found for the local hybrids compared to TPSSh and PBE0 closely match those obtained for the Furche and Ahlrichs test set that used experimental reference values (Section 5.3.1).

However, comparisons in terms of total MAEs do not necessarily give the best insight into the applicability of a given functional for ES structure optimizations. A more differentiated analysis regarding bond types is desirable and provided in Figure 5.4 for the MAEs (top) and mean signed errors (MSEs, bottom). First note that the BLYP GGA

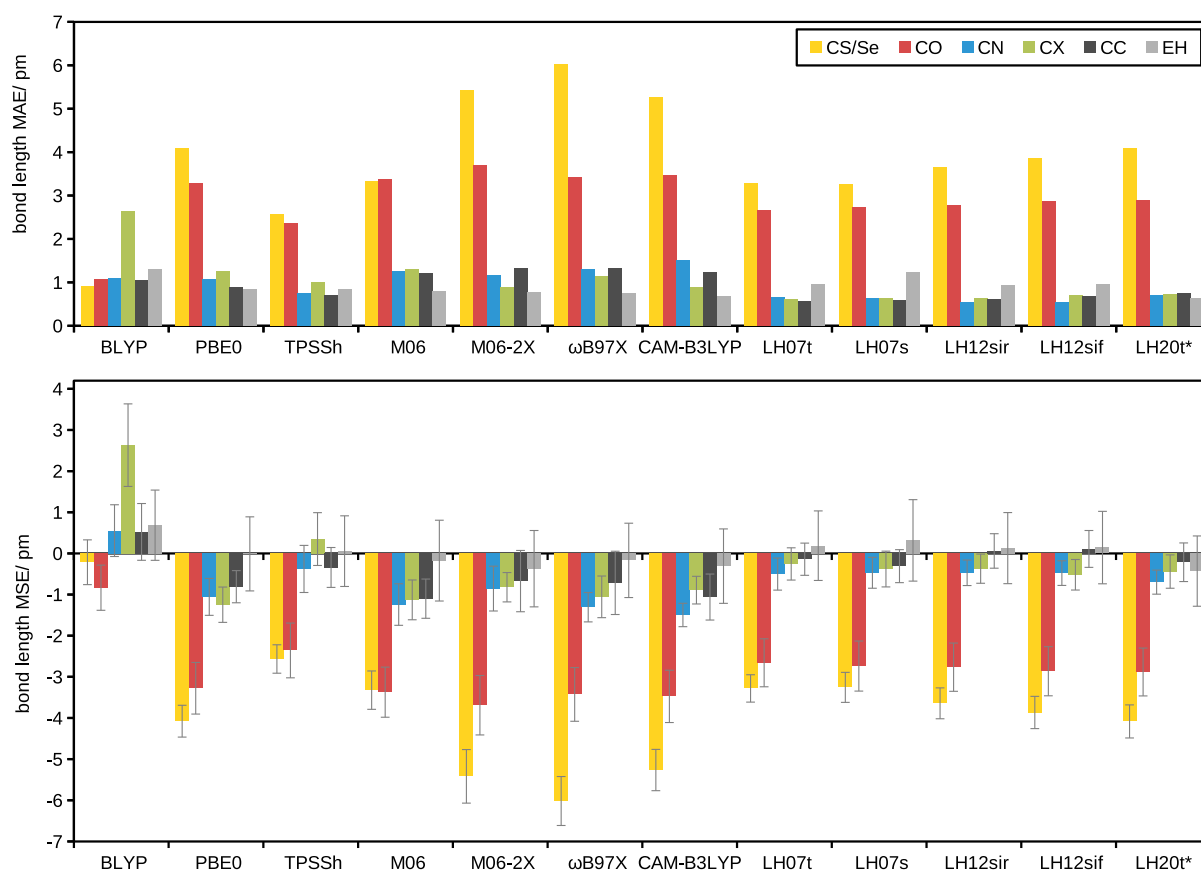


Figure 5.4: Mean absolute errors (top) and mean signed errors (bottom) in pm for ES bond lengths obtained with various XC functionals for different bond types, where $X = \text{F, Cl, Br}$ and $E = \text{C, N, O, Si, P}$. CO, CN and CC exclude all clear-cut single bonds to improve comparability. The underlying numerical data are given in ref. 264. In the bottom plot, the total heights of the error bars reflect one standard deviation. Functional abbreviations: LH07t: LH07t-SVWN, LH07s: LH07s-SVWN, LH12sir: LH12ct-SsirPW92, LH12sif: LH12ct-SsifPW92, LH20t*: LH20t w/o CF.

functional (and other GGA functionals such as PBE or B97D^[267]) gives overall larger bond lengths than the hybrids; moderate EXX admixture in the bonding region as in TPSSh and partly in the LHs seems to provide a good compromise for the different bond types; and functionals with substantial EXX admixture, such as CAM-B3LYP, ω B97X and M06-2X, give the overall shortest bonds.

Starting with element-hydrogen (EH) bonds (gray bars in Figure 5.4), the overall smallest error is found with LH20t* (0.6 pm) and CAM-B3LYP (0.7 pm) while BLYP gives the largest MAE (1.3 pm) and overestimates the bond lengths more or less systematically with an MSE of 0.7 pm, which may still be classified as moderate deviations. MAEs for the LHs based on a t-LMF and LSDA exchange and correlation are very similar, rang-

ing from 0.9 pm to 1.0 pm. LH07s-SVWN, which is based on an s-LMF, falls somewhat behind the t-LMF-based LHs for the EH bonds. This might be related to the peculiar shape of the t-LMF along an EH bond.^[285] It is characterized by a steep increase towards hydrogen (and therefore elevated EXX admixture) in the bonding region and a constant value (prefactor of the LMF) behind the hydrogen atom. While the deteriorated description of nondynamical correlation in the bonding region was found to be potentially detrimental for other properties like hydrogen nuclear shieldings^[245] and molecular dipole moments^[286] (see also Section 6.3.1), the enhanced EXX admixture seems to be beneficial for the ES bond lengths. Reduced left-right correlation tends to give shorter bonds^[111] and therefore reduces their typical overestimation in the present EH bond set.

The carbon-halogen (CX) bonds (green bars in Figure 5.4) are the most prominent outliers for the otherwise well-performing BLYP functional (MAE 2.6 pm, MSE +2.6 pm). Here the overall longer bonds at the BLYP level are detrimental, whereas the best results are achieved by the LHs (down to MAEs as low as 0.6 pm for LH12ct-SsirPW92). Comparing the MSEs of the local and global hybrids suggests that LHs reduce the underestimation of CX bond lengths seen with most GHs. But overall the performance for the CX bond lengths is reasonable for most functionals. Given that ES bond lengths are typically more difficult to compute than GS ones,^[266,267] the lengths of the carbon-nitrogen (CN) and carbon-carbon (CC) bonds (blue and black bars, respectively, in Figure 5.4) are generally reproduced relatively well by most functionals. Only M06 and CAM-B3LYP exhibit underestimates beyond 1 pm.

The carbonyl (CO), thionyl and selenonyl (CS/Se) bond lengths (red and yellow bars in Figure 5.4) are clearly the most challenging for all hybrid functionals, featuring MSEs below -3.0 pm for the majority of functionals. Note that even LR-CC2 and EOM-CCSD struggle with an accurate description of the carbonyl ES bond lengths, giving MSEs of +2.9 pm and -2.5 pm, respectively (while CC methods including triple excitations reduce errors to below 1.0 pm).^[266] Here, the overall relatively long bonds of BLYP are beneficial, leading to an almost vanishing MSE and an MAE of 1.1 pm, while a shortening due to EXX admixture in the various types of hybrid functionals seems detrimental. The low EXX admixture of TPSSh gives better agreement with the reference values than larger admixtures in global or range-separated hybrids, and the LHs with the lowest t-LMF prefactors provide somewhat less negative MSEs than those with larger prefactors.

Considering the good performance of hybrid functionals for CN and CX bonds, their inferior performance for CO (and CS/Se) bonds cannot be explained merely by the polarized nature of such bonds. A more detailed analysis of the relevant electronic transitions in systems with carbonyl bonds reveals that the performance of hybrid functionals corre-

lates with the $n \rightarrow \pi^*$ nature of the transition (cf. Table A.6 in Appendix A.9). In fact, the $1^1A''$ ES of ketene is the only state among the carbonyl compounds with no $n \rightarrow \pi^*$ character, and its CO bond length is much better reproduced by hybrid functionals (MSE -1.4 pm for PBE0 and -1.0 pm for LH12ct-SsifPW92). On the flip side, even nonpolar bonds like CC bonds can be challenging for hybrid functionals. For example, the $H_2C=C$ carbon-carbon bond length of the 1^1A_2 ES of H_2C_3 is underestimated (MSEs -3.3 pm for PBE0, -2.6 pm for LH12ct-SsifPW92, compared to general MAEs for CC bonds of 0.9 pm and 0.7 pm, respectively). As shown in Figure A.6, the shapes of the orbitals involved in the transition of this ES are almost identical to the prototypical $n \rightarrow \pi^*$ transition in formaldehyde. Similarly, Filippi and coworkers found that the carbonyl bond in *s-trans*-acrolein is well described by both hybrid functionals and CC2 for the $\pi \rightarrow \pi^*$ excitation but poorly for the $n \rightarrow \pi^*$ excitation.^[287] In a recent study by Wang and Durbeej,^[288] CO bond lengths were found to be not particularly challenging for TDDFT which was rationalized by the predominant $\pi \rightarrow \pi^*$ character of the investigated transitions. There is evidence that the difficulties with $n \rightarrow \pi^*$ excited states are related to static correlation. This is indicated, e.g., by the importance of triple excitations in CC approaches (see above),^[266] by large D1 and D2 diagnostics for CC2,^[289] or by the detrimental effects of increased EXX admixture observed here. However, more definite conclusions require further investigations that are outside the scope of this work.

So far, only bond lengths were discussed because the changes for bond angles were found to be much more system-dependent and a meaningful breakdown and classification (as for bond types) is less obvious. Notably, however, the bond angles formed by a carbonyl group and some adjacent atom show a somewhat reversed trend to what was seen for the C=O bond lengths. While errors with BLYP (2.8°) and TPSSh (2.2°) are comparatively large, M06-2X (1.1°) and the LHs LH12ct-SsifPW92 (1.2°) and LH12ct-SsifPW92 (1.2°) give the best results for these angles.

5.4 Results for Excitation Energies

5.4.1 Adiabatic Excitation Energies and 0–0 Energies

As discussed by Send *et al.*,^[229] benchmark studies of 0–0 energies (or AEEs) give a more realistic view of the performance of different functionals for the simulation of absorption spectra than VEE benchmarks do. Hence, the following results for LHs complement the insights obtained from previous studies of VEEs.^[17,24,25] In addition to the MAEs in Figure 5.5, error histograms are given in Appendix A.8 (Figure A.3).

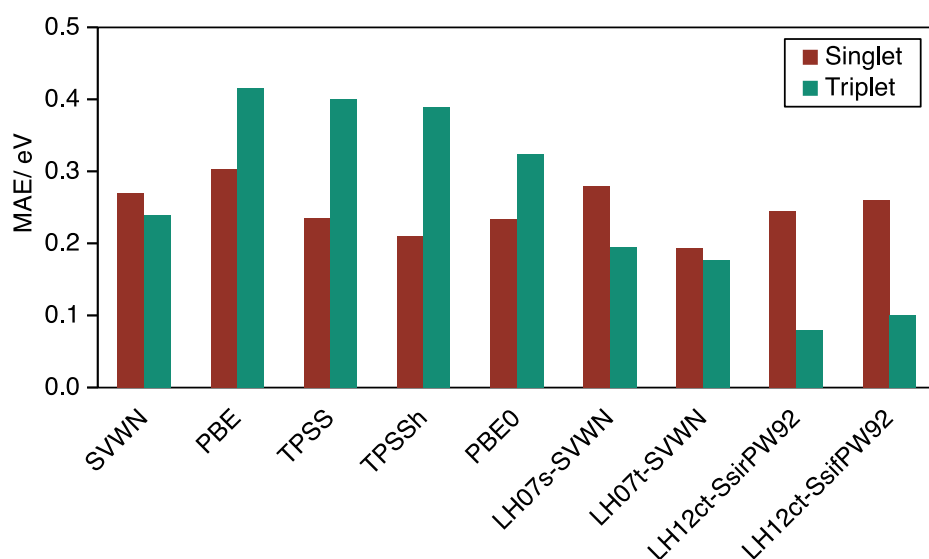


Figure 5.5: Mean absolute errors in eV for AEEs (0–0 energies for polyatomic molecules) of singlet and triplet ESs from the Furche and Ahlrichs test set^[35,39] calculated with various standard functionals and four LHs.

In terms of total MAEs, LHs show slightly superior performance compared to GHs with the lowest MAE being 0.22 eV for LH07t-SVWN compared to 0.26 eV for PBE0. Besides, the performance with LH07t-SVWN is somewhat more uniform, i.e. errors are distributed more densely around the median signed error of -0.07 eV (PBE0: -0.17 eV) as can be seen from Figure A.3. A larger error of 1.11 eV for the $1^2\Sigma^+$ state of NO (PBE0: 0.60 eV) gives rise to a larger maximum error (outlier in Figure A.3). Considering only singlet ESs, the performance for LH07t-SVWN is further improved with an MAE of 0.19 eV, which can be attributed to the omission of the open-shell $1^2\Sigma^+$ state of NO (see above). In contrast, a slight performance drop for LH12ct-SsifPW92 is noticed, indicating that the overall EXX admixture with this LH might be too large for the given cases.

For triplet ESs, LH12ct-SsifPW92 outperforms the standard functionals, giving an MAE of 0.08 eV. Errors are also closely distributed (cf. green bars in Figure A.3) around the median of -0.02 eV, with a maximum error of -0.16 eV. Similar performance is seen for LH12ct-SsifPW92, while LH07s-SVWN and LH07t-SVWN perform well but somewhat less dramatically so in triplet excitations. In contrast, most GHs are known to underestimate triplet excitation energies systematically. This is exposed here by the distribution of errors in Figure A.3 (green bars) and manifests in typically negative median signed errors of, for instance, -0.31 eV for PBE0. The improvement of triplet AEEs/ 0–0 energies with LHs is consistent with previous observations for VEEs.^[24,25] These had suggested that the LMF-weighted EXX admixture introduces additional static correlation effects

that improve the description of triplet ESs. The importance of such left-right correlation effects is supported by the observation that the performance is further improved when a common t-LMF ("ct") instead of a spin-channel t-LMF is used, as additional cross-term contributions arise in this case.^[24]

Note, however, that the remarkable performance for triplet AEEs/ 0–0 energies is not derived from a significantly improved description of the underlying ground- and excited-state structures. A correlation plot of signed AEEs/ 0–0 energy errors obtained with LH12ct-SsifPW92 at LH12ct-SsifPW92 structures and with LH12ct-SsifPW92 at PBE0 structures reveals that the structural effects do not exceed ± 0.02 eV (cf. Figure A.5). This is as expected and does not invalidate the need for ES gradients at the given computational level.

5.4.2 Fluorescence Energies

For the study of fluorescence energies, a subset of 40 singlet ESs for which CC reference energies were provided in ref. 271 and 272 is analyzed. Generally, TDDFT energies were computed at the relaxed ES structures optimized with the respective XC functional. To assess the impact of the underlying structures, single-point calculations with LH12ct-SsifPW92 at relaxed BLYP ES structures and with BLYP at relaxed LH12ct-SsifPW92 ES structures were also performed. The statistical results for the investigated XC functionals are given in Table 5.2 and the raw data and reference values are provided in ref. 264 as Supporting Information. Overall, the differences in the MAEs are rather small, ranging from 0.29 eV for BLYP to 0.45 eV for ω B97X. Also among the top performers are TPSSh (0.32 eV) and LH07s-SVWN (0.32 eV). For BLYP, the errors are almost entirely caused by a systematic underestimation (MSE of -0.21 eV) while they are stochastic for TPSSh and LH07s-SVWN (MSEs of 0.02 eV and -0.05 eV respectively). In terms of error distributions, most functionals are comparable with standard deviations of around 0.4 eV and maximum absolute errors of around 0.8 eV. Notably, the highly empirical M06-2X functional exhibits larger maximum absolute errors (1.52 eV) and standard deviations (0.60 eV). The t-LMF based LHs are not particularly better or worse than the remaining hybrid functionals but larger prefactors seem to lead to an overestimation of fluorescence energies and therefore increased MAEs.

Considering the good performance of LH12ct-SsifPW92 and LH12ct-SsifPW92 for the singlet VEEs of the Thiel test set,^[24] their less convincing performance for fluorescence energies is conspicuous. The results obtained with LH12ct-SsifPW92 at BLYP structures are, however, significantly better than at the relaxed (LH12ct-SsifPW92) structures

Table 5.2: Mean absolute errors, mean signed errors, maximum signed errors, and standard deviations (σ) in eV for 40 fluorescence emission energies using various XC functionals and the def2-TZVPD basis set. Unless stated otherwise, ES structures were optimized with the same functional.

Functional	MAE	MSE	MaxE	σ
BLYP	0.29	-0.21	0.77	0.33
PBE0	0.36	0.03	0.87	0.42
TPSSh	0.32	0.02	0.76	0.37
M06	0.36	-0.09	1.13	0.47
M06-2X	0.44	-0.10	1.52	0.60
ω B97X	0.45	0.11	0.93	0.52
CAM-B3LYP	0.40	0.07	0.85	0.47
LH07t-SVWN	0.36	0.08	0.88	0.41
LH07s-SVWN	0.32	-0.05	0.78	0.39
LH12ct-SsifPW92	0.40	0.12	0.96	0.46
LH12ct-SsifPW92	0.42	0.13	0.98	0.48
LH20t*	0.42	0.13	0.94	0.48
LH12ct-SsifPW92//BLYP	0.32	-0.02	0.87	0.43
BLYP//LH12ct-SsifPW92	0.32	-0.08	0.73	0.38

(MAE 0.32 eV). Obviously, the LH12ct-SsifPW92 structures have an adverse effect on the fluorescence energies. This can be traced back to the rather poor description of carbonyl and thionyl compounds (cf. Section 5.3.2) with LH12ct-SsifPW92 as compared to BLYP. In Figure 5.6, the absolute errors with LH12ct-SsifPW92 at the BLYP structures are plotted against those at the LH12ct-SsifPW92 structures. All larger errors with LH12ct-SsifPW92 at LH12ct-SsifPW92 structures are associated with excitations in which a CO or CS/Se bond is predominantly involved (Figure 5.6, red diamonds). The errors are drastically reduced in these cases when BLYP structures are used. The opposite is seen for many excitations that mostly affect CC or CN bonds (blue squares), which is in line with the good performance of LH12ct-SsifPW92 for these bond lengths (see above).

5.4.3 Phosphorescence Energies

As outlined in Section 5.2.3, new reference values were obtained for the phosphorescence energies from the Adamo and Ehara test set using the SAC-CI/D95(d) structures from ref. 274 at which CC2/CBS+CC3 single-point energies were obtained. The results are compared against SAC-CI, RI-CC2, CC3/cc-pVDZ and some experimental values in Table A.8 (Appendix A.10). The better agreement of the new CC3/CC2/CBS values with the available experimental data is in line with the established and broad reliability of CC3 for VEEs.^[26,290–292] Therefore, the CC3/CC2/CBS values are used as the reference

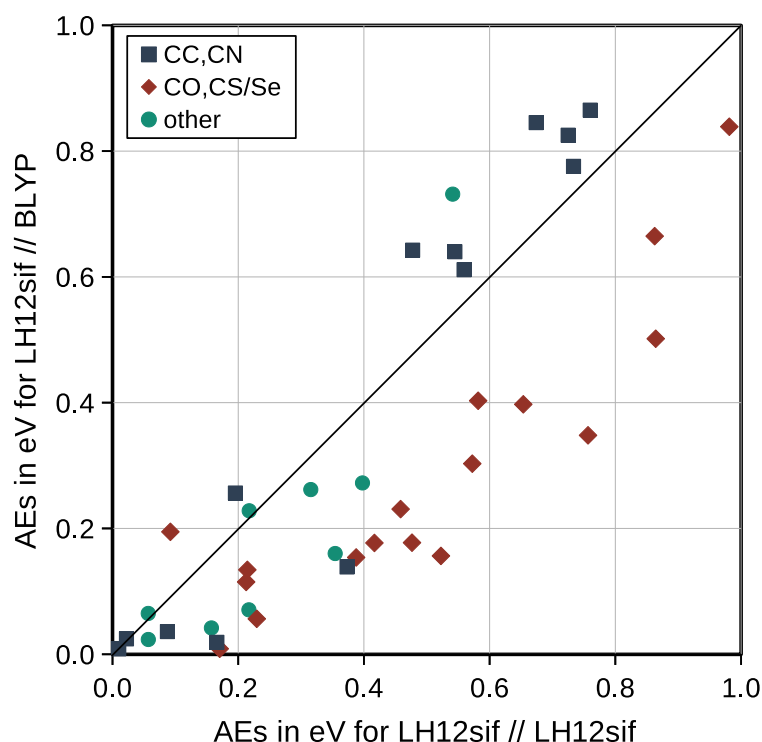


Figure 5.6: Effect of the ES structures on the absolute errors for fluorescence energies with LH12ct-SsifPW92. The classification of the data points is based on the bond that is predominantly involved in the excitation (breakdown in Supporting Information of ref. 264).

data for the present benchmarking. Note, that it is possible, however, to draw the same qualitative conclusions when using the SAC-CI/D95(d) phosphorescence energies from ref. 274.

As for fluorescence (cf. Section 5.4.2), TDDFT energies were computed at the relaxed ES structures optimized with the respective XC functional. Additionally, BLYP and LH12ct-SsifPW92 single-point calculations were performed at LH12ct-SsifPW92 and BLYP structures and analogous comparisons were done for PBE0. The statistical results are summarized in Table 5.3 and the raw data is provided in ref. 264 as Supporting Information. Overall, the errors for phosphorescence energies show a much stronger dependence on the XC functional than the fluorescence energies (cf. Section 5.4.2). The MSEs and maximum signed errors are negative throughout, consistent with the well known underestimation of triplet excitation energies by TDDFT.^[24,27] While BLYP performs best for fluorescence energies (cf. Section 5.4.2), it exhibits the largest MAE (0.65 eV) for the phosphorescence energies. Similarly, TPSSh (0.61 eV) and PBE0 (0.53 eV) also trail behind. In contrast to fluorescence, larger EXX admixtures tend to be beneficial for the phosphorescence

Table 5.3: Mean absolute errors, mean signed errors, maximum signed errors, and standard deviations (σ) in eV for 23 phosphorescence emission energies using various XC functionals and the def2-TZVPD basis set. Unless stated otherwise, ES structures were optimized with the same functional.^a

Functional	MAE	MSE	MaxE	σ
BLYP	0.65	−0.65	−1.54	0.36
PBE0	0.53	−0.53	−1.02	0.23
TPSSh	0.61	−0.42	−1.06	0.24
M06	0.41	−0.41	−0.83	0.21
M06-2X	0.20	−0.13	−0.75	0.22
ω B97X ^a	0.35	−0.26	−0.97	0.40
CAM-B3LYP ^b	0.44	−0.42	−1.34	0.39
LH07t-SVWN	0.35	−0.35	−0.72	0.18
LH07s-SVWN	0.42	−0.42	−0.73	0.17
LH12ct-SsirPW92	0.20	−0.16	−0.57	0.18
LH12ct-SsifPW92	0.19	−0.13	−0.56	0.19
LH20t*	0.22	−0.19	−0.71	0.21
LH12ct-SsifPW92//BLYP	0.23	−0.20	−0.60	0.18
BLYP//LH12ct-SsifPW92	0.56	−0.55	−1.37	0.31
LH12ct-SsifPW92//PBE0	0.21	−0.13	−0.62	0.21
PBE0//LH12ct-SsifPW92	0.52	−0.52	−0.96	0.21
TDA PBE0	0.24	−0.24	−0.51	0.15
TDA M06-2X	0.14	0.06	0.39	0.17
TDA LH12ct-SsifPW92	0.12	0.03	0.30	0.15

Due to convergence problems (instabilities) results exclude:

^a Furan (1^3B_2), uracil ($1^3A'$), and coumarin ($1^3A'$).

^b Uracil ($1^3A'$) and coumarin ($1^3A'$).

energies. This is also observed for the M06-type functionals for which the MAE is drastically reduced from of 0.41 eV to 0.20 eV when the amount of EXX is doubled from 27% in M06 to 54% in M06-2X. The RSHs ω B97X and CAM-B3LYP do not improve over GHs, and CAM-B3LYP even produces the largest individual error of -1.34 eV. LH12ct-SsifPW92 exhibits the overall best performance (MAE of 0.19 eV and maximum signed error -0.56 eV). LH12ct-SsirPW92 performs almost as well as LH12ct-SsifPW92. Errors with LH07t-SVWN and LH07s-SVWN are distinctly larger but not worse than with GHs. The good performance of LHs for phosphorescence energies is consistent with previous results for triplet absorption energies^[24,25] and for AEEs/ 0–0 energies (see above, Section 5.4.1). The superior performance of the LH12 local hybrids compared to the LH07 functionals is largely due to the use of a *common* t-LMF in LH12ct-SsirPW92 and LH12ct-SsifPW92, i.e. an LMF constructed from the total (spin summed) quantities as given in eq. 2.79a-b. For closed-shell GSs and singlet excitations, these common-LMFs are identical to the spin-resolved versions used in LH07t-SVWN and LH07s-SVWN. However, for

triplet excitations, where the α and β transition density matrices carry opposite signs, the common LMF leads to cross terms in the XC kernel. It is assumed that these terms recover some of the static correlation of the triplet excited states (cf. Section 2.3.2).

The single-point calculations with LH12ct-SsifPW92 at BLYP and PBE0 optimized ES structures give slightly larger MAEs (0.23 eV and 0.21 eV) than those obtained at LH12ct-SsifPW92 optimized structures (0.19 eV) and also slightly larger maximum signed errors and standard deviations. But the differences are too small (particularly with PBE0) to indicate a significant advantage of using triplet ES structures optimized using LHs. Note, however, that optimized ES structures at a given computational level are required if ES vibrational frequencies are to be calculated at the respective level.

The effect of the Tamm–Dancoff approximation (eq. 2.146) has also been studied as it is well known that the TDA mitigates the triplet instability problem^[293] and counteracts the systematic underestimation of triplet VEEs.^[24,25,294] For the present test set of phosphorescence energies, these trends are confirmed for the GHs PBE0 and M06-2X as well as for LH12ct-SsifPW92 (Table 5.3). The underestimation of phosphorescence energies is significantly reduced, as indicated by increased (less negative) MSEs and maximum signed errors. This blue-shift is associated with a considerable reduction of the MAE for all three functionals. The effect is strongest for PBE0, which shows the most distinct underestimation at the full linear-response level of theory and hence benefits most from the blue-shift. LH12ct-SsifPW92 and M06-2X already perform well at the full linear-response level and exhibit only a moderate underestimation of phosphorescence energies. Therefore, the blue-shift by the TDA also turns out to be less effective in reducing the MAE and even leads to a slight overestimation of phosphorescence energies in some individual cases.

5.5 Results for Vibrational Frequencies and Vibronic Spectra

5.5.1 Harmonic Excited-State Vibrational Frequencies

The analysis of ES vibrational frequencies indicates how well a given XC functional describes the curvature of the ES potential-energy surface at stationary points. It must be noted, however, that vibrational frequencies are usually significantly overestimated (cf. error distribution in Figure A.4 in Appendix A.8). This is largely due to the harmonic approximation and can be addressed by calculating a functional-specific scaling factor

Table 5.4: Mean absolute errors (in cm^{-1}) for raw (unscaled, ν^{raw}) and scaled (ν^{scal}) vibrational ES frequencies from the Furche and Ahlrichs test set^[35,39] calculated with various standard XC functionals and four LHs. The number of parameters for each subset is given in parentheses in the header line. 'Total' also contains unrestricted calculations not falling into the 'Singlet' or 'Triplet' categories.

Functional	Total (80)		Singlet (64)		Triplet(11)	
	ν^{raw}	ν^{scal}	ν^{raw}	ν^{scal}	ν^{raw}	ν^{scal}
SVWN	70 ^a	68 ^a	75	72	63	62
PBE	48 ^b	48 ^b	50 ^b	48 ^b	49	53
TPSS	53 ^{b,c}	48 ^{b,c}	56 ^b	49 ^b	46 ^c	54 ^c
TPSSh	63	45	67	46	41	47
PBE0	76	44	81	45	50	40
LH07s-SVWN	70	46	74	48	50	40
LH07t-SVWN	75	44	80	45	52	39
LH12ct-SsirPW92	81	45	85	46	60	42
LH12ct-SsifPW92	82	47	86	48	66	42

Due to instabilities of the reference state, the statistics exclude:

^a $1^2\Sigma^+$ state of NO.

^b 2^1A state of propynal.

^c $1^3A''$ state of CH_2O .

based on a minimization of the mean squared error that evens out the systematic overestimations.^[295] Hence, the scaled MAEs give a more adequate view of the statistical errors of a given functional.

From the results in Table 5.4, it can be seen that LHs perform comparably well as the GH PBE0, regardless of whether scaled or raw MAEs are considered (unprocessed data is provided in ref. 212). Overall, TPSS and TPSSh show the smallest raw MAEs, but their advantages disappear for scaled MAEs and TPSSh falls behind somewhat for triplet ESs. Turning to the LHs, the performance for triplet-state vibrational frequencies is better than for singlet states. A slight systematic increase in the raw MAEs is observed with increasing prefactor of the t-LMF, most apparently so for triplet ESs.

5.5.2 Vibronic Spectra

Technical Considerations

The accuracy of the seminumerical integration scheme used for the LH implementation depends on the quality and size of the quadrature grid. In contrast to the conventional analytical implementation used for GHs, the rate-determining step of the LH implementation scales linearly with the total number of grid points (cf. Section 4.3.4). It is therefore

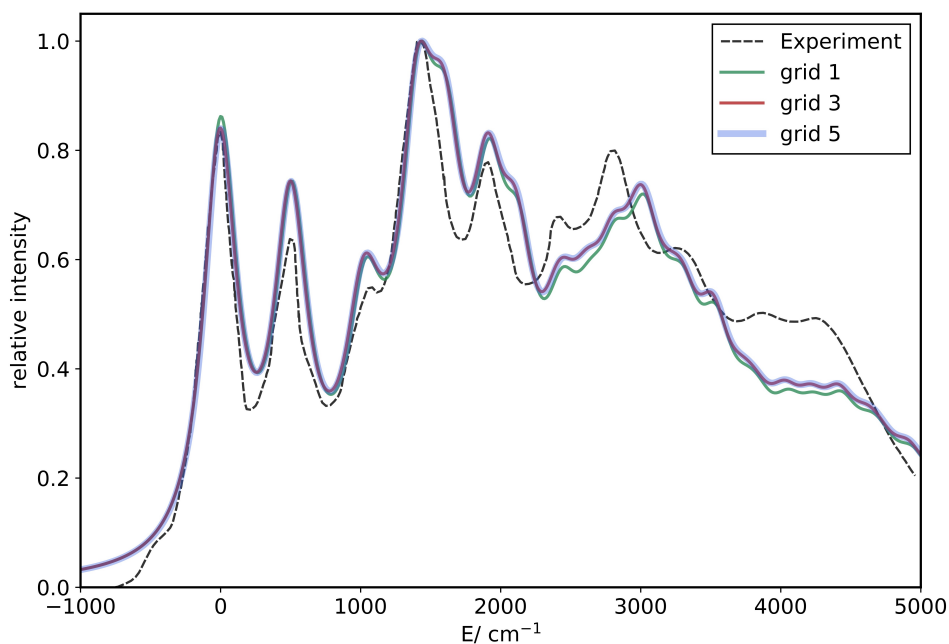


Figure 5.7: Influence of the DFT quadrature grid size on the shape of the vibronic absorption spectra for the $1^1A_g \rightarrow 1^1B_{2u}$ transition of naphthalene computed at the LH07t-SVWN/ def2-TZVP level. The blue bold line shows the grid 5 result, which serves as a reference for the other grid settings. The dashed line corresponds to the experimental spectrum from ref. 296.

desirable to keep the grid size reasonably small, especially when several hundred LH gradients are to be calculated within a finite-difference calculation of vibrational frequencies. As analyzed in Section 4.3.2, using the smallest TURBOMOLE grid (grid size 1) is usually sufficient for accurate ES structures. However, some outliers occurred, and the effect on vibrational frequencies was not scrutinized so far. Hence, the effect on the shape of the vibronic spectra for the $1^1A_g \rightarrow 1^1B_{2u}$ transition of naphthalene for three grid sizes was investigated and is shown in Figure 5.7. The spectrum obtained with grid size 3 is virtually identical to the one using the very large grid (grid size 5) and only small deviations are observed for grid size 1. While these are certainly irrelevant for most applications, the medium-sized grid (grid size 3) is used for the present benchmarking. The mean absolute deviations (maximum signed deviations) for the GS vibrational frequencies with the smaller grids compared to the large grid (grid size 5) are $5.0 \text{ cm}^{-1} (+17.8 \text{ cm}^{-1})$ for grid size 1 and $0.4 \text{ cm}^{-1} (-1.6 \text{ cm}^{-1})$ for grid size 3. They are slightly larger for the ES, $6.2 \text{ cm}^{-1} (+24.8 \text{ cm}^{-1})$ for grid 1 and $0.5 \text{ cm}^{-1} (-1.9 \text{ cm}^{-1})$ for grid size 3.

Note that a technical discussion of the features and peculiarities of the real-time generating function approach within the **radless** implementation is outside the scope of this thesis. It is discussed in detail in works of Tapavicza, Sundholm and coworkers.^[217,226,228,297]

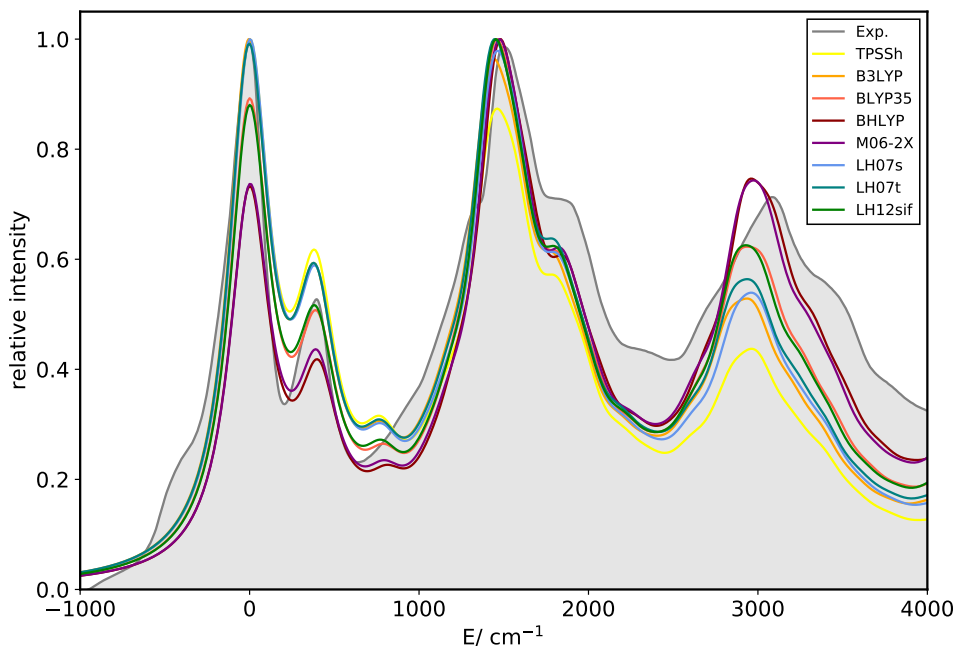


Figure 5.8: Vibronic absorption spectra for the $1^1A_g \rightarrow 1^1B_{2u}$ transition of anthracene computed with various XC functionals in comparison with the experimental vapor absorption spectrum.^[296] A lifetime of 36.3 fs was used for the line broadening. Functional abbreviations: LH07s: LH07s-SVWN, LH07t: LH07t-SVWN, LH12sif: LH12ct-SsifPW92.

Closed-Shell Singlet Absorption Spectra

First, several absorption spectra of molecules with a closed-shell GS are considered. The $1^1A_g \rightarrow 1^1B_{2u}$ transition of anthracene is used as an illustrative example for the differences among the XC functionals evaluated (Figure 5.8). Comparing B3LYP (20% EXX), BLYP35 (35% EXX), and BHLYP (50% EXX) gives a good impression of how EXX admixture can affect the shape of vibronic spectra. While the intensity of the first two peaks is lowered with increasing EXX admixture, and the large middle peak remains rather unaffected, the trend is reversed for the last dominant peak where the intensities increase. This trend is in line with the observations by Grimme and coworkers.^[275] The mGGA-based GH TPSSh, which was very successful for CC and EH bond lengths (cf. Section 5.3.2) and for the fluorescence energies (cf. Section 5.4.2), was tested here as well. Note, however, that advantages for energetics are not visible in the zero-shifted spectra and that good structures do not necessarily entail correct vibrational frequencies. Then the comparatively poor intensity ratios with TPSSh can be understood. They underline that the amount of EXX admixture is usually more important than the choice of the (semi-)local XC contributions. Even results with the highly empirical mGGA-based M06-2X GH (54% EXX) closely resemble the spectra obtained with the much simpler BHLYP functional. Likewise,

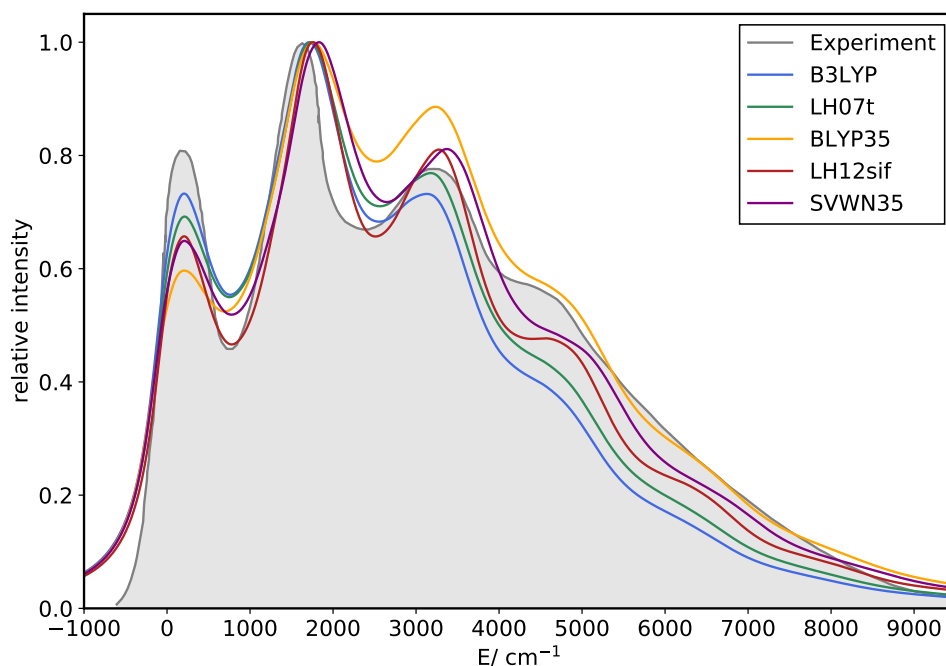


Figure 5.9: Vibronic absorption spectra for the $1^1A_g \rightarrow 1^1B_u$ transition of stilbene computed with the LHs LH07t-SVWN and LH12ct-SsifPW92 as well as with the GHs B3LYP, BLYP35 and SVWN35 in comparison with the experimental spectrum (recorded at 77 K in methylpentane).^[298] A lifetime of 20.6 fs was used for the line broadening to match the experimental spectrum.

the LH spectra are similar to spectra of GHs with comparable (density-averaged) EXX admixture, i.e. LH07t-SVWN is close to B3LYP and LH12ct-SsifPW92 almost coincides with BLYP35. This resemblance is observed for many of the investigated absorption spectra, which are compiled in Appendix A.11. This mainly applies to molecules with a rather rigid structure like acenes. For transitions in more flexible molecules like the $1^1A_g \rightarrow 1^1B_u$ transition of stilbene (Figure 5.9), somewhat larger differences are observed. In this case, LH12ct-SsifPW92 gives slightly better results than BLYP35, and the resulting overall fit with the experimental spectrum is remarkable. To validate that these differences are not the result of the altered underlying (semi-)local exchange and correlation functional in the LHs, the calculations were repeated with an SVWN-based GH with 35% EXX. This provides a spectrum that differs distinctly from that obtained with LH12ct-SsifPW92. For the $1^1A_g \rightarrow 1^1B_u$ transition of a similar molecule with an extended polyene bridge between the two phenyl moieties (1,14-diphenyltetradecaheptaene), the differences are smaller but interestingly in favor of the LH for both comparison settings, i.e. B3LYP vs. LH07t-SVWN and BLYP35 vs. LH12ct-SsifPW92, respectively (Figure 5.10). The differences are relatively subtle, and counterexamples likely exist. Hence, at this stage, the

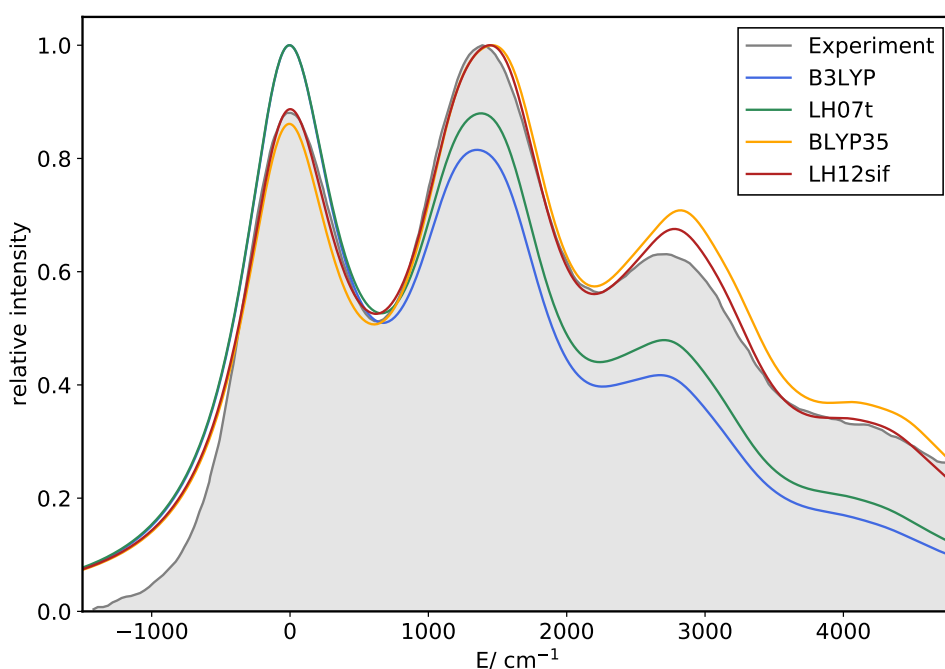


Figure 5.10: Vibronic absorption spectra for the $1^1A_g \rightarrow 1^1B_u$ transition of 1,14-diphenyltetradecaheptaene computed with the LHs LH07t-SVWN and LH12ct-SsifPW92 as well as with the GHs B3LYP and BLYP35 in comparison with the experimental spectrum (recorded at 18 °C in carbon disulfide).^[299] A lifetime of 13.3 fs was used for the line broadening to match the experimental spectrum.

overall conclusion is that LHs do not significantly improve or deteriorate results obtained with comparable GHs for the simulation of the shape of singlet absorption spectra of ordinary organic molecules.

Open-Shell Absorption Spectra

For the eleven spectra of open-shell molecules (two are shown in Figure 5.11 and 5.12) a more definite statement is possible. The general observation is that for larger EXX admixture, i.e. when comparing BLYP35 and LH12ct-SsifPW92, the LH usually gives somewhat better results than the GH. The only exception is the $1^2A_u \rightarrow 1^2B_{2g}$ transition of the PMDA radical anion (Figure A.33 in Appendix A.11). Overall, for lower EXX admixture (i.e. B3LYP vs. LH07t-SVWN) the differences are smaller and the LH is not necessarily better. The good performance of LHs in the case of open-shell molecules can be understood in terms of the more balanced description of spin localization/ delocalization and left-right (static) correlation in local hybrid functionals.^[18] The benefits are expected to be much more pronounced for systems with a mixed-valence GS or ES, where this delicate balance is often decisive.

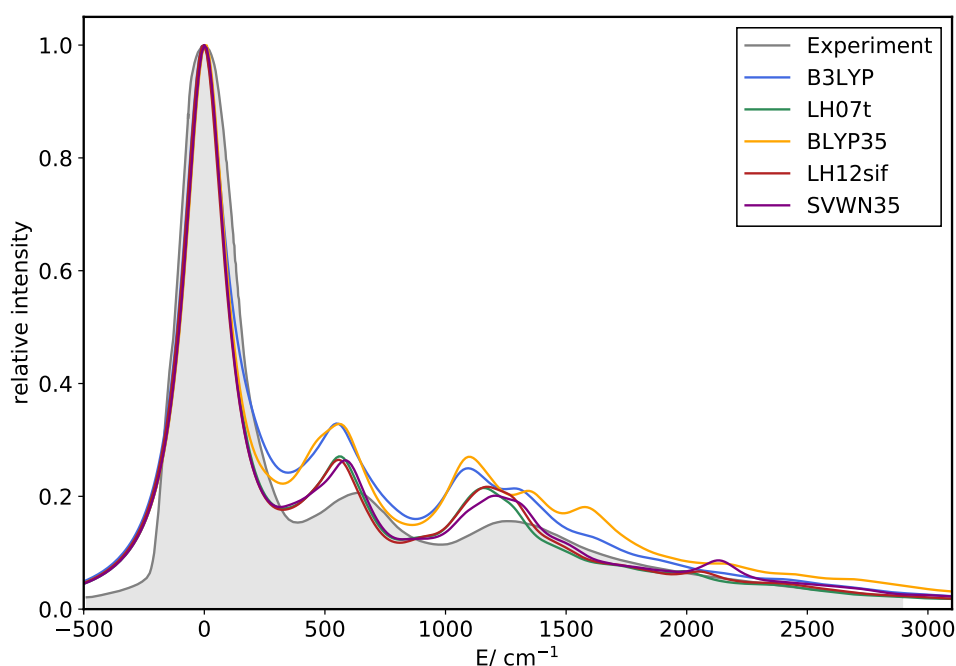


Figure 5.11: Vibronic absorption spectra for the $1^2A_2 \rightarrow 1^2A_2$ transition of the naphthalic anhydride radical anion computed with the LHs LH07t-SVWN and LH12ct-SsifPW92 as well as with the GHs B3LYP, BLYP35 and SVWN35 in comparison with the experimental spectrum (recorded at 77 K in methyltetrahydrofuran).^[300] A lifetime of 50.8 fs was used for the line broadening to match the experimental spectrum.

For the spectra of the $1^2A_2 \rightarrow 1^2A_2$ transition of the naphthalic anhydride radical anion, a striking similarity of the LH07t-SVWN and LH12ct-SsifPW92 spectra on one side and of the B3LYP and BLYP35 spectra on the other side is observed (Figure 5.11). At first sight, this seemed like a potential showcase for the intrinsic advantages of LHs. However, additional test calculations with a GH based on the SVWN functional (SVWN35) indicate that, in this case, favorable error compensation from the underlying LSDA exchange and correlation functionals, rather than the sophistication of the LHs, provides advantages over the GGA-based BLYP-GHs.

As a final case, the agreement of the LH12ct-SsifPW92 absorption spectrum with the experimental spectrum for the $1^2B_{2g} \rightarrow 1^2B_{1u}$ transition of the tetracyanoquinodimethane anion deserves special notice. As analyzed by Tapavicza *et al.*,^[217] this case is particularly challenging in the sense that the vibronic effects cannot be recovered by a BO molecular dynamics sampling but require a quantum harmonic oscillator treatment as achieved by their **radless** implementation. Compared to the PBE0 spectrum reported in ref. 217, LH12ct-SsifPW92 gives an even better agreement with the experimental spectrum. Such

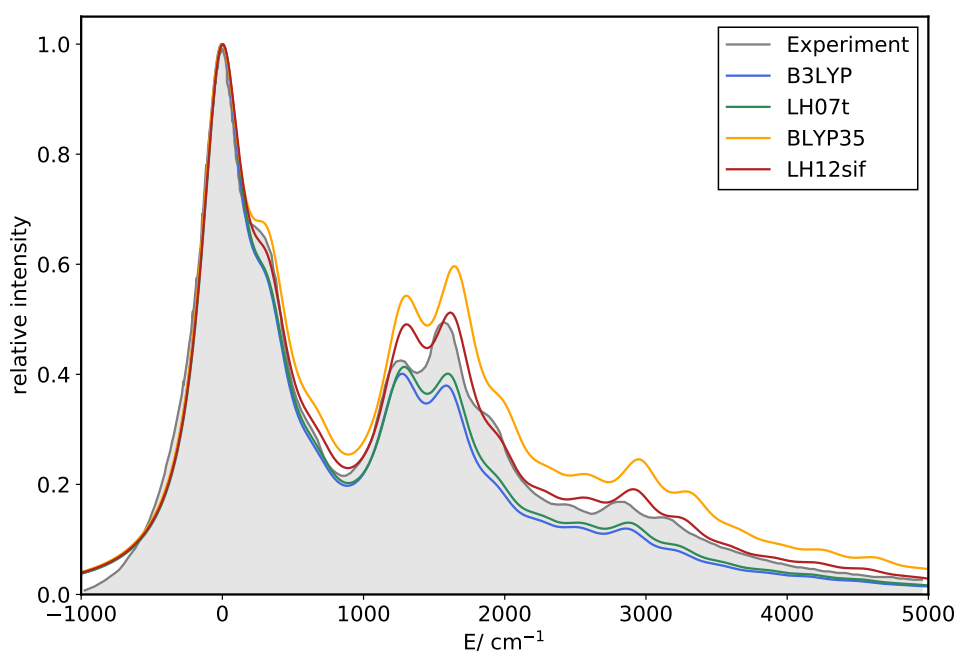


Figure 5.12: Vibronic absorption spectra for the $1^2B_{2g} \rightarrow 1^2B_{1u}$ transition of the tetracyanoquinodimethane radical anion computed with the local hybrids LH07t-SVWN and LH12ct-SsifPW92 as well as with the global hybrids B3LYP and BLYP35 in comparison with the experimental spectrum (recorded in acetonitrile).^[301] A lifetime of 29.0 fs was used for the line broadening to match the experimental spectrum.

cases highlight the importance of the availability of ES gradients at a certain computational level already for supposedly simple tasks such as computing absorption spectra.

Phosphorescence Spectra

Finally, vibronic phosphorescence spectra for the $T_1 \rightarrow S_0$ transition of *p*-methylacetophenone (Figure 5.13) and *p*-hydroxybenzaldehyde (Figure 5.14) are presented as illustrative examples for the favorable interplay of the good performance of LHs for ES structural parameters and for the shape of vibronic spectra on one hand and the remarkable performance for phosphorescence energies on the other hand. First, it is important to note, that triplet-singlet transitions are spin-forbidden and that oscillator strengths calculated from the electronic transition dipole moment obtained within a non-relativistic TDDFT calculations are therefore not physically meaningful. In the scaled vibronic spectra, however, the ratio of the intensities depends on the ratio of the underlying FC factors, i.e. on overlap integrals of the nuclear vibrational wave functions. Hence, the same approach as for singlet transition spectra is applied here.

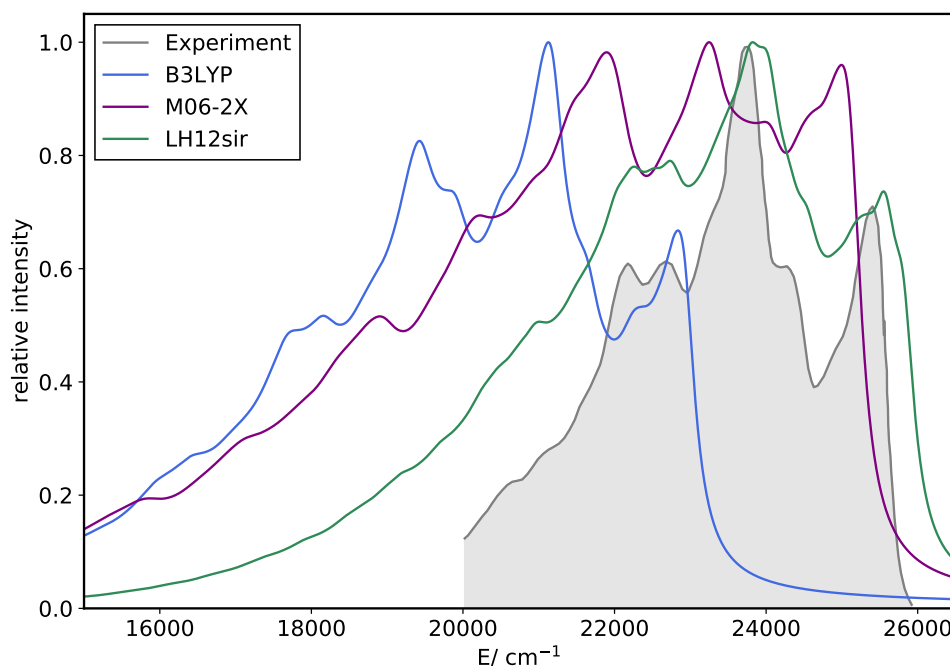


Figure 5.13: Vibronic phosphorescence spectra for the $T_1 \rightarrow S_0$ transition of *p*-methylacetophenone computed with LH12ct-SsirPW92 as well as with B3LYP and M06-2X in comparison with the experimental spectrum (recorded at 77 K in EPA glass).^[302] The position of the absorption maxima was not adjusted for this plot. A lifetime of 30.0 fs was used for the line broadening to match the experimental spectrum.

The shape of the B3LYP spectrum for *p*-methylacetophenone in Figure 5.13 exhibits the best agreement with the experimental spectrum. In particular, B3LYP gets the intensity ratio of the two rightmost peaks correct. As with the other functionals, the drop of the intensity for lower wavenumbers is not as rapid as in the experimental spectrum. The major shortcoming of the B3LYP spectrum is the distinct underestimation of the phosphorescence energy (red shift) by ca. 2500 cm^{-1} (0.31 eV). M06-2X gives a much better agreement in terms of energies, underestimating the phosphorescence energy by only ca. 300 cm^{-1} (0.04 eV), but it gives a poorer description for the shape of the spectrum. The LH12ct-SsirPW92 spectrum offers both, an excellent agreement of the transition energy (blue shift by ca. 200 cm^{-1} or 0.02 eV) and a reasonable description of the major features and intensity ratios of the vibronic fine structure of the spectrum. The situation is similar for the spectra of *p*-hydroxybenzaldehyde (Figure 5.14). While the shape of the B3LYP and LH12ct-SsirPW92 spectra are very similar, the LH12ct-SsirPW92 spectrum is much less red shifted. Again, the red shift is also small with M06-2X but the overall shape of the spectrum does not fit as well with experiment. For a more definite assessment, further phosphorescence spectra will have to be considered, which is beyond the scope

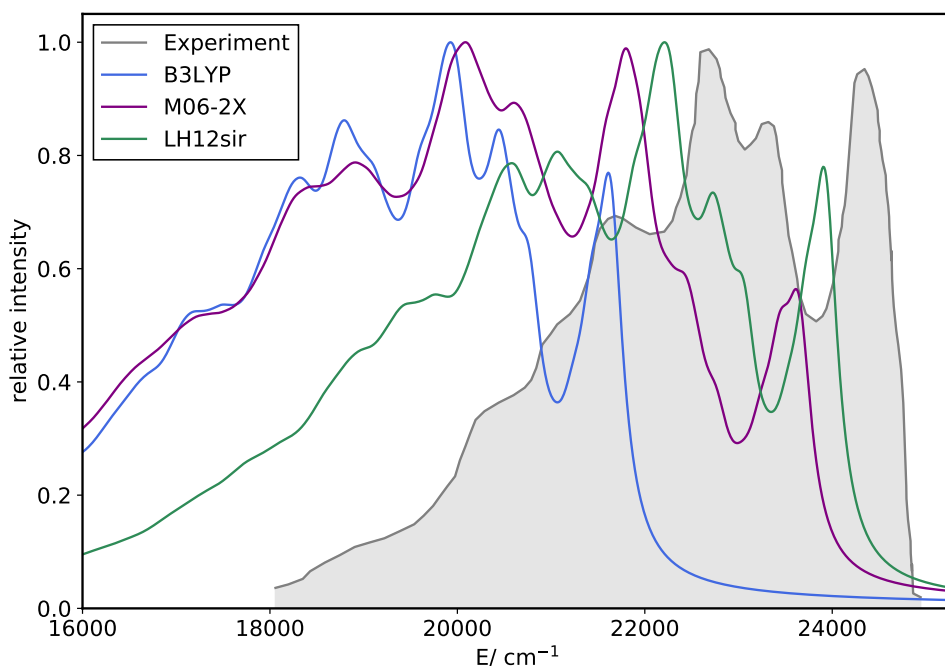


Figure 5.14: Vibronic phosphorescence spectra for the $T_1 \rightarrow S_0$ transition of *p*-hydroxybenzaldehyde computed with LH12ct-SsirPW92 as well as with B3LYP and M06-2X in comparison with the experimental spectrum (recorded at 77 K in PME).^[303] The position of the absorption maxima was not adjusted for this plot. A lifetime of 33.1 fs was used for the line broadening to match the experimental spectrum.

of this thesis. For completeness, note that some unsuccessful attempts to simulate the phosphorescence spectra of *p*-chloroacetophenone and indanone are included in ref. 264, where none of the tested functionals delivered satisfactory agreement with the shape of the experimental spectra, presumably because of the neglect of environmental effects.

5.6 Conclusions

The ES gradients implementation of LHs described in Chapter 4 was used to validate LHs for a wide range of ES properties including ES structures, emission energies, AEEs, 0–0 energies, and harmonic vibrational frequencies. Moreover, the implementation was used to compute the ingredients for the simulation of vibronically resolved spectra within the FC approximation.

For the ES structural parameters, a first assessment for a test set of small molecules with available experimental gas-phase data revealed comparable performance as with standard GHs such as PBE0. No significant differences were observed regarding the multiplicity of the ESs. For a larger test set of small to medium-sized molecules that employs coupled-

cluster reference values, a more differentiated analysis w.r.t. bond types was conducted. The overall performance is mixed: Compared to a range of semilocal functionals, GHs, and RSHs, the investigated LHs provide some of the best ES carbon-nitrogen, carbon-carbon, element-hydrogen, and particularly carbon-halogen bond lengths. They do not, however, improve notably on the too short ES carbonyl, thiocarbonyl, or selenocarbonyl bonds provided by most GHs and RSHs. Here any type of EXX admixture appears to deteriorate the agreement with the high-level reference data. Notably, however, these are also the bonds where the inclusion of triple excitations is crucial in ES coupled-cluster computations as well.

The benchmark of spectroscopic AEEs/ 0–0 energies revealed competitive performance of LHs for singlet excitations and remarkable performance for triplet excitations outperforming standard GHs. These findings are consistent with previous findings for VEEs. In the case of fluorescence energies, the currently available LHs also do not generally improve over standard GHs such as TPSSh or even over the BLYP semilocal functional. However, closer analysis revealed this to be due to the too short ES carbonyl or thiocarbonyl bonds (see above). The already proven strength of LHs for VEEs and AEEs/ 0–0 energies of triplet ESs has also been confirmed for the emission energies of triplet ESs for a test set of medium-sized organic chromophores. Only the highly parameterized M06-2X functional was found to be on a par with the most successful LHs LH12ct-SsirPW92, LH12ct-SsifPW92, and LH20t* for these phosphorescence energies.

LHs were found to be reliable for the calculation of harmonic ES vibrational frequencies without particular advantages over standard GHs. Likewise, the shapes of vibronic absorption spectra for singlet ESs did not provide any indications for substantial improvements by LHs over standard global ones. In particular, LHs do not overcome the system dependence of optimal EXX admixtures found previously with GHs.^[275] The vibronic absorption spectra with LHs for closed-shell GSs are on par with those obtained with GHs, while a slight improvement of the shapes appears to be achieved for systems with open-shell GSs. The advantages for phosphorescence energies and the robust performance for the shape of vibronic spectra worked together for reliable emulation of some experimental phosphorescence spectra. The M06-2X functional, which was also among the top performers for phosphorescence energies, has been found to give the position of the peaks correctly but was not capable to reproduce the vibronic shape of these spectra accurately. The opposite was seen with B3LYP, whereas local hybrids provide both good energies and spectral shapes. Therefore, local hybrids could become a valuable tool for the prediction of phosphorescence spectra.

6 Validation of Local Hybrid Functionals for Electric Properties

In this chapter, an extensive benchmark study of local hybrid functionals for dipole moments and static and dynamic polarizabilities is conducted. It is reproduced (adapted) and reprinted with permission from ref. 286 [R. Grotjahn, G. J. Lauter, M. Haasler, M. Kaupp, *J. Chem. Phys. A*, **2020**, *124*, 8346]. Copyright 2020 American Chemical Society.

6.1 Introduction

As discussed in previous chapters, the accuracy of (TD)DFT results depends on the selected XC functional and the associated XC potential, kernel and hyper-kernel. To guide this selection process, meaningful benchmark studies are a vital source of information and numerous such studies attracted considerable attention (see, e.g., ref. 6,7,118,304–307 and references cited therein). As most of chemistry happens on GS potential-energy surfaces, flexible parameters in (semi-)empirical XC functionals are often optimized with respect to GS energies, e.g. thermochemistry and reaction barriers.^[7] Lately, this energy-focused approach has led to lively discussions if DFT is "straying from the path toward the exact functional" by not producing very good electron densities.^[49–56] While opinions are divided on this issue, a bottom line may be that an XC functional's ability to give reasonable electron densities should not be sacrificed light-mindedly. Spectroscopic examples where electronic (spin-)densities in particular regions of space are sampled, e.g. near nuclei as for hyperfine couplings,^[308,309] are pertinent to this discussion. As a simple, more global measure of the electron density, and of bond polarity, a molecule's dipole moment may be considered.^[204] In the context of ES properties, which are related to the response of the density to an external electromagnetic field, a logical extension is to also consider polarizabilities, i.e. the first-order change of the dipole moment due to an external electric field (cf. Section 2.4.1). Improving the accuracy for such simple electric properties may then also translate into improved performance for more complex photophysical and photochemical aspects,^[310] and evaluation of such parameters at the same time may serve as an important check on the underlying physical soundness of a given XC functional.

Besides some smaller studies,^[311–315] the by far most comprehensive benchmark data sets available to date for dipole moments and static polarizabilities are those by Hait and Head-Gordon.^[204,205] They generated CCSD(T) reference values extrapolated to the complete basis set limit (CBS) for 152 dipole moments (HHdip-152)^[204] as well as polarizabilities (HHpol-132)^[205] for 132 small molecules and atoms, and they assessed the performance of a considerable number of popular and modern XC functionals. While for both properties improvements were seen when stepping up the Jacob’s Ladder of XC functionals,^[112] differences in performance between individual functionals from the same rung were substantial. For comparison, note that the (regularized) root-mean-square errors (RMSEs) of the wave function methods Hartree–Fock and coupled-cluster singles and doubles (CCSD) are 18.61% and 3.95%, respectively, for the dipole moments,^[204] and 8.45% and 1.62%, respectively, for static polarizabilities.^[205] Considering now only rung 4 functionals, performances for dipole moments range from 4.84% (SOGGA11-X) up to 27.11% (MN12-SX) with standard GH functionals like PBE0 (5.18%), B3LYP (6.98%), or TPSSh (7.42%) falling in between.^[204] For polarizabilities, the RMSEs range from 3.27% (MPW1K) up to 10.69% (M06-HF), and the simpler standard hybrid functionals PBE0 (4.29%), B3LYP(6.25%), and TPSSh (5.44%) are again in the middle.^[205] The authors also noted that the poorer performances of some mGGA or hybrid mGGA functionals are caused by rare but severe failures for some molecules of the test sets, which might be related to overfitting.^[205]

Compared to conventional, global hybrids, the additional flexibility introduced by the LMF in local hybrids allows to adaptively compensate the self-interaction error in some areas of the molecule while maintaining the benefits of the (semi-)local exchange functional in other areas (cf. Section 2.3.2 for details). The recently reported LH20t functional^[17] showed excellent performance for the GMTKN55 main-group energetics test suite,^[6] where it outperformed all GHs and was found to be among the best rung 4 functionals evaluated to date and performs excellent also in other areas such as mixed-valence systems or excitation energies (see Section 2.3.4 for a detailed discussion). However, LH20t exhibits a more sophisticated construction compared to previous, typically one- or two-parameter LSDA-based LHs with nine optimized parameters.^[17] While this is still a small number compared to many highly parameterized semi-empirical hGGAs in wide use, in view of the exclusive optimization for energy quantities and the excellent energetic performance^[17] it seems prudent to make sure that this performance is not obtained by sacrificing the quality of the density distribution and related properties. That is, it should be assured that this new LH “has not strayed from the path”.^[49–56] To assess this issue, and as a basis for evaluating future LHs, here LH20t and some simpler first-generation

LHs are evaluated for their performance for dipole moments and polarizabilities as simple global measures for the accuracy of electron densities and electric-field response. So far only two early LHs have been studied for polarizabilities but for the much narrower case of (hyper)polarizabilities of hydrogen chains and noble-gas atoms using a finite-field approach, which gave promising results.^[316]

The dipole moment $\boldsymbol{\mu}$ of a molecule is readily accessible from the charge density and is defined in eq. 2.101. Alternatively, e.g. when densities are not available at a given computational level, the k -th component ($k \in \{x, y, z\}$) of $\boldsymbol{\mu}$ may be obtained from the change of the energy E when a static external electric field $\boldsymbol{\mathcal{E}}$ with field strength \mathcal{E}_k is applied

$$\mu_k = - \left. \frac{\partial E}{\partial \mathcal{E}_k} \right|_{\mathcal{E}_k=0} \approx - \frac{E(+\delta\mathcal{E}_k) - E(-\delta\mathcal{E}_k)}{2\delta\mathcal{E}_k}, \quad (6.1)$$

which is typically approximated (truncation error $\mathcal{O}(\delta\mathcal{E}_k^2)$) within a central FD approach (eq. 4.7) with finite-field strength $\delta\mathcal{E}_k$. This approach was used in ref. 204 to obtain reference dipole moments at the CCSD(T)/CBS level of theory. In a similar spirit, the components of the static polarizability tensor $\boldsymbol{\alpha}$, which is defined as the first-order change of the dipole moment w.r.t. a static external electric field (eq. 2.103) may be obtained as a second derivative of the energy

$$\alpha_{kk} = - \left. \frac{\partial^2 E}{\partial \mathcal{E}_k^2} \right|_{\mathcal{E}_k=0} \approx - \frac{E(+\delta\mathcal{E}_k) - 2E(0) + E(-\delta\mathcal{E}_k)}{\delta\mathcal{E}_k^2}, \quad (6.2)$$

written here only for the diagonal components and again approximated using a FD formula. Alternatively, the static polarizability as well as the frequency-dependent (dynamic) polarizability can be obtained via LR-TDDFT as outlined in Section 2.4.1.

6.2 Computational Details

The HHdip-152 test set was evaluated using TURBOMOLE's `dscf` module, i.e. dipole moments were obtained from the converged densities following eq 2.101. All calculations were performed as unrestricted Kohn–Sham calculations using the structures provided in ref. 204. No point-group symmetry was exploited. As suggested in ref. 204, the aug-pc-4 basis set^[261,262,317–319] was used to work essentially at the basis-set limit. Dipole moment calculations for the HF and FCl dissociation curves were performed with the aug-pc-3 basis set. As a recent study by Zapata *et al.* showed,^[320] calculations employing somewhat smaller basis sets do not deliver significantly less accurate results for this test set as long as diffuse functions are included. The DFT quadrature grid settings from ref.

204 were best matched by TURBOMOLE’s `gridsize 7`. This grid was solely chosen for benchmark purposes and is impractically large for most applications. For the scans of the GH mixing factor and LMF prefactor, a smaller grid (`gridsize 4`) was used to reduce the computational costs. For the HHpol-132 test set, the structures from ref. 205 and the same settings as for dipole moments were used. In contrast to ref. 205, the default methodology of the present work for the calculation of polarizabilities uses the response approach described in Section 2.4.1. For comparison, the finite-field scheme (eq 6.2) was applied for the global hybrid PBE0 as well as the local hybrid LH20t. For consistency with the original publication, the calculation of static and dynamic polarizabilities from ref. 310 used different settings: the structures for benzene, furan, pyrrole, imidazole, pyridine, pyrimidine, pyrazine, and pyridazine were taken from the Thiel test set,^[26] and the remaining structures (benzonitrile, oxazole, phenol, phosphole, thiazole, thiophene) were optimized at the same level (MP2/6-31G(d)) using Gaussian 16.^[321] For the calculation of (dynamic) polarizabilities, the aug-cc-pVTZ basis set^[259,260] was used. Dynamic polarizabilities were calculated at frequencies of 0.072003 au and 0.093215 au chosen in ref. 310 to match experimentally relevant laser wave lengths (632.8 nm and 488.8 nm, respectively).

The LHs LH07t-SVWN, LH07s-SVWN, LH12ct-SsirPW92, LH12ct-SsifPW92, LH14t-calPBE, and LH20t were investigated (see Section 2.3.4 for a detailed description). To evaluate the impact of the CF, the LH20t* functional obtained upon removing the CF was also studied. The impact of cross spin-channel terms in common-LMFs, which are thought to bring in some additional nondynamical correlation contributions,^[178] was assessed by examining a common-LMF variant of LH07t-SVWN with the same prefactor $b = 0.48$ (LH-0.48ct-SVWN). To explore the impact of the self-interaction reduction in the correlation part of the LH12 functionals, a custom local hybrid termed LH-0.709ct-SVWN, which uses the LMF of LH12ct-SsifPW92 but the simpler VWN correlation functional, was studied. Some additional results for comparison were obtained with the XC functionals PBE,^[123] B3-LYP,^[10,124] PBE0,^[123,138] BHLYP,^[9,124] TPSSH,^[132,140] M06,^[143] M06-2X,^[143] PW6B95,^[142] ω B97M-V,^[155] SCAN0,^[139] and CAM-B3LYP.^[151] To analyze how EXX admixture affects dipole moments and static polarizabilities, the hybrid mixing factor in GHs and the LMF prefactor in LHs were scanned systematically in steps of 0.05 from 0.0 to 1.0 for some GHs and LHs (keeping all other parameters the same for a given type of functional). This was done for the subset of 58 non-spin-polarized (NSP) cases contained in both the HHdip-152 and the HHpol-132 test sets. The NSP character makes SCF and TDDFT convergence easier for the more extreme parameter ranges.

The dipole moments from the HHdip-152 test set span a range of almost three orders of magnitude ranging from 0.021 D for the OF molecule to 9.007 D for the ionic NaCl species

(CCSD(T)/ CBS values). This is a challenge for the statistical evaluation, i.e. which error definition is appropriate to use. On the one hand, rather small absolute changes in the dipole moment can lead to considerable relative errors if the respective dipole moment is small. On the other hand, absolute errors can become relatively large and dominate the statistics for species with large dipole moments. As a solution to this problem, a “regularized” error is used in ref. 204, which is adopted for this work. That is, up to reference dipole moments of 1 D, (dimensionless) total errors enter the statistics, and above that mark relative errors are considered. With that convention, the “regularized” root-mean-square error (RMSE) and mean signed error (MSE) read

$$\text{RMSE} = \sqrt{\frac{1}{n} \sum_{i=1}^n \left(\frac{\mu_i - \mu_i^{\text{ref}}}{\max(\mu_i^{\text{ref}}, 1\text{D})} \right)^2} \quad (6.3)$$

and

$$\text{MSE} = \frac{1}{n} \sum_{i=1}^n \frac{\mu_i - \mu_i^{\text{ref}}}{\max(\mu_i^{\text{ref}}, 1\text{D})} \quad (6.4)$$

respectively. Although μ_i generally refers to the norm of the dipole moment vector $|\boldsymbol{\mu}|$ for a given molecule, it does include the sign of the vector if the direction of the calculated (DFT) dipole moment vector is opposite to that of the reference dipole moment vector. For the static polarizabilities from the HHpol-132 test set, the regularization used for dipole moments is not needed and errors are defined as:

$$\text{RMSE} = \frac{1}{3} \sum_{k=x,y,z} \sqrt{\frac{1}{n} \sum_{i=1}^n \left(\frac{\alpha_{kk,i} - \alpha_{kk,i}^{\text{ref}}}{\alpha_{kk,i}^{\text{ref}}} \right)^2}, \quad (6.5)$$

$$\text{MSE} = \frac{1}{3n} \sum_{k=x,y,z} \sum_{i=1}^n \frac{\alpha_{kk,i} - \alpha_{kk,i}^{\text{ref}}}{\alpha_{kk,i}^{\text{ref}}}. \quad (6.6)$$

Finally, for the set of static and dynamical polarizabilities from ref. 310, isotropic polarizabilities, i.e. the average of the three diagonal components of the polarizability tensor ($\frac{1}{3} \text{tr}(\boldsymbol{\alpha})$), were considered for consistency with the available reference data, and the RMSE is defined as

$$\text{RMSE} = \sqrt{\frac{1}{n} \sum_{i=1}^n \left(\frac{\text{tr}(\boldsymbol{\alpha}_i) - \text{tr}(\boldsymbol{\alpha}_i^{\text{ref}})}{\text{tr}(\boldsymbol{\alpha}_i^{\text{ref}})} \right)^2}. \quad (6.7)$$

Note that all raw data for this study are provided as Supporting Information in ref. 286.

6.3 Results

6.3.1 Dipole Moments

Results for the Benchmark Set

The HHdip-152 test set contains 71 spin-polarized (SP) and 81 non-spin-polarized (NSP) molecules. This classification was made by Hait *et al.*^[204] based on unrestricted HF calculations for which SP molecules do and NSP systems do not break the spin symmetry. Regularized RMSEs for both subsets are presented in Figure 6.1 for a variety of functionals and additional statistical data for the LHs are in Table 6.1. Overall, the results for all LHs cover a relatively narrow range from a total RMSE of 7.46% for LH-0.709ct-SVWN to 5.87% with the most recent LH20t functional. In comparison, the rung 4 functionals investigated in ref. 204 span a much larger range from 27.11% (MN12-SX) down to 4.84% (SOGGA11-X). On one side, this is a natural consequence of the conceptual similarity of the investigated LHs, in particular the almost exclusive use of a scaled t-LMF with LH07s-SVWN being the only functional using a different LMF. On the other side, it also shows that none of the local hybrids studied here has a serious problem with the prediction of dipole moments.

For a more differentiated discussion, first note the impact of the LMF on the performance for dipole moments. LH07s-SVWN is the only LH in this study that uses an s-LMF. It gives a very similar RMSE as the t-LMF based LH07t-SVWN for the NSP subset but a very slightly improved performance for the SP subset. More notably, all

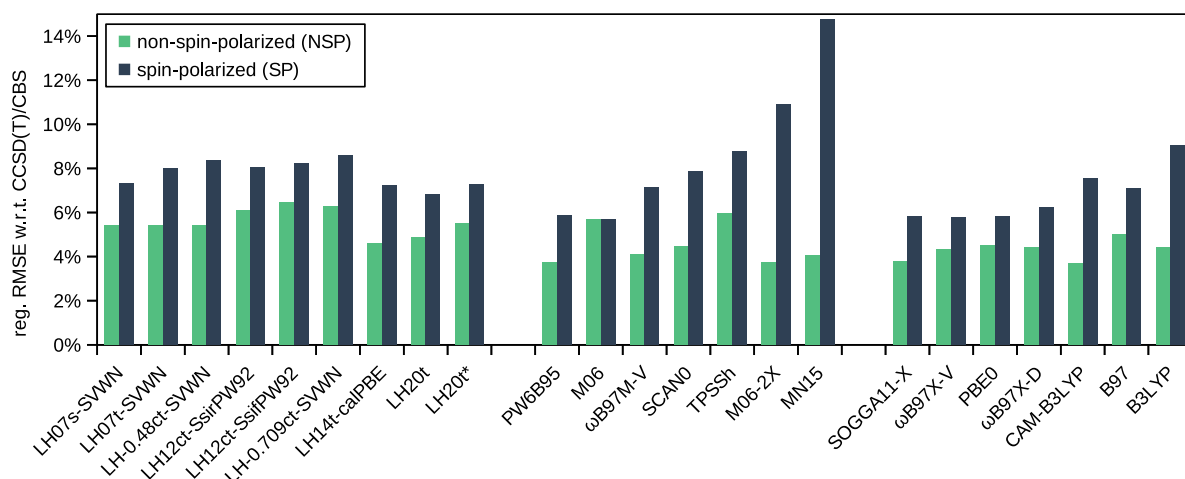


Figure 6.1: Regularized root-mean-square percentage errors w.r.t. CCSD(T)/CBS reference values for various LHs for the HHdip-152 test set^[204] in comparison with previous results^[204] for some hybrid-mGGAs and hybrid-GGAs.

Table 6.1: Statistical measures in percentages w.r.t. CCSD(T)/CBS reference values for the HHdip-152 test set^[204] for LHs. RMSE is the root-mean-square regularized error, MAX the maximum absolute regularized error, MSE the mean signed regularized error, and σ the standard deviation. SP (NSP) is the subset of (non-)spin-polarized systems.

Functional	RMSE			MAX	MSE	σ
	all	NSP	SP			
LH07s-SVWN	6.39	5.44	7.32	30.69	0.67	6.37
LH07t-SVWN	6.75	5.43	8.00	31.46	2.15	6.42
LH-0.48ct-SVWN	6.94	5.43	8.35	33.17	2.13	6.63
LH12ct-SsirPW92	7.08	6.10	8.06	26.57	3.10	6.39
LH12ct-SsifPW92	7.36	6.48	8.24	24.37	3.42	6.53
LH-0.709ct-SVWN	7.46	6.29	8.59	27.10	3.90	6.38
LH14t-calPBE	6.00	4.62	7.26	28.07	1.96	5.69
LH20t	5.87	4.86	6.84	22.63	3.39	4.81
LH20t*	6.40	5.52	7.28	22.21	3.53	5.36

t-LMF-based LHs have a positive MSE between 2-4%, indicating a small but systematic overestimate of the dipole moments, while that for LH07s-SVWN is only 0.67%. This will be analyzed in more detail further below. Going from a spin-channel to a common t-LMF (from LH07t-SVWN to LH-0.48ct-SVWN), while keeping all other things equal, increases the RMSE and standard deviation for the SP systems only very slightly (Table 6.1). Considering the advantages of the common version of the t-LMF for other properties like triplet excitation energies (cf. Section 5.4.1 and 5.4.3 as well as ref. 24 and 25) this minor drawback for dipole moments of SP molecules is probably of secondary importance. As expected, results for the NSP subset remain unaffected because the two LMF versions become identical if the α and β spin channels are equivalent. Increasing just the t-LMF prefactor from LH-0.48ct-SVWN to LH-0.709ct-SVWN increases the RMSE further somewhat for both NSP and SP systems. This finding is consistent with a general trend found also for simpler GHs: larger EXX admixtures can lead to overestimated dipole moments, e.g., PBE0 gives an RMSE of 4.52% for the NSP set and PBE50 an RMSE of 5.15%.^[204] A more detailed analysis of the impact of the LMF prefactor is provided in Section 6.3.3 below.

Replacing VWN correlation in LH-0.709ct-SVWN by short-range self-interaction-free (sif) PW92 correlation gives the energy-optimized LH12ct-SsifPW92.^[178] Effects are marginal, with a slightly increased/ decreased RMSE for NSP/ SP systems, respectively. LH12ct-SsirPW92 has short-range self-interaction-reduced (sir) PW92 correlation and a slightly smaller prefactor ($b = 0.646$).^[178] As one might expect from the above discussion, it gives an overall somewhat smaller RMSE and MSE. Introduction of PBE exchange and

correlation and a pig1 CF in LH14t-calPBE (and having $b = 0.50$) gives a more notable improvement for both NSP and SP systems and the lowest MSE of all t-LMF-based LHs.

LH20t, which is based on PBE exchange and B95 correlation and a more advanced pig2 CF, has a larger t-LMF prefactor ($b = 0.715$) and thus gives a larger positive MSE than LH14t-calPBE. However, the RMSE is similar for both NSP and SP systems, and thus the two more advanced LHs with calibrated energy densities perform slightly better than the uncalibrated ones (LH20t also exhibits the smallest standard deviation, Table 6.1). Removing the pig2 CF that adjusts the gauge of semilocal and exact exchange-energy densities^[17] worsens performance of LH20t slightly. These results show clearly that the more sophisticated construction and parameterization that gives LH20t major advantages over other LHs for, e.g., GMTKN55 energetics,^[17] has no disadvantageous effects on dipole moments as indicators of electron density distributions.

Figure 6.1 includes results from ref. 204 for a selection of other rung 4 XC functionals and several of them provide slightly better dipole moments than LHs. In particular, PW6B95, which uses the B95 correlation functional also utilized in LH20t, surpasses the performance of LH20t with a total RMSE of 4.87%.^[204] For some of the highly parameterized XC functionals, such as M06-2X, the difference between the NSP and SP subset is striking. It is caused by some isolated cases with significant errors that deteriorate the performance for the SP subset, which may indicate overparameterization of the respective functionals.^[204] The data for LHs, especially the MaxEs stated in Table 6.1, confirm that none of the LHs suffer from this problem.

Analysis of Performance for Specific Subsets

To further explore the strengths and weaknesses of local hybrids for dipole moments, smaller selections of molecules are analyzed in more detail. First, a subset of 11 molecules classified in ref. 204 as “difficult cases” is considered. Individual errors are given in Table 6.2. For these molecules, even the best performers from ref. 204, SOGGA11-X or PW6B95, exhibit appreciable RMSEs (10.5% and 13.6%, respectively), while functionals like M06-2X or TPSSh perform even more poorly. The earlier LH07s-SVWN and LH07t-SVWN also fall behind but the new LH20t is overall on par with the best-performing functionals for this subset (RMSE 11.7%). Notably, the errors for SOGGA11-X and PW6B95 are largely statistical (small MSE) but those for LH20t exhibit a positive MSE. Indeed, the critical molecules are different for those functionals: LH20t has somewhat larger positive deviations for BF or BCl compared to those two global hybrids, but it does not share with them the systematic underestimate for NaLi and for fluoroethyne (HCCF)

Table 6.2: Comparison of local hybrids and other rung 4 functionals for the “difficult cases”^[204] from the HHdip-152 test set expressed as regularized percentage deviations.^a

Mol.	TPSSh ^b	ω B97M-V ^b	PW6B95 ^b	SOGGA11-X ^b	M06-2X ^b	LH07s	LH07t	LH12sif	LH20t	LH20t*
BF	21.0	10.1	7.7	10.4	2.7	19.5	22.8	22.8	15.3	18.9
BS	1.6	12.5	6.3	9.6	15.4	14.0	12.7	13.7	17.1	15.2
CF	14.5	10.2	5.0	4.2	-1.6	13.2	13.6	12.0	4.3	7.6
CF ₂	14.0	6.1	3.9	3.0	-2.0	13.0	13.7	11.9	4.5	7.5
H ₂ O-Cl	29.0	10.1	19.2	11.0	3.9	25.6	25.7	22.1	18.8	20.0
H ₂ O-F	31.9	15.6	23.2	11.2	3.5	30.7	31.5	24.4	21.2	21.5
H ₂ O-Li	-12.8	-26.2	-24.2	0.6	-21.5	-0.2	-4.1	12.1	-2.4	7.6
HCCCl	-13.4	-10.0	-12.2	-8.5	-8.1	-13.0	-8.0	-4.9	-0.2	-1.9
HCCF	-16.9	-11.2	-7.2	-8.9	-1.7	-16.3	-11.5	-11.0	-0.3	-5.2
NaLi	25.2	-31.9	-9.9	-23.9	-67.1	3.2	-13.3	4.8	-2.6	10.7
NOCl	-10.5	-4.1	-10.2	-3.6	-6.9	-10.6	-11.4	-7.8	-10.7	-8.7
MSE	7.6	-1.7	0.1	0.5	-7.6	7.2	6.5	9.1	5.9	8.5
RMSE	19.3	15.6	13.6	10.5	22.1	16.7	17.1	14.9	11.7	12.9

^a Abbreviations: LH07s: LH07s-SVWN, LH07t: LH07t-SVWN, LH12sif: LH12ct-SsifPW92.^b Results from ref. 204.

and chloroethyne (HCCCl). Hait *et al.* hypothesized that unrecognized delocalization errors connected to the C \equiv C-X moiety might be the reason for the poor performance of established functionals for the two substituted acetylenes.^[204] LH20t, which was designed with a good balance between (de)localization and left-right correlation in mind,^[17] gives an almost perfect agreement for these systems. LH20t also performs particularly well for the H₂O-Li complex. Neglecting the CF used in LH20t (i.e. LH20t*) deteriorates the accuracy for weakly bound systems like NaLi or H₂O-Li, consistent with the importance of the gauge problem for weaker noncovalent interactions.^[16,17,185] Also note that all LHs and TPSSh have positive MSEs for this subset, while M06-2X exhibits a negative one, and SOGGA11-X, PW6B95 and ω B97M-V show more statistical behavior. This may be of interest in the construction future LH functionals.

Except for LH07s-SVWN, all local hybrids studied here are based on a (spin-channel or common) t-LMF. While this LMF has proven its suitability for many properties, its shortcomings have also been pointed out.^[12] In particular, its steep increase in bonds towards hydrogen atoms was suspected to be undesirable for the nuclear shieldings of protons or of their neighboring nuclei,^[245] and possibly for the atomization energies of element-hydrogen bonds.^[12] Results in Table 6.3 suggest that this feature of the t-LMF may also manifest in systematically overestimated dipole moments for simple diatomic hydride species. The MSEs of all t-LMF-based LHs are clearly more positive than with the s-LMF (LH07s-SVWN), which exhibits a more gradual increase along the E-H bond. While this functional still overestimates the dipole moments to some extent, its overall RMSE of 4.5% for this particular subset of molecules is comparable to that of other rung 4

Table 6.3: Comparison of local hybrids and other rung 4 functionals for dipole moments of diatomic hydrides from the HHdip-152 test set expressed as regularized percentage deviations.^a

Mol.	TPSSh ^b	ω B97M-V ^b	PW6B95 ^b	SOGGA11-X ^b	M06-2X ^b	LH07s	LH07t	LH12sif	LH20t	LH20t*
LiH	-1.1	-1.2	-1.6	0.4	-1.1	0.7	2.9	4.0	2.6	3.6
BeH	-3.7	10.3	7.9	-3.0	1.9	5.5	3.8	-4.8	2.4	-0.2
BH	-1.1	7.7	7.6	12.0	10.6	11.9	18.8	22.5	22.6	22.2
CH	-2.2	2.3	0.2	1.6	3.4	3.1	8.0	8.5	8.7	8.8
NH	-1.2	-0.1	-1.8	-1.7	0.3	-0.3	3.4	2.9	3.7	3.8
OH	-2.1	-0.1	-0.4	-0.3	1.3	0.5	2.7	3.9	3.9	4.0
HF	-1.7	-0.6	0.1	0.3	1.4	0.7	2.1	3.4	3.5	3.5
NaH	-2.2	-0.1	-3.5	3.7	1.1	3.8	6.0	9.5	6.5	8.6
SiH	6.4	-9.0	-4.8	5.2	-2.3	5.5	8.7	12.7	6.7	10.3
PH	2.6	-4.6	-3.8	1.9	-1.9	3.3	6.2	8.5	3.6	6.6
SH	-0.3	-1.9	-2.3	1.3	-1.0	2.5	5.1	8.0	4.3	6.4
HCl	-1.2	-0.8	-1.3	1.2	-0.2	1.7	3.9	6.5	4.3	5.6
MSE	-0.7	0.2	-0.3	1.9	1.1	3.2	6.0	7.1	6.1	6.9
RMSE	2.6	4.8	3.9	4.2	3.5	4.5	7.4	9.5	8.1	8.8

^a Abbreviations: LH07s: LH07s-SVWN, LH07t: LH07t-SVWN, LH12sif: LH12ct-SsifPW92.^b Results from ref. 204.

functionals. This gives further indications that improved LH constructions, e.g., using more sophisticated LMFs, may provide additional improvements for dipole moments.

Dipole Moments Along Dissociation Curves of HF and FCl

For an assessment of the quality of XC functionals in challenging stretched-bond situations, Hait *et al.* provided CCSD(2) and CCSD(T) reference data for the dipole moments along the dissociation curves of the HF and FCl molecule, respectively. They found that many semilocal XC functionals exhibit delocalization errors and thus produce a residual charge and non-vanishing dipole moments at large nuclear separations for HF (less so for the less polar FCl).^[204] GHs improve the long-range behavior but, depending on the EXX admixture, still tend to decay too slowly towards neutral atoms at intermediate distances. Double hybrids were found to exhibit some specific artifacts due to MP2 correlation added post-SCF.^[204] However, orbital-optimized double hybrids may resolve these issues.^[322,323] Figure 6.2 compares the curves for LH20t and LH12ct-SsifPW92 with those of ω B97X-V and PW6B95 and the benchmark CC data. For the dissociation of HF, all functionals shown in Figure 6.2 (top) give reasonably fast decay to neutral atoms at larger distances, with PW6B95 having a somewhat longer tail. The largest dipole moments near the Coulson–Fischer point are overestimated by all XC functionals, likely reflecting strong correlation effects at this distance. This holds also for the two LHs which, however, decay particularly fast, indicating low delocalization errors. The trends

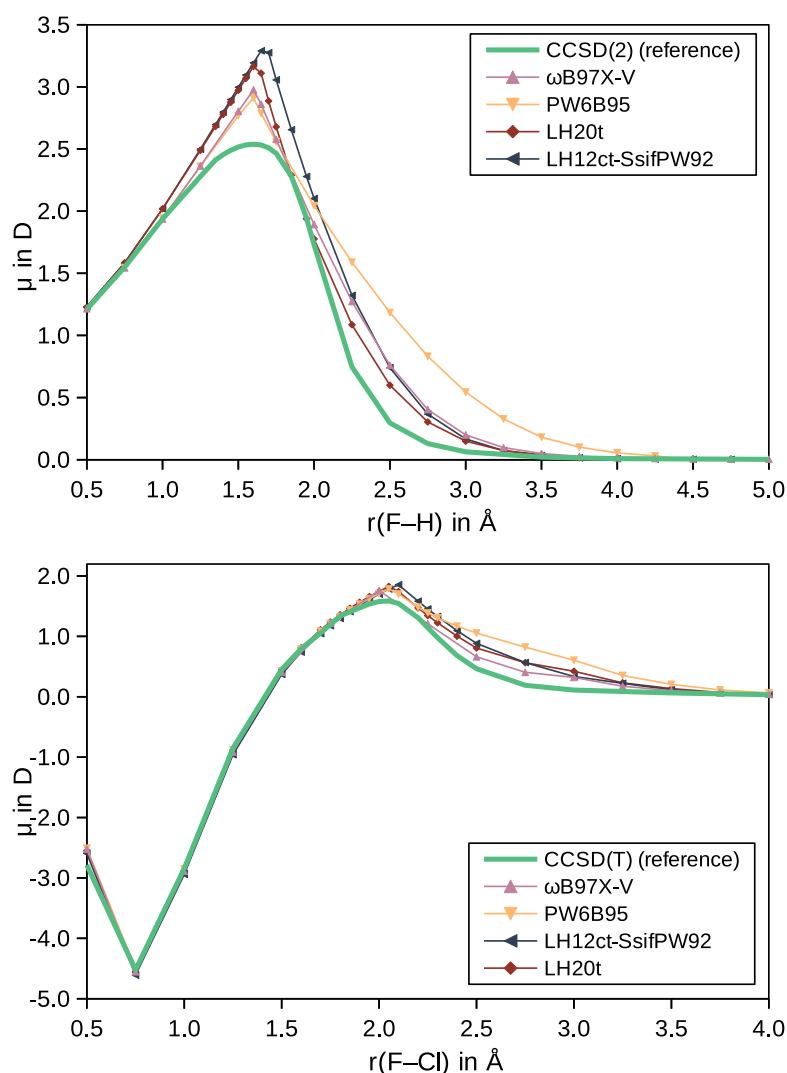


Figure 6.2: Dipole moments (in Debye) along the dissociation curves of HF (top) and FCl (bottom) with selected XC functionals compared to CCSD(2) or CCSD(T) reference data from ref. 204. Data for PW6B95 and ω B97X-V are also from ref. 204.

for the dissociation of FCl (Figure 6.2, bottom) confirm smaller residual charges for all functionals, with ω B97X-V performing marginally better than the two LHs.

6.3.2 Static Polarizabilities

Comparison of Response and Finite-Field Approaches

In ref. 205, the polarizabilities for the HHpol-132 test set were computed within a finite-field scheme (eq. 6.2) at both CCSD(T) reference level and for DFT. Here TURBOMOLE's LR-TDDFT implementation of polarizabilities is used. It is not only more convenient but

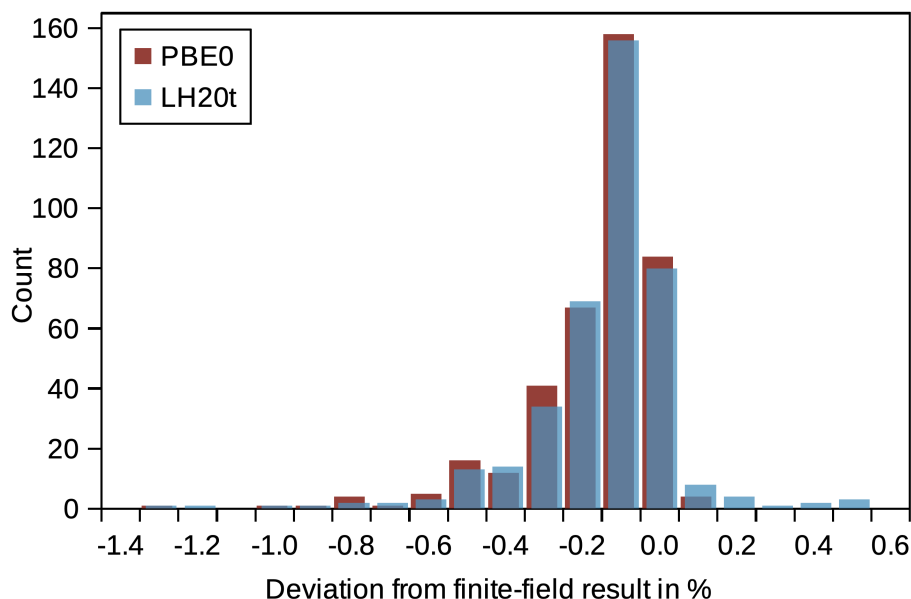


Figure 6.3: Histogram of the relative deviations of LR-TDDFT results from results obtained within a finite-field approach for the static polarizabilities (α_{xx} , α_{yy} , and α_{zz}) of the HHpol-132 test set.^[205] An artificial offset between the two distributions is used to unveil their overlap.

also more closely related to the calculation of other optical or spectroscopical properties, which are typically obtained within response theory. Also, the finite-field scheme is susceptible to errors from an improper choice of the differentiation increment. Too large differentiation increments could introduce non-negligible contributions from higher-order terms, whereas too small increments can lead to numerical problems, i.e. energy changes are not detected with sufficient accuracy. To ensure comparability of the LR-TDDFT results and the finite-field results from ref. 205, the deviations between both schemes are quantified first. This was done for the GH PBE0, for which finite-field results are also available from ref. 205, as well as for LH20t to ensure transferability to local hybrids. Deviations of the LR-TDDFT calculations from the finite-field results are negligibly small, with a mean signed deviation of -0.21% for PBE0 and of -0.19% for LH20t. The distribution of deviations shown in Figure 6.3 confirms that in the vast majority of cases LR-TDDFT gives marginally smaller polarizabilities than the finite-field approach, presumably because non-vanishing higher order terms in the finite-difference evaluation lead to artificially a bit increased polarizabilities. Absolute deviations above 0.3% are relatively rare indicating that such errors from the finite-difference scheme are well under control. Note that for a handful of systems smaller differentiation increments than those chosen in ref. 205 (0.001 au instead of 0.01 au) would give even better accuracy (see Supporting

Information of ref. 286 for details). Similarly, a recent study by Brakestad *et al.*,^[324] that uses multiwavelet basis sets and linear response theory, found some rather large individual errors associated with the finite-field scheme. Also note that the focus of that study was on basis-set completeness, and the aug-pc-4 basis set used in ref. 205 and in the present work was found to be adequate.

Judging from the marginal differences between PBE0 and LH20t in Figure 6.3, the XC functional seems to have a negligible impact on the comparability of the finite-field and LR-TDDFT results. Overall, the conclusion from this is that the present LR-TDDFT results can be compared straightforwardly to the finite-field results from ref. 205.

Results for the Benchmark Set

Results for the HHpol-132 test set that contains 57 spin-polarized (SP) and 75 non-spin-polarized (NSP) systems, are presented in the form of RMSEs for a variety of functionals in Figure 6.4 along with additional statistical data for LHs in Table 6.4. The overall picture resulting from Figure 6.4 appears quite similar to the findings for dipole moments. LHs are among the better-performing rung 4 functionals without claiming the top performance (which in this case is held by MPW1K^[205]), and they notably do not exhibit larger outliers as some other hGGAs do for the SP cases. Taking a closer look at the individual LHs, the role of the LMF is discussed first. In contrast to the above findings for dipole moments, the s-LMF-based LH07s-SVWN gives inferior polarizabilities when compared to the t-LMF-based LH07t-SVWN (including a more positive MSE, Table 6.4). This may

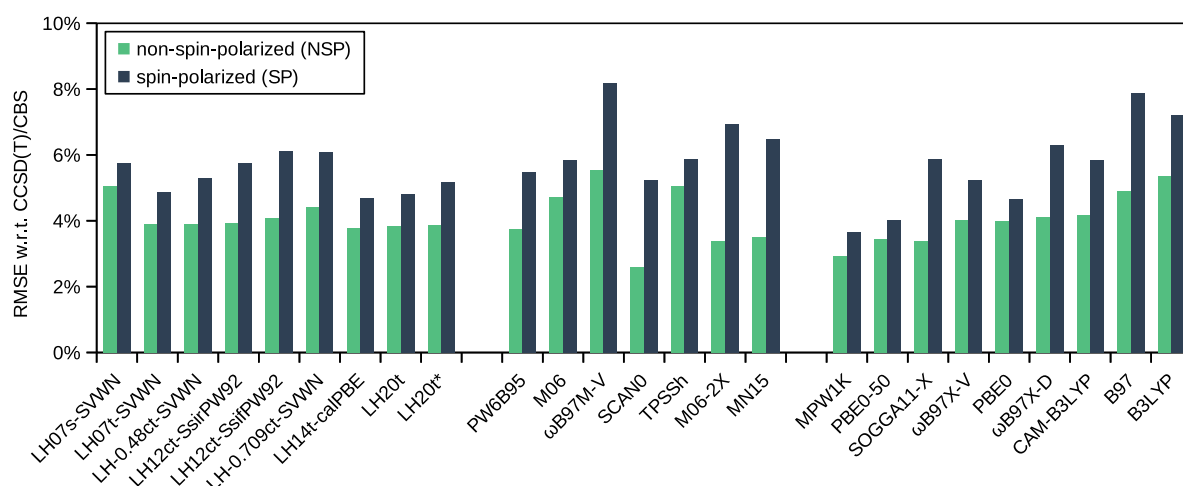


Figure 6.4: Root-mean-square percentage errors w.r.t. CCSD(T)/CBS reference values for static polarizabilities of the HHpol-132 test set.^[205] for various LHs compared to previous results^[205] for some hybrid-mGGAs and hybrid-GGAs.

Table 6.4: Statistical measures in percentages w.r.t. CCSD(T)/CBS reference values for static polarizabilities from the HHpol-132 test set^[205] for LHs. RMSE is the root-mean-square error, MAX the maximum absolute error, MSE the mean signed error, and σ the standard deviation. SP (NSP) is the subset of (non-)spin-polarized systems.

Functional	RMSE			MAX	MSE	σ
	all	NSP	SP			
LH07s-SVWN	5.38	5.05	5.77	19.37	4.26	3.27
LH07t-SVWN	4.35	3.89	4.88	19.39	2.81	3.30
LH-0.48ct-SVWN	4.56	3.89	5.30	19.39	2.98	3.42
LH12ct-SsirPW92	4.83	3.94	5.76	21.49	2.60	4.05
LH12ct-SsifPW92	5.08	4.07	6.11	22.33	2.62	4.33
LH-0.709ct-SVWN	5.25	4.40	6.09	24.91	1.15	5.10
LH14t-calPBE	4.19	3.77	4.68	17.63	2.59	3.26
LH20t	4.30	3.84	4.83	19.60	1.76	3.91
LH20t*	4.50	3.87	5.18	20.09	1.58	4.21

be related to the different behavior of s- and t-LMFs in the intermediate region between valence and asymptotics, which is thought to be responsible for t-LMFs to perform better, e.g., for low-lying Rydberg states.^[24] As already seen for the dipole moments, use of a common LMF (LH-0.48ct-SVWN) and increase of the prefactor very slightly deteriorate the polarizabilities. A more detailed analysis of the impact of the LMF prefactor is provided in Section 6.3.3 below. Using the short-range self-interaction-free PW92 correlation functional (LH12ct-SsifPW92) improves the results somewhat compared to LH-0.709ct-SVWN, but the effects are minor. The recent LH20t functional is among the best LHs for polarizabilities, but the differences to the earlier LHs are again not very pronounced (the RMSE is the second-lowest). Probably, disadvantages from the common t-LMF with large prefactor ($b = 0.715$) are compensated by the more advanced GGA/mGGA XC contributions. This is supported also by the results for the second PBE-based LH, LH14t-calPBE. It has a spin-channel t-LMF with smaller prefactor ($b = 0.50$) and performs slightly better than the closely related LH07t-SVWN ($b = 0.48$). The CF seems to have a small impact, as indicated by the effect of its removal (cf. LH20t* entry in Table 6.4). Importantly, the more highly parameterized LH20t performs robustly and exhibits no sign whatsoever of overparameterization.

6.3.3 Influence of the LMF Prefactor and GH Mixing Factor

In extension of the discussion on the LMF prefactor, it is analyzed in more detail how EXX admixture, as encoded by the constant admixture of GHs and the t-LMF prefactor for LHs, influences both dipole moments and static polarizabilities. Figure 6.5 provides

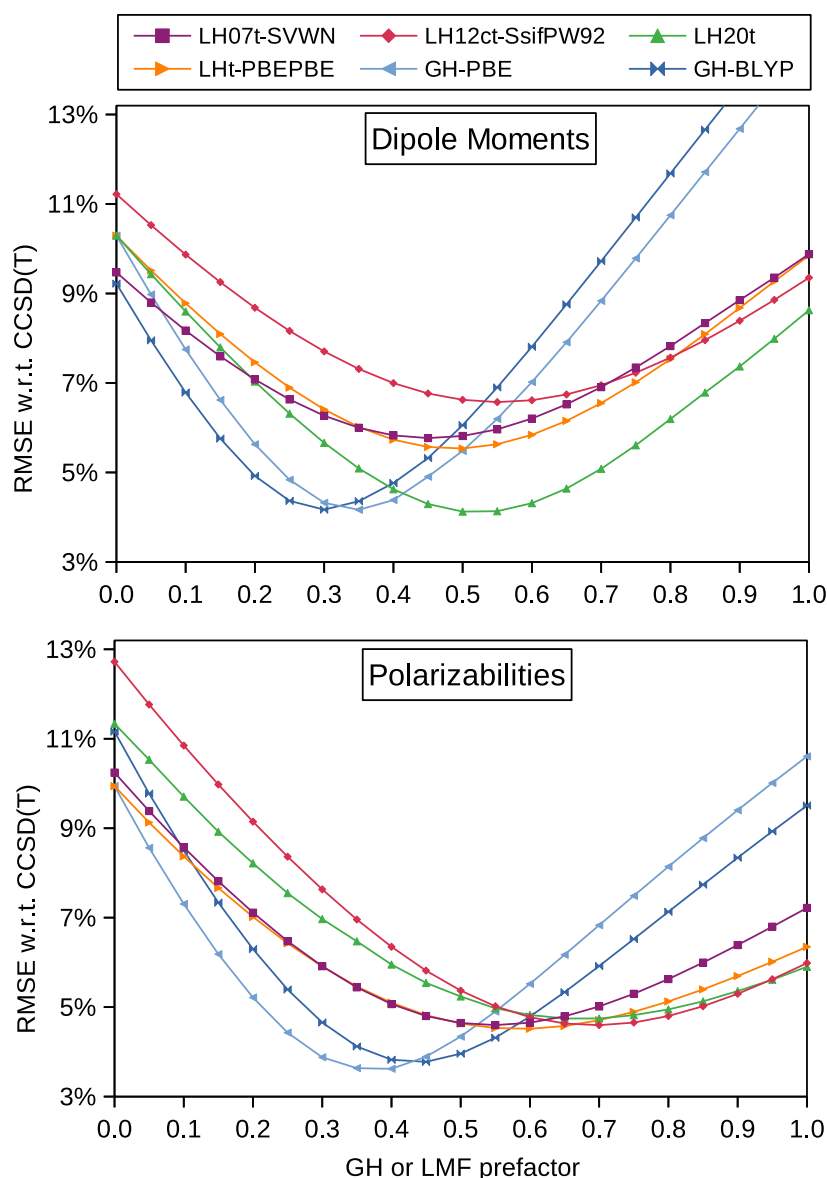


Figure 6.5: RMSEs for dipole moments (top) and polarizabilities (bottom) for 58 non-spin-polarized molecules from refs. 204 and 205 with global and local hybrids using different EXX admixtures (GHs) or t-LMF prefactors (LHs).

plots of the computed RMSEs for increasing hybrid mixing parameters in GHs and increasing t-LMF prefactors in LHs respectively. Additionally, histograms reflecting the distribution of optimal prefactors with each functional are provided in Figure A.36-A.37 in Appendix A.12.

As a t-LMF-based LH features EXX real-space admixtures between 0 and the LMF prefactor, the density-averaged EXX admixture will always be lower than for a GH with

the same prefactor. The exact ratio depends on the molecule, but as a rule of thumb, the appropriate t-LMF prefactor to generate the same density-averaged admixture as the corresponding GH is about twice the EXX admixture of the latter.^[212,285,325] This explains why all curves for LHs in Figure 6.5 are shifted to higher prefactors. For the PBE-based GH (light blue curves in Figure 6.5), the optimal prefactor for both properties is 0.35, i.e. 35% EXX admixture. This is somewhat larger than in the popular PBE0 functional but close to the prefactor in PBE0-1/3, for which theoretical and numerical arguments have been put forward,^[326,327] and which performs better than PBE0 for the MVO-10 test set of gas-phase mixed-valence oxo systems.^[18] For the BLYP-based GH (dark blue curves in Figure 6.5), the optimal prefactor differs notably between dipole moments and polarizabilities, with larger EXX admixtures performing better for the latter. The scan for LH07t-SVWN (purple curves in Figure 6.5) confirms that the thermochemically optimized t-LMF prefactor of $b = 0.48$ ^[13] is also optimal for the prediction of dipole moments and close to optimal for polarizabilities. For LH12ct-SsifPW92 (red curves in Figure 6.5), the thermochemically optimized t-LMF prefactor of $b = 0.709$ ^[178] is a bit too high for dipole moments but optimal for polarizabilities. LH12ct-SsifPW92 is also known to give very reliable excitation energies and other ES properties (see, e.g., ref. 24,25,30 and Chapter 5). Apparently, a prefactor of around 0.7 is generally optimal for electric-field response calculations with this type of functional. A very similar picture is found for LH20t (green curves in Figure 6.5), except that much smaller RMSEs are achieved for dipole moments. The energy-optimized LMF prefactor $b = 0.715$ ^[17] turns out to be close to optimal for polarizabilities, yet a bit too large for dipole moments. Comparison to a specifically constructed PBE-based LHt-PBEPBE functional that uses a t-LMF (orange curves in Figure 6.5), shows that the advantages of LH20t for dipole moments cannot be emulated by simply replacing the LSDA components from LH07t-SVWN with GGA ones. Besides, LHt-PBEPBE would yield a smaller optimal prefactor for polarizabilities, which is undesirable for other properties like excitation energies or the balance of (de-)localization and left-right correlation.^[17] The construction of LH20t allows such larger LMF prefactors without compromising on the accuracy for electric-field response.

6.3.4 Dynamic Polarizabilities

By definition, static polarizabilities, as those from the HHpol-132 test set, are evaluated in the zero-frequency limit. Excitation energies or other ES properties, on the other hand, are clearly not obtained in this limit. To widen the view on the performance of LHs and other XC functionals for electric response further, they are evaluated here for a recent test set

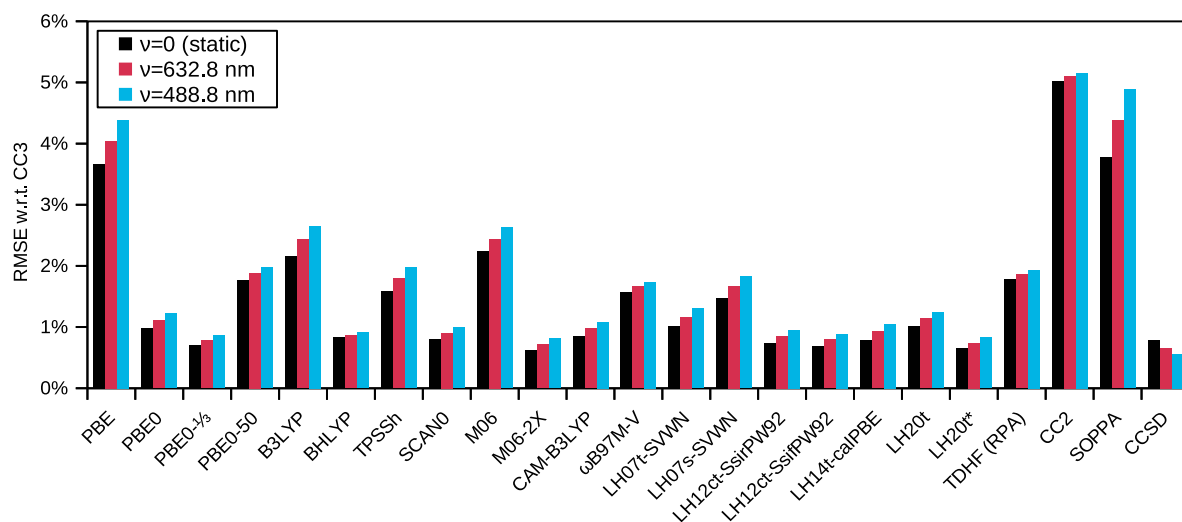


Figure 6.6: Root-mean-square percentage errors (RMSEs) w.r.t. CC3 reference values for static and dynamic polarizabilities of 14 (hetero)aromatic molecules.^[310] Errors for CC2, SOPPA and CCSD are for data from ref. 310.

of dynamic (frequency-dependent) polarizabilities of 14 (hetero)aromatic medium-sized molecules.^[310] Figure 6.6 shows percentage RMSEs relative to CC3 reference data^[310] for a series of LHs and some other XC functionals and wave-function methods, looking at static polarizabilities and at dynamic polarizabilities at two different frequencies. Compared to the HHpol-132 test set, the percentage deviations of DFT results from the reference data are overall smaller. This can be rationalized by the larger size of the molecules contained (which are furthermore exclusively NSP cases), which leads to larger polarizabilities and therefore smaller relative errors. Also, isotropic polarizabilities are given, which may help with some error compensation, as suggested by a comparison of RMSEs for the HHpol-132 test set calculated on the basis of individual polarizability components and on isotropic polarizabilities, respectively (see Supporting Information of ref. 286). Notably, CC2 and the second-order polarization propagator approximation (SOPPA) methods studied in ref. 310 perform worse than time-dependent Hartree–Fock (TDHF, also referred to as the random phase approximation, RPA). Except for one outlier (see Supporting Information of ref. 286 for details), the TDHF results from this work are in almost perfect agreement with those obtained in a separate study.^[328] Going from CC2 to CCSD gives results close to the CC3 reference data.

The GGA functional PBE is inferior to HF, reflecting the overestimated polarizabilities of such π systems at semilocal levels.^[329,330] Judging from the general trend of the errors with increasing EXX admixture in GHs, somewhat larger fractions are required to perform

better than HF. For instance, errors are reduced significantly for BHLYP (50%) compared to B3LYP (20%) or for M06-2X (54%) compared to M06 (27%). This trend is much more pronounced than for the mostly smaller (NSP and SP) molecules of the HHpol-132 test set discussed above (cf., e.g., Figure 6.4). On the other hand, errors with PBE0-50 (50%) are significantly larger than with BHLYP. This agrees with the trends seen for the scan of the GH mixing parameter for static polarizabilities (Figure 6.5) and indicates that the underlying semilocal functionals are also important. The larger importance of EXX admixture carries over also to the LHs. For example, LH12ct-SsifPW92 gives significantly better results than LH07t-SVWN. Note that the pig2 CF in LH20t actually now deteriorates agreement with the reference data somewhat for this set of molecules, i.e. LH20t* exhibits a smaller percentage deviation than LH20t. This is also different from the HHpol-132 data above, indicating that the choice of molecules clearly matters for those trends.

Deviations for dynamic polarizabilities in Figure 6.6 are strongly correlated with those for the static polarizabilities of the same set. In contrast to CCSD data, but as for HF and CC2, for each XC functional deviations to the CC3 reference data increase with increasing frequency, likely due to the AA (eq. 2.129) for the XC kernel becoming more critical with increasing frequency.^[215] For the frequencies considered here, the increase in the deviations is, however, rather small compared to the total error of a given XC functional, which indicates that the AA is not a major concern in the UV-Vis-NIR frequency range.

6.4 Conclusions

Given their relation to the GS electron density and to ESs, dipole moments and polarizabilities, respectively, are good measures of the quality of an electronic-structure method when going beyond energies. In the context of recent discussions on how the development of XC functionals in KS-DFT has progressed since the year 2000, two recent large test sets of dipole moments and static polarizabilities, as well as a smaller set of dynamic polarizabilities, were used here to evaluate the status of first-generation and more recent LHs for electric properties, in comparison with other functionals from the literature.

Overall LHs are found to be reliable for these properties, among the better and more robust hybrid functionals without outperforming the leading functionals in each case (SOGGA11-X for dipole moments, MPW1K for polarizabilities). Given that the performance approaches CCSD quality, and that no larger outliers are observed, the results for these purely energy-optimized LHs are thus encouraging. This holds also for the most recent LH20t functional, which has a more advanced construction than earlier LHs and

thus exhibits nine adjustable energy-optimized parameters. No indications of overparameterization are found, in contrast to some other semi-empirical rung 4 functionals. Indeed, deviations are overall even slightly below those of the simpler LHs evaluated. The introduction of CFs to deal with the gauge problem of exchange-energy densities in LHs also does not introduce any artifacts. This is borne out by the good performance of both “calibrated” LHs evaluated here. The AA used for the XC kernel in TDDFT computations of dynamic polarizabilities also does not seem to introduce any larger errors.

7 Conclusions and Outlook

In this work, the development of local hybrid functionals and the knowledge base around the performance of this class of functionals has been advanced. The focus was on excited-state properties, where the first implementation of excited-state gradients for local hybrids has been presented and extensively validated. As another aspect, the performance of local hybrids for the prediction of dipole moments as well as static and dynamic polarizabilities has been assessed to provide evidence that reasonable electron densities and electric-field response are obtained with functionals from this rather new class.

For the ES gradients, the original derivation for global hybrids by Furche and Ahlrichs^[35] was reassessed and extended to cover the more general local hybrid scheme. The local hybrid hyper-kernel, kernel gradients, and potential gradients were derived. Because of the explicit orbital dependence of local hybrids the density-matrix derivative scheme from ref. 67 was applied and extended to cover third derivatives, additional matrix-vector contractions, and mixed derivative w.r.t. density-matrices and nuclear coordinates. These developments were implemented in the **egrad** program of the TURBOMOLE software suite using seminumerical techniques for exact-exchange like integrals. The correctness of the implementation was assured by comparison with ES gradients calculated from ES energies via numerical differentiation. The impact of the size of the numerical quadrature grid was carefully investigated and no special grid requirements were identified for the seminumerical local hybrid implementation as compared to that of the conventional numerical quadrature for other XC functionals. The smallest standard grid available in TURBOMOLE was found to be sufficient in most cases, while weakly bound systems may require slightly larger grids. The efficiency of the implementation has been compared to other TURBOMOLE programs where seminumerical local hybrid implementations are available. The scaling w.r.t. system size for the ES gradients implementation was found to be almost quadratic and thereby similar to that of the ES energy and GS gradients implementations. Like for the analytical implementation of global hybrids, the seminumerical local hybrid implementation of ES gradients exhibits an about 3.6 (5.0) times larger prefactor compared to ES energies (GS gradients) due to the additional steps involved including also one (two) additional iterative step(s). Compared to the standard

analytical implementation used for global hybrids, slightly inferior scaling w.r.t. system size and somewhat longer total computation times were found when using the medium-sized def2-TZVP basis set. However, the absolute difference in computation times between these implementations strongly depends on the grid and basis set size. As expected, the seminumerical ES gradients implementation of local hybrids features much better scaling w.r.t. basis set size and lower total computation times for calculations with larger basis sets when compared to the standard analytical implementation of global hybrids.

The new implementation was used to study the performance of local hybrid functionals for various ES properties. For many categories, the performance was found to be similar to that of state-of-the-art global or range-separated hybrid functionals. This applies to ES structural parameters, adiabatic excitation energies/ 0–0 energies for singlet states, fluorescence energies, and harmonic ES vibrational frequencies. While some trends could be extracted from a detailed analysis of the benchmark results, such as slight advantages of local hybrids for some specific bond types (carbon-nitrogen, carbon-carbon, and carbon-halogen) or slightly inferior performance for fluorescence energies, the differences to global hybrids are not particularly striking. More definite conclusions can be drawn regarding AEEs/ 0–0 energies for triplet ES as well as for emission energies from triplet ESs (phosphorescence) for which some local hybrids outperform most global and range-separated hybrids and are only matched by the highly empirical M06-2X functional. The decisive feature here is the use of a common t-LMF with relatively large prefactors as in LH12ct-SsirPW92, LH12ct-SsifPW92, and LH20t. This is in agreement with previous results for vertical absorption energies and underlines the great potential of this class of functionals for applications involving triplet ESs. With the ability to efficiently optimize ES structures and to obtain harmonic ES vibrational frequencies via numerical differentiation of the ES gradients, the emulation of vibronically resolved spectra has become possible with local hybrid functionals. The initial hope to overcome the strong system dependence of the optimal exact-exchange admixture previously observed with global hybrids has not been fulfilled. While the performance for the prediction of absorption spectra of closed-shell species was found to be comparable to that of standard global hybrids, some advantages for the absorption spectra of open-shell systems are promising. Moreover, two case studies for phosphorescence spectra suggest that the outstanding performance of some local hybrids for phosphorescence energies and their reliability for the prediction of the band-shape work together to accurately reproduce the experimental spectra which was not achieved with the studied global hybrids.

In a separate study of dipole moments and polarizabilities, it could be shown that present local hybrids are reliable for the prediction of these quantities. The main reason

to study these properties has been to analyze if the energy-focused optimization approach used for the parameterization of modern local hybrids such as LH20t has negative side effects on the quality of the density as argued for other highly parameterized global and range-separated hybrid functionals. With dipole moments and polarizabilities being well described even with the nine-parameter LH20t functional without exhibiting strikingly large outliers, it is concluded that overparameterization is not an issue with this functional and the other investigated local hybrids. However, since more subtle local features of the electron density are concealed in the dipole moments due to the (position-weighted) averaging over space, this study should only be viewed as a first step towards considering the quality of the electron density in the development of local hybrid functionals.

With regard to the development of new local hybrids, the local mixing function plays a key role. Despite some remarkable results obtained with the simple t-LMF and its broad applicability, its steep increase towards hydrogen is suspected to cause the significantly overestimated dipole moments observed here for some hydride species. Similarly, hydrogen nuclear shieldings are known to be more difficult to reproduce with t-LMF based local hybrids compared to shieldings for other nuclei. However, such adverse effects are absent for polarizabilities of hydrides and also for element-hydrogen ES bond lengths. Nonetheless, a more uniform and robust behavior of the LMF would be desirable. For new LMF models being under development at this point in time,^[331] it will be interesting to reconsider these hydrogen-related subsets.

One field of remaining development work regarding the ES gradients is related to the inclusion of a calibration function to address the gauge problem. While this is in principle possible with the existing implementation, the dependence of currently available CFs on the density Laplacian and reduced spin density Hessian requires an extension of the ES gradients implementation to cover contributions from these terms. While the implementation of partial derivatives of the CF with respect to these quantities is trivial if aided by computer algebra systems, accounting for all combinations of these derivatives with the respective density-matrix derivatives of the Laplacian or reduced spin density Hessian as well as contracted versions of the latter is tremendously more involved. For the present implementation that covers dependence up to mGGA level, i.e. 7 semilocal quantities ($\rho_\alpha, \rho_\beta, \gamma_{\alpha\alpha}, \gamma_{\alpha\beta}, \gamma_{\beta\beta}, \tau_\alpha, \tau_\beta$), there are already $\binom{7+3-1}{3} = 84$ unique third partial derivatives of a (hypothetical) CF that have to be mapped on the corresponding derivatives of semilocal quantities. Including the Laplacian (l_α, l_β) and reduced spin density Hessian ($\eta_{\alpha,\alpha\alpha}, \eta_{\alpha,\alpha\beta}, \eta_{\alpha,\beta\beta}, \eta_{\beta,\alpha\alpha}, \eta_{\beta,\alpha\beta}, \eta_{\beta,\beta\beta}$) increases this number to $\binom{15+3-1}{3} = 680$ unique third partial derivatives (in addition to 120 unique second and 15 first derivatives). While the impact of the CF was found to be small for most ES structures studied herein, the

CF could become important for weakly bound systems or in stretched-bond situations as during dissociation and thus could become relevant if local hybrids should be used for molecular dynamics simulations of ESs. Apart from that, new LMF models^[67] suggest the use of the Laplacian and Hessian terms. If these developments lead to promising new functionals, this could also justify the considerable effort to extend the ES gradient implementation for Laplacian and Hessian terms.

Considering that local hybrids and in particular the recent LH20t functional were previously shown to perform well for ground-state properties and vertical absorption energies of mixed-valence systems, which typically require a fine balance of (de)localization errors and left-right correlation, such benefits are also expected for excited-states. Because the solvent typically has a strong influence on the electronic structure of mixed-valence systems, meaningful comparisons with experimental data have to include these effects at least at the level of a continuum model. While such models have been developed for ES gradients, they are currently not available in TURBOMOLE’s `egrad` program. They are envisaged by other developers already.^[332] Together with the ES gradients implementation presented here, this is expected to make local hybrids even more useful for the study of mixed-valence systems.

Another direction of possible methodological improvements concerns the neglect of the current-density response in the present implementation. Although it was shown here that this hardly affects the ES structural parameters, a proper inclusion would still be desirable to avoid problems with any unforeseen special cases. The lack of the current-density response for ES gradients does not only apply to local hybrids but τ -dependent functionals in general and is also not covered in other quantum chemical programs. One obstacle for the inclusion of the current-density response is the lack of antisymmetric XC hyperkernel and antisymmetric XC kernel gradient contributions in standard global hybrid implementations. This has been overcome with the developments presented herein since local hybrids require antisymmetric contributions already when neglecting the current-density response. Hence, this lowers the hurdle for future developments.

The development of the local hybrid hyperkernel also paves the way for the development of quadratic response theory^[215,333] for these functionals, which could become important if nonlinear optical properties such as hyperpolarizabilities or state-to-state absorption amplitudes are on demand. Aside from the use in structure optimizations, which was exclusively considered here, ES gradients can also be used in nonadiabatic molecular dynamics simulations of ESs to compute the forces. To perform such simulations, additional work on the nonadiabatic coupling matrix elements^[251] for local hybrids

is required. Given the excellent performance of local hybrids for triplet ES states, this also is a promising direction.

At this point in time, local hybrid functionals have not yet entered the mainstream of quantum chemical methods. The work presented here contributes to this up-and-coming field with the development of excited-state gradients for these functionals and with numerous benchmark studies for excited-state related properties as well as for more fundamental electric properties. The availability of excited-state gradients now opens up several new fields of application for local hybrids and their efficient implementation in a widely used quantum chemical program provides this new tool to the scientific community.

A Appendix

A.1 Solutions for the Energy-Weighted Difference Density Matrix \mathbf{W}

The solutions for the different blocks of \mathbf{W} read:

$$\begin{aligned}
 W_{ij\sigma} = & \frac{1}{1 + \delta_{ij}} \left(\sum_c \Omega [(X + Y)_{ic\sigma}(X - Y)_{jc\sigma} + (X - Y)_{ic\sigma}(X + Y)_{jc\sigma}] \right. \\
 & - \sum_c \epsilon_c^\sigma [(X + Y)_{ic\sigma}(X + Y)_{jc\sigma} + (X - Y)_{ic\sigma}(X - Y)_{jc\sigma}] + H_{ij\sigma}^+[\mathbf{P}] \\
 & \left. + \sum_{kc\sigma'ld\sigma''} \left[g_{+ijkld}^{\sigma\sigma'\sigma''}(X + Y)_{kc\sigma'}(X + Y)_{ld\sigma''} + g_{-ijkld}^{\sigma\sigma'\sigma''}(X - Y)_{kc\sigma'}(X - Y)_{ld\sigma''} \right] \right), \quad (\text{A.1})
 \end{aligned}$$

$$\begin{aligned}
 W_{ab\sigma} = & \frac{1}{1 + \delta_{ab}} \left(\sum_i \Omega [(X + Y)_{ia\sigma}(X - Y)_{ib\sigma} + (X - Y)_{ia\sigma}(X + Y)_{ib\sigma}] \right. \\
 & \left. + \sum_i \epsilon_i^\sigma [(X + Y)_{ia\sigma}(X + Y)_{ib\sigma} + (X - Y)_{ia\sigma}(X - Y)_{ib\sigma}] \right), \quad (\text{A.2})
 \end{aligned}$$

$$W_{ia\sigma} = \sum_k [(X + Y)_{ka\sigma} H_{kia\sigma}^+[(\mathbf{X} + \mathbf{Y})] + (X - Y)_{ka\sigma} H_{kia\sigma}^-[(\mathbf{X} - \mathbf{Y})]] + \epsilon_i^\sigma Z_{ia\sigma}. \quad (\text{A.3})$$

A.2 Derivation of the Local Hybrid Hyper-Kernel

The LH hyper-kernel is obtained as the third derivative of the LH energy (eq. 2.75)

$$\begin{aligned}
 E_{xc}^{\text{LH}} = & -\frac{1}{2} \sum_\varsigma \sum_{mnkl} D_{mn}^\varsigma D_{kl}^\varsigma \iint a_\varsigma(\mathbf{r}) \cdot w_{mlkn}^{\varsigma\varsigma} d\mathbf{r}' d\mathbf{r} \\
 & + \sum_\varsigma \int [1 - a_\varsigma(\mathbf{r})] \cdot e_{x,\varsigma}^{\text{sl}}(\mathbf{r}) d\mathbf{r} + \int e_c^{\text{sl}}(\mathbf{r}) d\mathbf{r} \quad (\text{A.4})
 \end{aligned}$$

w.r.t. the density matrix

$$g_{pqrstu}^{\sigma\sigma'\sigma''} = \frac{\delta^3 E_{xc}^{\text{LH}}}{\delta D_{pq}^\sigma \delta D_{rs}^{\sigma'} \delta D_{tu}^{\sigma''}}. \quad (\text{A.5})$$

Note that the CF $G_\sigma(\mathbf{r})$ was omitted in eq. A.4 to simplify notations as it can be formally treated as a part of the (semi)local exchange energy density. Moreover, the exact exchange energy-density has been written using eq. 3.24. Derivatives are now obtained via the product rule of differentiation. For the explicitly density-matrix depended part, the derivatives are directly taken using the relations derived in eq. 3.26, eq. 3.27, and eq. 3.28. For the implicitly density-matrix dependent (semi)local quantities, i.e. the LMF $a_\zeta(\mathbf{r})$ and the exchange and correlation energy densities $e_{x/c,\zeta}^{\text{sl}}(\mathbf{r})$, the derivatives are obtained via the functional chain rule denoted using the semilocal potential operator (eq. 3.32) to condense the otherwise lengthy expressions. Proceeding step-by-step, the first derivative, i.e. the LH potential, reads

$$\begin{aligned} \frac{\delta E_{\text{xc}}^{\text{LH}}}{\delta D_{pq}^\sigma} = & -\frac{1}{2} \iint a_\sigma(\mathbf{r}) \cdot \sum_{mn} D_{mn}^\sigma [w_{mqpn}^{\sigma\sigma}(\mathbf{r}, \mathbf{r}') + w_{pnmq}^{\sigma\sigma}(\mathbf{r}, \mathbf{r}')] d\mathbf{r}' d\mathbf{r} \\ & - \sum_\zeta \iint \hat{d}_{pq\sigma} a_\zeta(\mathbf{r}) \cdot \left[\frac{1}{2} \sum_{mnkl} D_{mn}^\zeta D_{kl}^\zeta w_{mlkn}^{\zeta\zeta}(\mathbf{r}, \mathbf{r}') + e_{x,\zeta}^{\text{sl}}(\mathbf{r}) \right] d\mathbf{r}' d\mathbf{r} \\ & + \sum_\zeta \int [1 - a_\zeta(\mathbf{r})] \cdot \hat{d}_{pq\sigma} e_{x,\zeta}^{\text{sl}}(\mathbf{r}) d\mathbf{r} + \int \hat{d}_{pq\sigma} e_c^{\text{sl}}(\mathbf{r}) d\mathbf{r} \end{aligned} \quad (\text{A.6})$$

in agreement with the expression derived in ref. 67. Taking the derivative of this expression gives the LH kernel, which reads

$$\begin{aligned} \frac{\delta^2 E_{\text{xc}}^{\text{LH}}}{\delta D_{rs}^{\sigma'} \delta D_{pq}^\sigma} = & -\frac{1}{2} \iint a_\sigma(\mathbf{r}) \cdot \delta_{\sigma\sigma'} [w_{rqp\sigma}^{\sigma\sigma}(\mathbf{r}, \mathbf{r}') + w_{psrq}^{\sigma\sigma}(\mathbf{r}, \mathbf{r}')] d\mathbf{r}' d\mathbf{r} \\ & - \frac{1}{2} \iint \hat{d}_{rs\sigma'} a_\sigma(\mathbf{r}) \cdot \sum_{mn} D_{mn}^\sigma [w_{mqpn}^{\sigma\sigma}(\mathbf{r}, \mathbf{r}') + w_{pnmq}^{\sigma\sigma}(\mathbf{r}, \mathbf{r}')] d\mathbf{r}' d\mathbf{r} \\ & - \frac{1}{2} \iint \hat{d}_{pq\sigma} a_{\sigma'}(\mathbf{r}) \cdot \sum_{mn} D_{mn}^{\sigma'} [w_{msrn}^{\sigma'\sigma'}(\mathbf{r}, \mathbf{r}') + w_{rnm\sigma}^{\sigma'\sigma'}(\mathbf{r}, \mathbf{r}')] d\mathbf{r}' d\mathbf{r} \\ & - \sum_\zeta \int \hat{d}_{pq\sigma} a_\zeta(\mathbf{r}) \cdot \hat{d}_{rs\sigma'} e_{x,\zeta}^{\text{sl}}(\mathbf{r}) d\mathbf{r} \\ & - \sum_\zeta \iint \hat{d}_{rs\sigma'} \hat{d}_{pq\sigma} a_\zeta(\mathbf{r}) \cdot \left[\frac{1}{2} \sum_{mnkl} D_{mn}^\zeta D_{kl}^\zeta w_{mlkn}^{\zeta\zeta} + e_{x,\zeta}^{\text{sl}}(\mathbf{r}) \right] d\mathbf{r}' d\mathbf{r} \\ & - \sum_\zeta \int \hat{d}_{rs\sigma'} a_\zeta(\mathbf{r}) \cdot \hat{d}_{pq\sigma} e_{x,\zeta}^{\text{sl}}(\mathbf{r}) d\mathbf{r} \\ & + \sum_\zeta \int [1 - a_\zeta(\mathbf{r})] \cdot \hat{d}_{rs\sigma'} \hat{d}_{pq\sigma} e_{x,\zeta}^{\text{sl}}(\mathbf{r}) d\mathbf{r} + \int \hat{d}_{rs\sigma'} \hat{d}_{pq\sigma} e_c^{\text{sl}}(\mathbf{r}) d\mathbf{r} . \end{aligned} \quad (\text{A.7})$$

This equation is equivalent to the equation derived by Maier in ref. 16, where flipped index orders for some of the $w_{psrq}^{\sigma\sigma}$ terms are noted as an interchange of the integration variable of the LMF.

Eventually, taking the derivative of the XC kernel following the same rules as before leads to the XC hyper-kernel given in eq. 3.48.

A.3 Derivatives w.r.t. MO Coefficients

Derivatives of the type denoted in eq. 3.12 are frequently used in the derivation of the Z vector equation. The involved steps are demonstrated here for the derivative of the XC potential (leading to two XC kernel terms) and is completely analogous for derivatives of the XC kernel (leading to two XC hyper-kernel terms). Consider the derivative of the exchange-correlation potential w.r.t. C_{ip} , multiplied by C_{iq} and summed over the atomic-orbital index i . Evaluation of this term gives two XC kernel terms with a flipped index pair (spin indices are dropped for clarity)

$$\begin{aligned}
& \sum_i \frac{\partial V_{rs}^{\text{xc}}}{\partial C_{ip}} C_{iq} \\
&= \sum_i \left[\frac{\partial}{\partial C_{ip}} \sum_{\mu\nu} V_{\mu\nu}^{\text{xc}} C_{\mu r} C_{\nu s} \right] C_{iq} \quad (\text{expanded } V_{rs}^{\text{xc}} \text{ in AO basis}) \\
&= \sum_i \sum_{\mu\nu} \left[\frac{\partial V_{\mu\nu}^{\text{xc}}}{\partial C_{ip}} C_{\mu r} C_{\nu s} + V_{\mu\nu}^{\text{xc}} \frac{\partial C_{\mu r}}{\partial C_{ip}} C_{\nu s} + V_{\mu\nu}^{\text{xc}} C_{\mu r} \frac{\partial C_{\nu s}}{\partial C_{ip}} \right] C_{iq} \quad (\text{applied product rule}) \\
&= \sum_i \left[\sum_{\mu\nu} \frac{\partial V_{\mu\nu}^{\text{xc}}}{\partial C_{ip}} C_{\mu r} C_{\nu s} \right] C_{iq} + \sum_{i\mu\nu} [V_{\mu\nu}^{\text{xc}} \delta_{rp} \delta_{\mu\nu} C_{\nu s} + V_{\mu\nu}^{\text{xc}} C_{\mu r} \delta_{sp} \delta_{\nu i}] C_{iq} \quad (\text{took derivatives}) \\
&= \sum_i \left[\sum_{\mu\nu} \frac{\partial V_{\mu\nu}^{\text{xc}}}{\partial C_{ip}} C_{\mu r} C_{\nu s} \right] C_{iq} + V_{qs}^{\text{xc}} \delta_{rp} + V_{rq}^{\text{xc}} \delta_{sp} \quad (\text{back-transformed to MO basis})
\end{aligned}$$

Working only on the remaining term:

$$\begin{aligned}
& \sum_i \left[\sum_{\mu\nu} \frac{\partial V_{\mu\nu}^{\text{xc}}}{\partial C_{ip}} C_{\mu r} C_{\nu s} \right] C_{iq} \\
&= \sum_{\mu\nu i} \left[\sum_{\kappa\lambda} \frac{\partial D_{\kappa\lambda}}{\partial C_{ip}} \frac{\partial V_{\mu\nu}^{\text{xc}}}{\partial D_{\kappa\lambda}} \right] C_{\mu r} C_{\nu s} C_{iq} \quad (\text{applied chain rule}) \\
&= \sum_{\mu\nu i\kappa\lambda} \frac{\partial}{\partial C_{ip}} \left[\sum_{tu} D_{tu} C_{\kappa t} C_{\lambda u} \right] f_{\kappa\lambda\mu\nu}^{\text{xc}} C_{\mu r} C_{\nu s} C_{iq} \quad (\text{took derivative and expanded } D_{\kappa\lambda})
\end{aligned}$$

$$\begin{aligned}
&= \sum_t D_{pt} \sum_{\mu\nu\kappa\lambda} [C_{\kappa q} C_{\lambda t} + C_{\lambda q} C_{\kappa t}] f_{\kappa\lambda\mu\nu}^{\text{xc}} C_{\mu r} C_{\nu s} && \text{(took MO coeff. derivative)} \\
&= \sum_{\mu\nu\kappa\lambda} [C_{\kappa q} C_{\lambda p} + C_{\lambda q} C_{\kappa p}] f_{\kappa\lambda\mu\nu}^{\text{xc}} C_{\mu r} C_{\nu s} && \text{(summed over } t, \text{ used } D_{pt} = \delta_{pt}) \\
&= f_{qpr s}^{\text{xc}} + f_{pqr s}^{\text{xc}} = f_{+pqrs}^{\text{xc}} \neq 2 \cdot f_{pqrs}^{\text{xc}}. && \text{(back-transformed to MO basis)}
\end{aligned}$$

A.4 Expanded Form of Operators

A.4.1 Semilocal Potential Operators

In the main part, the operators $\widehat{\partial}_{\mu\nu\sigma}$, $\widehat{\partial}^+$, $\widehat{\partial\partial}_{\mu\nu\sigma}^+$, $\widehat{\partial\partial}^{++}$, and $\widehat{\partial\partial\partial}_{\mu\nu\sigma}^{++}$ were used for a more convenient notation of the contracted local hybrid hyper-kernel and kernel/potential-gradients. Here, their definitions are given in expanded form. It is assumed that the (semi-)local quantities on which these operators act, themselves depend on the (semi)local quantities \mathcal{Q} from the set $\mathbb{Q} = \{\rho_\sigma, \gamma_{\sigma\sigma}, \gamma_{\sigma\sigma'}, \tau_\sigma, \dots\}$. Derivatives of these quantities w.r.t. density matrices read:

$$\begin{aligned}
\frac{\partial \rho_{\sigma'}}{\partial D_{\mu\nu}^\sigma} &= \frac{\partial}{\partial D_{\mu\nu}^\sigma} \sum_{\kappa\lambda} D_{\kappa\lambda}^{\sigma'} \chi_\kappa \chi_\lambda = \sum_{\kappa\lambda} \frac{\partial D_{\kappa\lambda}^{\sigma'}}{\partial D_{\mu\nu}^\sigma} \chi_\kappa \chi_\lambda = \sum_{\kappa\lambda} \delta_{\sigma\sigma'} \delta_{\kappa\mu} \delta_{\lambda\nu} \chi_\kappa \chi_\lambda = \delta_{\sigma\sigma'} \chi_\mu \chi_\nu \\
\frac{\partial \gamma_{\sigma'\sigma''}}{\partial D_{\mu\nu}^\sigma} &= \frac{\partial}{\partial D_{\mu\nu}^\sigma} [\nabla \rho_{\sigma'} \cdot \nabla \rho_{\sigma''}] = (\delta_{\sigma\sigma''} \nabla \rho_{\sigma'} + \delta_{\sigma\sigma'} \nabla \rho_{\sigma''}) \cdot \nabla [\chi_\mu \chi_\nu] \\
\frac{\partial \tau_{\sigma'}}{\partial D_{\mu\nu}^\sigma} &= \frac{\partial}{\partial D_{\mu\nu}^\sigma} \frac{1}{2} \sum_{\kappa\lambda} D_{\kappa\lambda}^{\sigma'} \nabla \chi_\kappa \cdot \nabla \chi_\lambda = \frac{1}{2} \delta_{\sigma\sigma'} \nabla \chi_\mu \cdot \nabla \chi_\nu.
\end{aligned} \tag{A.8}$$

Note that the spatial integration (grid summation) and dependencies on the space variable \mathbf{r} was omitted for brevity. To obtain explicit equations for an implementation, these derivatives (and their higher-order equivalents) have to be inserted into the following definitions of the semilocal potential operators for terms of the kind “ $\frac{\partial \mathcal{Q}}{\partial D_{\mu\nu}^\sigma}$ ”:

$$\begin{aligned}
\widehat{\partial}^+ &= \sum_{\mathcal{Q} \in \mathbb{Q}} \left[\sum_{\mu\nu\sigma} \frac{\partial \mathcal{Q}}{\partial D_{\mu\nu}^\sigma} U_{\mu\nu\sigma}^+ \right] \cdot \frac{\partial}{\partial \mathcal{Q}}, \\
\widehat{\partial\partial}_{\mu\nu\sigma}^+ &= \sum_{\mathcal{Q} \in \mathbb{Q}} \sum_{\mathcal{Q}' \in \mathbb{Q}} \left[\sum_{\kappa\lambda\sigma'} \frac{\partial \mathcal{Q}'}{\partial D_{\kappa\lambda}^{\sigma'}} U_{\kappa\lambda\sigma'}^+ \right] \cdot \frac{\partial \mathcal{Q}}{\partial D_{\mu\nu}^\sigma} \cdot \frac{\partial^2}{\partial \mathcal{Q} \partial \mathcal{Q}'} \\
&\quad + \sum_{\mathcal{Q} \in \mathbb{Q}} \left[\sum_{\kappa\lambda\sigma'} \frac{\partial^2 \mathcal{Q}}{\partial D_{\mu\nu}^\sigma \partial D_{\kappa\lambda}^{\sigma'}} U_{\kappa\lambda\sigma'}^+ \right] \cdot \frac{\partial}{\partial \mathcal{Q}},
\end{aligned}$$

$$\begin{aligned}
\widehat{\partial\partial}^{++} &= \sum_{Q \in \mathbb{Q}} \sum_{Q' \in \mathbb{Q}} \left[\sum_{\mu\nu\sigma} \frac{\partial Q}{\partial D_{\mu\nu}^{\sigma}} U_{\mu\nu\sigma}^{+} \right] \cdot \left[\sum_{\kappa\lambda\sigma'} \frac{\partial Q'}{\partial D_{\kappa\lambda}^{\sigma'}} U_{\kappa\lambda\sigma'}^{+} \right] \cdot \frac{\partial^2}{\partial Q \partial Q'} \\
&\quad + \sum_{Q \in \mathbb{Q}} \left[\sum_{\mu\nu\sigma\kappa\lambda\sigma'} \frac{\partial^2 Q}{\partial D_{\mu\nu}^{\sigma} \partial D_{\kappa\lambda}^{\sigma'}} U_{\mu\nu\sigma}^{+} U_{\kappa\lambda\sigma'}^{+} \right] \cdot \frac{\partial}{\partial Q}, \\
\widehat{\partial\partial\partial}_{\mu\nu\sigma}^{++} &= \sum_{Q \in \mathbb{Q}} \sum_{Q' \in \mathbb{Q}} \sum_{Q'' \in \mathbb{Q}} \left[\sum_{\kappa\lambda\sigma'} \frac{\partial Q'}{\partial D_{\kappa\lambda}^{\sigma'}} U_{\kappa\lambda\sigma'}^{+} \right] \cdot \left[\sum_{\eta\epsilon\sigma''} \frac{\partial Q''}{\partial D_{\eta\epsilon}^{\sigma''}} U_{\eta\epsilon\sigma''}^{+} \right] \cdot \frac{\partial Q}{\partial D_{\mu\nu}^{\sigma}} \cdot \frac{\partial^3}{\partial Q \partial Q' \partial Q''} \\
&\quad + 2 \sum_{Q \in \mathbb{Q}} \sum_{Q' \in \mathbb{Q}} \left[\sum_{\kappa\lambda\sigma'} \frac{\partial Q'}{\partial D_{\kappa\lambda}^{\sigma'}} U_{\kappa\lambda\sigma'}^{+} \right] \cdot \left[\sum_{\eta\epsilon\sigma''} \frac{\partial^2 Q}{\partial D_{\eta\epsilon}^{\sigma''} \partial D_{\mu\nu}^{\sigma}} U_{\eta\epsilon\sigma''}^{+} \right] \cdot \frac{\partial^2}{\partial Q \partial Q'} \\
&\quad + \sum_{Q \in \mathbb{Q}} \sum_{Q' \in \mathbb{Q}} \left[\sum_{\kappa\lambda\sigma'\eta\epsilon\sigma''} \frac{\partial^2 Q}{\partial D_{\kappa\lambda}^{\sigma'} \partial D_{\eta\epsilon}^{\sigma''}} U_{\kappa\lambda\sigma'}^{+} U_{\eta\epsilon\sigma''}^{+} \right] \cdot \frac{\partial Q'}{\partial D_{\mu\nu}^{\sigma}} \cdot \frac{\partial^2}{\partial Q \partial Q'} \\
&\quad + \sum_{Q \in \mathbb{Q}} \left[\sum_{\kappa\lambda\sigma'\eta\epsilon\sigma''} \frac{\partial^3 Q}{\partial D_{\kappa\lambda}^{\sigma'} \partial D_{\eta\epsilon}^{\sigma''} \partial D_{\mu\nu}^{\sigma}} U_{\kappa\lambda\sigma'}^{+} U_{\eta\epsilon\sigma''}^{+} \right] \cdot \frac{\partial}{\partial Q}. \tag{A.9}
\end{aligned}$$

A.4.2 Semilocal Gradient Operators

In the main part, the operators $\widehat{\nabla}_{\xi}\partial^{+}$ and $\widehat{\nabla}_{\xi}\partial\partial^{++}$ were used. The definitions of operators containing the gradient operator $\widehat{\nabla}_{\xi}$ are defined in complete analogy to those in Appendix A.4.1. It was also exploited that nuclear derivatives of atom-centered Gaussian basis functions are only non-zero if the derivatives refer to the atom on which the basis function χ is centered and then may be expressed as a derivative w.r.t. the electronic coordinate

$$\nabla_{\xi}\chi = -\nabla\chi. \tag{A.10}$$

The gradient of the semilocal quantities are given in eq. 3.59a-c. To obtain the explicit equations for the semilocal gradient operators, these derivatives (and their higher-order equivalents) have to be inserted into the following definitions of the gradient operators for terms of the kind “ $\frac{\partial Q}{\partial \xi}$ ”:

$$\widehat{\nabla}_{\xi}\partial^{+} = \sum_{Q \in \mathbb{Q}} \sum_{Q' \in \mathbb{Q}} \left[\sum_{\kappa\lambda\sigma'} \frac{\partial Q'}{\partial D_{\kappa\lambda}^{\sigma'}} U_{\kappa\lambda\sigma'}^{+} \right] \cdot \frac{\partial Q}{\partial \xi} \cdot \frac{\partial^2}{\partial Q \partial Q'}$$

$$\begin{aligned}
& + \sum_{Q \in \mathbb{Q}} \left[\sum_{\kappa\lambda\sigma'} \frac{\partial^2 Q}{\partial \xi \partial D_{\kappa\lambda}^{\sigma'}} U_{\kappa\lambda\sigma'}^+ \right] \cdot \frac{\partial}{\partial Q}, \\
\widehat{\nabla_\xi \partial \partial}^{++} = & \sum_{Q \in \mathbb{Q}} \sum_{Q' \in \mathbb{Q}} \sum_{Q'' \in \mathbb{Q}} \left[\sum_{\kappa\lambda\sigma'} \frac{\partial Q'}{\partial D_{\kappa\lambda}^{\sigma'}} U_{\kappa\lambda\sigma'}^+ \right] \cdot \left[\sum_{\eta\epsilon\sigma''} \frac{\partial Q''}{\partial D_{\eta\epsilon}^{\sigma''}} U_{\eta\epsilon\sigma''}^+ \right] \cdot \frac{\partial Q}{\partial \xi} \cdot \frac{\partial^3}{\partial Q \partial Q' \partial Q''} \\
& + 2 \sum_{Q \in \mathbb{Q}} \sum_{Q' \in \mathbb{Q}} \left[\sum_{\kappa\lambda\sigma'} \frac{\partial Q'}{\partial D_{\kappa\lambda}^{\sigma'}} U_{\kappa\lambda\sigma'}^+ \right] \cdot \left[\sum_{\eta\epsilon\sigma''} \frac{\partial^2 Q}{\partial D_{\eta\epsilon}^{\sigma''} \partial \xi} U_{\eta\epsilon\sigma''}^+ \right] \cdot \frac{\partial^2}{\partial Q \partial Q'} \\
& + \sum_{Q \in \mathbb{Q}} \sum_{Q' \in \mathbb{Q}} \left[\sum_{\kappa\lambda\sigma'\eta\epsilon\sigma''} \frac{\partial^2 Q}{\partial D_{\kappa\lambda}^{\sigma'} \partial D_{\eta\epsilon}^{\sigma''}} U_{\kappa\lambda\sigma'}^+ U_{\eta\epsilon\sigma''}^+ \right] \cdot \frac{\partial Q'}{\partial \xi} \cdot \frac{\partial^2}{\partial Q \partial Q'} \\
& + \sum_{Q \in \mathbb{Q}} \left[\sum_{\kappa\lambda\sigma'\eta\epsilon\sigma''} \frac{\partial^3 Q}{\partial D_{\kappa\lambda}^{\sigma'} \partial D_{\eta\epsilon}^{\sigma''} \partial \xi} U_{\kappa\lambda\sigma'}^+ U_{\eta\epsilon\sigma''}^+ \right] \cdot \frac{\partial}{\partial Q}. \tag{A.11}
\end{aligned}$$

A.5 Timings

Table A.1: Wall times (in seconds) and the number of primitive basis functions N_{prim} and grid points N_{grid} for calculations with different TURBOMOLE programs for polyene chains. The LH07t-SVWN calculations use the seminumerical EXX evaluation scheme and PBE0 the standard analytical EXX integrals.

Molecule	N_{grid}	N_{prim}	LH07t-SVWN			PBE0		
			escf	rdgrad	egrad	escf	rdgrad	egrad
C ₂ H ₄ ^a	6970	124	4	3	9	2	1	4
C ₄ H ₆ ^a	12160	232	23	11	65	14	6	36
C ₆ H ₈	17336	340	69	30	189	47	17	114
C ₈ H ₁₀	22506	448	147	59	378	100	34	233
C ₁₀ H ₁₂	27684	556	239	96	616	167	56	383
C ₁₂ H ₁₄	32852	664	354	143	944	246	84	561
C ₁₄ H ₁₆	38024	772	540	199	1358	362	115	803
C ₁₆ H ₁₈	43196	880	710	263	1794	476	152	1036
C ₁₈ H ₂₀	48374	988	752	337	2288	609	192	1312
C ₂₀ H ₂₂	53548	1096	1123	429	2828	746	237	1608
C ₄₀ H ₄₂	105432	2176	4988	1772	12061	2882	862	5906
C ₆₀ H ₆₂	157222	3256	11397	4025	27449	6096	1714	12585
C ₈₀ H ₈₂	208976	4336	22130	7246	52688	10318	2770	20791

^a This data point is not included in Figure 4.4 and the linear fits because of the potentially large relative errors for small computation times on logarithmic scales. The data is shown here for completeness.

Table A.2: Wall times (in seconds) and the number of primitive basis functions N_{prim} for calculations with different TURBOMOLE programs for the BODIPY molecule using various basis sets. The LH07t-SVWN calculations use the seminumerical EXX evaluation scheme and PBE0 the standard analytical EXX integrals.

basis set	N_{prim}	LH07t-SVWN			PBE0		
		escf	rdgrad	egrad	escf	rdgrad	egrad
STO-3G	231	20	12	59	4	2	12
def2-SV(P)	364	95	32	249	33	12	80
def2-SVP	385	106	35	275	38	13	93
pc-1	441	114	40	297	48	17	117
def2-SVPD	496	265	77	682	232	81	555
cc-pVDZ	525	135	52	357	72	25	181
aug-cc-pVDZ	679	390	124	996	567	200	1385
def2-TZVP	700	559	200	1408	527	140	1203
def2-TZVPP	756	647	223	1619	661	163	1490
def2-TZVPD	811	920	290	2281	1613	459	3663
cc-pVTZ	812	642	237	1618	646	163	1483
pc-2	833	642	232	1576	657	158	1500
def2-TZVPPD	867	1035	319	2551	1908	515	4300
aug-cc-pVTZ	1099	1827	644	4592	5776	1644	13168
cc-pVQZ	1302	2800	891	6979	5253	741	11285
def2-QZVP	1309	2968	914	7313	6069	803	12944
def2-QZVPD	1420	3826	1123	9392	12917	2229	27601
pc-3	1550	3521	1085	8706	9115	1077	19398
aug-cc-pVQZ	1764	7960	2378	19581	48930	8163	104478

A.6 Grid Dependence

Table A.3: Results for the optimization of the $1^1A''$ excited state of HCN using the PBE0 functional within the new seminumerical EXX evaluation scheme in **egrad**. Results for different grid sizes are reported both for calculations neglecting and including weight derivatives (WD).

		without WD			with WD		
grid size ^a		C–H/pm	$\angle(\text{HCN})/^\circ$	E_{ES}/ha	C–H/pm	$\angle(\text{HCN})/^\circ$	E_{ES}/ha
seminumerical results							
1	2583	112.0850982	122.5930666	–93.12434322	112.0934825	122.6500454	–93.12434696
2	5113	112.1170726	122.6798110	–93.12445774	112.1061817	122.6633526	–93.12445816
3	8901	112.1062114	122.6651366	–93.12442473	112.1046236	122.6644097	–93.12442472
4	17358	112.1047449	122.6669796	–93.12442742	112.1045244	122.6664808	–93.12442742
5	27748	112.1044829	122.6655968	–93.12442734	112.1045807	122.6662419	–93.12442733
6	54887	112.1045506	122.6660600	–93.12442732	112.1045596	122.6661110	–93.12442732
7	86137	112.1045412	122.6660012	–93.12442728	112.1045588	122.6659615	–93.12442728
analytical results							
1	2583	112.0773749	122.6079200	–93.12434376	112.0969835	122.6538886	–93.12434397
2	5113	112.1172879	122.6800026	–93.12445798	112.1062459	122.6634861	–93.12445801
3	8901	112.1059022	122.6639690	–93.12442493	112.1045146	122.6648053	–93.12442493
4	17358	112.1047382	122.6669435	–93.12442736	112.1045276	122.6664436	–93.12442736
5	27748	112.1044988	122.6656861	–93.12442733	112.1045910	122.6662110	–93.12442733
6	54887	112.1045518	122.6660710	–93.12442731	112.1045591	122.6660832	–93.12442731
7	86137	112.1045422	122.6660037	–93.12442728	112.1045620	122.6659854	–93.12442728
deviations from analytical results evaluated at grid size 7 (Figure A.1)							
1	2583	–1.94E–02	–7.29E–02	8.41E–05	–1.11E–02	–1.59E–02	8.03E–05
2	5113	1.25E–02	1.38E–02	–3.05E–05	1.62E–03	–2.63E–03	–3.09E–05
3	8901	1.67E–03	–8.67E–04	2.55E–06	6.16E–05	–1.58E–03	2.56E–06
4	17358	2.03E–04	9.76E–04	–1.41E–07	–3.76E–05	4.95E–04	–1.40E–07
5	27748	–5.93E–05	–4.07E–04	–5.29E–08	1.87E–05	2.57E–04	–5.01E–08
6	54887	8.40E–06	5.63E–05	–3.41E–08	–2.40E–06	1.26E–04	–3.81E–08
7	86137	–1.00E–06	–2.50E–06	–3.00E–10	–3.20E–06	–2.39E–05	8.00E–10
deviations from analytical results evaluated at the same grid size (Figure 4.2)							
1	2583	7.72E–03	–1.49E–02	5.39E–07	–3.50E–03	–3.84E–03	–2.99E–06
2	5113	–2.15E–04	–1.92E–04	2.33E–07	–6.42E–05	–1.34E–04	–1.54E–07
3	8901	3.09E–04	1.17E–03	1.95E–07	1.09E–04	–3.96E–04	2.01E–07
4	17358	6.70E–06	3.61E–05	–6.41E–08	–3.20E–06	3.72E–05	–6.41E–08
5	27748	–1.59E–05	–8.93E–05	–3.40E–09	–1.03E–05	3.09E–05	–2.70E–09
6	54887	–1.20E–06	–1.10E–05	–3.90E–09	5.00E–07	2.78E–05	–8.10E–09
7	86137	–1.00E–06	–2.50E–06	–3.00E–10	–3.20E–06	–2.39E–05	8.00E–10

^a TURBOMOLE grid size and total number of grid points for the HCN molecule.

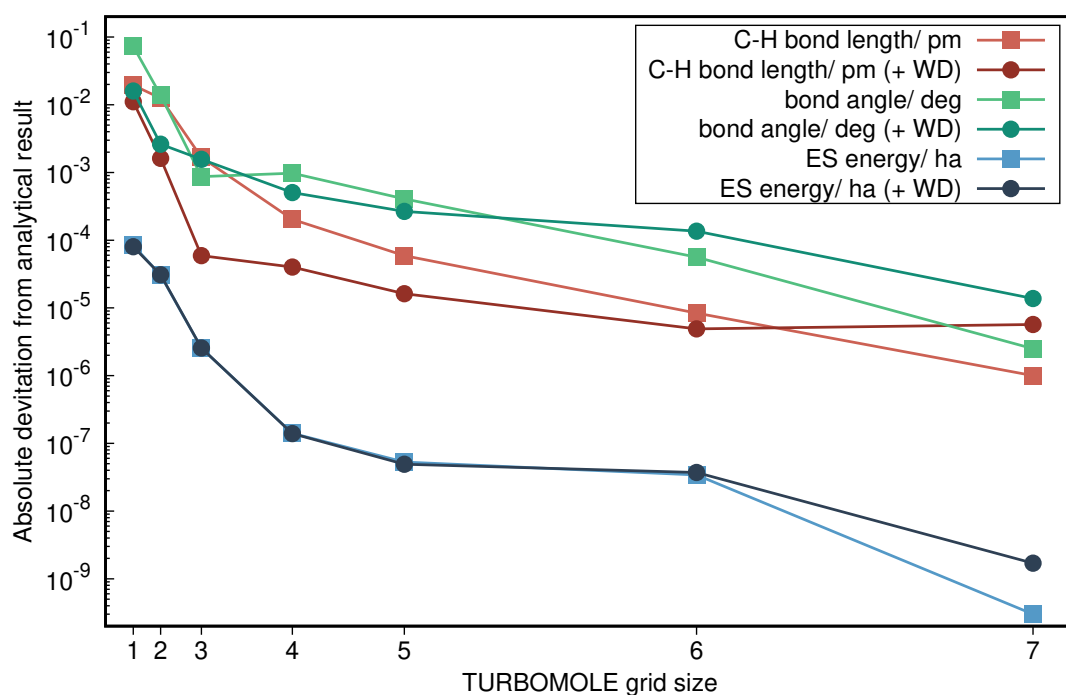


Figure A.1: Deviation of seminumerical PBE0 results from the corresponding analytical results (at grid size 7) for the C–H bond length, the $\angle(\text{HCN})$ bond angle and the energy of the optimized $1^1\text{A}''$ excited state of HCN for different grid sizes.

Table A.4: ES structural parameters for the molecules from the test set from ref. 35 and 39 optimized at the PBE0/ def2-QZVPPD level of theory using different grid sizes and integration schemes for EXX. The upper half of the table is plotted in Figure 4.3.

Molecule	State	Param.	analytical			seminumerical	
			reference ^a	grid 2 diff. 1	grid 1	grid2 diff. 1	grid 1
AsF	1 ³ Π	r_e	195.22	195.17	195.61	195.16	195.70
BeO	1 ¹ Π	r_e	142.95	142.96	142.62	142.97	142.57
CH ₂ O	1 ¹ A''	ϕ	30.72	30.71	31.13	30.67	31.25
CH ₂ O	1 ³ A''	ϕ	47.42	47.40	47.63	47.40	47.69
CH ₂ O	1 ¹ A''	$\angle(\text{HCH})$	116.36	116.37	116.21	116.38	116.17
CH ₂ O	1 ³ A''	$\angle(\text{HCH})$	110.00	110.01	109.91	110.01	109.88
CH ₂ S	1 ³ A''	ϕ	15.42	15.41	17.93	15.41	18.42
CH ₂ S	1 ³ A''	$\angle(\text{HCH})$	119.00	118.99	118.63	118.99	118.55
CH ₂ S	1 ¹ A ₂	$\angle(\text{HCH})$	119.14	119.13	119.33	119.13	119.38
CS ₂	1 ³ A ₂	$\angle(\text{SCS})$	139.18	139.18	138.99	139.21	138.93
H ₂ O	1 ¹ B ₁	$\angle(\text{HOH})$	104.88	104.89	104.35	104.89	104.50
H ₂ O	1 ¹ B ₁	O–H	98.95	98.95	98.98	98.95	98.79
HCP	1 ¹ A''	$\angle(\text{HCP})$	131.00	131.01	130.91	131.01	130.89
Li ₂	1 ¹ Σ ⁺ _g	r_e	304.85	305.06	305.04	305.02	305.11
Mg ₂	1 ¹ Σ ⁺ _u	r_e	319.78	320.28	321.09	320.43	321.54
P ₂	1 ¹ Π _g	r_e	197.73	197.73	198.06	197.73	198.17
Propynal	2 ¹ A	$\angle(\text{HC}_{\text{acet}}\text{C})$	179.52	179.52	179.11	179.52	178.97
Propynal	2 ¹ A	C–O	129.54	129.54	129.68	129.54	129.71
ScO	1 ² Π	r_e	167.16	167.16	166.94	167.16	166.90
SiF ₂	1 ¹ B ₁	$\angle(\text{FSiF})$	114.06	114.07	114.23	114.08	114.59
SiF ₂	1 ¹ B ₁	Si–F	161.13	161.14	160.93	161.13	160.82
SiO	1 ¹ Π	r_e	159.60	159.62	159.46	159.63	159.42
SO ₂	1 ³ B ₁	$\angle(\text{OSO})$	127.52	127.54	127.08	127.54	126.95
<i>tr.</i> -(CH ₂ O) ₂	1 ¹ A _u	$\angle(\text{HCC})$	113.00	113.00	112.89	113.00	112.85
VO	1 ⁴ Π	r_e	163.02	163.05	162.90	163.05	162.87
Deviations below 0.1 pm/ deg ^b							
SO ₂	1 ³ B ₁	S–O	148.13	148.13	148.20	148.13	148.22
BH	1 ¹ Π	r_e	121.35	121.35	121.42	121.35	121.43
<i>tr.</i> -(CH ₂ O) ₂	1 ¹ A _u	C–C	147.62	147.63	147.68	147.63	147.70
N ₂	1 ¹ Π _g	r_e	120.61	120.61	120.56	120.61	120.54
BF	1 ¹ Π	r_e	129.72	129.78	129.66	129.80	129.66
CH ₂ S	1 ¹ A ₂	C–S	166.07	166.06	166.11	166.06	166.13
CO	1 ³ Π	r_e	119.52	119.51	119.48	119.50	119.46
N ₂	1 ³ Π _g	r_e	119.79	119.79	119.74	119.79	119.73
CS ₂	1 ³ A ₂	C–S	161.61	161.60	161.66	161.60	161.67
CH ₂ S	1 ³ A''	C–H	108.19	108.19	108.23	108.19	108.24
CO	1 ¹ Π	r_e	122.30	122.28	122.27	122.27	122.25
<i>tr.</i> -(CH ₂ O) ₂	1 ¹ A _u	C–O	122.08	122.08	122.04	122.08	122.03
N ₂	1 ¹ Σ ⁺ _u	r_e	126.89	126.90	126.93	126.91	126.94
C ₂ H ₂	1 ¹ A _u	C–C	136.37	136.37	136.41	136.37	136.42
CH ₂ S	1 ³ A''	C–S	165.74	165.71	165.78	165.71	165.79
C ₂ H ₂	1 ¹ A _u	$\angle(\text{HCC})$	122.47	122.48	122.44	122.48	122.43
HCP	1 ¹ A''	P–C	168.85	168.85	168.89	168.85	168.89
CH ₂ O	1 ³ A''	C–H	110.48	110.47	110.51	110.47	110.51
N ₂	1 ¹ Δ _u	r_e	126.20	126.21	126.23	126.21	126.23
Benzene	1 ¹ B _{2u}	C–C	141.72	141.71	141.74	141.71	141.75
NH	1 ³ Π	r_e	103.79	103.79	103.81	103.79	103.82
BeH	1 ² Π	r_e	132.96	132.96	132.93	132.96	132.94
CH ₂ O	1 ¹ A''	C–H	109.61	109.60	109.62	109.60	109.63
<i>tr.</i> -(CH ₂ O) ₂	1 ¹ A _u	C–H	110.07	110.06	110.05	110.07	110.05
HCN	1 ¹ A''	$\angle(\text{HCN})$	122.67	122.67	122.65	122.67	122.65
Propynal	2 ¹ A	C≡C	121.50	121.50	121.48	121.51	121.48
HCN	1 ¹ A''	N–C	129.37	129.37	129.39	129.37	129.39
PH ₂	1 ² A ₁	P–H	139.73	139.72	139.72	139.73	139.71
Propynal	2 ¹ A	C _{acet} –H	106.31	106.29	106.29	106.28	106.30
Benzene	1 ¹ B _{2u}	C–H	108.11	108.11	108.12	108.10	108.12
CH ₂ O	1 ¹ A''	C–O	128.13	128.14	128.12	128.15	128.12
CH ₂ O	1 ³ A''	C–O	128.25	128.26	128.26	128.26	128.26
CuH	2 ¹ Σ ⁺	r_e	156.91	156.91	156.91	156.92	156.92
HCN	1 ¹ A''	C–H	112.10	112.10	112.09	112.10	112.09
CH ₂ S	1 ¹ A ₂	C–H	108.30	108.30	108.30	108.30	108.30
<i>tr.</i> -(CH ₂ O) ₂	1 ¹ A _u	$\angle(\text{OCC})$	125.11	125.11	125.11	125.10	125.11
NO	1 ² Σ ⁺	r_e	104.76	104.76	104.76	104.76	104.76
PH ₂	1 ² A ₁	$\angle(\text{HPH})$	121.73	121.71	121.73	121.71	121.73

^a Grid settings: grid size 5 diffuse 2.

^b Ordered by decreasing deviations of the last column (seminumerical, grid size 1) from the reference.

A.7 Effect of the Calibration Function on ESs

Table A.5: Effect of the pig2 calibration function on ES bond lengths (r_e in pm) and emission energies (ΔE in eV) for diatomic molecules from the Furche and Ahlrichs test set^[35,39] calculated at the LH20t/def2-QZVPPD level of theory. MAEs refer to experimental values and MADs to results without pig2.

Mol.	State	ES bond lengths/ pm					Emission energy/ eV		
		Exp.	$r_e^{\text{no pig2}}$	r_e^{pig2}	Δr_e	$\frac{\Delta r_e}{r_e^{\text{pig2}}}$	$\Delta E^{\text{no pig2}}$	ΔE^{pig2}	$\Delta \Delta E$
AsF	1 $^3\Pi$	195	194.6	197.4	2.8	1.4%	2.79	2.84	0.04
BeH	1 $^2\Pi$	133	131.8	132.6	0.7	0.5%	2.61	2.63	0.02
BeO	1 $^1\Pi$	146	143.4	143.8	0.4	0.3%	1.36	1.32	-0.04
BF	1 $^1\Pi$	130	130.3	131.0	0.7	0.5%	6.12	6.10	-0.02
BH	1 $^1\Pi$	122	120.0	120.8	0.7	0.6%	2.72	2.77	0.05
CO	1 $^1\Pi$	124	122.5	122.9	0.4	0.3%	7.61	7.59	-0.02
CO	1 $^3\Pi$	121	119.6	120.0	0.4	0.4%	5.69	5.69	0.00
CuH	2 $^1\Sigma^+$	157	156.0	157.1	1.1	0.7%	2.87	2.85	-0.02
Li ₂	1 $^1\Sigma_u^+$	311	323.1	330.1	7.0	2.2%	2.55	2.57	0.02
Mg ₂	1 $^1\Sigma_u^+$	308	317.3	324.0	6.7	2.1%	3.05	3.02	-0.03
N ₂	1 $^1\Delta_u$	127	125.8	126.0	0.2	0.2%	6.05	6.04	-0.01
N ₂	1 $^1\Pi_g$	122	120.7	120.9	0.2	0.2%	7.92	7.88	-0.04
N ₂	1 $^1\Sigma_u^-$	128	126.9	127.2	0.4	0.3%	6.94	6.85	-0.08
N ₂	1 $^3\Pi_g$	121	119.8	120.0	0.3	0.2%	6.63	6.63	0.00
NH	1 $^3\Pi$	104	104.1	103.9	-0.2	-0.2%	3.75	3.75	0.00
P ₂	1 $^1\Pi_g$	197	197.1	197.7	0.6	0.3%	3.95	3.93	-0.02
SiO	1 $^1\Pi$	162	159.0	160.0	0.9	0.6%	5.17	5.17	0.00
ScO	1 $^2\Pi$	169	167.7	168.1	0.3	0.2%	1.72	1.76	0.04
MAE/MAD			2.3	2.9	1.3	0.6%			0.03
MAE*/MAD* ^b			1.2	1.1	0.6	0.4%			0.03

^a Optimizations without inclusion of the pig2 calibration function ($r_e^{\text{no pig2}}$, $\Delta E^{\text{no pig2}}$) were performed using the **egrad** implementation, while optimizations with inclusion of pig2 (r_e^{pig2} , ΔE^{pig2}) were performed using a linear-search algorithm for ES single-point energies.

^b Calculated excluding Li₂ and Mg₂.

A.8 Additional Statistics for the Furche and Ahlrichs Test Set

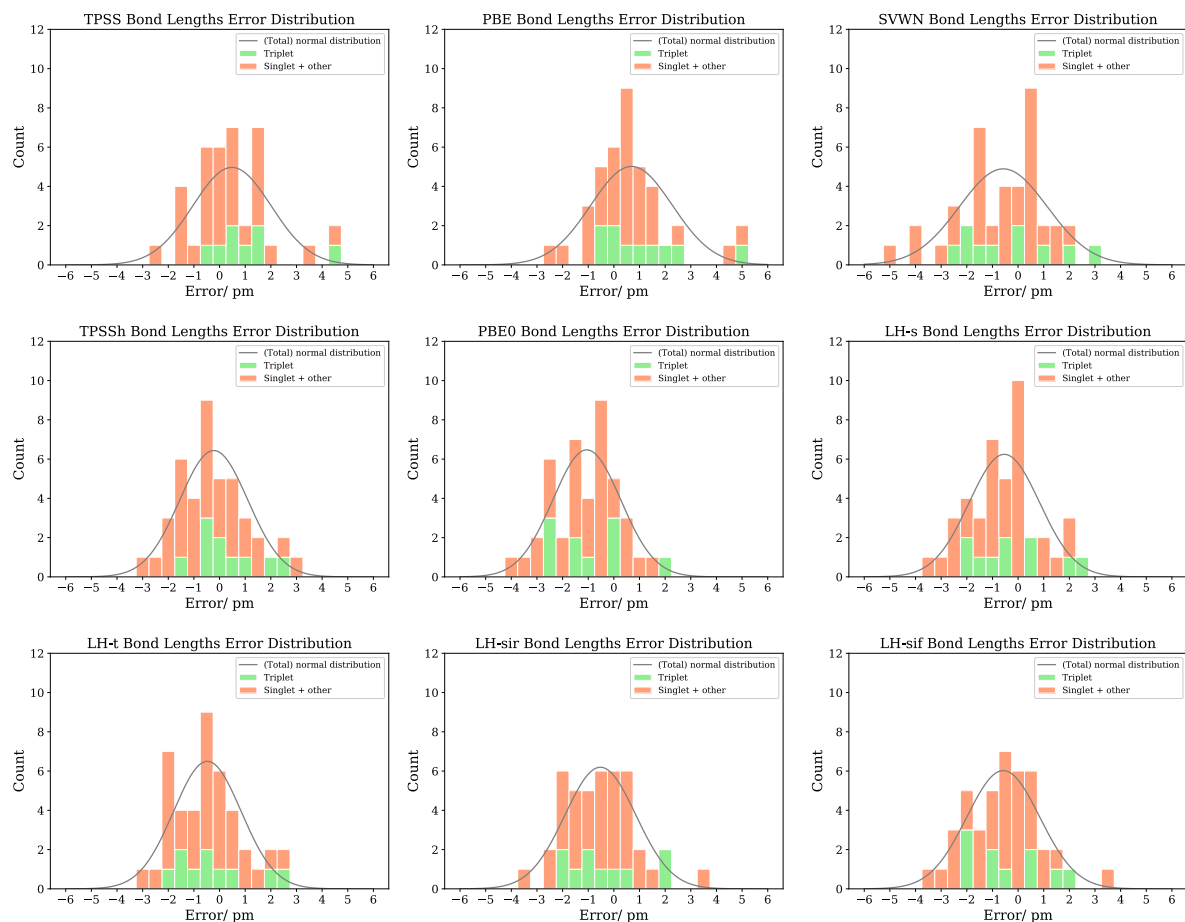


Figure A.2: Error histograms of bond lengths obtained with several functionals for the Furche and Ahlrichs test set.^[35,39] Triplet states are highlighted in green (vertical bars are stacked). Normal distributions were computed using the mean signed error and standard deviation of the total set of states. Functional abbreviations are LH-s: LH07s-SVWN, LH-t: LH07t-SVWN, LH-sir: LH12ct-SsirPW92, LH-sif: LH12ct-SsifPW92.

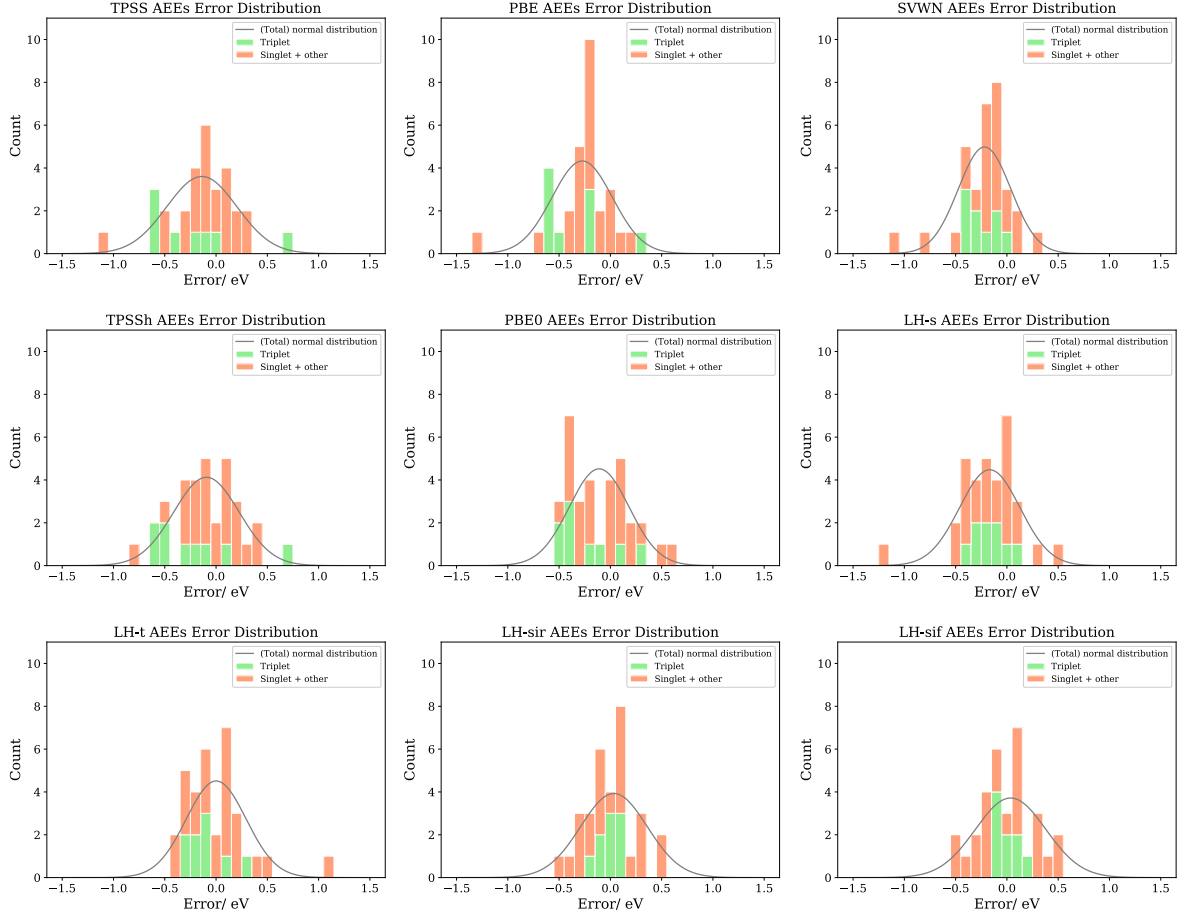


Figure A.3: Error histograms of AEEs/ 0-0 energies obtained with several functionals for the Furche and Ahlrichs test set.^[35,39] Triplet states are highlighted in green (vertical bars are stacked). Normal distributions were computed using the mean signed error and standard deviation of the total set of states. Functional abbreviations are LH-s: LH07s-SVWN, LH-t: LH07t-SVWN, LH-sir: LH12ct-SsirPW92, LH-sif: LH12ct-SsifPW92.

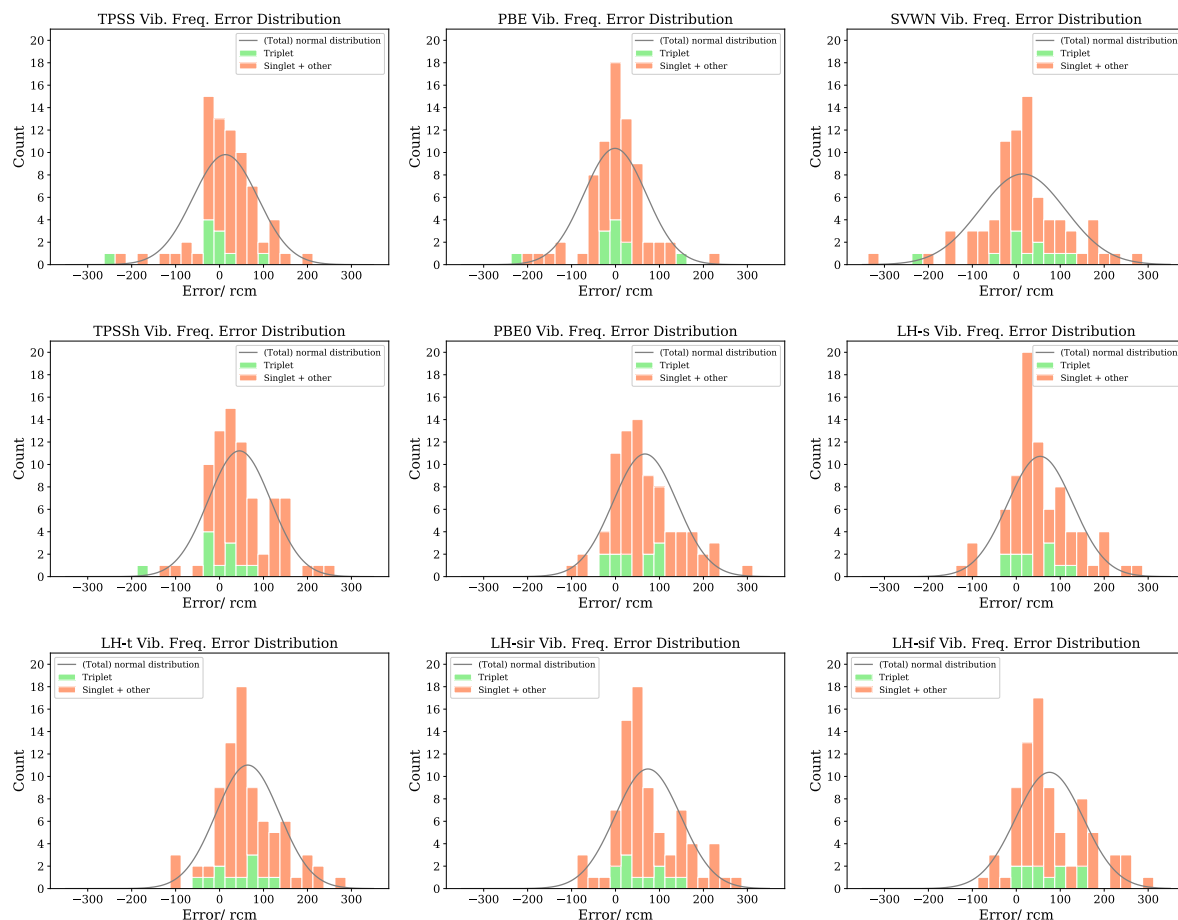


Figure A.4: Error histograms of harmonic ES vibrational frequencies obtained with several functionals for the Furche and Ahlrichs test set.^[35,39] Triplet states are highlighted in green (vertical bars are stacked). Normal distributions were computed using the mean signed error and standard deviation of the total set of states. Functional abbreviations are LH-s: LH07s-SVWN, LH-t: LH07t-SVWN, LH-sir: LH12ct-SsirPW92, LH-sif: LH12ct-SsifPW92.

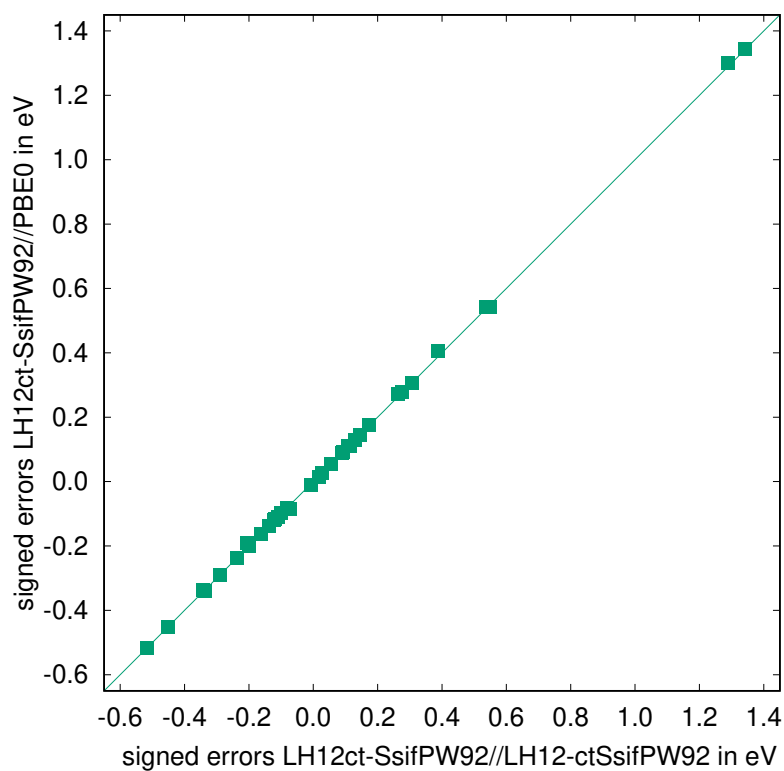


Figure A.5: Comparison of signed errors of AEEs/ 0–0 energies obtained with LH12ct-SsifPW92 at LH12ct-SsifPW92 structures and with LH12ct-SsifPW92 at PBE0 structures for the Furche and Ahlrichs test set.^[35,39]

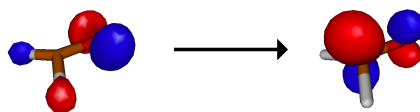
A.9 Analysis of Excitation Character in Carbonyl Compounds

Table A.6: Errors for ES CO bond lengths and the nature of the involved transitions. Rows are ordered by PBE0 errors. $2n$ stands for a molecular orbital dominated by two lone pairs. π_{conj}^* stands for a π^* molecular orbital from a conjugated π system.

Molecule	State	Transition	BLYP	PBE0	LH12ct-SsifPW92
Maleimide	1^1B_1	$2n \rightarrow \pi_{\text{conj}}^*$	0.6	-1.4	-1.2
Ketene	$1^1A''$	$\pi \rightarrow n$	0.1	-1.4	-1.0
Benzoquinone	1^1A_u	$2n \rightarrow \pi_{\text{conj}}^*$	0.7	-1.6	-1.6
Propenoic acid anion	$1^1A''$	$n \rightarrow \pi_{\text{conj}}^*$	-1.0	-2.0	-1.3
Glyoxal	1^1A_u	$2n \rightarrow \pi_{\text{conj}}^*$	0.4	-2.1	-1.8
Propenoic acid anion	$1^1A''$	$2n \rightarrow \pi_{\text{conj}}^*$	-0.5	-2.4	-1.9
Formylfluoride	2^1A	$n \rightarrow \pi^*$	-0.5	-3.4	-3.1
Acetaldehyde	$1^1A''$	$n \rightarrow \pi^*$	-0.2	-3.6	-3.6
Carbonyldifluoride	$1^1A''$	$n \rightarrow \pi^*$	-1.8	-3.7	-3.3
Acetone	$1^1A''$	$n \rightarrow \pi^*$	-0.4	-3.9	-4.1
Formic acid	2^1A	$n \rightarrow \pi^*$	-1.7	-4.0	-3.5
Propynal	$1^1A''$	$n \rightarrow \pi_{\text{conj}}^*$	-1.7	-4.3	-3.6
Formaledehyde	$1^1A''$	$n \rightarrow \pi^*$	-1.2	-4.4	-3.9
Acrolein	$1^1A''$	$n \rightarrow \pi_{\text{conj}}^*$	-2.9	-4.7	-3.7
Phosgene	$1^1A''$	$n \rightarrow \pi^*$	- ^a	-4.7	-4.2
Cyanoformaldehyde	$1^1A''$	$n \rightarrow \pi_{\text{conj}}^*$	-2.4	-4.9	-4.3

^a Optimization failed.

Formaldehyde:



H_2C_3 :

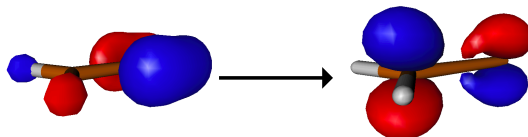


Figure A.6: Comparison of the molecular orbitals predominantly involved in the $n \rightarrow \pi^*$ excitation in formaldehyde (top) and the $\pi \rightarrow \pi^*$ excitation in H_2C_3 (bottom). Plotted at a contour value of ± 0.1 au using gMolden.

A.10 New Reference Values for the Adamo and Ehara Test Set

Table A.7: Validation of the high level correction scheme (CC2/CBS+CC3) from eq. 5.1 by comparison with conventional CC3/aug-cc-pVTZ results. All values in eV.

Molecule	State	CC2/CBS	CC3/cc-pVDZ	CC2/CBS+CC3	CC3/aug-cc-pVTZ	Δ^a
Furan	1^3B_2	3.2597	3.0814	3.0053	2.9925	0.0128
	1^3A_1	5.0077	4.8894	4.8101	4.7854	0.0247
Pyrrole	1^3B_2	3.6500	3.5146	3.4284	3.4138	0.0146
	1^3A_1	5.1060	5.0058	4.8847	4.8747	0.0100
Pyridine	1^3A_1	3.6784	3.4630	3.4634	3.4461	0.0174
	1^3B_1	3.5939	3.5770	3.5493	3.5329	0.0164
	1^3B_2	4.5592	4.5319	4.3639	4.3642	-0.0003

^a Deviation of CC2/CBS+CC3 result from CC3/aug-cc-pVTZ.

Table A.8: Phosphorescence energies in eV obtained at SAC-CI/D95(d) structures from ref. 274 using CC2 with the aug-cc-pVXZ (X=D,T,Q) basis set and CC3 with the cc-pVDZ basis set. The last value in each row is the reference value used for benchmarking the TDDFT results. Experimental values are given as compiled in ref. 274.

Molecule	State	Exp.	SAC-CI ^a	CC2				CC3/DZ	CC2/CBS+CC3 ^c
				augDZ	augTZ	augQZ	CBS ^b		
Furan	1^3B_2		2.97	3.264	3.247	3.251	3.260	3.081	3.005
	1^3A_1		4.93	4.995	4.982	4.992	5.008	4.889	4.810
Pyrrole	1^3B_2		3.40	3.657	3.635	3.640	3.650	3.515	3.428
	1^3A_1		5.04	5.100	5.084	5.092	5.106	5.006	4.885
Pyridine	1^3A_1		3.32	3.666	3.659	3.667	3.678	3.463	3.463
	1^3B_1		3.59	3.570	3.565	3.577	3.594	3.577	3.549
	1^3B_2		4.54	4.586	4.552	4.552	4.559	4.532	4.364
1,4-Benzoquinone	1^3A_u	2.25 ^d , 2.28 ^e	2.29	2.173	2.190	2.207	2.227	2.187	2.247
	1^3B_{1g}	2.30 ^d , 2.31 ^e	2.41	2.289	2.295	2.309	2.325	2.330	2.359
Uracil	$1^3A'_g$		2.70	2.978	2.973	2.983	2.998	2.904	2.893
	$1^3A''$		3.41	3.360	3.332	3.344	3.368	3.491	3.480
Adenine	$1^3A'$	2.99 ^f	2.92	3.180	3.172	3.177	3.185	3.028	2.967
	$1^3A''$		3.74	3.794	3.770	3.778	3.794	3.909	3.860
9,10-Anthraquinone	1^3B_{1g}	$\sim 2.53^g$	2.51	2.674	2.679	2.696	2.717	2.818	2.784
	1^3B_{1u}		2.91	3.161	3.154	3.162	3.174	2.976	2.972
Coumarin	$1^3A'$	$\sim 2.48^h$	2.26	2.560	2.554	2.560	2.571	2.404	2.415
	$2^3A'$		2.93	3.439	3.430	3.437	3.447	3.383	3.351
Naphthalimide	1^3A_1	2.31 ⁱ	1.83	2.283	2.280	2.285	2.293	2.150	2.127
	1^3B_1		3.25	3.312	3.314	3.332	3.357	3.477	3.484
	1^3B_2		3.58	3.666	3.651	3.654	3.663	3.580	3.504
Formaldehyde	$1^3A''$		—	2.332	2.358	2.377	2.400	2.307	2.390 (2.360) ^j
Thioformaldehyde	$1^3A''$		—	1.769	1.757	1.769	1.788	1.785	1.796 (1.769) ^j
Selenoformaldehyde	1^3A_2		—	1.466	1.476	1.501	1.606	1.514	1.636 (1.504) ^j

^a SAC-CI/D95(d) values taken from ref. 274.

^b Complete basis set limit, extrapolated as described in Section 5.2.3.

^c Complete basis set limit (CBS) with a high-level CC3/cc-pVDZ correction as described in Section 5.2.3.

^{d-i} As cited in ref. 274: ^d ref. 334, ^e ref. 335, ^f ref. 336, ^g ref. 334 (maximum peak ~ 490 nm), ^h ref. 337 (maximum second peak ~ 500 nm), ⁱ ref. 338.

^j Values in parentheses are obtained at the CC3/aug-cc-pVQZ level of theory and are used as the reference for this state.

A.11 Vibronic Absorption Spectra

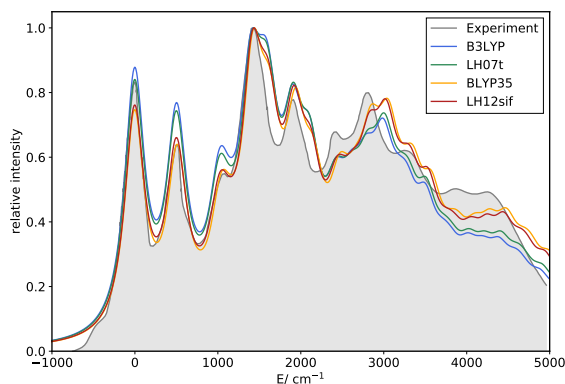


Figure A.7: Vibronic absorption spectra for the $1^1A_g \rightarrow 1^1B_{2u}$ transition of naphthalene computed with different LHs and GHs in comparison with the experimental vapor absorption spectrum.^[296] A lifetime of 36.3 fs was used for the line broadening to match the experimental spectrum.

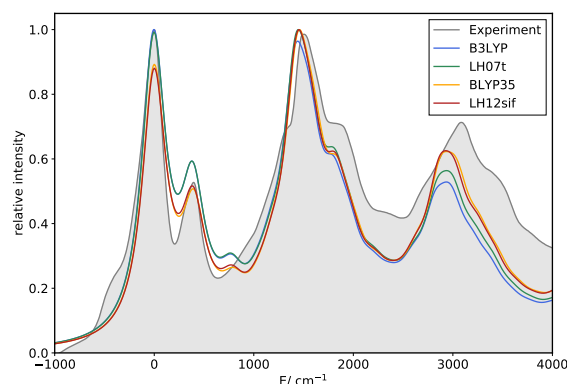


Figure A.10: Vibronic absorption spectra for the $1^1A_g \rightarrow 1^1B_{2u}$ transition of anthracene computed with different LHs and GHs in comparison with the experimental vapor absorption spectrum.^[296] A lifetime of 36.3 fs was used for the line broadening to match the experimental spectrum.

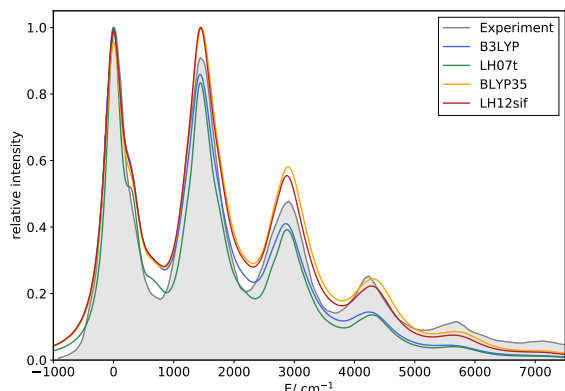


Figure A.8: Vibronic absorption spectra for the $1^1A_g \rightarrow 1^1B_{2u}$ transition of tetracene computed with different LHs and GHs in comparison with the experimental spectrum (recorded in benzene).^[339] A lifetime of 29.0 fs was used for the line broadening to match the experimental spectrum.

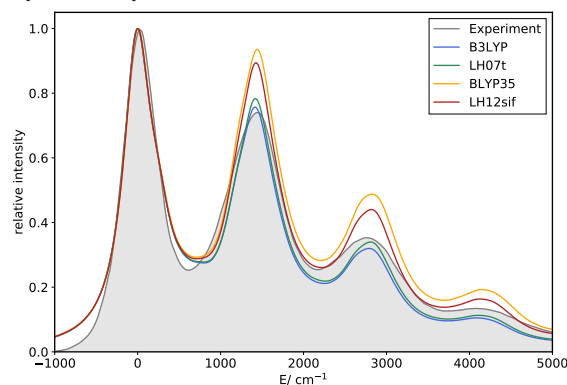


Figure A.11: Vibronic absorption spectra for the $1^1A_g \rightarrow 1^1B_{2u}$ transition of pentacene with different LHs and GHs in comparison with the experimental spectrum (recorded in 1,2-dichlorobenzene).^[340] A lifetime of 26.6 fs was used for the line broadening to match the experimental spectrum.

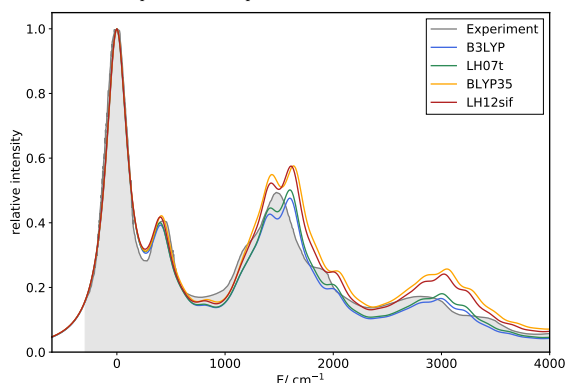


Figure A.9: Vibronic absorption spectra for the $1^1A_g \rightarrow 1^1B_{3u}$ transition of pyrene computed with different LHs and GHs in comparison with the experimental vapor absorption spectrum.^[296] A lifetime of 43.5 fs was used for the line broadening to match the experimental spectrum.

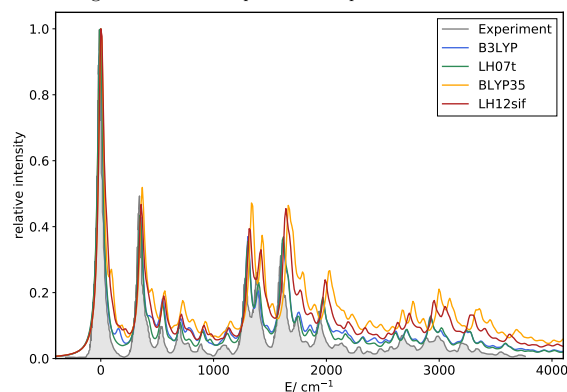


Figure A.12: Vibronic absorption spectra for the $1^1A_g \rightarrow 1^1B_{3u}$ transition of perylene with different LHs and GHs in comparison with the experimental spectrum (recorded in neon).^[341] A lifetime of 193.5 fs was used for the line broadening to match the experimental spectrum.

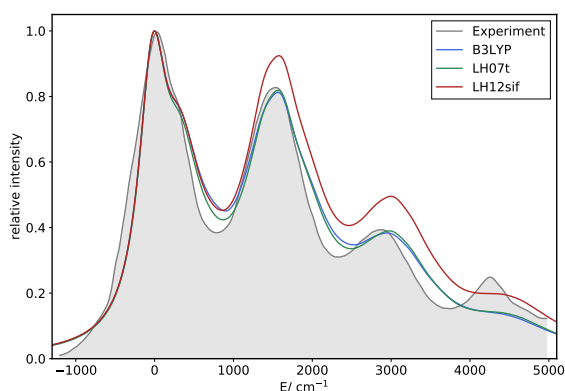


Figure A.13: Vibronic absorption spectra for the $1^1A_g \rightarrow 1^1B_1$ transition of benzoperylene computed with different LHs and the GH B3LYP in comparison with the experimental spectrum (recorded in cyclohexane).^[342] A lifetime of 24.2 fs was used for the line broadening to match the experimental spectrum.

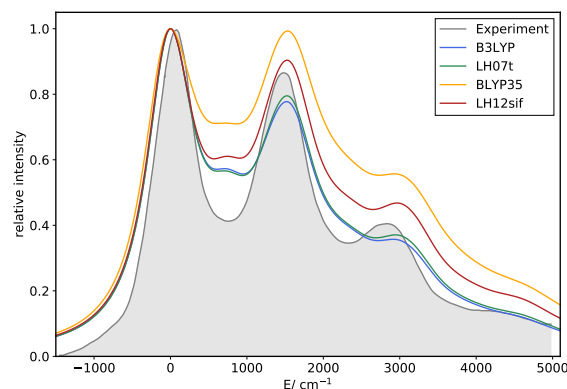


Figure A.14: Vibronic absorption spectra for the $1^1A_g \rightarrow 1^1B_u$ transition of LPPP-2 (ladder-type poly-(*p*-phenylene), cf. ref 343) computed with different LHs and GHs in comparison with the experimental spectrum (recorded in dichloromethane).^[343] A lifetime of 15.7 fs was used for the line broadening to match the experimental spectrum.

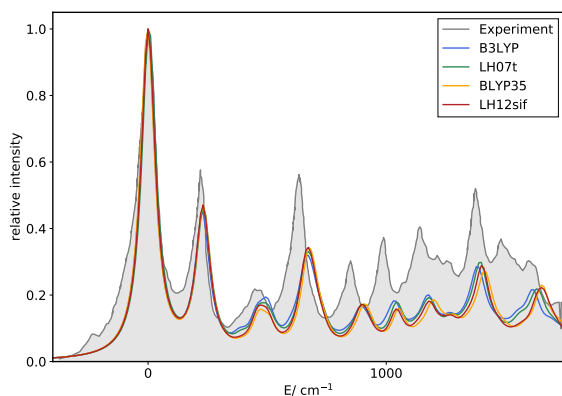


Figure A.15: Vibronic absorption spectra for the $1^1A_g \rightarrow 2^1A_1$ transition of xanthone computed with different LHs and GHs in comparison with the experimental spectrum (recorded in a supersonic argon jet).^[344] A lifetime of 145.1 fs was used for the line broadening to match the experimental spectrum.

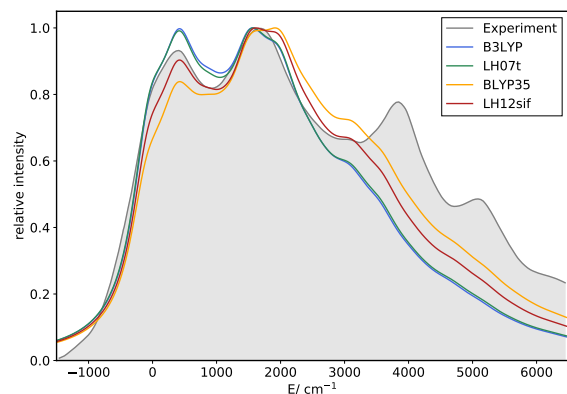


Figure A.16: Vibronic absorption spectra for the $1^1A_g \rightarrow 1^1B_1$ transition of thieno[2',3':4,5]thieno[2,3-d]thiophene ("pentathienoacene") computed with different LHs and GHs in comparison with the experimental spectrum (recorded in dichloromethane).^[345] A lifetime of 16.9 fs was used for the line broadening to match the experimental spectrum.

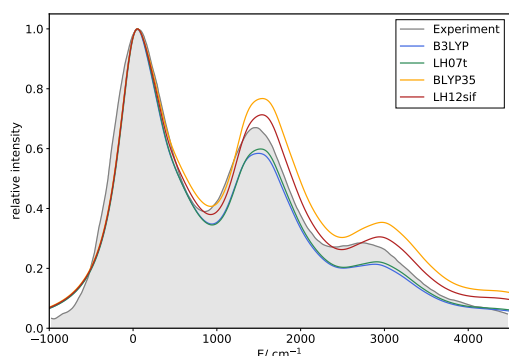


Figure A.17: Vibronic absorption spectra for the $1^1A_g \rightarrow 1^1B_{3u}$ transition of 3,4,9,10-perylene-tetracarboxylic-dianhydride computed with different LHs and GHs in comparison with the experimental spectrum (recorded in dimethyl sulfoxide).^[346] A lifetime of 21.0 fs was used for the line broadening to match the experimental spectrum.

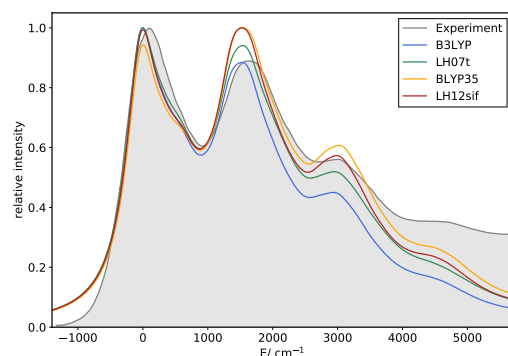


Figure A.18: Vibronic absorption spectra for the $1^1A_g \rightarrow 1^1B_{3u}$ transition of benzo[*lmn*][3,8]phenanthroline-1,3,6,8(2*H*,7*H*)-tetrone computed with different LHs and GHs in comparison with the experimental spectrum (recorded in toluene).^[347] A lifetime of 18.9 fs was used for the line broadening to match the experimental spectrum. The experimentally studied molecule has C_6H_{13} entities bound to the nitrogen atoms (replaced by hydrogen atoms in computations).

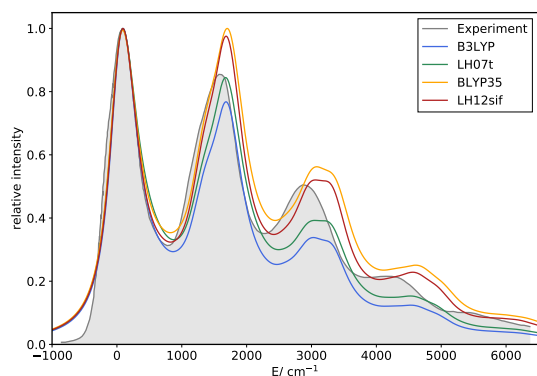


Figure A.19: Vibronic absorption spectra for the $1^1A_g \rightarrow 1^1B_u$ transition of 1,4-bis((E)-4-((E)-styryl)styryl)benzene computed with different LHs and GHs in comparison with the experimental spectrum.^[348] A lifetime of 26.8 fs was used for the line broadening to match the experimental spectrum.

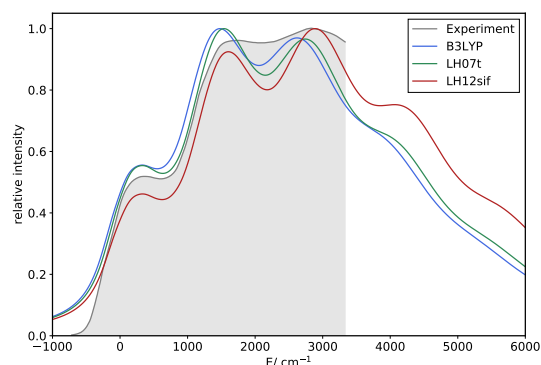


Figure A.20: Vibronic absorption spectra for the $1^1A_1 \rightarrow 1^1B_1$ transition of azobenzene computed with different LHs and the GH B3LYP in comparison with the experimental spectrum (recorded in 2-methyltetrahydrofuran).^[349] A lifetime of 19.4 fs was used for the line broadening to match the experimental spectrum.

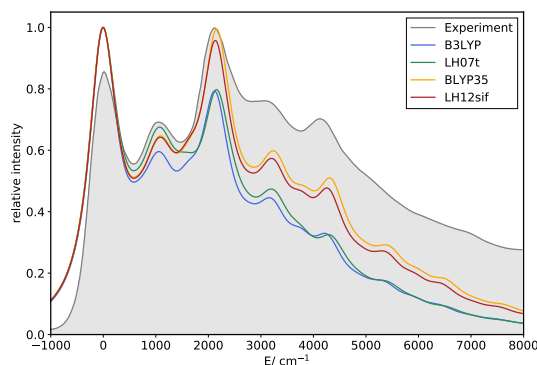


Figure A.21: Vibronic absorption spectra for the $1^1A_g \rightarrow 1^1B_{3u}$ transition of diphenylacetylene computed with different LHs and GHs in comparison with the experimental spectrum (recorded in cyclohexane).^[350] A lifetime of 16.9 fs was used for the line broadening to match the experimental spectrum.

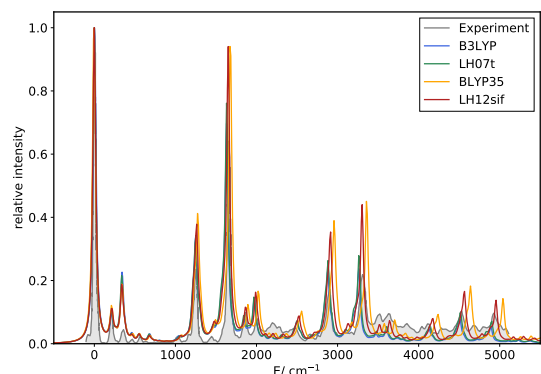


Figure A.22: Vibronic absorption spectra for the $1^1A_g \rightarrow 1^1B_u$ transition of octatetraene computed with different LHs and GHs in comparison with the experimental spectrum (recorded in a supersonic argon jet).^[351] A lifetime of 241.9 fs was used for the line broadening to match the experimental spectrum.

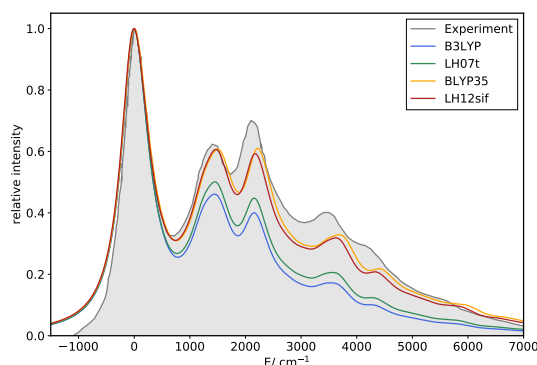


Figure A.23: Vibronic absorption spectra for the $1^1A_g \rightarrow 1^1B_u$ transition of (3E,7E,11E)-tetradeca-3,7,11-trien-1,5,9,13-tetrayne computed with different LHs and GHs in comparison with the experimental spectrum (recorded in 3-methylpentane).^[352] A lifetime of 19.8 fs was used for the line broadening to match the experimental spectrum.

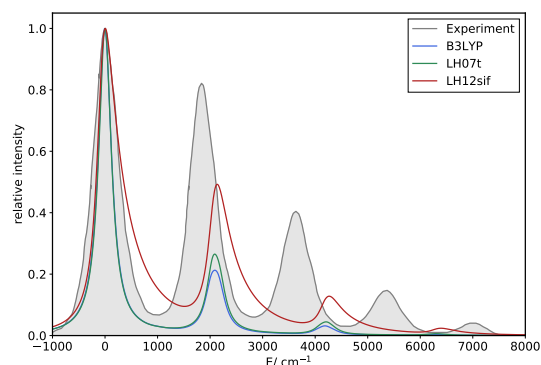


Figure A.24: Vibronic absorption spectra for the $1^1\Sigma_g^+ \rightarrow 1^1\Sigma_u^+$ transition of decayne computed with different LHs and the GH B3LYP in comparison with the experimental spectrum (TIPS end-capped derivative, spectrum recorded in hexane).^[353] A lifetime of 36.3 fs was used for the line broadening to match the experimental spectrum.

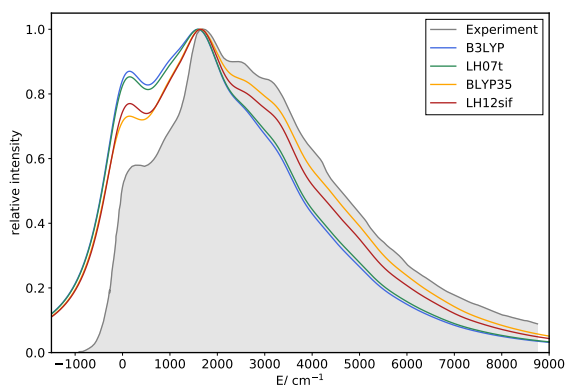


Figure A.25: Vibronic absorption spectra for the $1^1A_1 \rightarrow 1^1B_1$ transition of diphenylfuran computed with different LHs and GHs in comparison with the experimental spectrum (recorded in cyclohexane).^[354] A lifetime of 9.7 fs was used for the line broadening to match the experimental spectrum.

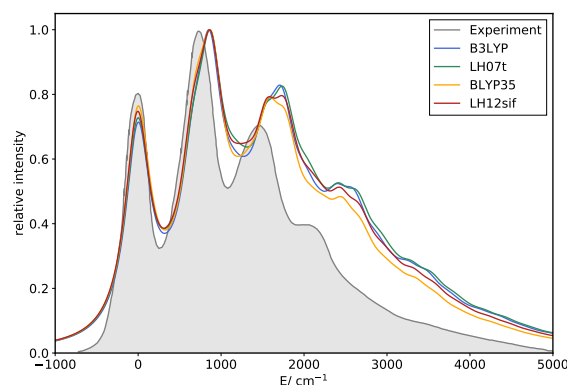


Figure A.26: Vibronic absorption spectra for the $1^1A_1 \rightarrow 1^1B_2$ transition of 3H-1,2,4-triazole-3,5(4H)-dione computed with different LHs and GHs in comparison with the experimental spectrum (recorded in carbon tetrachloride).^[355] A lifetime of 29.0 fs was used for the line broadening to match the experimental spectrum.

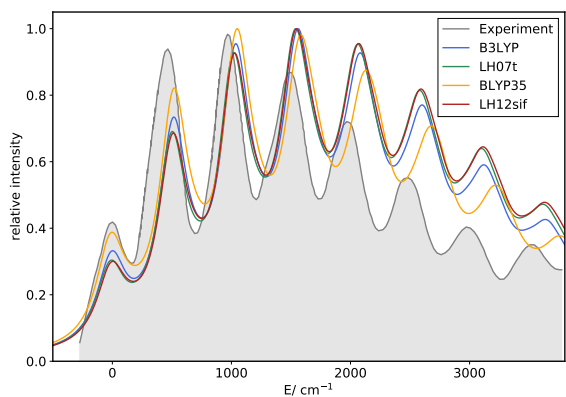


Figure A.27: Vibronic absorption spectra for the $1^2B_2 \rightarrow 1^2A_2$ transition of the phenoxyl radical computed with different LHs and GHs in comparison with the experimental spectrum (recorded in cryogenic argon matrix).^[356] A lifetime of 36.3 fs was used for the line broadening to match the experimental spectrum.

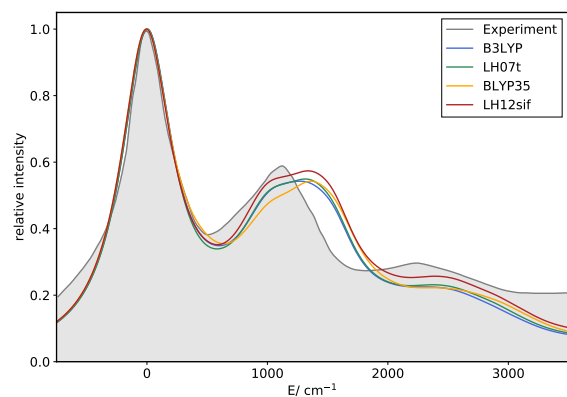


Figure A.28: Vibronic absorption spectra for the $1^2B_2 \rightarrow 2^2A_2$ transition of the benzyl radical computed with different LHs and GHs in comparison with the experimental spectrum.^[357] A lifetime of 20.3 fs was used for the line broadening to match the experimental spectrum.

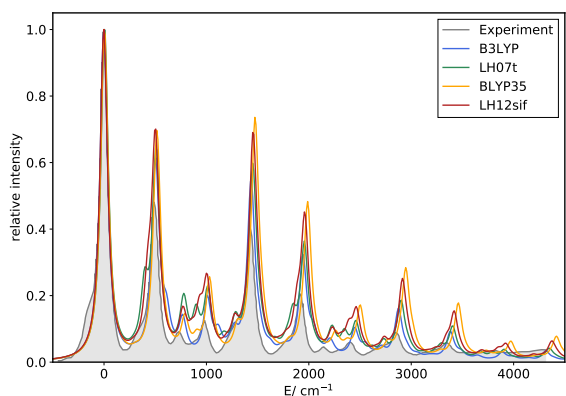


Figure A.29: Vibronic absorption spectra for the $1^2A_u \rightarrow 1^2B_{3g}$ transition of the naphthalene radical cation computed with different LHs and GHs in comparison with the experimental spectrum (recorded in Ar:CCl₄:N = 300:4:1 matrix).^[358] A lifetime of 120.9 fs was used for the line broadening to match the experimental spectrum.

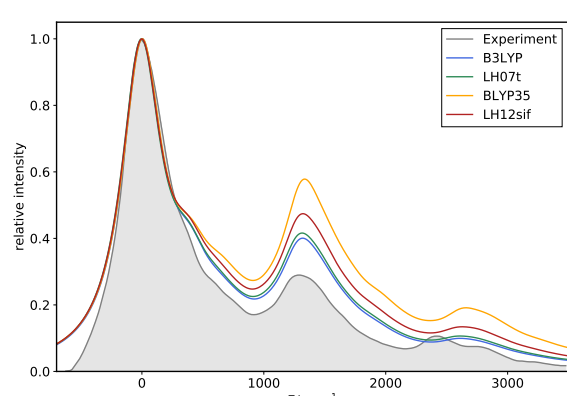


Figure A.30: Vibronic absorption spectra for the $1^2B_{3g} \rightarrow 1^2A_u$ transition of the anthracene radical cation computed with different LHs and GHs in comparison with the experimental spectrum (recorded in argon matrix).^[359] A lifetime of 26.6 fs was used for the line broadening to match the experimental spectrum.

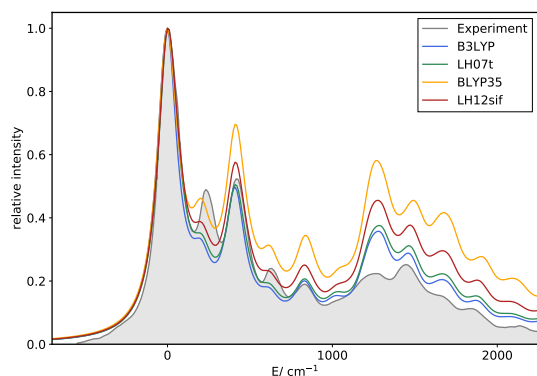


Figure A.31: Vibronic absorption spectra for the $1^2A_2 \rightarrow 1^2B_2$ transition of the fluorene radical cation computed with different LHs and GHs in comparison with the experimental spectrum (recorded in neon matrix).^[360] A lifetime of 72.6 fs was used for the line broadening to match the experimental spectrum.

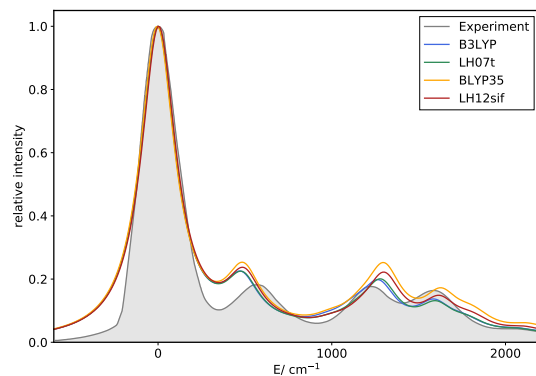


Figure A.32: Vibronic absorption spectra for the $1^2A_u \rightarrow 1^2B_g$ transition of the 1H,3H-benzo[1,2-c:4,5-c']difuran-1,3,5,7-tetraone radical anion computed with different LHs and GHs in comparison with the experimental spectrum.^[357] A lifetime of 43.5 fs was used for the line broadening to match the experimental spectrum.

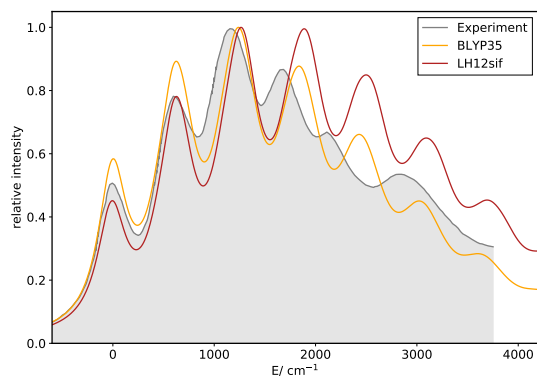


Figure A.33: Vibronic absorption spectra for the $1^2A_u \rightarrow 1^2B_g$ transition of the 1H,3H-benzo[1,2-c:4,5-c']difuran-1,3,5,7-tetraone radical anion computed with LH12ct-SsifPW92 and BLYP35 in comparison with the experimental spectrum.^[357] A lifetime of 31.4 fs was used for the line broadening to match the experimental spectrum.

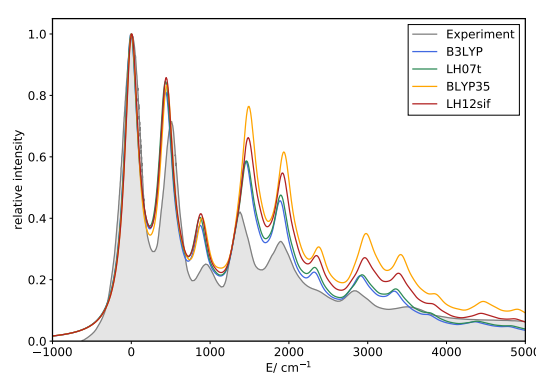


Figure A.34: Vibronic absorption spectra for the $1^2A_2 \rightarrow 1^2B_2$ transition of the naphthalic anhydride radical anion computed with different LHs and GHs in comparison with the experimental spectrum (recorded in methyltetrahydrofuran).^[300] A lifetime of 50.8 fs was used for the line broadening to match the experimental spectrum.

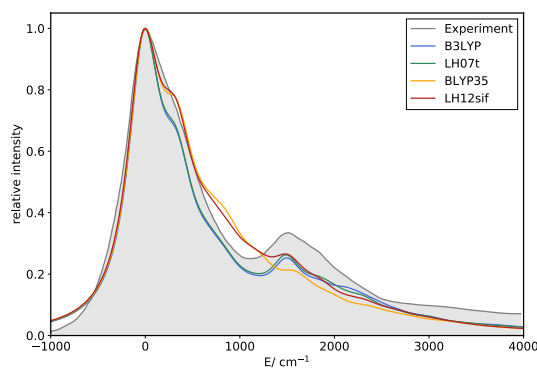


Figure A.35: Vibronic absorption spectra for the $1^2B_2 \rightarrow 1^2A_2$ transition of the 2,2'-(2,4,5-trioxocyclopentane-1,3-diylidene)dimalononitrile ("croconate violet") radical anion computed with different LHs and GHs in comparison with the experimental spectrum (recorded in dimethylformamide).^[361] A lifetime of 26.6 fs was used for the line broadening to match the experimental spectrum.

A.12 Additional Data for Studies on Dipole Moments and Polarizabilities

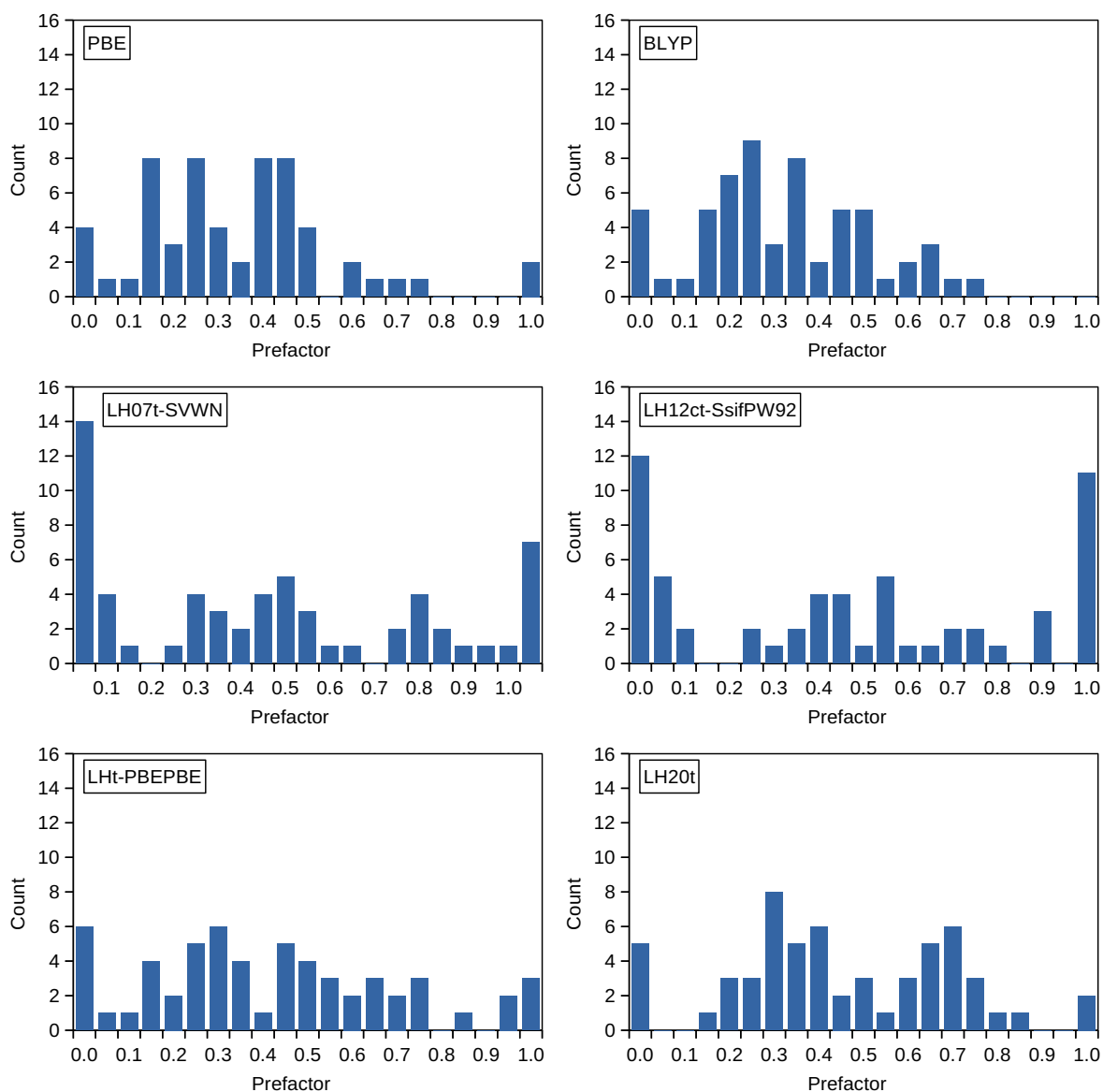


Figure A.36: Histograms reflecting the distribution of optimal GH or LH prefactors for dipole moments of 58 molecules from the HHdip-152 test set,^[204] i.e. how often a given prefactor yields the lowest absolute percentage error for a given molecule.

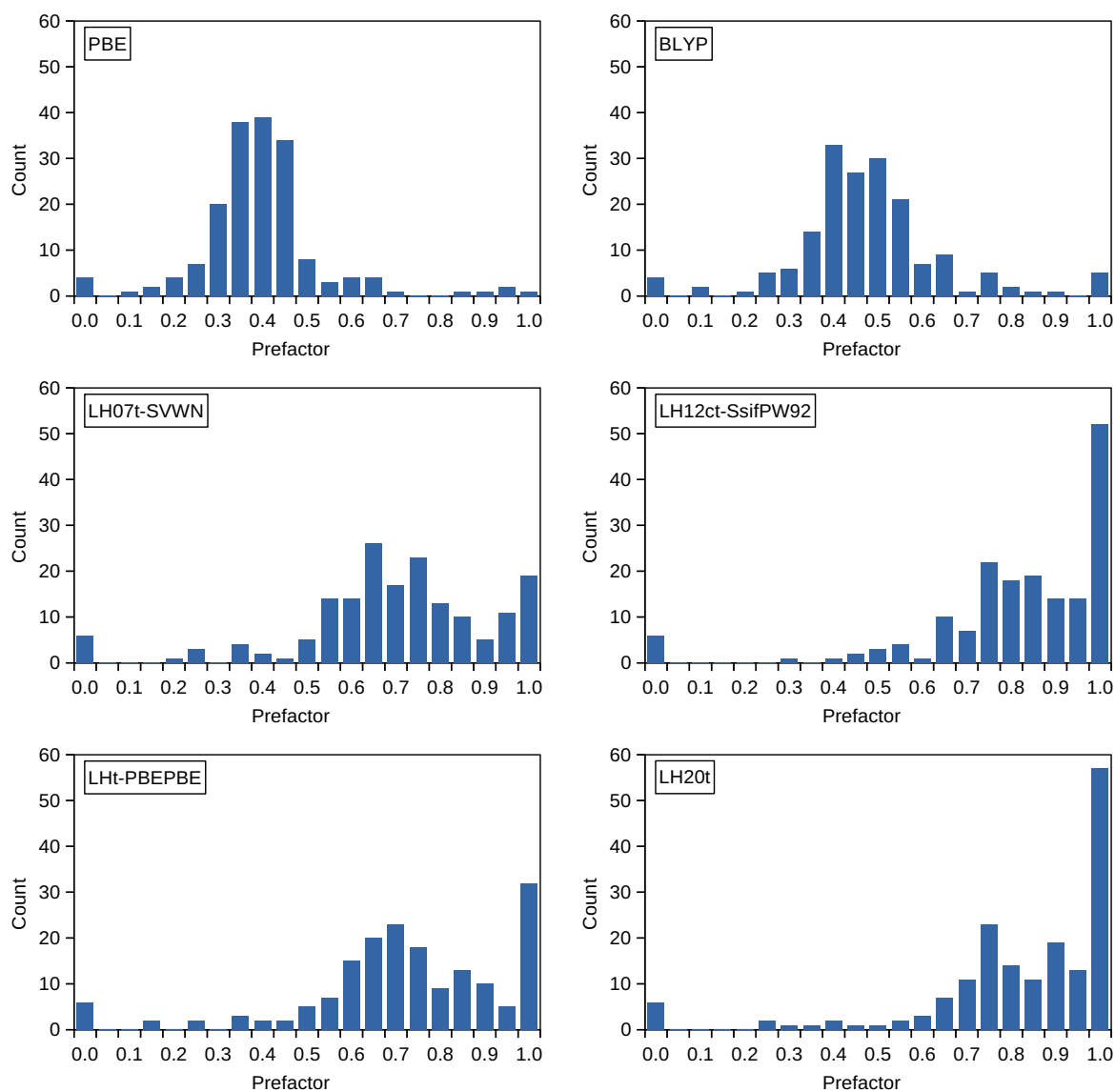


Figure A.37: Histograms reflecting the distribution of optimal GH or LH prefactors for static polarizabilities of 58 molecules from the HHpol-132 test set,^[205] i.e. how often a given prefactor yields the lowest absolute percentage error for a given molecule (total: $3 \cdot 58 = 174$ polarizabilities).

Bibliography

- [1] Dirac, P. A. M. Quantum mechanics of many-electron systems. *Proc. R. Soc. Lond. A* **1929**, *123*, 714–733.
- [2] Hohenberg, P.; Kohn, W. Inhomogeneous Electron Gas. *Phys. Rev.* **1964**, *136*, B864–B871.
- [3] Kohn, W.; Sham, L. J. Self-Consistent Equations Including Exchange and Correlation Effects. *Phys. Rev.* **1965**, *140*, A1133–A1138.
- [4] Ahlrichs, R.; Elliott, S. D.; Huniar, U. Quantum chemistry: Large molecules – small computers. *Ber. Bunsen. Phys. Chem.* **1998**, *102*, 795–804.
- [5] Mohr, S.; Ratcliff, L. E.; Genovese, L.; Caliste, D.; Boulanger, P.; Goedecker, S.; Deutsch, T. Accurate and efficient linear scaling DFT calculations with universal applicability. *Phys. Chem. Chem. Phys.* **2015**, *17*, 31360–31370.
- [6] Goerigk, L.; Hansen, A.; Bauer, C.; Ehrlich, S.; Najibi, A.; Grimme, S. A look at the density functional theory zoo with the advanced GMTKN55 database for general main group thermochemistry, kinetics and noncovalent interactions. *Phys. Chem. Chem. Phys.* **2017**, *19*, 32184–32215.
- [7] Mardirossian, N.; Head-Gordon, M. Thirty years of density functional theory in computational chemistry: an overview and extensive assessment of 200 density functionals. *Mol. Phys.* **2017**, *115*, 2315–2372.
- [8] McAnanama-Brereton, S.; Waller, M. P. Rational Density Functional Selection Using Game Theory. *J. Chem. Inf. Model.* **2018**, *58*, 61–67.
- [9] Becke, A. D. A new mixing of Hartree–Fock and local density-functional theories. *J. Chem. Phys.* **1993**, *98*, 1372–1377.
- [10] Becke, A. D. Density-functional thermochemistry. III. The role of exact exchange. *J. Chem. Phys.* **1993**, *98*, 5648–5652.

- [11] Jaramillo, J.; Scuseria, G. E.; Ernzerhof, M. Local hybrid functionals. *J. Chem. Phys.* **2003**, *118*, 1068–1073.
- [12] Maier, T. M.; Arbuznikov, A. V.; Kaupp, M. Local hybrid functionals: Theory, implementation, and performance of an emerging new tool in quantum chemistry and beyond. *Wiley Interdiscip. Rev. Comput. Mol. Sci.* **2019**, *9*, e1378.
- [13] Bahmann, H.; Rodenberg, A.; Arbuznikov, A. V.; Kaupp, M. A thermochemically competitive local hybrid functional without gradient corrections. *J. Chem. Phys.* **2007**, *126*, 011103.
- [14] Tao, J.; Staroverov, V. N.; Scuseria, G. E.; Perdew, J. P. Exact-exchange energy density in the gauge of a semilocal density-functional approximation. *Phys. Rev. A* **2008**, *77*, 012509.
- [15] Arbuznikov, A. V.; Kaupp, M. Towards improved local hybrid functionals by calibration of exchange-energy densities. *J. Chem. Phys.* **2014**, *141*, 204101.
- [16] Maier, T. M.; Haasler, M.; Arbuznikov, A. V.; Kaupp, M. New approaches for the calibration of exchange-energy densities in local hybrid functionals. *Phys. Chem. Chem. Phys.* **2016**, *18*, 21133–21144.
- [17] Haasler, M.; Maier, T. M.; Grotjahn, R.; Gückel, S.; Arbuznikov, A. V.; Kaupp, M. A Local Hybrid Functional with Wide Applicability and Good Balance between (De)Localization and Left–Right Correlation. *J. Chem. Theory Comput.* **2020**, *16*, 5645–5657.
- [18] Klawohn, S.; Kaupp, M.; Karton, A. MVO-10: A Gas-Phase Oxide Benchmark for Localization/Delocalization in Mixed-Valence Systems. *J. Chem. Theory Comput.* **2018**, *14*, 3512–3523.
- [19] Gückel, S.; Gluyas, J. B. G.; El-Tarhuni, S.; Sobolev, A. N.; Whiteley, M. W.; Halet, J.-F.; Lapinte, C.; Kaupp, M.; Low, P. J. Iron versus Ruthenium: Clarifying the Electronic Differences between Prototypical Mixed-Valence Organometallic Butadienyldiyl Bridged Molecular Wires. *Organometallics* **2018**, *37*, 1432–1445.
- [20] Gückel, S.; Gluyas, J. B. G.; Eaves, S. G.; Safari, P.; Yufit, D. S.; Sobolev, A. N.; Kaupp, M.; Low, P. J. A Spectroscopic and Computationally Minimal Approach to the Analysis of Charge-Transfer Processes in Conformationally Fluxional Mixed-Valence and Heterobimetallic Complexes. *Chem. Eur. J.* **2019**, *25*, 8837–8853.

- [21] González, L.; Escudero, D.; Serrano-Andrés, L. Progress and Challenges in the Calculation of Electronic Excited States. *ChemPhysChem* **2012**, *13*, 28–51.
- [22] Casida, M. E. Time-Dependent Density Functional Response Theory for Molecules. In: *Recent Advances In Density Functional Methods*, Vol. 1; Chong, D. P., Ed.; World Scientific: Singapore, **1995**.
- [23] Maier, T. M.; Bahmann, H.; Kaupp, M. Efficient Semi-numerical Implementation of Global and Local Hybrid Functionals for Time-Dependent Density Functional Theory. *J. Chem. Theory Comput.* **2015**, *11*, 4226–4237.
- [24] Maier, T. M.; Bahmann, H.; Arbuznikov, A. V.; Kaupp, M. Validation of local hybrid functionals for TDDFT calculations of electronic excitation energies. *J. Chem. Phys.* **2016**, *144*, 074106.
- [25] Grotjahn, R.; Maier, T. M.; Michl, J.; Kaupp, M. Development of a TDDFT-Based Protocol with Local Hybrid Functionals for the Screening of Potential Singlet Fission Chromophores. *J. Chem. Theory Comput.* **2017**, *13*, 4984–4996.
- [26] Schreiber, M.; Silva-Junior, M. R.; Sauer, S. P. A.; Thiel, W. Benchmarks for electronically excited states: CASPT2, CC2, CCSD, and CC3. *J. Chem. Phys.* **2008**, *128*, 134110.
- [27] Silva-Junior, M. R.; Schreiber, M.; Sauer, S. P. A.; Thiel, W. Benchmarks for electronically excited states: Time-dependent density functional theory and density functional theory based multireference configuration interaction. *J. Chem. Phys.* **2008**, *129*, 104103.
- [28] Peach, M. J. G.; Benfield, P.; Helgaker, T.; Tozer, D. J. Excitation energies in density functional theory: An evaluation and a diagnostic test. *J. Chem. Phys.* **2008**, *128*, 044118.
- [29] Besley, N. A.; Peach, M. J. G.; Tozer, D. J. Time-dependent density functional theory calculations of near-edge X-ray absorption fine structure with short-range corrected functionals. *Phys. Chem. Chem. Phys.* **2009**, *11*, 10350–10358.
- [30] Wen, J.; Turowski, M.; Dron, P. I.; Chalupský, J.; Grotjahn, R.; Maier, T. M.; Fatur, S. M.; Havlas, Z.; Johnson, J. C.; Kaupp, M.; Michl, J. Electronic States of 2,3-Diamino-1,4-naphthoquinone and Its N-Alkylated Derivatives. *J. Phys. Chem. C* **2020**, *124*, 60–69.

- [31] Santoro, F.; Jacquemin, D. Going beyond the vertical approximation with time-dependent density functional theory. *Wiley Interdiscip. Rev. Comput. Mol. Sci.* **2016**, *6*, 460–486.
- [32] Adamo, C.; Jacquemin, D. The calculations of excited-state properties with Time-Dependent Density Functional Theory. *Chem. Soc. Rev.* **2013**, *42*, 845–856.
- [33] Caillie, C. V.; Amos, R. D. Geometric derivatives of excitation energies using SCF and DFT. *Chem. Phys. Lett.* **1999**, *308*, 249–255.
- [34] Caillie, C. V.; Amos, R. D. Geometric derivatives of density functional theory excitation energies using gradient-corrected functionals. *Chem. Phys. Lett.* **2000**, *317*, 159–164.
- [35] Furche, F.; Ahlrichs, R. Adiabatic time-dependent density functional methods for excited state properties. *J. Chem. Phys.* **2002**, *117*, 7433–7447.
- [36] TURBOMOLE V7.5 2020, a development of University of Karlsruhe and Forschungszentrum Karlsruhe GmbH, 1989-2007, TURBOMOLE GmbH, since 2007; available from <https://www.turbomole.org>.
- [37] Balasubramani, S. G.; Chen, G. P.; Coriani, S.; Diedenhofen, M.; Frank, M. S.; Franzke, Y. J.; Furche, F.; Grotjahn, R.; Harding, M. E.; Hättig, C.; Hellweg, A.; Helmich-Paris, B.; Holzer, C.; Huniar, U.; Kaupp, M.; Marefat Khah, A.; Karbalaee Khani, S.; Müller, T.; Mack, F.; Nguyen, B. D.; Parker, S. M.; Perlt, E.; Rappoport, D.; Reiter, K.; Roy, S.; Rückert, M.; Schmitz, G.; Sierka, M.; Tapavicza, E.; Tew, D. P.; van Wüllen, C.; Voora, V. K.; Weigend, F.; Wodyński, A.; Yu, J. M. TURBOMOLE: Modular program suite for *ab initio* quantum-chemical and condensed-matter simulations. *J. Chem. Phys.* **2020**, *152*, 184107.
- [38] Hutter, J. Excited state nuclear forces from the Tamm–Dancoff approximation to time-dependent density functional theory within the plane wave basis set framework. *J. Chem. Phys.* **2003**, *118*, 3928–3934.
- [39] Rappoport, D.; Furche, F. Analytical time-dependent density functional derivative methods within the RI-*J* approximation, an approach to excited states of large molecules. *J. Chem. Phys.* **2005**, *122*, 064105.

- [40] Chiba, M.; Tsuneda, T.; Hirao, K. Excited state geometry optimizations by analytical energy gradient of long-range corrected time-dependent density functional theory. *J. Chem. Phys.* **2006**, *124*, 144106.
- [41] Scalmani, G.; Frisch, M. J.; Mennucci, B.; Tomasi, J.; Cammi, R.; Barone, V. Geometries and properties of excited states in the gas phase and in solution: Theory and application of a time-dependent density functional theory polarizable continuum model. *J. Chem. Phys.* **2006**, *124*, 094107.
- [42] Sitt, A.; Kronik, L.; Ismail-Beigi, S.; Chelikowsky, J. R. Excited-state forces within time-dependent density-functional theory: A frequency-domain approach. *Phys. Rev. A* **2007**, *76*, 054501.
- [43] Liu, F.; Gan, Z.; Shao, Y.; Hsu, C.-P.; Dreuw, A.; Head-Gordon, M.; Miller, B. T.; Brooks, B. R.; Yu, J.-G.; Furlani, T. R.; Kong, J. A parallel implementation of the analytic nuclear gradient for time-dependent density functional theory within the Tamm–Dancoff approximation. *Mol. Phys.* **2010**, *108*, 2791–2800.
- [44] Si, D.; Li, H. Analytic energy gradient in combined time-dependent density functional theory and polarizable force field calculation. *J. Chem. Phys.* **2010**, *133*, 144112.
- [45] Petrenko, T.; Kossmann, S.; Neese, F. Efficient time-dependent density functional theory approximations for hybrid density functionals: Analytical gradients and parallelization. *J. Chem. Phys.* **2011**, *134*, 054116.
- [46] Zeng, Q.; Liang, W. Analytic energy gradient of excited electronic state within TDDFT/MMpol framework: Benchmark tests and parallel implementation. *J. Chem. Phys.* **2015**, *143*, 134104.
- [47] Klawohn, S.; Bahmann, H.; Kaupp, M. Implementation of Molecular Gradients for Local Hybrid Density Functionals Using Seminumerical Integration Techniques. *J. Chem. Theory Comput.* **2016**, *12*, 4254–4262.
- [48] Neese, F.; Wennmohs, F.; Hansen, A.; Becker, U. Efficient, approximate and parallel Hartree–Fock and hybrid DFT calculations. A ‘chain-of-spheres’ algorithm for the Hartree–Fock exchange. *Chem. Phys.* **2009**, *356*, 98–109.
- [49] Medvedev, M. G.; Bushmarinov, I. S.; Sun, J.; Perdew, J. P.; Lyssenko, K. A. Density functional theory is straying from the path toward the exact functional. *Science* **2017**, *355*, 49–52.

- [50] Kepp, K. P. Comment on “Density functional theory is straying from the path toward the exact functional”. *Science* **2017**, 356, 496.
- [51] Medvedev, M. G.; Bushmarinov, I. S.; Sun, J.; Perdew, J. P.; Lyssenko, K. A. Response to Comment on “Density functional theory is straying from the path toward the exact functional”. *Science* **2017**, 356, 496–496.
- [52] Brorsen, K. R.; Yang, Y.; Pak, M. V.; Hammes-Schiffer, S. Is the Accuracy of Density Functional Theory for Atomization Energies and Densities in Bonding Regions Correlated?. *J. Phys. Chem. Lett.* **2017**, 8, 2076–2081.
- [53] Wang, Y.; Wang, X.; Truhlar, D. G.; He, X. How Well Can the M06 Suite of Functionals Describe the Electron Densities of Ne, Ne⁶⁺, and Ne⁸⁺?. *J. Chem. Theory Comput.* **2017**, 13, 6068–6077.
- [54] Gould, T. What Makes a Density Functional Approximation Good? Insights from the Left Fukui Function. *J. Chem. Theory Comput.* **2017**, 13, 2373–2377.
- [55] Hammes-Schiffer, S. A conundrum for density functional theory. *Science* **2017**, 355, 28–29.
- [56] Su, N. Q.; Zhu, Z.; Xu, X. Doubly hybrid density functionals that correctly describe both density and energy for atoms. *Proc. Natl. Acad. Sci. U.S.A.* **2018**, 115, 2287–2292.
- [57] Stefanucci, G.; van Leeuwen, R. *Nonequilibrium Many-Body Theory of Quantum Systems: A Modern Introduction*; Cambridge University Press: New York, **2013**, pp. 1–17.
- [58] Pauli jr., W. Über den Zusammenhang des Abschlusses der Elektronengruppen im Atom mit der Komplexstruktur der Spektren. *Z. Phys.* **1925**, 31, 765–783.
- [59] Born, M.; Oppenheimer, R. Zur Quantentheorie der Molekeln. *Ann. Phys.* **1927**, 389, 457–484.
- [60] Jensen, F. *Introduction to Computational Chemistry*; Wiley: Hoboken, NJ, 3rd ed.; **2017**, pp. 90–94.
- [61] Koch, W.; Holthausen, M. C. *A Chemist’s Guide to Density Functional Theory*; Wiley-VCH: Weinheim, 2nd ed.; **2001**, pp. 3–6.

- [62] Stefanucci, G.; van Leeuwen, R. *Nonequilibrium Many-Body Theory of Quantum Systems: A Modern Introduction*; Cambridge University Press: New York, **2013**, p. 82.
- [63] Ritz, W. Über eine neue Methode zur Lösung gewisser Variationsprobleme der mathematischen Physik.. *J. Reine Angew. Math.* **1909**, 1909, 1–61.
- [64] Szabo, A.; Ostlund, N. S. *Modern Quantum Chemistry: Introduction to Advanced Electronic Structure Theory*; Macmillan: New York, **1982**. Reprint: Dover Publications: Mineola, NY, 1996, pp. 31–33.
- [65] Austin, B. M.; Zubarev, D. Y.; Lester, Jr, W. A. Quantum Monte Carlo and related approaches. *Chem. Rev.* **2012**, 112, 263–288.
- [66] Szabo, A.; Ostlund, N. S. *Modern Quantum Chemistry: Introduction to Advanced Electronic Structure Theory*; Macmillan: New York, **1982**. Reprint: Dover Publications: Mineola, NY, 1996, p. 50.
- [67] Maier, T. M. *Development of Local Hybrid Functionals for Time-Dependent Density Functional Theory*, Thesis, Technische Universität Berlin, **2016**.
- [68] Helgaker, T.; Jørgensen, P.; Olsen, J. *Molecular Electronic-Structure Theory*; Wiley: Hoboken, NJ, **2000**, pp. 19–25.
- [69] Szabo, A.; Ostlund, N. S. *Modern Quantum Chemistry: Introduction to Advanced Electronic Structure Theory*; Macmillan: New York, **1982**. Reprint: Dover Publications: Mineola, NY, 1996, p. 111.
- [70] Szabo, A.; Ostlund, N. S. *Modern Quantum Chemistry: Introduction to Advanced Electronic Structure Theory*; Macmillan: New York, **1982**. Reprint: Dover Publications: Mineola, NY, 1996, pp. 115–119.
- [71] McWeeny, R. Some Recent Advances in Density Matrix Theory. *Rev. Mod. Phys.* **1960**, 32, 335–369.
- [72] Szabo, A.; Ostlund, N. S. *Modern Quantum Chemistry: Introduction to Advanced Electronic Structure Theory*; Macmillan: New York, **1982**. Reprint: Dover Publications: Mineola, NY, 1996, p. 121.
- [73] Jensen, F. *Introduction to Computational Chemistry*; Wiley: Hoboken, NJ, 3rd ed.; **2017**, pp. 99–100.

- [74] Jensen, F. *Introduction to Computational Chemistry*; Wiley: Hoboken, NJ, 3rd ed.; **2017**, pp. 101–102.
- [75] Roothaan, C. C. J. New Developments in Molecular Orbital Theory. *Rev. Mod. Phys.* **1951**, *23*, 69–89.
- [76] Hall, G. G. The molecular orbital theory of chemical valency VIII. A method of calculating ionization potentials. *Proc. R. Soc. Lond. A* **1951**, *205*, 541–552.
- [77] Jensen, F. *Introduction to Computational Chemistry*; Wiley: Hoboken, NJ, 3rd ed.; **2017**, p. 190.
- [78] Dupuis, M.; Rys, J.; King, H. F. Evaluation of molecular integrals over Gaussian basis functions. *J. Chem. Phys.* **1976**, *65*, 111–116.
- [79] Obara, S.; Saika, A. Efficient recursive computation of molecular integrals over Cartesian Gaussian functions. *J. Chem. Phys.* **1986**, *84*, 3963–3974.
- [80] McMurchie, L. E.; Davidson, E. R. One- and two-electron integrals over cartesian gaussian functions. *J. Comput. Phys.* **1978**, *26*, 218–231.
- [81] Häser, M.; Ahlrichs, R. Improvements on the direct SCF method. *J. Comput. Chem.* **1989**, *10*, 104–111.
- [82] Horn, H.; Weiß, H.; Häser, M.; Ehrig, M.; Ahlrichs, R. Prescreening of two-electron integral derivatives in SCF gradient and Hessian calculations. *J. Comput. Chem.* **1991**, *12*, 1058–1064.
- [83] Eichkorn, K.; Treutler, O.; Öhm, H.; Häser, M.; Ahlrichs, R. Auxiliary basis sets to approximate Coulomb potentials. *Chem. Phys. Lett.* **1995**, *240*, 283–290.
- [84] Früchtl, H. A.; Kendall, R. A.; Harrison, R. J.; Dyall, K. G. An implementation of RI–SCF on parallel computers. *Int. J. Quantum Chem.* **1997**, *64*, 63–69.
- [85] Weigend, F. A fully direct RI-HF algorithm: Implementation, optimised auxiliary basis sets, demonstration of accuracy and efficiency. *Phys. Chem. Chem. Phys.* **2002**, *4*, 4285–4291.
- [86] Löwdin, P.-O. Quantum Theory of Many-Particle Systems. III. Extension of the Hartree-Fock Scheme to Include Degenerate Systems and Correlation Effects. *Phys. Rev.* **1955**, *97*, 1509–1520.

- [87] Szabo, A.; Ostlund, N. S. *Modern Quantum Chemistry: Introduction to Advanced Electronic Structure Theory*; Macmillan: New York, **1982**. Reprint: Dover Publications: Mineola, NY, 1996, p. 231.
- [88] Mok, D. K. W.; Neumann, R.; Handy, N. C. Dynamical and Nondynamical Correlation. *J. Phys. Chem.* **1996**, *100*, 6225–6230.
- [89] Ramos-Cordoba, E.; Salvador, P.; Matito, E. Separation of dynamic and nondynamic correlation. *Phys. Chem. Chem. Phys.* **2016**, *18*, 24015–24023.
- [90] Hollett, J. W.; Gill, P. M. W. The two faces of static correlation. *J. Chem. Phys.* **2011**, *134*, 114111.
- [91] Boys, S. F. Electronic wave functions II. A calculation for the ground state of the beryllium atom. *Proc. R. Soc. Lond. A* **1950**, *201*, 125–137.
- [92] Szabo, A.; Ostlund, N. S. *Modern Quantum Chemistry: Introduction to Advanced Electronic Structure Theory*; Macmillan: New York, **1982**. Reprint: Dover Publications: Mineola, NY, 1996, pp. 231–270.
- [93] Møller, C.; Plesset, M. S. Note on an Approximation Treatment for Many-Electron Systems. *Phys. Rev.* **1934**, *46*, 618–622.
- [94] Cremer, D. Møller-Plesset perturbation theory: from small molecule methods to methods for thousands of atoms. *Wiley Interdiscip. Rev. Comput. Mol. Sci.* **2011**, *1*, 509–530.
- [95] Bartlett, R. J.; Musiał, M. Coupled-cluster theory in quantum chemistry. *Rev. Mod. Phys.* **2007**, *79*, 291–352.
- [96] Crawford, T. D.; Schaefer, H. F. An Introduction to Coupled Cluster Theory for Computational Chemists. In: *Reviews in Computational Chemistry*, Vol. 14; Lipkowitz, K. B.; Boyd, D. B., Eds.; Wiley: New York, **2000**.
- [97] Roos, B. O. Multiconfigurational quantum chemistry. In: *Theory and Applications of Computational Chemistry: The First Forty Years*; Dykstra, C. E.; Frenking, G.; Kim, K. S.; Scuseria, G. E., Eds.; Elsevier: Amsterdam, **2005**.
- [98] Veryazov, V.; Malmqvist, P. Å.; Roos, B. O. How to select active space for multiconfigurational quantum chemistry?. *Int. J. Quantum Chem.* **2011**, *111*, 3329–3338.

- [99] García-Aldea, D.; Alvarellos, J. E. Kinetic-energy density functionals with nonlocal terms with the structure of the Thomas-Fermi functional. *Phys. Rev. A* **2007**, *76*, 052504.
- [100] Laricchia, S.; Constantin, L. A.; Fabiano, E.; Sala, F. D. Laplacian-Level Kinetic Energy Approximations Based on the Fourth-Order Gradient Expansion: Global Assessment and Application to the Subsystem Formulation of Density Functional Theory. *J. Chem. Theory Comput.* **2013**, *10*, 164–179.
- [101] Jensen, F. *Introduction to Computational Chemistry*; Wiley: Hoboken, NJ, 3rd ed.; **2017**, p. 235.
- [102] Scuseria, G. E.; Staroverov, V. N. Progress in the development of exchange-correlation functionals. In: *Theory and Applications of Computational Chemistry: The First Forty Years*; Dykstra, C. E.; Frenking, G.; Kim, K. S.; Scuseria, G. E., Eds.; Elsevier: Amsterdam, **2005**.
- [103] Koch, W.; Holthausen, M. C. *A Chemist's Guide to Density Functional Theory*; Wiley-VCH: Weinheim, 2nd ed.; **2001**, p. 24.
- [104] Becke, A. D. Correlation energy of an inhomogeneous electron gas: A coordinate-space model. *J. Chem. Phys.* **1988**, *88*, 1053–1062.
- [105] Harris, J. Adiabatic-connection approach to Kohn-Sham theory. *Phys. Rev. A* **1984**, *29*, 1648–1659.
- [106] Koch, W.; Holthausen, M. C. *A Chemist's Guide to Density Functional Theory*; Wiley-VCH: Weinheim, 2nd ed.; **2001**, pp. 67–70.
- [107] Koch, W.; Holthausen, M. C. *A Chemist's Guide to Density Functional Theory*; Wiley-VCH: Weinheim, 2nd ed.; **2001**, p. 26.
- [108] Jensen, F. *Introduction to Computational Chemistry*; Wiley: Hoboken, NJ, 3rd ed.; **2017**, p. 245.
- [109] Perdew, J. P.; Tao, J.; Staroverov, V. N.; Scuseria, G. E. Meta-generalized gradient approximation: Explanation of a realistic nonempirical density functional. *J. Chem. Phys.* **2004**, *120*, 6898–6911.
- [110] Koch, W.; Holthausen, M. C. *A Chemist's Guide to Density Functional Theory*; Wiley-VCH: Weinheim, 2nd ed.; **2001**, p. 86.

- [111] Handy, N. C.; Cohen, A. J. Left-right correlation energy. *Mol. Phys.* **2001**, *99*, 403–412.
- [112] Perdew, J. P.; Schmidt, K. Jacob’s ladder of density functional approximations for the exchange-correlation energy. *AIP Conf. Proc.* **2001**, *577*, 1–20.
- [113] Jensen, F. *Introduction to Computational Chemistry*; Wiley: Hoboken, NJ, 3rd ed.; **2017**, pp. 247–248.
- [114] Slater, J. C. A Simplification of the Hartree-Fock Method. *Phys. Rev.* **1951**, *81*, 385–390.
- [115] Koch, W.; Holthausen, M. C. *A Chemist’s Guide to Density Functional Theory*; Wiley-VCH: Weinheim, 2nd ed.; **2001**, pp. 72–74.
- [116] Vosko, S. H.; Wilk, L.; Nusair, M. Accurate spin-dependent electron liquid correlation energies for local spin density calculations: a critical analysis. *Can. J. Phys.* **1980**, *58*, 1200–1211.
- [117] Perdew, J. P. Accurate and simple analytic representation of the electron-gas correlation energy. *Phys. Rev. B* **1992**, *45*, 13244–13249.
- [118] Peverati, R.; Truhlar, D. G. Quest for a universal density functional: the accuracy of density functionals across a broad spectrum of databases in chemistry and physics. *Philos. Trans. R. Soc. A* **2014**, *372*, 20120476.
- [119] Gupta, A. K.; Singwi, K. S. Gradient corrections to the exchange-correlation energy of electrons at metal surfaces. *Phys. Rev. B* **1977**, *15*, 1801–1810.
- [120] Perdew, J. P.; Langreth, D. C.; Sahni, V. Corrections to the Local Density Approximation: Gradient Expansion versus Wave-Vector Analysis for the Metallic Surface Problem. *Phys. Rev. Lett.* **1977**, *38*, 1030–1033.
- [121] Koch, W.; Holthausen, M. C. *A Chemist’s Guide to Density Functional Theory*; Wiley-VCH: Weinheim, 2nd ed.; **2001**, pp. 75–78.
- [122] Becke, A. D. Density-functional exchange-energy approximation with correct asymptotic behavior. *Phys. Rev. A* **1988**, *38*, 3098–3100.
- [123] Perdew, J. P.; Burke, K.; Ernzerhof, M. Generalized gradient approximation made simple. *Phys. Rev. Lett.* **1996**, *77*, 3865–3868.

- [124] Lee, C.; Yang, W.; Parr, R. G. Development of the Colle-Salvetti correlation-energy formula into a functional of the electron density. *Phys. Rev. B* **1988**, *37*, 785–789.
- [125] Colle, R.; Salvetti, O. Approximate calculation of the correlation energy for the closed shells. *Theor. Chem. Acc.* **1975**, *37*, 329–334.
- [126] Ernzerhof, M.; Perdew, J. P.; Burke, K. Coupling-constant dependence of atomization energies. *Int. J. Quantum Chem.* **1997**, *64*, 285–295.
- [127] Jensen, F. *Introduction to Computational Chemistry*; Wiley: Hoboken, NJ, 3rd ed.; **2017**, p. 251.
- [128] Becke, A. D. Density-functional thermochemistry. IV. A new dynamical correlation functional and implications for exact-exchange mixing. *J. Chem. Phys.* **1996**, *104*, 1040–1046.
- [129] Perdew, J. P.; Kurth, S.; Zupan, A.; Blaha, P. Accurate Density Functional with Correct Formal Properties: A Step Beyond the Generalized Gradient Approximation. *Phys. Rev. Lett.* **1999**, *82*, 2544–2547.
- [130] Becke, A. D.; Roussel, M. R. Exchange holes in inhomogeneous systems: A coordinate-space model. *Phys. Rev. A* **1989**, *39*, 3761–3767.
- [131] Becke, A. D. Perspective: Fifty years of density-functional theory in chemical physics. *J. Chem. Phys.* **2014**, *140*, 18A301.
- [132] Tao, J.; Perdew, J. P.; Staroverov, V. N.; Scuseria, G. E. Climbing the Density Functional Ladder: Nonempirical Meta-Generalized Gradient Approximation Designed for Molecules and Solids. *Phys. Rev. Lett.* **2003**, *91*, 146401.
- [133] Sun, J.; Ruzsinszky, A.; Perdew, J. P. Strongly Constrained and Appropriately Normed Semilocal Density Functional. *Phys. Rev. Lett.* **2015**, *115*, 036402.
- [134] Koch, W.; Holthausen, M. C. *A Chemist’s Guide to Density Functional Theory*; Wiley-VCH: Weinheim, 2nd ed.; **2001**, p. 79.
- [135] Stephens, P. J.; Devlin, F. J.; Chabalowski, C. F.; Frisch, M. J. Ab Initio Calculation of Vibrational Absorption and Circular Dichroism Spectra Using Density Functional Force Fields. *J. Phys. Chem.* **1994**, *98*, 11623–11627.
- [136] Cohen, A. J.; Mori-Sánchez, P.; Yang, W. Challenges for Density Functional Theory. *Chem. Rev.* **2012**, *112*, 289–320.

- [137] Noorden, R. V.; Maher, B.; Nuzzo, R. The top 100 papers. *Nature* **2014**, *514*, 550–553.
- [138] Adamo, C.; Barone, V. Toward reliable density functional methods without adjustable parameters: The PBE0 model. *J. Chem. Phys.* **1999**, *110*, 6158–6170.
- [139] Hui, K.; Chai, J.-D. SCAN-based hybrid and double-hybrid density functionals from models without fitted parameters. *J. Chem. Phys.* **2016**, *144*, 044114.
- [140] Staroverov, V. N.; Scuseria, G. E.; Tao, J.; Perdew, J. P. Comparative assessment of a new nonempirical density functional: Molecules and hydrogen-bonded complexes. *J. Chem. Phys.* **2003**, *119*, 12129–12137.
- [141] Becke, A. D. Density-functional thermochemistry. V. Systematic optimization of exchange-correlation functionals. *J. Chem. Phys.* **1997**, *107*, 8554–8560.
- [142] Zhao, Y.; Truhlar, D. G. Design of Density Functionals That Are Broadly Accurate for Thermochemistry, Thermochemical Kinetics, and Nonbonded Interactions. *J. Phys. Chem. A* **2005**, *109*, 5656–5667.
- [143] Zhao, Y.; Truhlar, D. G. The M06 suite of density functionals for main group thermochemistry, thermochemical kinetics, noncovalent interactions, excited states, and transition elements: two new functionals and systematic testing of four M06-class functionals and 12 other functionals. *Theor. Chem. Acc.* **2008**, *120*, 215–241.
- [144] Becke, A. D. A real-space model of nondynamical correlation. *J. Chem. Phys.* **2003**, *119*, 2972–2977.
- [145] Becke, A. D. Real-space post-Hartree–Fock correlation models. *J. Chem. Phys.* **2005**, *122*, 064101.
- [146] Renz, M.; Theilacker, K.; Lambert, C.; Kaupp, M. A Reliable Quantum-Chemical Protocol for the Characterization of Organic Mixed-Valence Compounds. *J. Am. Chem. Soc.* **2009**, *131*, 16292–16302.
- [147] Koch, W.; Holthausen, M. C. *A Chemist’s Guide to Density Functional Theory*; Wiley-VCH: Weinheim, 2nd ed.; **2001**, p. 88.
- [148] Vydrov, O. A.; Scuseria, G. E. Assessment of a long-range corrected hybrid functional. *J. Chem. Phys.* **2006**, *125*, 234109.

- [149] Zhou, P.; Zhao, L. Accurate description of excited state intramolecular proton transfer that involves zwitterionic state using optimally tuned range-separated time-dependent density functional theory. *Int. J. Quantum Chem.* **2018**, *118*, e25618.
- [150] Jensen, F. *Introduction to Computational Chemistry*; Wiley: Hoboken, NJ, 3rd ed.; **2017**, p. 254.
- [151] Yanai, T.; Tew, D. P.; Handy, N. C. A new hybrid exchange–correlation functional using the Coulomb-attenuating method (CAM-B3LYP). *Chem. Phys. Lett.* **2004**, *393*, 51–57.
- [152] Chai, J.-D.; Head-Gordon, M. Long-range corrected hybrid density functionals with damped atom–atom dispersion corrections. *Phys. Chem. Chem. Phys.* **2008**, *10*, 6615–6620.
- [153] Chai, J.-D.; Head-Gordon, M. Systematic optimization of long-range corrected hybrid density functionals. *J. Chem. Phys.* **2008**, *128*, 084106.
- [154] Mardirossian, N.; Head-Gordon, M. ω B97X-V: A 10-parameter, range-separated hybrid, generalized gradient approximation density functional with nonlocal correlation, designed by a survival-of-the-fittest strategy. *Phys. Chem. Chem. Phys.* **2014**, *16*, 9904–9924.
- [155] Mardirossian, N.; Head-Gordon, M. ω B97M-V: A combinatorially optimized, range-separated hybrid, meta-GGA density functional with VV10 nonlocal correlation. *J. Chem. Phys.* **2016**, *144*, 214110.
- [156] Stein, T.; Kronik, L.; Baer, R. Prediction of charge-transfer excitations in coumarin-based dyes using a range-separated functional tuned from first principles. *J. Chem. Phys.* **2009**, *131*, 244119.
- [157] Körzdörfer, T.; Sears, J. S.; Sutton, C.; Brédas, J.-L. Long-range corrected hybrid functionals for π -conjugated systems: Dependence of the range-separation parameter on conjugation length. *J. Chem. Phys.* **2011**, *135*, 204107.
- [158] Baer, R.; Livshits, E.; Salzner, U. Tuned Range-Separated Hybrids in Density Functional Theory. *Annu. Rev. Phys. Chem.* **2010**, *61*, 85–109.
- [159] Almbladh, C.-O.; von Barth, U. Exact results for the charge and spin densities, exchange-correlation potentials, and density-functional eigenvalues. *Phys. Rev. B* **1985**, *31*, 3231–3244.

- [160] Krukau, A. V.; Scuseria, G. E.; Perdew, J. P.; Savin, A. Hybrid functionals with local range separation. *J. Chem. Phys.* **2008**, *129*, 124103.
- [161] Klawohn, S.; Bahmann, H. Self-Consistent Implementation of Hybrid Functionals with Local Range Separation. *J. Chem. Theory Comput.* **2020**, *16*, 953–963.
- [162] Grimme, S. Semiempirical hybrid density functional with perturbative second-order correlation. *J. Chem. Phys.* **2006**, *124*, 034108.
- [163] Almlöf, J. Elimination of energy denominators in Møller—Plesset perturbation theory by a Laplace transform approach. *Chem. Phys. Lett.* **1991**, *181*, 319–320.
- [164] Goerigk, L.; Grimme, S. Efficient and Accurate Double-Hybrid-Meta-GGA Density Functionals—Evaluation with the Extended GMTKN30 Database for General Main Group Thermochemistry, Kinetics, and Noncovalent Interactions. *J. Chem. Theory Comput.* **2011**, *7*, 291–309.
- [165] Goerigk, L.; Grimme, S. Double-hybrid density functionals. *Wiley Interdiscip. Rev. Comput. Mol. Sci.* **2014**, *4*, 576–600.
- [166] Benighaus, T.; DiStasio, R. A.; Lochan, R. C.; Chai, J.-D.; Head-Gordon, M. Semiempirical Double-Hybrid Density Functional with Improved Description of Long-Range Correlation. *J. Phys. Chem. A* **2008**, *112*, 2702–2712.
- [167] Casanova-Páez, M.; Dardis, M. B.; Goerigk, L. ω B2PLYP and ω B2GPPLYP: The First Two Double-Hybrid Density Functionals with Long-Range Correction Optimized for Excitation Energies. *J. Chem. Theory Comput.* **2019**, *15*, 4735–4744.
- [168] Kalai, C.; Toulouse, J. A general range-separated double-hybrid density-functional theory. *J. Chem. Phys.* **2018**, *148*, 164105.
- [169] Furche, F. Developing the random phase approximation into a practical post-Kohn–Sham correlation model. *J. Chem. Phys.* **2008**, *129*, 114105.
- [170] Chen, G. P.; Voora, V. K.; Agee, M. M.; Balasubramani, S. G.; Furche, F. Random-Phase Approximation Methods. *Annu. Rev. Phys. Chem.* **2017**, *68*, 421–445.
- [171] Jensen, F. *Introduction to Computational Chemistry*; Wiley: Hoboken, NJ, 3rd ed.; **2017**, p. 267.

- [172] Cruz, F. G.; Lam, K.-C.; Burke, K. Exchange–Correlation Energy Density from Virial Theorem. *J. Phys. Chem. A* **1998**, *102*, 4911–4917.
- [173] Burke, K.; Cruz, F. G.; Lam, K.-C. Unambiguous exchange-correlation energy density. *J. Chem. Phys.* **1998**, *109*, 8161–8167.
- [174] Arbuznikov, A. V.; Bahmann, H.; Kaupp, M. Local Hybrid Functionals with an Explicit Dependence on Spin Polarization. *J. Phys. Chem. A* **2009**, *113*, 11898–11906.
- [175] Janesko, B. G.; Krukau, A. V.; Scuseria, G. E. Self-consistent generalized Kohn-Sham local hybrid functionals of screened exchange: Combining local and range-separated hybridization. *J. Chem. Phys.* **2008**, *129*, 124110.
- [176] Haunschild, R.; Scuseria, G. E. Range-separated local hybrids. *J. Chem. Phys.* **2010**, *132*, 224106.
- [177] Arbuznikov, A. V.; Kaupp, M. Local hybrid exchange-correlation functionals based on the dimensionless density gradient. *Chem. Phys. Lett.* **2007**, *440*, 160–168.
- [178] Arbuznikov, A. V.; Kaupp, M. Importance of the correlation contribution for local hybrid functionals: Range separation and self-interaction corrections. *J. Chem. Phys.* **2012**, *136*, 014111.
- [179] Schmidt, T.; Kraisler, E.; Makmal, A.; Kronik, L.; Kümmel, S. A self-interaction-free local hybrid functional: Accurate binding energies vis-à-vis accurate ionization potentials from Kohn-Sham eigenvalues. *J. Chem. Phys.* **2014**, *140*, 18A510.
- [180] de Silva, P.; Corminboeuf, C. Local hybrid functionals with orbital-free mixing functions and balanced elimination of self-interaction error. *J. Chem. Phys.* **2015**, *142*, 074112.
- [181] de Silva, P.; Corminboeuf, C. Simultaneous Visualization of Covalent and Noncovalent Interactions Using Regions of Density Overlap. *J. Chem. Theory Comput.* **2014**, *10*, 3745–3756.
- [182] Haunschild, R.; Janesko, B. G.; Scuseria, G. E. Local hybrids as a perturbation to global hybrid functionals. *J. Chem. Phys.* **2009**, *131*, 154112.
- [183] Janesko, B. G.; Scuseria, G. E. Parameterized local hybrid functionals from density-matrix similarity metrics. *J. Chem. Phys.* **2008**, *128*, 084111.

- [184] Arbuznikov, A. V.; Kaupp, M. What can we learn from the adiabatic connection formalism about local hybrid functionals?. *J. Chem. Phys.* **2008**, *128*, 214107.
- [185] Theilacker, K.; Arbuznikov, A. V.; Kaupp, M. Gauge effects in local hybrid functionals evaluated for weak interactions and the GMTKN30 test set. *Mol. Phys.* **2016**, *114*, 1118–1127.
- [186] Grimme, S.; Antony, J.; Ehrlich, S.; Krieg, H. A consistent and accurate *ab initio* parametrization of density functional dispersion correction (DFT-D) for the 94 elements H-Pu. *J. Chem. Phys.* **2010**, *132*, 154104.
- [187] Caldeweyher, E.; Ehlert, S.; Hansen, A.; Neugebauer, H.; Spicher, S.; Banwarth, C.; Grimme, S. A generally applicable atomic-charge dependent London dispersion correction. *J. Chem. Phys.* **2019**, *150*, 154122.
- [188] Najibi, A.; Goerigk, L. The Nonlocal Kernel in van der Waals Density Functionals as an Additive Correction: An Extensive Analysis with Special Emphasis on the B97M-V and ω B97M-V Approaches. *J. Chem. Theory Comput.* **2018**, *14*, 5725–5738.
- [189] Parthey, M.; Kaupp, M. Quantum-chemical insights into mixed-valence systems: within and beyond the Robin–Day scheme. *Chem. Soc. Rev.* **2014**, *43*, 5067–5088.
- [190] Kaupp, M.; Karton, A.; Bischoff, F. A. $[\text{Al}_2\text{O}_4]^-$, a Benchmark Gas-Phase Class II Mixed-Valence Radical Anion for the Evaluation of Quantum-Chemical Methods. *J. Chem. Theory Comput.* **2016**, *12*, 3796–3806.
- [191] Gunnarsson, O.; Lundqvist, B. I. Exchange and correlation in atoms, molecules, and solids by the spin-density-functional formalism. *Phys. Rev. B* **1976**, *13*, 4274–4298.
- [192] Jones, R. O.; Gunnarsson, O. The density functional formalism, its applications and prospects. *Rev. Mod. Phys.* **1989**, *61*, 689–746.
- [193] Ziegler, T.; Seth, M.; Krykunov, M.; Autschbach, J.; Wang, F. On the relation between time-dependent and variational density functional theory approaches for the determination of excitation energies and transition moments.. *J. Chem. Phys.* **2009**, *130*, 154102.

- [194] Cullen, J.; Krykunov, M.; Ziegler, T. The formulation of a self-consistent constricted variational density functional theory for the description of excited states. *Chem. Phys.* **2011**, *391*, 11–18.
- [195] Ziegler, T.; Krykunov, M.; Cullen, J. The implementation of a self-consistent constricted variational density functional theory for the description of excited states. *J. Chem. Phys.* **2012**, *136*, 124107.
- [196] Krykunov, M.; Ziegler, T. Self-consistent Formulation of Constricted Variational Density Functional Theory with Orbital Relaxation. Implementation and Applications. *J. Chem. Theory Comput.* **2013**, *9*, 2761–2773.
- [197] Krykunov, M.; Seth, M.; Ziegler, T. Introducing constricted variational density functional theory in its relaxed self-consistent formulation (RSCF-CV-DFT) as an alternative to adiabatic time dependent density functional theory for studies of charge transfer transitions. *J. Chem. Phys.* **2014**, *140*, 18A502.
- [198] Vitale, V.; Sala, F. D.; Görling, A. Open-shell localized Hartree–Fock method based on the generalized adiabatic connection Kohn–Sham formalism for a self-consistent treatment of excited states. *J. Chem. Phys.* **2005**, *122*, 244102.
- [199] Yabana, K.; Bertsch, G. F. Time-dependent local-density approximation in real time. *Phys. Rev. B* **1996**, *54*, 4484–4487.
- [200] Goings, J. J.; Lestrangle, P. J.; Li, X. Real-time time-dependent electronic structure theory. *Wiley Interdiscip. Rev. Comput. Mol. Sci.* **2018**, *8*, e1341.
- [201] Rüger, R. *Approximations in Density Functional Based Excited State Calculations*, Thesis, Vrije Universiteit Amsterdam, **2018**.
- [202] Schiff, L. I. *Quantum Mechanics*; McGraw-Hill: New York, 3rd ed.; **1968**, pp. 280–282.
- [203] Yabana, K.; Nakatsukasa, T.; Iwata, J.-I.; Bertsch, G. F. Real-time, real-space implementation of the linear response time-dependent density-functional theory. *Phys. Status Solidi B* **2006**, *243*, 1121–1138.
- [204] Hait, D.; Head-Gordon, M. How Accurate Is Density Functional Theory at Predicting Dipole Moments? An Assessment Using a New Database of 200 Benchmark Values. *J. Chem. Theory Comput.* **2018**, *14*, 1969–1981.

- [205] Hait, D.; Head-Gordon, M. How accurate are static polarizability predictions from density functional theory? An assessment over 132 species at equilibrium geometry. *Phys. Chem. Chem. Phys.* **2018**, *20*, 19800–19810.
- [206] Runge, E.; Gross, E. K. U. Density-Functional Theory for Time-Dependent Systems. *Phys. Rev. Lett.* **1984**, *52*, 997–1000.
- [207] Dreuw, A.; Head-Gordon, M. Single-Reference ab Initio Methods for the Calculation of Excited States of Large Molecules. *Chem. Rev.* **2005**, *105*, 4009–4037.
- [208] Casida, M. E. Time-dependent density-functional theory for molecules and molecular solids. *J. Mol. Struct. THEOCHEM* **2009**, *914*, 3–18.
- [209] Vignale, G. Real-time resolution of the causality paradox of time-dependent density-functional theory. *Phys. Rev. A* **2008**, *77*, 062511.
- [210] Bauernschmitt, R.; Ahlrichs, R. Treatment of electronic excitations within the adiabatic approximation of time dependent density functional theory. *Chem. Phys. Lett.* **1996**, *256*, 454–464.
- [211] Bates, J. E.; Furche, F. Harnessing the meta-generalized gradient approximation for time-dependent density functional theory. *J. Chem. Phys.* **2012**, *137*, 164105.
- [212] Grotjahn, R.; Furche, F.; Kaupp, M. Development and Implementation of Excited-State Gradients for Local Hybrid Functionals. *J. Chem. Theory Comput.* **2019**, *15*, 5508–5522.
- [213] Hirata, S.; Head-Gordon, M. Time-dependent density functional theory within the Tamm–Dancoff approximation. *Chem. Phys. Lett.* **1999**, *314*, 291–299.
- [214] Weiss, H.; Ahlrichs, R.; Häser, M. A direct algorithm for self-consistent-field linear response theory and application to C₆₀: Excitation energies, oscillator strengths, and frequency-dependent polarizabilities. *J. Chem. Phys.* **1993**, *99*, 1262–1270.
- [215] Furche, F. On the density matrix based approach to time-dependent density functional response theory. *J. Chem. Phys.* **2001**, *114*, 5982–5992.
- [216] Atkins, P.; Friedman, R. *Molecular Quantum Mechanics*; Oxford University Press: New York, 4th ed.; **2005**, pp. 365–368.

- [217] Tapavicza, E.; Furche, F.; Sundholm, D. Importance of Vibronic Effects in the UV–Vis Spectrum of the 7,7,8,8-Tetracyanoquinodimethane Anion. *J. Chem. Theory Comput.* **2016**, *12*, 5058–5066.
- [218] Atkins, P.; Friedman, R. *Molecular Quantum Mechanics*; Oxford University Press: New York, 4th ed.; **2005**, pp. 386–389.
- [219] Condon, E. U. Nuclear Motions Associated with Electron Transitions in Diatomic Molecules. *Phys. Rev.* **1928**, *32*, 858–872.
- [220] Duschinsky, F. The importance of the electron spectrum in multi atomic molecules. Concerning the Franck-Condon principle. *Acta Physicochim. U.R.S.S.* **1937**, *7*, 551–566; as cited in: Tapavicza, E.; Furche, F.; Sundholm, D. *J. Chem. Theory Comput.* **2016**, *12*, 5058–5066.
- [221] Sharp, T. E.; Rosenstock, H. M. Franck–Condon Factors for Polyatomic Molecules. *J. Chem. Phys.* **1964**, *41*, 3453–3463.
- [222] Kupka, H.; Cribb, P. H. Multidimensional Franck–Condon integrals and Duschinsky mixing effects. *J. Chem. Phys.* **1986**, *85*, 1303–1315.
- [223] Norman, P.; Ruud, K.; Saue, T. *Principles and Practices of Molecular Properties: Theory, Modeling, and Simulations*; Wiley: Hoboken, NJ, **2018**, p. 248.
- [224] Jankowiak, H.-C.; Stuber, J. L.; Berger, R. Vibronic transitions in large molecular systems: Rigorous prescreening conditions for Franck-Condon factors. *J. Chem. Phys.* **2007**, *127*, 234101.
- [225] Etinski, M.; Tatchen, J.; Marian, C. M. Time-dependent approaches for the calculation of intersystem crossing rates. *J. Chem. Phys.* **2011**, *134*, 154105.
- [226] Benkyi, I.; Tapavicza, E.; Fliegl, H.; Sundholm, D. Calculation of vibrationally resolved absorption spectra of acenes and pyrene. *Phys. Chem. Chem. Phys.* **2019**, *21*, 21094–21103.
- [227] Mehler, F. G. Ueber die Entwicklung einer Function von beliebig vielen Variablen nach Laplaceschen Functionen höherer Ordnung.. *J. Reine Angew. Math.* **1866**, *1866*, 161–176.
- [228] Tapavicza, E. Generating Function Approach to Single Vibronic Level Fluorescence Spectra. *J. Phys. Chem. Lett.* **2019**, *10*, 6003–6009.

- [229] Send, R.; Kühn, M.; Furche, F. Assessing Excited State Methods by Adiabatic Excitation Energies. *J. Chem. Theory Comput.* **2011**, *7*, 2376–2386.
- [230] Jacquemin, D.; Planchat, A.; Adamo, C.; Mennucci, B. TD-DFT Assessment of Functionals for Optical 0–0 Transitions in Solvated Dyes. *J. Chem. Theory Comput.* **2012**, *8*, 2359–2372.
- [231] Jacquemin, D.; Duchemin, I.; Blase, X. 0–0 Energies Using Hybrid Schemes: Benchmarks of TD-DFT, CIS(D), ADC(2), CC2, and BSE/ *GW* formalisms for 80 Real-Life Compounds. *J. Chem. Theory Comput.* **2015**, *11*, 5340–5359.
- [232] Loos, P.-F.; Jacquemin, D. Chemically Accurate 0-0 Energies with Not-so-Accurate Excited State Geometries. *J. Chem. Theory Comput.* **2019**, *15*, 2481–2491.
- [233] Charaf-Eddin, A.; Planchat, A.; Mennucci, B.; Adamo, C.; Jacquemin, D. Choosing a Functional for Computing Absorption and Fluorescence Band Shapes with TD-DFT. *J. Chem. Theory Comput.* **2013**, *9*, 2749–2760.
- [234] Bahmann, H.; Kaupp, M. Efficient Self-Consistent Implementation of Local Hybrid Functionals. *J. Chem. Theory Comput.* **2015**, *11*, 1540–1548.
- [235] Handy, N. C.; Schaefer, H. F. On the evaluation of analytic energy derivatives for correlated wave functions. *J. Chem. Phys.* **1984**, *81*, 5031–5033.
- [236] Becke, A. D. A multicenter numerical integration scheme for polyatomic molecules. *J. Chem. Phys.* **1988**, *88*, 2547–2553.
- [237] Lebedev, V. Quadratures on a sphere. *USSR Comput. Math. Math. Phys.* **1976**, *16*, 10–24.
- [238] Murray, C. W.; Handy, N. C.; Laming, G. J. Quadrature schemes for integrals of density functional theory. *Mol. Phys.* **1993**, *78*, 997–1014.
- [239] Michels, H. H. Abscissas and weight coefficients for Lobatto quadrature. *Math. Comp.* **1963**, *17*, 237–237.
- [240] Treutler, O.; Ahlrichs, R. Efficient molecular numerical integration schemes. *J. Chem. Phys.* **1995**, *102*, 346–354.
- [241] Johnson, B. G.; Gill, P. M. W.; Pople, J. A. The performance of a family of density functional methods. *J. Chem. Phys.* **1993**, *98*, 5612–5626.

- [242] Friesner, R. A. Solution of self-consistent field electronic structure equations by a pseudospectral method. *Chem. Phys. Lett.* **1985**, *116*, 39–43.
- [243] Plessow, P.; Weigend, F. Seminumerical calculation of the Hartree-Fock exchange matrix: Application to two-component procedures and efficient evaluation of local hybrid density functionals. *J. Comput. Chem.* **2012**, *33*, 810–816.
- [244] Laqua, H.; Kussmann, J.; Ochsenfeld, C. Efficient and Linear-Scaling Seminumerical Method for Local Hybrid Density Functionals. *J. Chem. Theory Comput.* **2018**, *14*, 3451–3458.
- [245] Schattenberg, C. J.; Reiter, K.; Weigend, F.; Kaupp, M. An Efficient Coupled-Perturbed Kohn–Sham Implementation of NMR Chemical Shift Computations with Local Hybrid Functionals and Gauge-Including Atomic Orbitals. *J. Chem. Theory Comput.* **2020**, *16*, 931–943.
- [246] Mack, F.; Schattenberg, C. J.; Kaupp, M.; Weigend, F. Nuclear Spin–Spin Couplings: Efficient Evaluation of Exact Exchange and Extension to Local Hybrid Functionals. *J. Phys. Chem. A* **2020**, *124*, 8529–8539.
- [247] Cao, Y.; Hughes, T.; Giesen, D.; Halls, M. D.; Goldberg, A.; Vadicherla, T. R.; Sastry, M.; Patel, B.; Sherman, W.; Weisman, A. L.; Friesner, R. A. Highly efficient implementation of pseudospectral time-dependent density-functional theory for the calculation of excitation energies of large molecules. *J. Comput. Chem.* **2016**, *37*, 1425–1441.
- [248] Laqua, H.; Thompson, T. H.; Kussmann, J.; Ochsenfeld, C. Highly Efficient, Linear-Scaling Seminumerical Exact-Exchange Method for Graphic Processing Units. *J. Chem. Theory Comput.* **2020**, *16*, 1456–1468.
- [249] Maier, T. M.; Ikabata, Y.; Nakai, H. Efficient Semi-Numerical Implementation of Relativistic Exact Exchange within the Infinite-Order Two-Component Method Using a Modified Chain-of-Spheres Method. *J. Chem. Theory Comput.* **2019**, *15*, 4745–4763.
- [250] Ahlrichs, R.; Bär, M.; Häser, M.; Horn, H.; Kölmel, C. Electronic structure calculations on workstation computers: The program system turbomole. *Chem. Phys. Lett.* **1989**, *162*, 165–169.

- [251] Send, R.; Furche, F. First-order nonadiabatic couplings from time-dependent hybrid density functional response theory: Consistent formalism, implementation, and performance. *J. Chem. Phys.* **2010**, *132*, 044107.
- [252] Rappoport, D.; Furche, F. Lagrangian approach to molecular vibrational Raman intensities using time-dependent hybrid density functional theory. *J. Chem. Phys.* **2007**, *126*, 201104.
- [253] Davidson, E. R. The iterative calculation of a few of the lowest eigenvalues and corresponding eigenvectors of large real-symmetric matrices. *J. Comp. Phys.* **1975**, *17*, 87–94.
- [254] Chari, M.; Salon, S. *Numerical Methods in Electromagnetism*; Academic Press: Cambridge, **2000**, pp. 105–122.
- [255] Weigend, F.; Ahlrichs, R. Balanced basis sets of split valence, triple zeta valence and quadruple zeta valence quality for H to Rn: Design and assessment of accuracy. *Phys. Chem. Chem. Phys.* **2005**, *7*, 3297–3305.
- [256] Weigend, F.; Furche, F.; Ahlrichs, R. Gaussian basis sets of quadruple zeta valence quality for atoms H–Kr. *J. Chem. Phys.* **2003**, *119*, 12753–12762.
- [257] Rappoport, D.; Furche, F. Property-optimized Gaussian basis sets for molecular response calculations. *J. Chem. Phys.* **2010**, *133*, 134105.
- [258] Hehre, W. J.; Stewart, R. F.; Pople, J. A. Self-Consistent Molecular-Orbital Methods. I. Use of Gaussian Expansions of Slater-Type Atomic Orbitals. *J. Chem. Phys.* **1969**, *51*, 2657–2664.
- [259] Dunning Jr., T. H. Gaussian basis sets for use in correlated molecular calculations. I. The atoms boron through neon and hydrogen. *J. Chem. Phys.* **1989**, *90*, 1007–1023.
- [260] Kendall, R. A.; Dunning, T. H.; Harrison, R. J. Electron affinities of the first-row atoms revisited. Systematic basis sets and wave functions. *J. Chem. Phys.* **1992**, *96*, 6796–6806.
- [261] Jensen, F. Polarization consistent basis sets: Principles. *J. Chem. Phys.* **2001**, *115*, 9113–9125.
- [262] Jensen, F. Polarization consistent basis sets. II. Estimating the Kohn–Sham basis set limit. *J. Chem. Phys.* **2002**, *116*, 7372–7379.

- [263] Furche, F.; Krull, B. T.; Nguyen, B. D.; Kwon, J. Accelerating molecular property calculations with nonorthonormal Krylov space methods. *J. Chem. Phys.* **2016**, *144*, 174105.
- [264] Grotjahn, R.; Kaupp, M. Validation of Local Hybrid Functionals for Excited States: Structures, Fluorescence, Phosphorescence, and Vibronic Spectra. *J. Chem. Theory Comput.* **2020**, *16*, 5821–5834.
- [265] Jensen, P.; Bunker, P. R. The geometry and the inversion potential function of formaldehyde in the \tilde{A}^1A_2 and \tilde{a}^3A_2 electronic states. *J. Mol. Spectrosc.* **1982**, *94*, 114–125.
- [266] Budzák, Š.; Scalmani, G.; Jacquemin, D. Accurate Excited-State Geometries: A CASPT2 and Coupled-Cluster Reference Database for Small Molecules. *J. Chem. Theory Comput.* **2017**, *13*, 6237–6252.
- [267] Brémond, E.; Savarese, M.; Adamo, C.; Jacquemin, D. Accuracy of TD-DFT Geometries: A Fresh Look. *J. Chem. Theory Comput.* **2018**, *14*, 3715–3727.
- [268] Huet, T.; Godefroid, M.; Herman, M. The \tilde{A} electronic state of acetylene: Geometry and axis-switching effects. *J. Mol. Spectrosc.* **1990**, *144*, 32–44.
- [269] Ventura, E.; Dallos, M.; Lischka, H. The valence-excited states T_1 – T_4 and S_1 – S_2 of acetylene: A high-level MR-CISD and MR-AQCC investigation of stationary points, potential energy surfaces, and surface crossings. *J. Chem. Phys.* **2003**, *118*, 1702–1713.
- [270] Kállay, M.; Gauss, J. Calculation of excited-state properties using general coupled-cluster and configuration-interaction models. *J. Chem. Phys.* **2004**, *121*, 9257–9269.
- [271] Loos, P.-F.; Galland, N.; Jacquemin, D. Theoretical 0–0 Energies with Chemical Accuracy. *J. Phys. Chem. Lett.* **2018**, *9*, 4646–4651.
- [272] Jacquemin, D. What is the Key for Accurate Absorption and Emission Calculations, Energy or Geometry?. *J. Chem. Theory Comput.* **2018**, *14*, 1534–1543.
- [273] Suellen, C.; Freitas, R. G.; Loos, P.-F.; Jacquemin, D. Cross-Comparisons between Experiment, TD-DFT, CC, and ADC for Transition Energies. *J. Chem. Theory Comput.* **2019**, *15*, 4581–4590.

- [274] Bousquet, D.; Fukuda, R.; Jacquemin, D.; Ciofini, I.; Adamo, C.; Ehara, M. Benchmark Study on the Triplet Excited-State Geometries and Phosphorescence Energies of Heterocyclic Compounds: Comparison Between TD-PBE0 and SAC-CI. *J. Chem. Theory Comput.* **2014**, *10*, 3969–3979.
- [275] Dierksen, M.; Grimme, S. The Vibronic Structure of Electronic Absorption Spectra of Large Molecules: A Time-Dependent Density Functional Study on the Influence of “Exact” Hartree–Fock Exchange. *J. Phys. Chem. A* **2004**, *108*, 10225–10237.
- [276] Dierksen, M.; Grimme, S. Density functional calculations of the vibronic structure of electronic absorption spectra. *J. Chem. Phys.* **2004**, *120*, 3544–3554.
- [277] Weigend, F. Accurate Coulomb-fitting basis sets for H to Rn. *Phys. Chem. Chem. Phys.* **2006**, *8*, 1057–1065.
- [278] Aidas, K.; Angeli, C.; Bak, K. L.; Bakken, V.; Bast, R.; Boman, L.; Christiansen, O.; Cimiraglia, R.; Coriani, S.; Dahle, P.; Dalskov, E. K.; Ekström, U.; Enevoldsen, T.; Eriksen, J. J.; Ettenhuber, P.; Fernández, B.; Ferrighi, L.; Fliegl, H.; Frediani, L.; Hald, K.; Halkier, A.; Hättig, C.; Heiberg, H.; Helgaker, T.; Hennum, A. C.; Hettema, H.; Hjertenæs, E.; Høst, S.; Høyvik, I.-M.; Iozzi, M. F.; Jansík, B.; Jensen, H. J. Aa.; Jonsson, D.; Jørgensen, P.; Kauczor, J.; Kirpekar, S.; Kjærgaard, T.; Klopper, W.; Knecht, S.; Kobayashi, R.; Koch, H.; Kongsted, J.; Krapp, A.; Kristensen, K.; Ligabue, A.; Lutnæs, O. B.; Melo, J. I.; Mikkelsen, K. V.; Myhre, R. H.; Neiss, C.; Nielsen, C. B.; Norman, P.; Olsen, J.; Olsen, J. M. H.; Osted, A.; Packer, M. J.; Pawłowski, F.; Pedersen, T. B.; Provasi, P. F.; Reine, S.; Rinkevicius, Z.; Ruden, T. A.; Ruud, K.; Rybkin, V. V.; Salek, P.; Samson, C. C. M.; de Merás, A. S.; Saue, T.; Sauer, S. P. A.; Schimmelpfennig, B.; Sneskov, K.; Steindal, A. H.; Sylvester-Hvid, K. O.; Taylor, P. R.; Teale, A. M.; Tellgren, E. I.; Tew, D. P.; Thorvaldsen, A. J.; Thøgersen, L.; Vahtras, O.; Watson, M. A.; Wilson, D. J. D.; Ziolkowski, M.; Ågren, H. The Dalton quantum chemistry program system. *Wiley Interdiscip. Rev. Comput. Mol. Sci.* **2014**, *4*, 269–284.
- [279] Hald, K.; Hättig, C.; Jørgensen, P. Triplet excitation energies in the coupled cluster singles and doubles model using an explicit triplet spin coupled excitation space. *J. Chem. Phys.* **2000**, *113*, 7765–7772.
- [280] Hald, K.; Hättig, C.; Olsen, J.; Jørgensen, P. CC3 triplet excitation energies using an explicit spin coupled excitation space. *J. Chem. Phys.* **2001**, *115*, 3545–3552.

- [281] Hättig, C.; Weigend, F. CC2 excitation energy calculations on large molecules using the resolution of the identity approximation. *J. Chem. Phys.* **2000**, *113*, 5154–5161.
- [282] Hättig, C.; Köhn, A.; Hald, K. First-order properties for triplet excited states in the approximated coupled cluster model CC2 using an explicitly spin coupled basis. *J. Chem. Phys.* **2002**, *116*, 5401–5410.
- [283] Hättig, C.; Hald, K. Implementation of RI-CC2 triplet excitation energies with an application to *trans*-azobenzene. *Phys. Chem. Chem. Phys.* **2002**, *4*, 2111–2118.
- [284] Feller, D. Benchmarks of improved complete basis set extrapolation schemes designed for standard CCSD(T) atomization energies. *J. Chem. Phys.* **2013**, *138*, 074103.
- [285] Arbuznikov, A. V.; Kaupp, M.; Bahmann, H. From local hybrid functionals to “localized local hybrid” potentials: Formalism and thermochemical tests. *J. Chem. Phys.* **2006**, *124*, 204102.
- [286] Grotjahn, R.; Lauter, G. J.; Haasler, M.; Kaupp, M. Evaluation of Local Hybrid Functionals for Electric Properties: Dipole Moments and Static and Dynamic Polarizabilities. *J. Phys. Chem. A* **2020**, *124*, 8346–8358.
- [287] Guareschi, R.; Filippi, C. Ground- and Excited-State Geometry Optimization of Small Organic Molecules with Quantum Monte Carlo. *J. Chem. Theory Comput.* **2013**, *9*, 5513–5525.
- [288] Wang, J.; Durbeej, B. How accurate are TD-DFT excited-state geometries compared to DFT ground-state geometries?. *J. Comput. Chem.* **2020**, *41*, 1718–1729.
- [289] Köhn, A.; Hättig, C. Analytic gradients for excited states in the coupled-cluster model CC2 employing the resolution-of-the-identity approximation. *J. Chem. Phys.* **2003**, *119*, 5021–5036.
- [290] Loos, P.-F.; Scemama, A.; Blondel, A.; Garniron, Y.; Caffarel, M.; Jacquemin, D. A Mountaineering Strategy to Excited States: Highly Accurate Reference Energies and Benchmarks. *J. Chem. Theory Comput.* **2018**, *14*, 4360–4379.
- [291] Loos, P.-F.; Lipparini, F.; Boggio-Pasqua, M.; Scemama, A.; Jacquemin, D. A Mountaineering Strategy to Excited States: Highly Accurate Energies and Benchmarks for Medium Sized Molecules. *J. Chem. Theory Comput.* **2020**, *16*, 1711–1741.

- [292] Loos, P.-F.; Scemama, A.; Boggio-Pasqua, M.; Jacquemin, D. Mountaineering Strategy to Excited States: Highly Accurate Energies and Benchmarks for Exotic Molecules and Radicals. *J. Chem. Theory Comput.* **2020**, *16*, 3720–3736.
- [293] Peach, M. J. G.; Williamson, M. J.; Tozer, D. J. Influence of Triplet Instabilities in TDDFT. *J. Chem. Theory Comput.* **2011**, *7*, 3578–3585.
- [294] Peach, M. J. G.; Tozer, D. J. Overcoming Low Orbital Overlap and Triplet Instability Problems in TDDFT. *J. Phys. Chem. A* **2012**, *116*, 9783–9789.
- [295] Scott, A. P.; Radom, L. Harmonic Vibrational Frequencies: An Evaluation of Hartree–Fock, Møller–Plesset, Quadratic Configuration Interaction, Density Functional Theory, and Semiempirical Scale Factors. *J. Phys. Chem.* **1996**, *100*, 16502–16513.
- [296] Ferguson, J.; Reeves, L. W.; Schneider, W. G. VAPOR ABSORPTION SPECTRA AND OSCILLATOR STRENGTHS OF NAPHTHALENE, ANTHRACENE, AND PYRENE. *Can. J. Chem.* **1957**, *35*, 1117–1136.
- [297] Greiner, J.; Sundholm, D. Calculation of vibrationally resolved absorption and fluorescence spectra of the rylenes. *Phys. Chem. Chem. Phys.* **2020**, *22*, 2379–2385.
- [298] Dyck, R. H.; McClure, D. S. Ultraviolet Spectra of Stilbene, *p*-Monohalogen Stilbenes, and Azobenzene and the *trans* to *cis* Photoisomerization Process. *J. Chem. Phys.* **1962**, *36*, 2326–2345.
- [299] Itoh, T. Solvent-polarizability dependence of the relative $2\ ^1A_g(S_1)$ - and $1\ ^1B_u(S_2)$ -fluorescence intensities of 1,14-diphenyl-1,3,5,7,9,11,13-tetradecaheptaene. *J. Chem. Phys.* **2003**, *119*, 4516–4521.
- [300] Shida, T.; Iwata, S.; Imamura, M. Electronic Absorption Spectra of Ion Radicals and Their Molecular Orbital Interpretation. IV. Anion Radicals of Aromatic and Unsaturated Aliphatic Carbonyl Compounds. *J. Phys. Chem.* **1974**, *78*, 741–748.
- [301] Jeanmaire, D. L.; Van Duyne, R. P. Resonance Raman spectroelectrochemistry. 2. Scattering spectroscopy accompanying excitation of the lowest $^2B_{1u}$ excited state of the tetracyanoquinodimethane anion radical. *J. Am. Chem. Soc.* **1976**, *98*, 4029–4033.

- [302] Li, Y. H.; Lim, E. C. Vibronic perturbation of the lowest triplet state and phosphorescence of aromatic ketones. *Chem. Phys. Lett.* **1970**, *7*, 15–18.
- [303] Takemura, T.; Baba, H. Effects of Substitution on the Phosphorescence Process of Aromatic Carbonyl Compounds. *Bull. Chem. Soc. Jpn.* **1969**, *42*, 2756–2762.
- [304] Karton, A.; Tarnopolsky, A.; Lamère, J.-F.; Schatz, G. C.; Martin, J. M. L. Highly Accurate First-Principles Benchmark Data Sets for the Parametrization and Validation of Density Functional and Other Approximate Methods. Derivation of a Robust, Generally Applicable, Double-Hybrid Functional for Thermochemistry and Thermochemical Kinetics. *J. Phys. Chem. A* **2008**, *112*, 12868–12886.
- [305] Jiang, W.; Laury, M. L.; Powell, M.; Wilson, A. K. Comparative Study of Single and Double Hybrid Density Functionals for the Prediction of 3d Transition Metal Thermochemistry. *J. Chem. Theory Comput.* **2012**, *8*, 4102–4111.
- [306] Laurent, A. D.; Jacquemin, D. TD-DFT benchmarks: A review. *Int. J. Quantum Chem.* **2013**, *113*, 2019–2039.
- [307] Ghosh, S.; Verma, P.; Cramer, C. J.; Gagliardi, L.; Truhlar, D. G. Combining Wave Function Methods with Density Functional Theory for Excited States. *Chem. Rev.* **2018**, *118*, 7249–7292.
- [308] Schattenberg, C. J.; Maier, T. M.; Kaupp, M. Lessons from the Spin-Polarization/Spin-Contamination Dilemma of Transition-Metal Hyperfine Couplings for the Construction of Exchange-Correlation Functionals. *J. Chem. Theory Comput.* **2018**, *14*, 5653–5672.
- [309] Wodyński, A.; Kaupp, M. Noncollinear Relativistic Two-Component X2C Calculations of Hyperfine Couplings Using Local Hybrid Functionals. Importance of the High-Density Coordinate Scaling Limit. *J. Chem. Theory Comput.* **2020**, *16*, 314–325.
- [310] Jørgensen, M. W.; Faber, R.; Ligabue, A.; Sauer, S. P. A. Benchmarking Correlated Methods for Frequency-Dependent Polarizabilities: Aromatic Molecules with the CC3, CCSD, CC2, SOPPA, SOPPA(CC2), and SOPPA(CCSD) Methods. *J. Chem. Theory Comput.* **2020**, *16*, 3006–3018.
- [311] Salek, P.; Helgaker, T.; Vahtras, O.; Ågren, H.; Jonsson, D.; Gauss, J. A comparison of density-functional-theory and coupled-cluster frequency-dependent polarizabilities and hyperpolarizabilities. *Mol. Phys.* **2005**, *103*, 439–450.

- [312] Hammond, J. R.; Govind, N.; Kowalski, K.; Autschbach, J.; Xantheas, S. S. Accurate dipole polarizabilities for water clusters $n = 2 - 12$ at the coupled-cluster level of theory and benchmarking of various density functionals. *J. Chem. Phys.* **2009**, *131*, 214103.
- [313] Hickey, A. L.; Rowley, C. N. Benchmarking Quantum Chemical Methods for the Calculation of Molecular Dipole Moments and Polarizabilities. *J. Phys. Chem. A* **2014**, *118*, 3678–3687.
- [314] Karne, A. S.; Vaval, N.; Pal, S.; Vásquez-Pérez, J. M.; Köster, A. M.; Calaminici, P. Systematic comparison of DFT and CCSD dipole moments, polarizabilities and hyperpolarizabilities. *Chem. Phys. Lett.* **2015**, *635*, 168–173.
- [315] Verma, P.; Truhlar, D. G. Can Kohn–Sham density functional theory predict accurate charge distributions for both single-reference and multi-reference molecules?. *Phys. Chem. Chem. Phys.* **2017**, *19*, 12898–12912.
- [316] Arbuznikov, A. V.; Kaupp, M. Advances in local hybrid exchange-correlation functionals: from thermochemistry to magnetic-resonance parameters and hyperpolarizabilities. *Int. J. Quantum Chem.* **2011**, *111*, 2625–2638.
- [317] Jensen, F.; Helgaker, T. Polarization consistent basis sets. V. The elements Si–Cl. *J. Chem. Phys.* **2004**, *121*, 3463–3470.
- [318] Jensen, F. Polarization consistent basis sets. III. The importance of diffuse functions. *J. Chem. Phys.* **2002**, *117*, 9234–9240.
- [319] Jensen, F. Polarization Consistent Basis Sets. 4: The Elements He, Li, Be, B, Ne, Na, Mg, Al, and Ar. *J. Phys. Chem. A* **2007**, *111*, 11198–11204.
- [320] Zapata, J. C.; McKemmish, L. K. Computation of Dipole Moments: A Recommendation on the Choice of the Basis Set and the Level of Theory. *J. Phys. Chem. A* **2020**, *124*, 7538–7548.
- [321] Frisch, M. J.; Trucks, G. W.; Schlegel, H. B.; Scuseria, G. E.; Robb, M. A.; Cheeseman, J. R.; Scalmani, G.; Barone, V.; Petersson, G. A.; Nakatsuji, H.; Li, X.; Caricato, M.; Marenich, A. V.; Bloino, J.; Janesko, B. G.; Gomperts, R.; Mennucci, B.; Hratchian, H. P.; Ortiz, J. V.; Izmaylov, A. F.; Sonnenberg, J. L.; Williams-Young, D.; Ding, F.; Lipparini, F.; Egidi, F.; Goings, J.; Peng, B.; Petrone, A.; Henderson, T.; Ranasinghe, D.; Zakrzewski, V. G.; Gao, J.;

- Rega, N.; Zheng, G.; Liang, W.; Hada, M.; Ehara, M.; Toyota, K.; Fukuda, R.; Hasegawa, J.; Ishida, M.; Nakajima, T.; Honda, Y.; Kitao, O.; Nakai, H.; Vreven, T.; Throssell, K.; Montgomery, Jr., J. A.; Peralta, J. E.; Ogliaro, F.; Bearpark, M. J.; Heyd, J. J.; Brothers, E. N.; Kudin, K. N.; Staroverov, V. N.; Keith, T. A.; Kobayashi, R.; Normand, J.; Raghavachari, K.; Rendell, A. P.; Burant, J. C.; Iyengar, S. S.; Tomasi, J.; Cossi, M.; Millam, J. M.; Klene, M.; Adamo, C.; Cammi, R.; Ochterski, J. W.; Martin, R. L.; Morokuma, K.; Farkas, O.; Foresman, J. B.; Fox, D. J. "Gaussian 16 Revision C.01", 2016 Gaussian Inc. Wallingford CT.
- [322] Peverati, R.; Head-Gordon, M. Orbital optimized double-hybrid density functionals. *J. Chem. Phys.* **2013**, *139*, 024110.
- [323] Sancho-García, J. C.; Pérez-Jiménez, A. J.; Savarese, M.; Brémond, E.; Adamo, C. Importance of Orbital Optimization for Double-Hybrid Density Functionals: Application of the OO-PBE-QIDH Model for Closed- and Open-Shell Systems. *J. Phys. Chem. A* **2016**, *120*, 1756–1762.
- [324] Brakestad, A.; Jensen, S. R.; Wind, P.; D'Alessandro, M.; Genovese, L.; Hopmann, K. H.; Frediani, L. Static Polarizabilities at the Basis Set Limit: A Benchmark of 124 Species. *J. Chem. Theory Comput.* **2020**, *16*, 4874–4882.
- [325] Arbuznikov, A. V.; Kaupp, M. Localized Hybrid Exchange-Correlation Potentials for Kohn–Sham DFT Calculations of NMR and EPR Parameters. *Int. J. Quantum Chem.* **2005**, *104*, 261–271.
- [326] Cortona, P. Note: Theoretical mixing coefficients for hybrid functionals. *J. Chem. Phys.* **2012**, *136*, 086101.
- [327] Guido, C. A.; Brémond, E.; Adamo, C.; Cortona, P. Communication: One third: A new recipe for the PBE0 paradigm. *J. Chem. Phys.* **2013**, *138*, 021104.
- [328] Jørgensen, M. W.; Sauer, S. P. A. Benchmarking doubles-corrected random-phase approximation methods for frequency dependent polarizabilities: Aromatic molecules calculated at the RPA, HRPDA, RPA(D), HRPDA(D), and SOPPA levels. *J. Chem. Phys.* **2020**, *152*, 234101.
- [329] Champagne, B.; Perpète, E. A.; van Gisbergen, S. J. A.; Baerends, E.-J.; Snijders, J. G.; Soubra-Ghaoui, C.; Robins, K. A.; Kirtman, B. Assessment of conventional density functional schemes for computing the polarizabilities and hyper-

- polarizabilities of conjugated oligomers: An *ab initio* investigation of polyacetylene chains. *J. Chem. Phys.* **1998**, *109*, 10489–10498.
- [330] Champagne, B.; Perpète, E. A.; Jacquemin, D.; van Gisbergen, S. J. A.; Baerends, E.-J.; Soubra-Ghaoui, C.; Robins, K. A.; Kirtman, B. Assessment of Conventional Density Functional Schemes for Computing the Dipole Moment and (Hyper)polarizabilities of Push–Pull π -Conjugated Systems. *J. Phys. Chem. A* **2000**, *104*, 4755–4763.
- [331] Haasler, M. Personal communication, **2020**.
- [332] Furche, F. Personal communication, **2019**.
- [333] Parker, S. M.; Rappoport, D.; Furche, F. Quadratic Response Properties from TDDFT: Trials and Tribulations. *J. Chem. Theory Comput.* **2018**, *14*, 807–819.
- [334] Itoh, T. Low-Lying Electronic States, Spectroscopy, and Photophysics of Linear Para Acenequinones. *Chem. Rev.* **1995**, *95*, 2351–2368.
- [335] Itoh, T.; Hashimoto, R. Temperature dependence of the emission spectra of *p*-benzoquinone in a *p*-dichlorobenzene matrix. *J. Lumin.* **2012**, *132*, 236–239.
- [336] Polewski, K.; Zinger, D.; Trunk, J.; Sutherland, J. C. Ultraviolet absorption and luminescence of matrix-isolated adenine. *Radiat. Phys. Chem.* **2011**, *80*, 1092–1098.
- [337] Mantulin, W. W.; Song, P.-S. Excited states of skin-sensitizing coumarins and psoralens. Spectroscopic studies. *J. Am. Chem. Soc.* **1973**, *95*, 5122–5129.
- [338] Manna, A.; Chakravorti, S. Charge Transfer in 1,8-Naphthalimide: A Combined Theoretical and Experimental Approach. *Photochem. Photobiol.* **2010**, *86*, 47–54.
- [339] Berlman, I. B. *Handbook of fluorescence spectra of aromatic molecules*; Academic Press: New York, **1965**, p. 133.
- [340] Sakamoto, Y.; Suzuki, T.; Kobayashi, M.; Gao, Y.; Fukai, Y.; Inoue, Y.; Sato, F.; Tokito, S. Perfluoropentacene: High-Performance p-n Junctions and Complementary Circuits with Pentacene. *J. Am. Chem. Soc.* **2004**, *126*, 8138–8140.
- [341] Halasinski, T. M.; Weisman, J. L.; Ruiterkamp, R.; Lee, T. J.; Salama, F.; Head-Gordon, M. Electronic Absorption Spectra of Neutral Perylene (C₂₀H₁₂), Terylene (C₃₀H₁₆), and Quaterylene (C₄₀H₂₀) and Their Positive and Negative Ions:

- Ne Matrix-Isolation Spectroscopy and Time-Dependent Density Functional Theory Calculations. *J. Phys. Chem. A* **2003**, *107*, 3660–3669.
- [342] Nijegorodov, N.; Mabbs, R.; Downey, W. Evolution of absorption, fluorescence, laser and chemical properties in the series of compounds perylene, benzo(ghi)perylene and coronene. *Spectrochim. Acta A* **2001**, *57*, 2673–2685.
- [343] Grimme, J.; Scherf, U. Planar *para*-phenylene oligomers. *Macromol. Chem. Phys.* **1996**, *197*, 2297–2304.
- [344] Ohshima, Y.; Fujii, T.; Fujita, T.; Inaba, D.; Baba, M. S_1 1A_2 ($n\pi^*$) and S_2 $^1A_1(\pi\pi^*)$ States of Jet-Cooled Xanthone. *J. Phys. Chem. A* **2003**, *107*, 8851–8855.
- [345] Mazaki, Y.; Kobayashi, K. Synthesis of tetrathieno-acene and pentathieno-acene: UV-spectral trend in a homologous series of thieno-acenes. *Tetrahedron Lett.* **1989**, *30*, 3315–3318.
- [346] Scholz, R.; Kobitski, A.; Kampen, T.; Schreiber, M.; Zahn, D.; Jungnickel, G.; Elstner, M.; Sternberg, M.; Frauenheim, T. Resonant Raman spectroscopy of 3,4,9,10-perylene-tetracarboxylic-dianhydride epitaxial films. *Phys. Rev. B* **2000**, *61*, 13659–13669.
- [347] Guo, X.; Gan, Z.; Luo, H.; Araki, Y.; Zhang, D.; Zhu, D.; Ito, O. Photoinduced Electron-Transfer Processes of Tetrathiafulvalene-(Spacer)-(Naphthalenediimide)-(Spacer)-Tertrathiafulvalene Triads in Solution. *J. Phys. Chem. A* **2003**, *107*, 9747–9753.
- [348] Oelkrug, D.; Egelhaaf, H.-J.; Gierschner, J.; Tompert, A. *Synth. Met.* **1996**, *76*, 249 (as cited in Dierksen, M.; Grimme, S. *J. Phys. Chem. A* **2004**, *108*, 10225–10237).
- [349] Luňák, S.; Nepraš, M.; Hrdina, R.; Mustroph, H. Excited states of azo compounds. II. Vibrational structure of the electronic absorption spectra of 4,4'-di-substituted azobenzene derivatives. *Chem. Phys.* **1994**, *184*, 255–260.
- [350] Takeuchi, S.; Tahara, T. Femtosecond absorption study of photodissociation of diphenylcyclopropanone in solution: Reaction dynamics and coherent nuclear motion. *J. Chem. Phys.* **2004**, *120*, 4768–4776.
- [351] Leopold, D. G.; Vaida, V.; Granville, M. F. Direct absorption spectroscopy of jet-cooled polyenes. I. The $1^1B_u^+ \leftarrow 1^1A_g^-$ transition of *trans*, *trans*-1,3,5,7-octatetraene. *J. Chem. Phys.* **1984**, *81*, 4210–4217.

- [352] Kohler, B. E.; Schilke, D. E. Low-lying singlet states of a short polydiacetylene oligomer. *J. Chem. Phys.* **1987**, *86*, 5214–5215.
- [353] Slepko, A. D.; Hegmann, F. A.; Eisler, S.; Elliott, E.; Tykwinski, R. R. The surprising nonlinear optical properties of conjugated polyyne oligomers. *J. Chem. Phys.* **2004**, *120*, 6807–6810.
- [354] Berlman, I. B. *Handbook of fluorescence spectra of aromatic molecules*; Academic Press: New York, **1965**, p. 142.
- [355] Pocius, A. V.; Yardley, J. T. Electronic Absorption Spectra of the 4-R-1,2,4-Triazoline-3,5-diones (R = H, CH₃, CH₂CH₃, CH₂CH₂CH₂CH₃). *J. Am. Chem. Soc.* **1973**, *95*, 721–725.
- [356] Radziszewski, J. G.; Gil, M.; Gorski, A.; Spanget-Larsen, J.; Waluk, J.; Mróz, B. J. Electronic states of the phenoxyl radical. *J. Chem. Phys.* **2001**, *115*, 9733–9738.
- [357] Shida, T. *Electronic Absorption Spectra of Radical Ions*. Elsevier: Amsterdam, 1988 (as cited in Dierksen, M.; Grimme, S. *J. Phys. Chem. A* **2004**, *108*, 10225–10237).
- [358] Andrews, L.; Keisall, B. J.; Blankenship, T. A. Vibronic Absorption Spectra of Naphthalene and Substituted Naphthalene Cations in Solid Argon. *J. Phys. Chem.* **1982**, *86*, 2916–2926.
- [359] Szczepanski, J.; Vala, M.; Talbi, D.; Parisel, O.; Ellinger, Y. Electronic and vibrational spectra of matrix isolated anthracene radical cations: Experimental and theoretical aspects. *J. Chem. Phys.* **1993**, *98*, 4494–4511.
- [360] Pino, T.; Bréchnignac, P.; Dartois, E.; Demyk, K.; d’Hendecourt, L. Electronic spectroscopy of a cyclopentafused PAH cation, the fluorene⁺: comparison between gas phase and matrix spectra. *Chem. Phys. Lett.* **2001**, *339*, 64–70.
- [361] Fabre, P.-L.; Dumestre, F.; Soula, B.; Galibert, A.-M. Spectroelectrochemical behaviour in dimethylformamide of pseudo-oxocarbons dianions derived from the croconate dianion. *Electrochim. Acta* **2000**, *45*, 2697–2705.